

NASA Contractor Report 4754

1N-26
10074

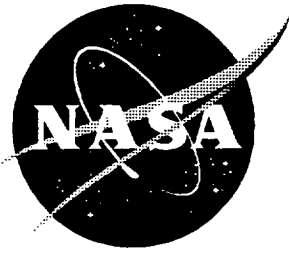
NASA-UVa Light Aerospace Alloy and Structures Technology Program: Aluminum-Based Materials for High Speed Aircraft

Semi-Annual Report January 1, 1993–June 30, 1993

Edited by
E. A. Starke, Jr.

Grant NAG1-745
Prepared for Langley Research Center

September 1996



NASA-UVa Light Aerospace Alloy and Structures Technology Program: Aluminum-Based Materials for High Speed Aircraft

Semi-Annual Report January 1, 1993–June 30, 1993

*Edited by
E. A. Starke, Jr.
University of Virginia • Charlottesville, Virginia*

Printed copies available from the following:

NASA Center for AeroSpace Information
800 Elkridge Landing Road
Linthicum Heights, MD 21090-2934
(301) 621-0390

National Technical Information Service (NTIS)
5285 Port Royal Road
Springfield, VA 22161-2171
(703) 487-4650

TABLE OF CONTENTS

	Page
Introduction	1
TASK 1. I/M 2XXX Alloy Development (Alcoa Lead; Boeing & Douglas Participation)	3
Subtask 1(i). I/M 2XXX and 6XXX Alloy Development (Boeing)	41
Subtask 1(ii). I/M 2XXX and 6XXX Alloy Development (Douglas)	48
TASK 2. I/M Al-Cu-Li-Mg-Ag Alloy Development (Reynolds Lead; UVa, Boeing & Douglas Participation)	51
Subtask 2A. Evaluate RX818 Variation Alloys as Model Materials to Understand the Role of Various Strengthening Phases During Thermal Exposure (Reynolds Metals Company)	54
Subtask 2B. A Study of the Microstructure/Property Evolution Characteristics of the Al-Li-Cu-Mg-Ag System with RX818 (University of Virginia)	77
Subtask 2C. Al-Cu-Li-Mg-Ag Alloy Development (Boeing)	94
Subtask 2D. Al-Cu-Li-Mg-Ag Alloy Development (Douglas)	94
TASK 3. Characterization of Alloy 1143 (Alcoa)	95
TASK 4A. Al-Si-Ge-X Alloy Development (University of Virginia)	96
TASK 4B. Texture and Precipitate Effects on Mechanical Properties and Anisotropy of Al-Cu-Mg-X Alloys (University of Virginia)	117

	Page
TASK 6. Processing-Based Improvements in the Mechanical Isotropy and Intermediate Temperature Damage Tolerance of Al-Fe-V-Si Alloy 8009 (University of Virginia)	129
TASK 8. Investigation of the Formation of the Ω Phase in Modified 2009 and Characterization of the Modified Alloys' Thermomechanical Properties (University of Virginia)	159
TASK 10A. Trade Studies in Support of an Aluminum HSCT (Boeing)	199
TASK 10B. Materials Technology Trade-Off Studies for the Airframe (Douglas)	210
TASK 11. Fracture Toughness Test Development (Boeing)	220

Introduction

Market projections indicate that a substantial potential demand exists for a high-speed civil transport (HSCT) to operate in the long-range international market. Preliminary design and technology development efforts are underway to better understand all requirements including the technical and economic feasibility of the HSCT. Ongoing studies show airplanes designed to fly between Mach 2.0 and 2.5, with a capacity of 250 to 300 passengers and a range of at least 5000 nmi, have the best opportunity of meeting the economic objectives. The key critical development issue for an economically viable HSCT airframe will be the development of materials and processes which allow a complex, highly-stressed, extremely weight-efficient airframe to be fabricated and assembled for a dollar-per-pound not greatly different than today's mature airframes. Considering challenges in environmental control, propulsion, and materials technologies, it is believed that an acceptable aircraft could be certified for airline service in 2005.

The present study titled "Aluminum-Based Materials for High Speed Aircraft" was initiated to identify the technology needs associated with advanced, low-cost aluminum base materials for use as primary structural materials. Using a reference baseline aircraft, these materials concepts will be further developed and evaluated both technically and economically to determine the most attractive combinations of designs, materials, and manufacturing techniques for major structural sections of an HSCT. Once this has been accomplished, the baseline aircraft will be resized, if applicable, and performance objectives and economic evaluations made to determine aircraft operating costs.

The two primary objectives of this study are: (1) to identify the most promising aluminum-based materials with respect to major structural use on the HSCT and to further develop those materials, and (2) to assess these materials through detailed

trade and evaluation studies with respect to their structural efficiency on the HSCT.

TASK 1. I/M 2XXX ALLOY DEVELOPMENT (Alcoa)

Principal Investigator: Dr. Lynne M. Angers

Objective

The primary objective of this task is to develop a damage tolerant aluminum-based material for the lower wing and fuselage of a Mach 2.0 aircraft. This material must first meet preliminary strength and toughness targets at room temperature and then several criteria associated with elevated temperature service (e.g., retention of room temperature properties after exposure, performance at the operating temperature and resistance to creep deformation).

The ingot metallurgy (I/M) 2XXX alloys are under consideration here because existing Al-Cu-Mg alloys combine relatively high strengths with good thermal stability.

Background

During the last two reporting periods, a series of four I/M 2XXX alloys were selected, fabricated and characterized [1,2]. In addition, six more alloys were carried through a companion program at Alcoa [3]. The four alloys included in the first iteration were designed to study the effects of Mg, Si and Ag on precipitation in 2519-type alloys. They were: S. No. 689245: a 2519 control; S. No. 689246: 2519 with 0.25 Si; S. No. 689247: 2519 with 0.5 Mg; and S. No. 689248: 2519 with 0.5 Mg and 0.5 Ag. The alloys in the companion study were designed to look at Ag effects, alternate Cu/Mg ratios and higher Mn levels.

All alloys were cast as 6" x 16" x > 60" ingots, preheated and rolled to 0.125" thick sheet. Sheet was solution heat treated, cold water quenched, stretched 8% and artificially aged

at 350°F to produce T8-type tempers. Characterization in Phase I emphasized microstructures and room temperature strength and plane stress fracture toughness. Alcoa uses the effective crack length to determine the net section stress and uses the value of 0.8 to be conservative. The ASTM criterion is less restrictive, using the physical crack length to determine the net section stress and requiring that the net section stress divided by the tensile yield strength be 1.0.

The best strength/toughness combinations were obtained in two of the alloys from the companion study. Plane stress fracture toughness is plotted as a function of tensile yield strength in Fig. 1 for the peak aged conditions of sheet from both studies. All plane stress toughness data were invalid, since the criterion requiring that the net section stress divided by the yield strength is less than or equal to 0.80 was not met. Sheet from S. Nos. 689250 (nominally Al-5.2 Cu-0.8 Mg-0.5 Ag-0.15 Zr) and two variants of 689251 (nominally Al-5.2 Cu-0.8 Mg-0.5 Ag-0.6 Mn-0.1 V-0.15 Zr) exhibited the best strength/toughness combinations. Promising strength/toughness combinations were also obtained in two of the alloys from the original study, e.g., S. Nos. 689247 (the high Mg version of 2519, nominally Al-5.85 Cu-0.5 Mg-0.3 Mn-0.1 V-0.15 Zr) and 689248 (the 2519 variant with Ag and high Mg, nominally Al-5.85 Cu-0.5 Ag-0.3 Mn-0.1 V-0.15 Zr). Included in that figure are data for the four variants from the last reporting period, i.e. S. Nos. 689245-T8, 689246-T8, 689247-T8, and 689248-T8, and for three variants from the Alcoa companion program, i.e. S. Nos. 689250-T8, 689251A-T8 and 689251C-T8. The designations of 689251A-T8 and 689251C-T8 indicate that two different sheet variants were produced from the alloy with S. No. 689251 by using different preheating and solution heat treating temperatures.

Optical metallography on the four alloys suggests that the grain structures vary. Sheet from the two alloys from the first iteration of this study, e.g., S. Nos. 689247 and 689248, appeared recrystallized. Sheet from S. Nos. 689250 and 689251 appeared

unrecrystallized. Since an unrecrystallized structure is expected to have a higher strength/toughness combination than a recrystallized structure, one might hypothesize that the better combinations for S. Nos. 689250 and 689251 may be due to the differences in grain structure of those two alloys compared to S. Nos. 689247 and 689248, rather than to inherent strength/toughness differences. Furthermore, one might guess that the properties of the recrystallized sheet would be more isotropic than those of the unrecrystallized sheet. Those recrystallized alloys might have better strength/toughness combinations than the unrecrystallized alloys in the transverse orientations. Therefore, all four alloys were judged to be worth further evaluation.

The nominal compositions of all four of the promising alloys contain more solute than can be put into an aluminum solid solution. That excess solute cannot be used for strengthening. Instead, it is present in coarse deleterious constituent. Therefore, all compositions must be adjusted eventually if they are to be commercialized. However, available ingot sections, having somewhat suboptimal compositions, were selected for use in the second phase of this program.

In Phase II, various T8-type aging practices will be studied for the four alloys. Room temperature strength/toughness combinations will be measured before and after elevated temperature exposures. Once one or two alloys are judged to be superior to the rest, the composition(s) will be adjusted and new ingot(s) will be cast.

Procedure

Two ingot sections, about 5.5" x 14" x 14", from each of four compositions were preheated and rolled to 0.125" thick sheet. Nominal and actual compositions, measured at the mid-width and mid-depth, are compared in Table I.

All metal was preheated and rolled to 0.125" thick sheet, at

least 22" wide. A single aggressive preheat practice was selected for each composition. Temperatures were selected using differential scanning calorimetry results on as-cast and preheated ingots. At least 11 pieces, about 60" long, were produced for each S. No. from the ingot stock.

Six pieces of each composition were solution heat treated, cold water quenched and stretched. Sheet from S. Nos. 689247, 689250 and 689251 were stretched 8%. Sheet from S. No. 689248 was stretched only 2%, as greater amounts of stretch caused failure of the sheet.

Processing parameters for the alloys, e.g., maximum temperatures of the preheats, solution heat treatment temperatures and the amounts of stretch, are summarized in Table II.

Sheet from each of the four alloys was aged using three practices:

- isothermal aging at 275°F
- isothermal aging at 325°F
- two step aging, using 24 hr at 275°F + various times at 325°F.

Longitudinal and transverse tensile tests were done to determine the peak aging times for each aging practice and alloy. Plane stress fracture toughness was measured for the peak aged conditions in the L-T and T-L orientations using duplicate 6.3" x 20" center cracked panels.

Additional sheet was peak aged and elevated temperature exposures of 1000 hr at 225°F and 1000 hr at 275°F were initiated.

Li-bearing Alloys: Four 2" x 10" x 14" Al-Cu-Li-Zr-(In) ingots were cast for UVA researchers. These alloys are 2020 variants which utilize Zr for grain structure control. They are identical to a set of ingots cast in 1992, except that the new ingots contain Mg. Two ingots contain In additions as nucleation aides and two do not. Their actual compositions are given in

Table III. The alloys were preheated and rolled to plate and sheet.

Results and Discussion

Optical micrographs of longitudinal sections of sheet are presented in Fig. 2. These micrographs reveal undissolved constituent in sheet from S. Nos. 689247-T8, 689250-T8 and 689251-T8 and rosettes which are characteristic of eutectic melting in sheet from S. No. 689248. The presence of undissolved constituent is consistent with the fact that compositions contain more solute than the maximum solubility in aluminum. The inability to obtain 8% stretch in sheet from S. No. 689248 without failure is consistent with the evidence of melting in that alloy.

The grain structures could not be described unambiguously with the techniques used in this study. Polarized light viewing of anodically etched samples revealed structures which appeared to be fully recrystallized in sheet from S. Nos. 689247 and 689248, with equiaxed grains at the surfaces and elongated grains at the center (Fig. 3). Extremely elongated grain structures were observed at the centers of sheet from S. Nos. 689250 and 689251 (Fig. 4). In the absence of other information, these elongated grains might have been interpreted as unrecrystallized structures.

However, Laue X-ray diffraction indicated that the sheet from all four alloys was completely recrystallized. Films from S. Nos. 689248-T8 and 689251-T8 are presented in Fig. 5. The film for S. No. 689251-T8 is representative of sheet samples which were given 8% stretch prior to artificial aging. The film for S. No. 689248-T8 shows less streaking than the others as a result of the lower level of strain (2%) prior to artificial aging. The ASTM grain size was estimated as -1.5 for all four alloys; however, this grain size is only approximate. The grain size could not be accurately determined because the samples were so highly strained.

In contrast to the indications of optical metallography, calculations of the orientation distribution functions for the

four sheet samples did not clear the confusion regarding grain structure. Optical metallography observations, Laue X-ray diffraction results and orientation distribution function data are summarized in Table IV. Although Laue X-ray diffraction would have suggested that all alloys were completely recrystallized, and optical metallography would have indicated that at least S. Nos. 689247 and 689248 were completely recrystallized, ODF on these two alloys revealed the brass rolling component to have nearly the greatest intensities (e.g., 7.1 and 6.6 times random for S. No. 689247 and 689248, respectively). S. No. 689247 also contained a significant cube recrystallization component (6.3 times random). In contrast, optical metallography on S. No. 689251 would have suggested this alloy, if any, was unrecrystallized at $t/2$, while ODF revealed an intensity of 21 times random for the goss recrystallization texture. S. No. 689250 contained predominantly rolling components of texture.

In these alloys, Mn is present in $\text{Al}_{20}\text{Cu}_2\text{Mn}_3$ dispersoids. Transmission electron microscopy on S. No. 689251-T8 showed these particles to be often rod-like, with a length of 0.5 microns or less (Fig. 6).

The Ag-bearing alloys, S. Nos. 689248-T8, 689250-T8 and 689251-T8, are strengthened by Ω phase. The bright field transmission electron micrograph in Fig. 7 from S. No. 689248-T8 shows the typical size of the Ω plates. The selected area diffraction pattern inset shows the characteristic Ω phase reflections. The alloy having no Ag, S. No. 689247-T8, is strengthened predominantly by Θ' ; however some Ω plates are also present (Fig. 8).

Room temperature tensile data for sheet aged using various practices are presented in Table V. Many samples from all of the alloys failed outside the middle half of the gage section but only three samples from S. No. 689248 failed before reaching 0.2% offset.

The plot of tensile yield strength versus time of Figure 9 presents data from S. No. 689251, but the general aging behavior is representative for all four alloys, except where noted.

- The four alloys reached peak tensile yield strength after 16 to 24 hr at 325°F.
- The two step practice, 24 hr at 275°F + various times at 325°F, produced the same peak tensile yield strengths that were produced by isothermal aging at 325°F.
- Only S. No. 689247 reached peak tensile yield strength in less than 168 hr at 275°F. All other alloys continued to increase in strength up through this aging time. Hence, peak aging times were not determined.

The highest tensile yield strengths were obtained in the two alloys with 5.2 Cu and 0.8 Mg, S. No. 689250 and 689251. Longitudinal tensile yield strength is plotted as a function of isothermal aging time at 325°F for the four alloys in Fig. 10. Tensile yield strengths of 75 and 77 ksi were achieved in S. Nos. 689250 and 689251, while tensile yield strengths less than 71 ksi were obtained in the other two alloys. The highest ultimate tensile strength, 80 ksi, was obtained in S. No. 689251 (Fig. 11).

There is some anisotropy of strength in sheet from these alloys. Tensile yield strength is plotted as a function of isothermal aging time at 325°F in Fig. 12 for the longitudinal and transverse orientations of S. No. 689247 and 689251 but data from the other two alloys show the same trend. Longitudinal strengths are 2 to 7 ksi higher than transverse strengths.

Additional tensile data are collected in Table VI. Once peak aging conditions were established for isothermal aging at 325°F, additional material was aged and two additional tensile tests were done: one to determine accurate values for tensile yield strength and the other to determine the work hardening exponent, n .

The highest strength alloys, S. Nos. 689250 and 689251, have

the lowest amount of work hardening. The difference between ultimate tensile strength and tensile yield strength and values for the work hardening exponent, n , are summarized for the peak aged condition (for isothermal aging at 325°F) of the four alloys in Table VII. Values for n were determined by fitting the stress-strain data to a power law expression. For longitudinal specimens, the values varied from a low value of 0.032 in the relatively high strength S. No. 689250 to a high value of 0.052 in the relatively low strength S. No. 689248. The values for transverse specimens were slightly higher than those from longitudinal specimens for the four variants in this study.

Plots of K_R , crack extension resistance, versus $\Delta a_{\text{effective}}$ (e.g., R-curves) from duplicate L-T specimens were extremely reproducible. Two of these R-curves from L-T specimens of S. No. 689247, peak aged at 325°F, are presented in Fig. 13. Closed symbols represent valid data and open symbols are data which failed the net section yielding criterion, e.g., the criterion requiring that net section stress divided by the yield strength is less than or equal to 0.8. R-curves from duplicate T-L specimens were nearly as reproducible. Two R-curves from T-L specimens of S. No. 689247, peak aged at 325°F, are presented in Fig. 14. The specimens were fatigue precracked using the load estimated to produce a maximum stress intensity at the end of fatigue precracking of 12 ksi $\sqrt{\text{in}}$.

If the entire R-curves are examined, L-T specimens appear to have greater crack extension resistance than T-L specimens. This is shown for sheet from S. No. 689251-T8, peak aged at 325°F, in Fig. 15. Note however, that the difference in crack extension resistance of the two orientations is small for values of $\Delta a_{\text{effective}}$ where data are valid. The most significant differences between orientations are seen in the portions of the curves for which data are invalid.

Values for tensile yield strength, K_c and K_{app} for both orientations of the peak aged conditions of the sheet are compiled in Table VIII. Included also are data from Phase I, the first iteration of testing of these alloys. In that phase, different preheating, heat treating and aging practices were used. All K_c data are invalid, except for data from S. No. 689251-T8 in the T-L orientation.

Some improvements in strength/toughness combination were realized in Phase II. K_c fracture toughness data for samples peak aged at 325°F are plotted as a function of tensile yield strength in Fig. 16. Open symbols represent data from Phase I and closed symbols represent data from this Phase II. Only strength improvements were realized.

As expected, based on earlier comments regarding anisotropy of strength and crack extension resistance, the strength/toughness combination for the L, L-T orientation is higher than for the T, T-L orientation (Fig. 17). It should be emphasized, however, that all K_c data, except for data from S. No. 689251-T8, are invalid.

The best strength/toughness combination in either orientation was obtained in S. No. 689251. The large variation in fracture toughness data for S. No. 689248-T8A (85 vs 114 ksi√in) shown in Fig. 17 is probably related to the use of too high preheating and solution heat-treating temperatures. Such temperatures may have caused eutectic melting which very likely limited the level to which those pieces could be stretched (2%) and caused very irreproducible values for fracture toughness.

Summary

- Four alloys have been evaluated in T8-type tempers of 0.125" thick sheet. They have nominal compositions of:
S. No. 689247: Al-5.85 Cu-0.5 Mg-0.3 Mn-0.1 V-0.15 Zr
S. No. 689248: Al-5.85 Cu-0.5 Mg-0.5 Ag-0.3 Mn-0.1 V-0.15 Zr

S. No. 689250: Al-5.2 Cu-0.8 Mg-0.5 Ag-0.15 Zr
S. No. 689251: Al-5.2 Cu-0.8 Mg-0.5 Ag-0.6 Mn-0.1 V-
0.15 Zr

- Undissolved constituent and/or eutectic melting rosettes limited the toughness measured in this phase of the program for the four alloys.
- Despite thorough microstructural characterization, the grain structures of sheet could not be definitively described as being recrystallized or unrecrystallized.
- For isothermal aging at 325°F, the dominant strengthening phase is Ω in S. Nos. 689248, 689250 and 689251 and Θ' in S. No. 689247. In Mn-bearing alloys, submicron $\text{Al}_{20}\text{Cu}_2\text{Mn}_3$ dispersoids are present.
- Strength and toughness are lower in T, T-L orientations than in L, L-T orientations.
- The best strength/toughness combination obtained by isothermal aging at 325°F was obtained in S. No. 689251.

References

1. E. A. Starke, "NASA-UVA Light Aerospace Alloy and Structure Technology Program Supplement: Aluminum-Based Materials for High Speed Aircraft," Semi-Annual Report January 1 - June 30, 1992, NASA Contractor Report 4517, June 1993.
2. E. A. Starke, "NASA-UVA Light Aerospace Alloy and Structure Technology Program Supplement: Aluminum-Based Materials for High Speed Aircraft," Semi-Annual Report July 1 - December 31, 1992, NASA Contractor Report 4645, February 1995.

Table I. Nominal and actual compositions of the four I/M 2XXX alloys studied in Phase II.

Alloy	Composition (wt. %)							
	Cu	Mg	Mn	Ag	Zr	V	Fe	Si
689247								
nominal	5.85	0.50	0.30	-	0.15	0.10	0.05	0.04
actual	5.71	0.50	0.32		0.15	0.09	0.06	0.05
689248								
nominal	5.85	0.50	0.30	0.50	0.15	0.10	0.05	0.04
actual	6.13	0.43	0.31	0.53	0.14	0.08	0.06	0.03
689250								
nominal	5.20	0.80	-	0.50	0.15	-	0.04	0.05
actual	5.32	0.78	0.00	0.50	0.16	0.00	0.05	0.05
689251								
nominal	5.20	0.80	0.60	0.50	0.15	0.10	0.04	0.05
actual	5.47	0.82	0.61	0.51	0.15	0.008	0.06	0.06

Component	Miller Indices		Euler Angles, °		
	{hkl}	<uvw>	φ_1	Φ	φ_2
Rolling Components					
Copper	{112}	<111>	90	35	45
S	{123}	<634>	59	37	63
Brass	{011}	<211>	35	45	0
Recrystallization Components					
Goss	{011}	<100>	0	45	0
Cube	{001}	<100>	90	0	0

Components 2 and 3 are intermediate on the skeleton line to the rolling components Brass and S and Components 4 and 5 are intermediate on the skeleton line to the rolling components S and Copper.

Table II. Maximum preheat temperatures, solution heat treatment temperatures and the amount of stretch for the four I/M 2XXX alloys.

S. No.	Max. Preheat Temperature, °F	Solution Heat Treatment Temperature, °F	% Stretch
689247	990	985	8
689248	995	995	2
689250	980	970	8
689251	980	970	8

Table III. Nominal and actual compositions of four Al-Cu-Li alloys cast for University of Virginia studies.

S. No.	Cu	Li	Mg	In	Zr	Fe	Si
725945A	4.27	1.30	0.54	0.084	0.15	0.05	0.04
725945B	4.28	1.28	0.54	0.084	0.16	0.06	0.05
725946A	4.17	1.28	0.54	n.m.	0.16	0.05	0.04
725946B	4.23	1.28	0.54	n.m.	0.16	0.05	0.04

Table IV. Summary of optical metallography observations, Laue X-ray diffraction results and orientation distribution function (ODF) data for grain structures in I/M 2XXX sheet. Sheet was heat treated, cold water quenched, stretched and isothermally aged at 325°F.

S. No.	Polarized Light Viewing of Anodically Etched Samples		Laue X-ray Diffraction at t/2			Orientation Distribution Function (ODF) at t/2**									
			Degree of Rx	ASTM* Grain Size	% Strain*	Recrystallization Components		Intensities, Times Random							
	Surface	t/2				Cube	Goss	Brass	2	3	S	4	5	Copper	
689247	Equiaxed	Elongated	Complete	-1.5	5-10%	6.3	0	7.1	4.3	4.7	5.5	4.6	4.9	3.8	
689248	Equiaxed	Elongated	Complete	-1.5	2-5%	2.4	0.3	6.6	6.8	2.4	2.5	1.7	5.5	3.5	
689250	Equiaxed	Very Elongated	Complete	-1.5	5-10%	0.3	2.9	5.9	5.9	2.4	2.9	2.0	6.2	3.3	
689251	Elongated	Extremely Elongated	Complete	-1.5	5-10%	2.4	21.3	4.3	2.9	3.0	2.5	2.5	3.0	3.7	

* Grain size could not be accurately determined because of extreme strain. Strain could not be accurately determined because of the coarse grain size.

** ODF data are approximate because of coarse grain size.

Table V. Room Temperature Tensile Data for I/M 2XXX Sheet Aged Using Various Practices.
All samples were solution heat treated, quenched, stretched and artificially aged as indicated.

		Aging Practice		Longitudinal				Transverse			
S Number	Dash No.	t (hr)	T (°F)	Tensile Yield Strength (ksi)	Ultimate Tensile Strength (ksi)	Elongation (%)	Comments	Tensile Yield Strength (ksi)	Ultimate Tensile Strength (ksi)	Elongation (%)	Comments
689247+	-1	2	325	58.5	71.2	23.0		52.2	68.2	19.0	
	-2	4	325	63.0	73.1	18.0		55.7	69.8	18.0	(a)
	-3	8	325	67.8	73.9	14.0		61.6	71.8	15.0	
	-4	16	325	70.5	74.9	13.0		66.2	73.3	13.0	(a)
	-5	24	325	70.7	75.0	12.0		66.8	74.2	14.0	(a)
	-6	48	325	70.1	74.7	11.0		66.8	74.0	10.0	(a)
	-7	24	275	58.9	73.8	21.0		54.1	70.3	20.0	
	-8	48	275	61.8	74.7	20.0	(a)	51.2	69.4	23.0	
	-9	72	275	64.9	74.8	17.0	(a)	57.9	71.5	17.0	
	-10	96	275	66.3	74.9	14.0		60.1	72.5	16.0	(a)
	-11	120	275	68.2	75.3	13.0		61.8	72.4	12.0	
	-12	168	275	63.6	69.0	13.0		64.3	73.7	12.0	
	-13	*+2	325	61.2	72.8	22.0	(a,d)	53.6	69.3	19.0	
	-14	*+4	325	64.4	73.2	16.0	(a,d)	57.0	69.5	14.0	(a)
	-15	*+8	325	68.0	74.3	14.0		57.7	66.8	13.0	
	-16	*+16	325	70.1	74.9	13.0	(a)	66.4	73.8	12.0	
	-17	*+24	325	71.0	75.3	12.0		66.5	74.2	12.0	
	-18	*+48	325	70.3	75.1	13.0		67.0	73.9	11.0	(a)

+ Solution heat treated at 985°F, cold water quenched, stretched 8% and aged as indicated.

* Samples were pre-aged 24 hr at 275°F prior to the aging practice indicated.

- (a) Failed outside middle half of gage section.
(b) Yield strength not obtained; failed before reaching 0.2% offset.
(c) Failed outside gage length.
(d) Failed through gage mark.
(e) Failed at fillet.

Table V (continued). Room Temperature Tensile Data for I/M 2XXX Sheet Aged Using Various Practices.
All samples were solution heat treated, quenched, stretched and artificially aged as indicated.

S Number	Dash No.	Aging Practice		Longitudinal				Transverse			
		t (hr)	T (°F)	Tensile Yield Strength (ksi)	Ultimate Tensile Strength (ksi)	Elongation (%)	Comments	Tensile Yield Strength (ksi)	Ultimate Tensile Strength (ksi)	Elongation (%)	Comments
689248+	-1	2	325	48.5	62.6	12.0		42.4	64.1	15.0	
	-2	4	325	54.9	71.0	22.0	(a)	51.2	65.2	10.0	
	-3	8	325	64.3	73.3	15.0		58.3	65.3	7.0	(a)
	-4	16	325	69.0	75.2	10.0		65.2	71.9	6.0	(a)
	-5	24	325	70.5	76.1	10.0		66.9	72.0	5.0	(a)
	-6	48	325	68.3	68.4	-	(a,c)	67.1	73.5	6.0	
	-7	24	275	49.3	70.4	22.0	(a,d)	44.4	60.3	10.0	(a)
	-8	48	275	52.8	72.1	23.0		46.7	50.3	4.0	
	-9	72	275	58.5	73.5	19.0		51.3	69.8	17.0	(a)
	-10	96	275	59.6	74.3	17.0		54.4	63.7	7.0	
	-11	120	275	62.7	74.8	15.0		56.6	69.6	10.0	(a)
	-12	168	275	65.8	75.0	12.0		-	51.2	-	(b)
	-13	*+2	325	52.2	70.1	21.0		45.7	65.9	13.0	(a)
	-14	*+4	325	57.7	71.1	14.0		54.0	62.6	6.0	(a)
	-15	*+8	325	67.0	73.9	9.0		-	58.7	-	(b,c,e)
	-16	*+16	325	67.5	72.9	10.0	(a)	-	58.7	-	(b,a)
	-17	*+24	325	71.0	76.4	10.0		68.9	70.8	4.0	
	-18	*+48	325	70.5	76.4	11.0	(a)	64.3	67.8	3.0	(a,d)

+ Solution heat treated at 995°F, cold water quenched, stretched 2% and aged as indicated.

* Samples were pre-aged 24 hr at 275°F prior to the aging practice indicated.

- (a) Failed outside middle half of gage section.
(b) Yield strength not obtained; failed before reaching 0.2% offset.
(c) Failed outside gage length.
(d) Failed through gage mark.
(e) Failed at fillet.

Table V (continued). Room Temperature Tensile Data for I/M 2XXX Sheet Aged Using Various Practices.
All samples were solution heat treated, quenched, stretched and artificially aged as indicated.

S Number	Dash No.	Aging Practice		Longitudinal				Transverse			
		t (hr)	T (°F)	Tensile Yield Strength (ksi)	Ultimate Tensile Strength (ksi)	Elongation (%)	Comments	Tensile Yield Strength (ksi)	Ultimate Tensile Strength (ksi)	Elongation (%)	Comments
689250+	-1	2	325	55.6	67.2	22.0		50.3	66.0	21.0	(a)
	-2	4	325	65.5	71.4	16.0	(a)	60.6	69.5	15.0	
	-3	8	325	71.8	75.4	13.0	(a,d)	65.0	72.7	12.0	(a)
	-4	16	325	75.0	78.4	11.0		72.8	79.2	10.0	
	-5	24	325	74.7	78.0	11.0		72.5	78.8	8.0	(a)
	-6	48	325	73.4	77.6	10.0	(a)	71.0	77.6	7.0	(a,d)
	-7	24	275	54.3	66.4	25.0	(a)	48.6	63.8	22.0	(a)
	-8	48	275	61.8	70.9	18.0		54.7	68.2	16.0	(a)
	-9	72	275	66.5	71.5	16.0		64.0	72.1	12.0	
	-10	96	275	71.3	75.8	16.0		66.1	74.9	15.0	
	-11	120	275	72.5	76.2	14.0		68.4	76.1	13.0	
	-12	168	275	75.5	78.4	12.0		67.0	72.9	9.0	
	-13	*+2	325	64.6	71.5	17.0		58.6	70.4	17.0	
	-14	*+4	325	71.0	75.3	15.0	(a)	66.7	72.9	10.0	
	-15	*+8	325	74.3	77.5	13.0		71.7	77.9	11.0	
	-16	*+16	325	74.8	77.9	12.0		72.3	76.1	7.0	
	-17	*+24	325	75.0	77.9	11.0	(a)	72.5	77.7	8.0	(a)
	-18	*+48	325	74.3	77.5	10.0	(a)	73.1	77.7	9.0	(a)

+ Solution heat treated at 970°F, cold water quenched, stretched 8% and aged as indicated.

* Samples were pre-aged 24 hr at 275°F prior to the aging practice indicated.

(a) Failed outside middle half of gage section.

(b) Yield strength not obtained; failed before reaching 0.2% offset.

(c) Failed outside gage length.

(d) Failed through gage mark.

(e) Failed at fillet.

Table V (continued). Room Temperature Tensile Data for I/M 2XXX Sheet Aged Using Various Practices.
All samples were solution heat treated, quenched, stretched and artificially aged as indicated.

S Number		Aging Practice		Longitudinal				Transverse			
		t (hr)	T (°F)	Tensile Yield Strength (ksi)	Ultimate Tensile Strength (ksi)	Elongation (%)	Comments	Tensile Yield Strength (ksi)	Ultimate Tensile Strength (ksi)	Elongation (%)	Comments
689251+	-1	2	325	62.8	73.2	19.0	(a)	57.0	73.0	19.0	(a)
	-2	4	325	66.3	76.3	16.0		67.1	77.1	15.0	(a)
	-3	8	325	75.6	79.5	13.0		71.3	79.7	12.0	(a)
	-4	16	325	77.4	80.2	12.0		74.4	80.8	10.0	
	-5	24	325	76.5	79.6	12.0	(a)	73.9	80.6	11.0	
	-6	48	325	75.4	78.7	12.0		72.5	80.0	9.0	
	-7	24	275	61.8	74.3	21.0		57.2	73.6	19.0	(a)
	-8	48	275	67.5	75.8	17.0		63.6	76.0	18.0	(a,d)
	-9	72	275	71.7	77.3	17.0	(a)	65.9	75.1	15.0	(a)
	-10	96	275	73.0	77.5	15.0		69.7	78.4	14.0	
	11	120	275	75.5	79.2	13.0		72.0	79.4	14.0	
	-12	168	275	76.4	79.4	13.0		73.5	80.2	12.0	(a,d)
	-13	*+2	325	69.0	75.9	16.0	(a,d)	64.0	75.5	16.0	(d)
	-14	*+4	325	73.8	78.0	15.0	(a,d)	63.0	77.9	13.0	
	-15	*+8	325	76.6	79.1	13.0		72.3	79.2	11.0	
	-16	*+16	325	76.8	79.4	13.0		74.0	79.8	12.0	
	-17	*+24	325	76.2	79.4	13.0		73.8	79.8	10.0	(a,d)
	-18	*+48	325	75.9	79.0	12.0		73.6	79.7	11.0	

+ Solution heat treated at 970°F, cold water quenched, stretched 8% and aged as indicated.

* Samples were pre-aged 24 hr at 275°F prior to the aging practice indicated.

- (a) Failed outside middle half of gage section.
(b) Yield strength not obtained; failed before reaching 0.2% offset.
(c) Failed outside gage length.
(d) Failed through gage mark.
(e) Failed at fillet.

Table VI. Longitudinal and Transverse Tensile Data for I/M 2XXX Sheet, Peak Aged at 325°F. One sample in each orientation was used to determine accurate values for tensile yield strength and the other sample was used to determine the work hardening exponent, n.

S Number (a)	Longitudinal						Transverse					
	Tensile Yield Strength (ksi)	Engineering Ultimate Tensile Strength (ksi)	True Ultimate Tensile Strength (ksi)	Uniform Elongation (%)	Total Elongation (%)	n	Tensile Yield Strength (ksi)	Engineering Ultimate Tensile Strength (ksi)	True Ultimate Tensile Strength (ksi)	Uniform Elongation (%)	Total Elongation (%)	n
689247	73.2	76.6			11.0		65.4	72.1			8.0	
	72.3	76.1	82.1	7.3	10.5	0.048	68.4	74.6	80.6	7.7	10.2	0.049
689248	71.8	76.8			10.0		66.5	67.0			2.0 (b)	
	70.0	76.3	82.6	7.4	11.3	0.052	68.3	75.3	81.4	7.4	10.7	0.055
689250	75.1	78.3			10.0		72.1	78.2			10.0	
	75.7	78.3	83.5	5.8	10.0	0.032	71.8	78.0	83.0	5.2	9.7	0.037
689251	77.9	80.3			11.0		74.7	80.9			10.0	
	78.1	81.1	86.3	5.6	10.3	0.034	74.7	80.4	84.4	4.6	6.9	0.035

(a) Processing Details

689247: SHT @ 985°F, CWQ, stretch 8%, age 24 hr @ 325°F

689248: SHT @ 995°F, CWQ, stretch 2%, age 24 hr @ 325°F

689250: SHT @ 970°F, CWQ, stretch 8%, age 16 hr @ 325°F

689251: SHT @ 970°F, CWQ, stretch 8%, age 16 hr @ 325°F

(b) Fragmented fracture

Table VII. Differences between ultimate tensile strength and tensile yield strength, UTS-TYS and work hardening exponent, n for the I/M 2XXX sheet, peak aged at 325°F.

S. No.	Orientation			
	Longitudinal		Transverse	
	UTS-TYS, ksi	n	UTS-TYS, ksi	n
689247	4	0.048	7	0.049
689248	6	0.052	7	0.055
689250	3	0.032	6	0.037
689251	3	0.034	6	0.035

Table VIII. Tensile and Fracture Toughness Data for Peak Aged Samples of I/M 2XXX Sheet. Data from the current investigation (Phase II), where samples were peak aged at 325°F, and an earlier study (Phase I), where different preheating, heat treating and aging practices were used, are included for comparison (c,d). Toughness values were obtained from 6.3" wide x 20" long center slot specimens. No fatigue precracking was done.

			L, L-T			T, T-L		
S Number	Sample ID	Program Phase	Tensile Yield Strength (ksi)	K _c	K _{app}	Tensile Yield Strength (ksi)	K _c	K _{app}
689247	1	II	73.2	112.9	76.6	65.4	96.9	68.9
	2	II		112.6	78.1		98.8	69.0
		I	70.3	94.5	69.2			
689248	1	II	71.8	112.1	75.1	66.5	72.2	64.7 (a)
	2	II		85.8	69.6		95.2	70.2 (b)
		I	70.4	110.4	73.5			
689250	1	II	75.1	115.0	79.8	72.1	85.9	69.7
	2	II		110.5	77.5		90.8	73.0
		I	73.4	102.4	72.9			
689251	1	II	77.9	110.7	79.3	74.7	76.9	66.7
	2	II		113.0	79.1		88.5	69.0
		I	76.2	107.7	76.7			
		I	77.4	129.4	85.7			

- (a) Failed in gripping section.
(b) Failed in a plane 1.6" from original crack plane. Fracture surface indicates dissimilar grain structure.
(c) Processing information for Phase I materials is included in Reference 1.
(d) All K_c data are invalid, except for data from 689251-T8A in the T-L orientation.

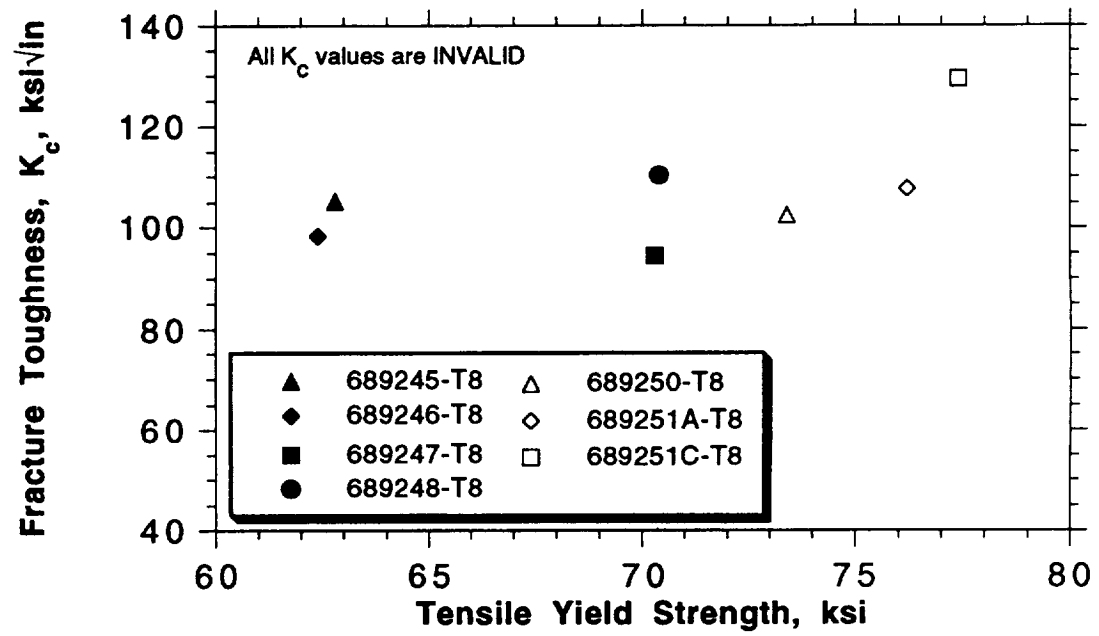
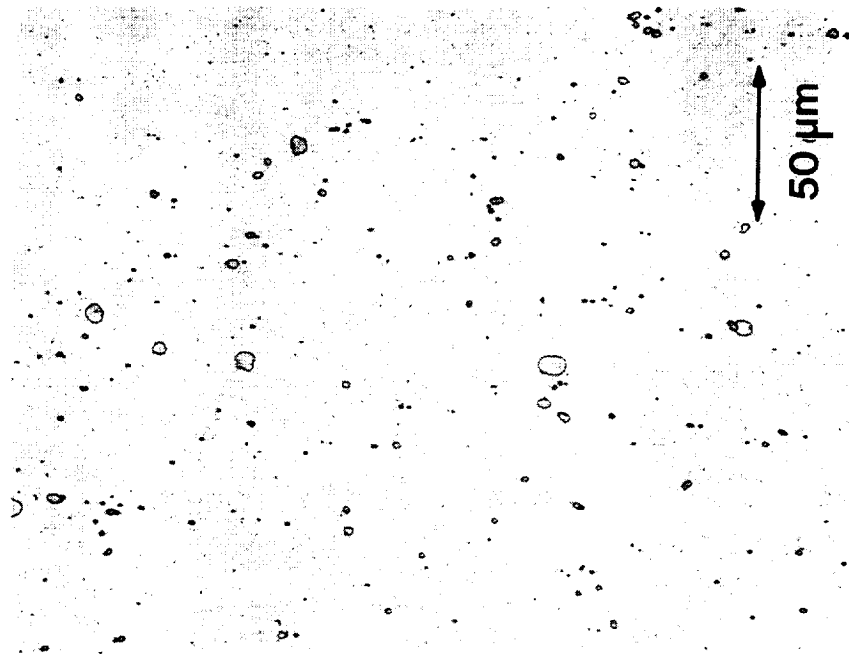
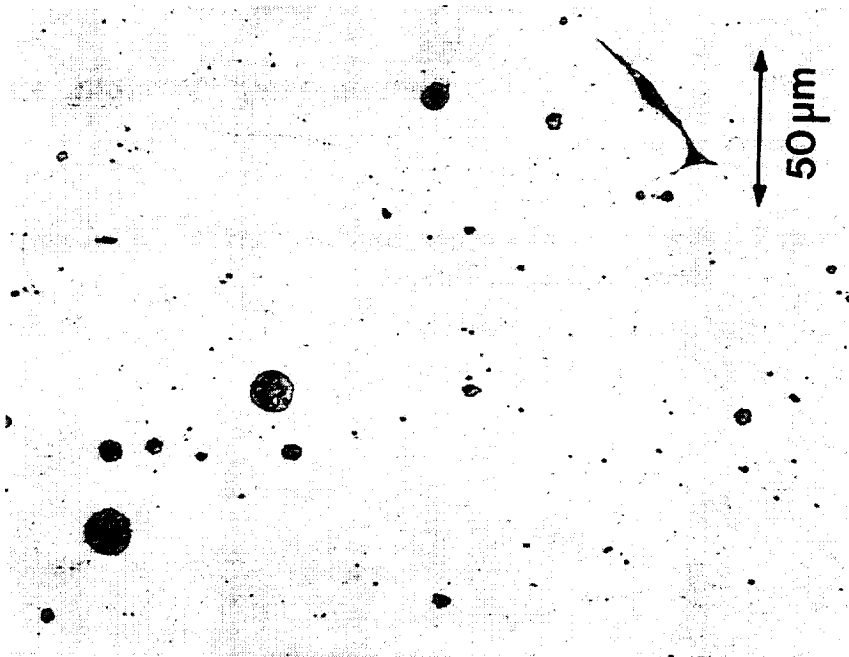


Figure 1. Fracture toughness as a function of tensile yield strength for I/M 2XXX sheet produced in Phase I.



(a)



(b)

Figure 2. Optical micrographs, illustrating (a, c, d) undissolved constituent in S Nos. 689247-T8A, 689250-T8A and 689251-T8A, and (b) eutectic melting in S. No. 689248-T8A.

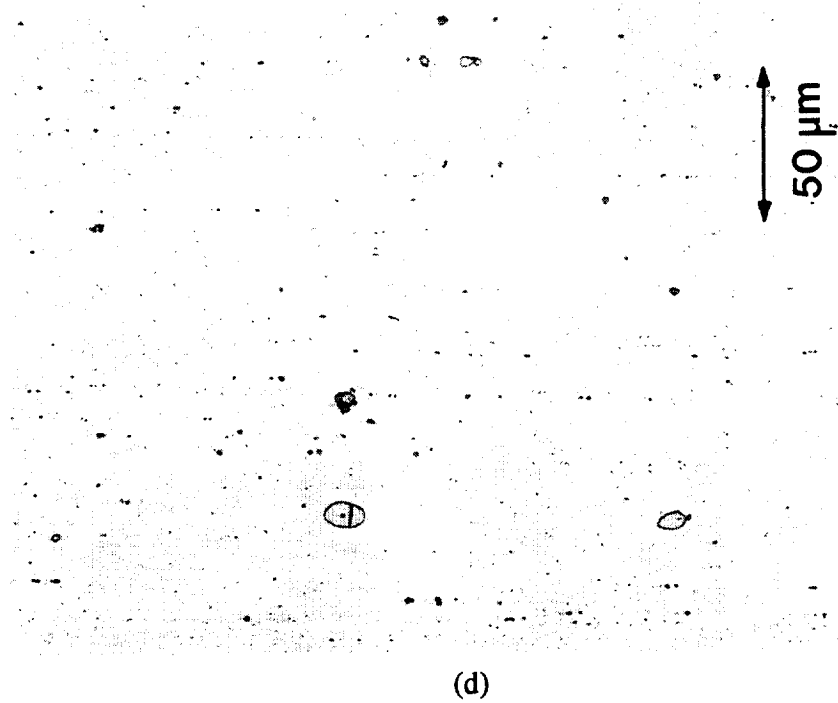
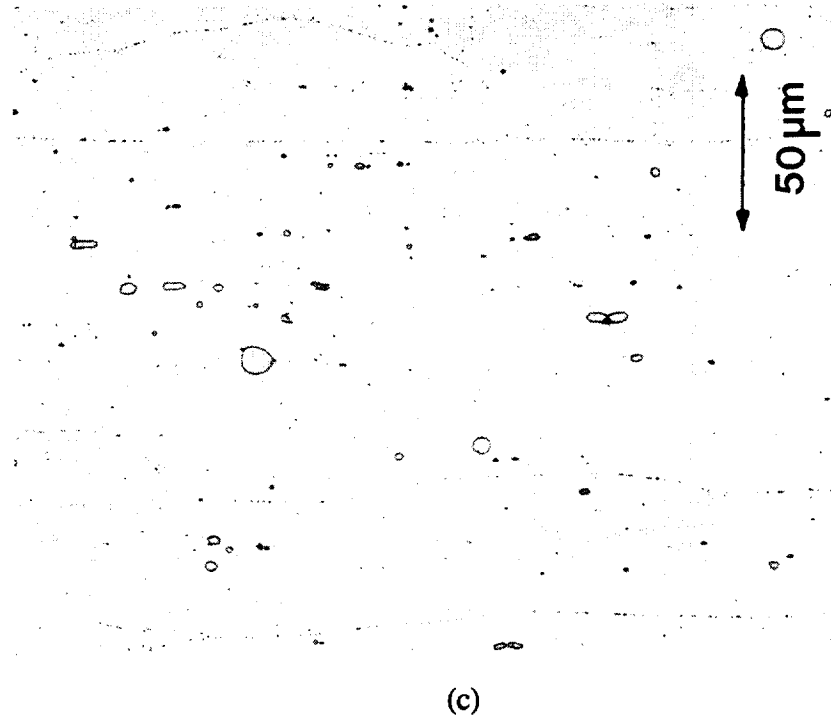
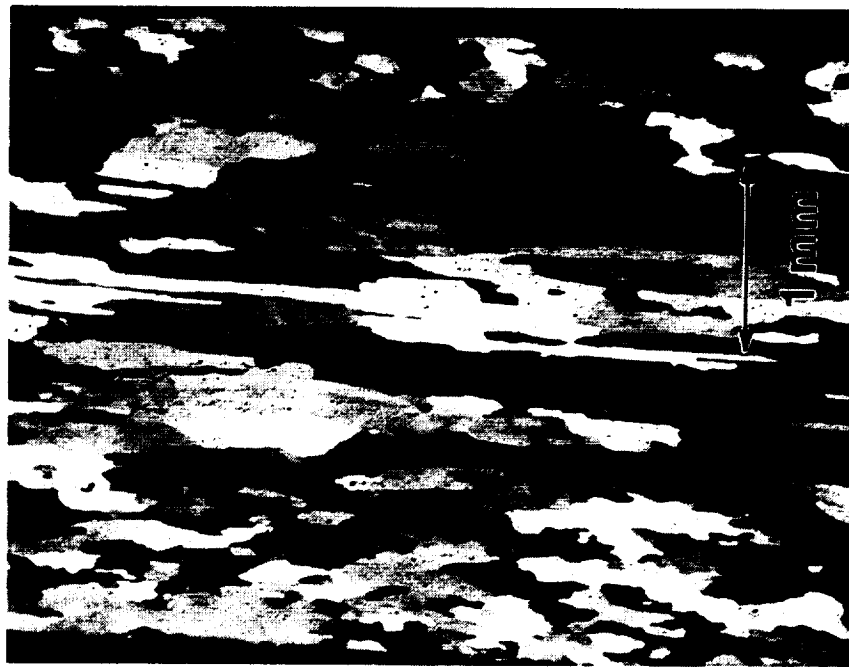


Figure 2 (continued) . Optical micrographs, illustrating (a, c, d) undissolved constituent in S Nos. 689247-T8A, 689250-T8A and 689251-T8A, and (b) eutectic melting in S. No. 689248-T8A.



(a)



(b)

Figure 3. Optical micrographs taken using polarized light, revealing fully recrystallized structures with equiaxed grains at the surfaces and elongated grains in the centers of sheet samples from (a) S. No. 689247-T8A and (b) S. No. 689248-T8A.



(a)



(b)

Figure 4. Optical micrographs taken using polarized light, revealing highly elongated grains in the centers of sheet samples from (a) S. No. 689250-T8A and (b) S. No. 689251-T8A.



(a)



(b)

Figure 5. Laue X-ray diffraction films from samples from the $t/2$ locations of sheet from (a) S. No. 689248-T8A and (b) S. No. 689251-T8A, revealing complete recrystallization.

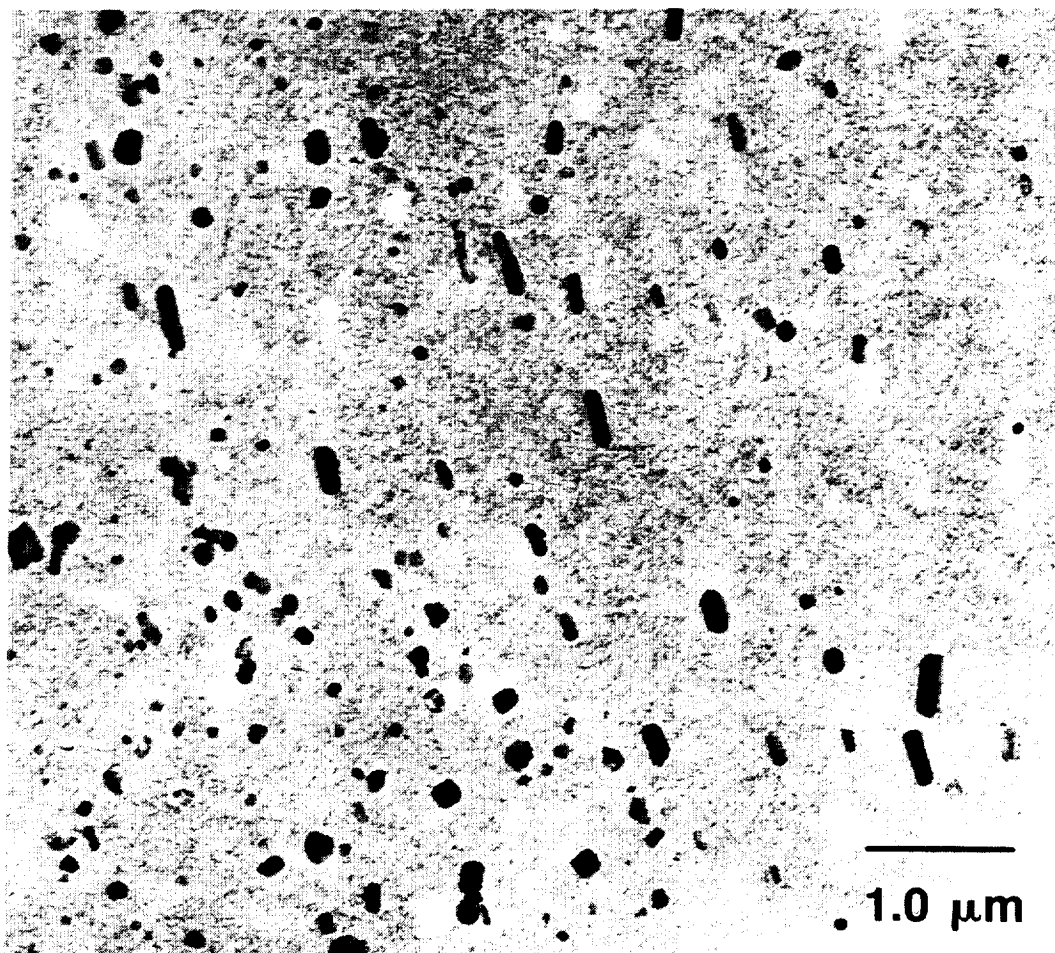


Figure 6. Bright field transmission electron micrograph from sheet from S. No. 689251-T8A revealing numerous $\text{Al}_{20}\text{Cu}_2\text{Mn}_3$ dispersoids.

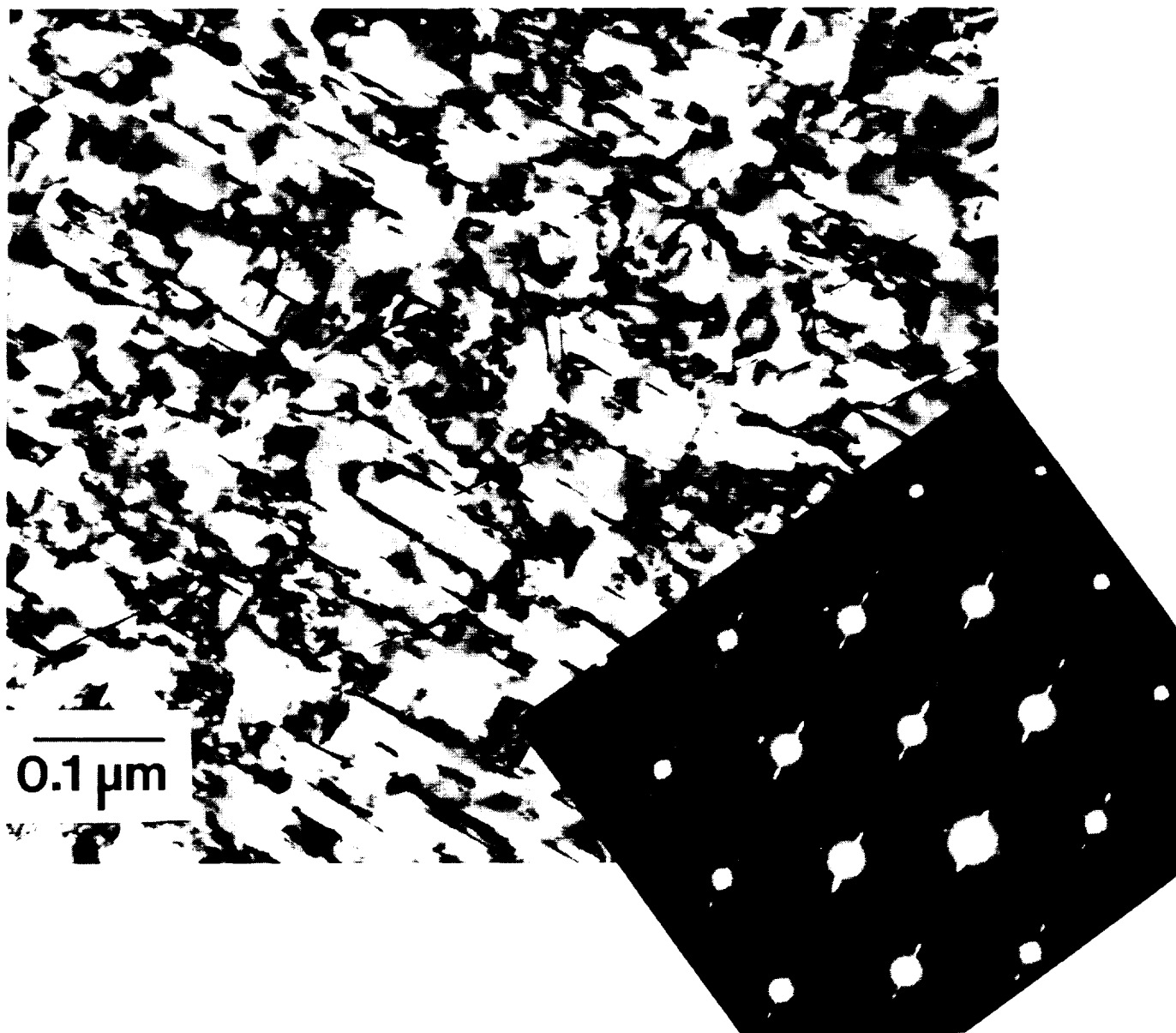


Figure 7. Bright field transmission electron micrograph with selected area diffraction inset, revealing Θ' as the dominant strengthening precipitate and a few Ω plates in S. No. 689247-T8A.

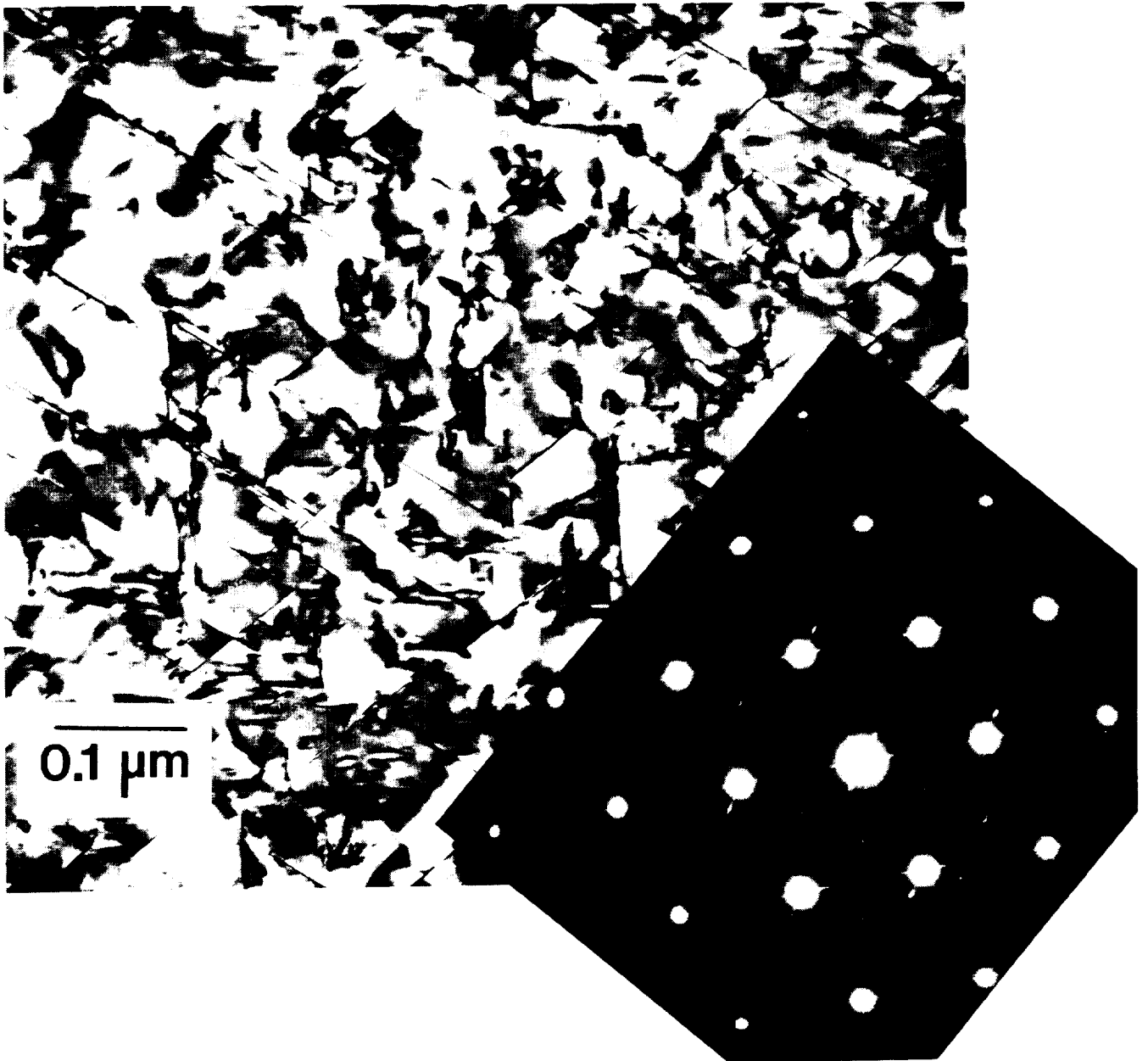


Figure 8. Bright field transmission electron micrograph with selected area diffraction inset, revealing Ω as the dominant strengthening precipitate in S. No. 689248-T8A.

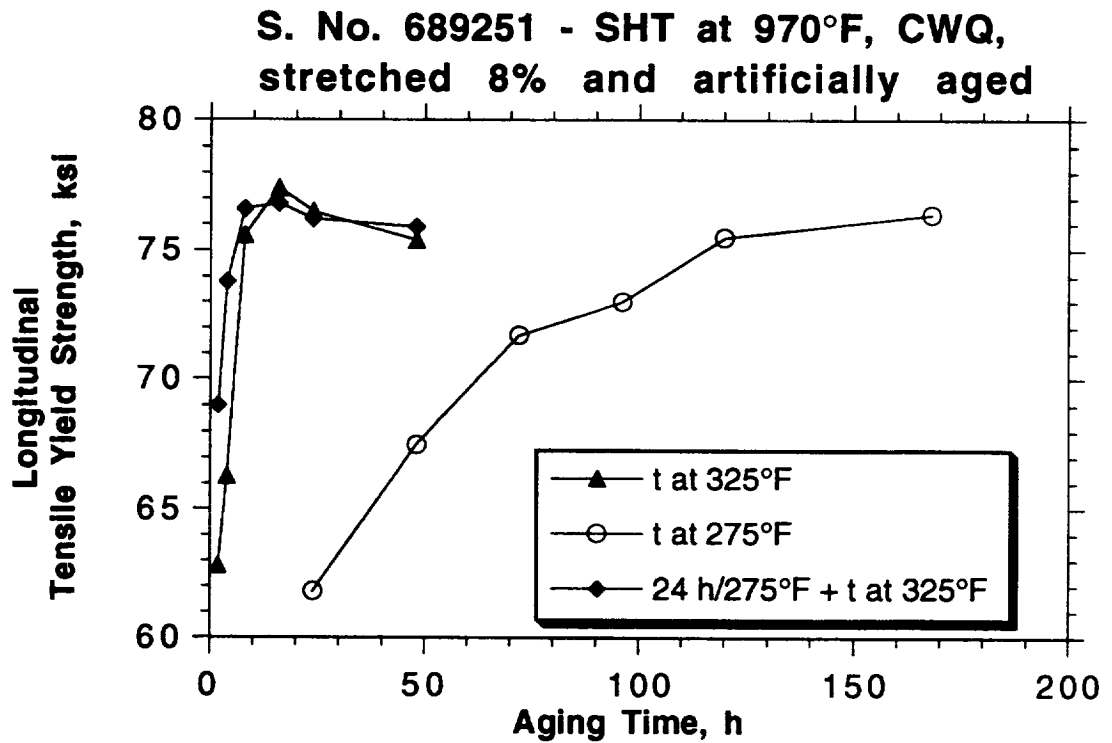


Figure 9. Longitudinal tensile yield strength as a function of aging time for sheet from S. No. 689251 which was solution heat treated at 970°F, cold water quenched, stretched 8% and aged using various practices: isothermally at 325°F, isothermally at 275°F and using a two step practice of 24 hr at 275°F followed by isothermal aging at 325°F.

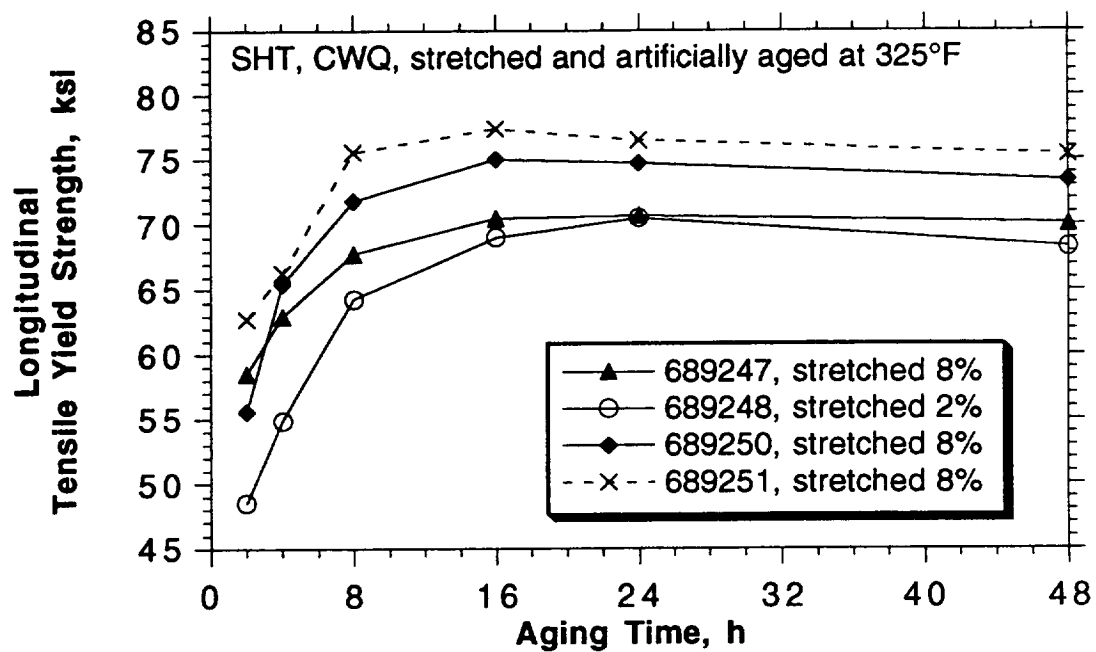


Figure 10. Longitudinal tensile yield strength as a function of aging time for sheet from S. Nos. 689247, 689248, 689250 and 689251. Sheet samples were solution heat treated, cold water quenched, stretched (either 8% or 2%, as indicated) and aged at 325°F.

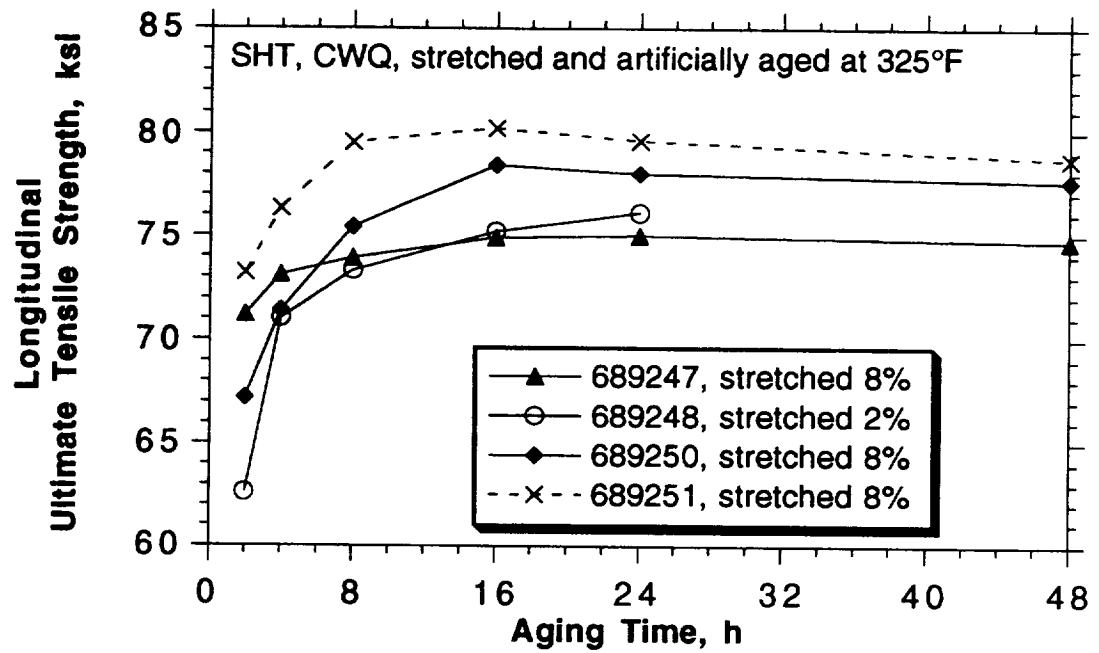


Figure 11. Longitudinal ultimate tensile strength as a function of aging time for sheet from S. Nos. 689247, 689248, 689250 and 689251. Sheet samples were solution heat treated, cold water quenched, stretched (either 8% or 2%, as indicated) and aged at 325°F.

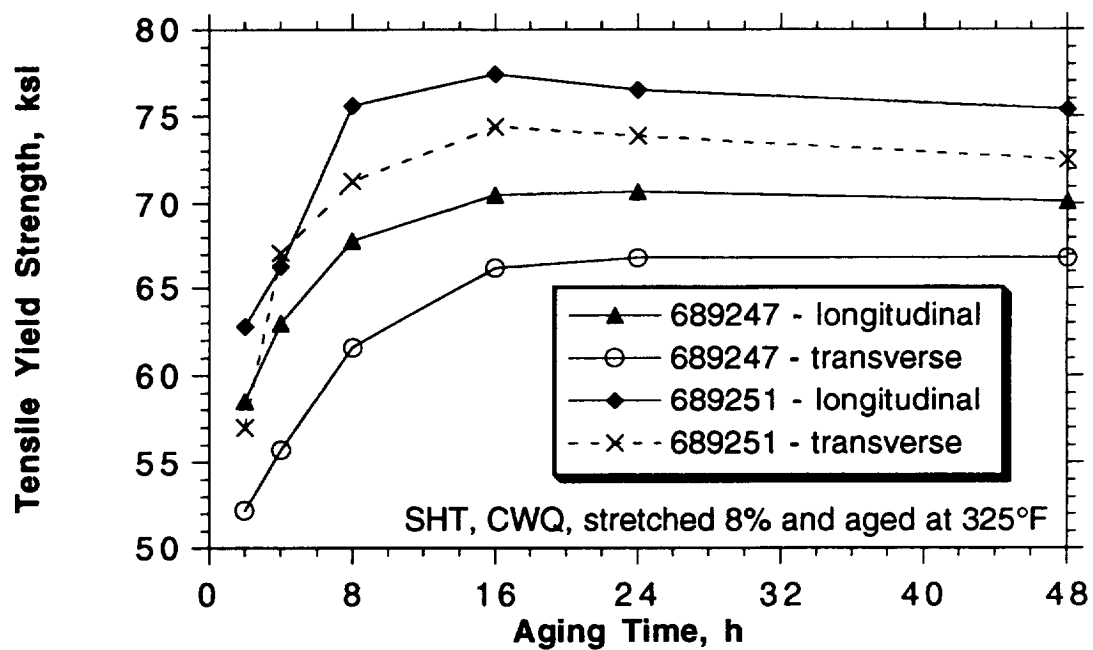


Figure 12. Longitudinal and transverse tensile yield strength as a function of aging time for sheet from S. Nos. 689247 and 689251. Sheet samples were solution heat treated, cold water quenched, stretched 8% and aged at 325°F.

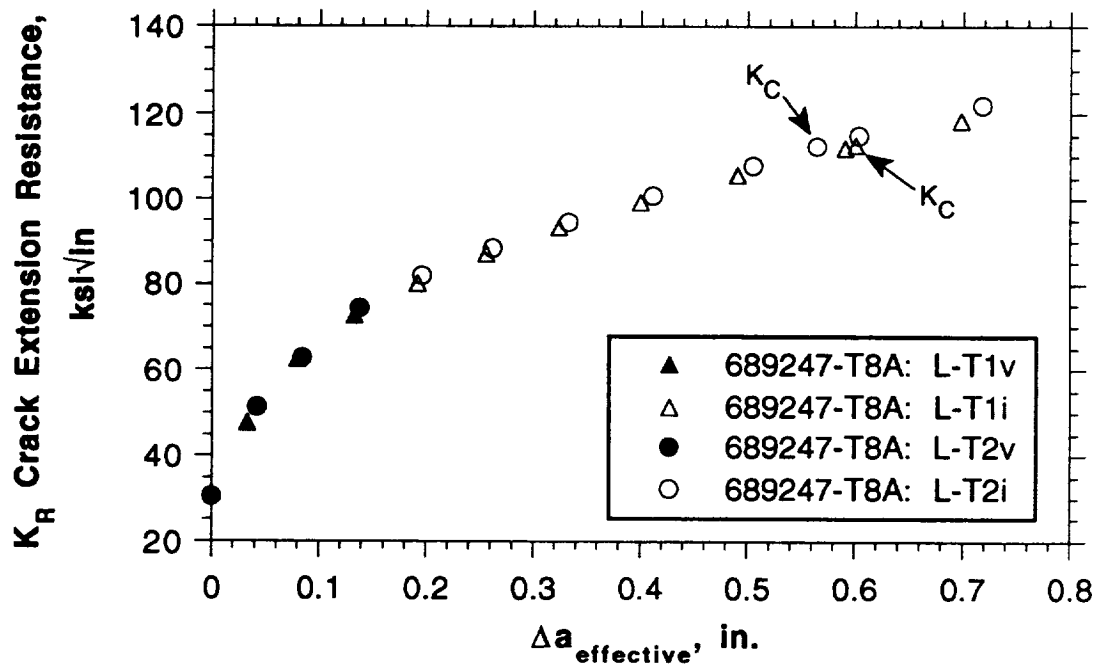


Figure 13. Crack extension resistance, K_R , as a function of $\Delta a_{\text{effective}}$ for duplicate L-T specimens from S. No. 689247-T8A. Specimens were solution heat treated, cold water quenched, stretched 8% and isothermally aged at 325°F. Closed symbols represent valid data, while open symbols represent data which failed the net section stress criterion.

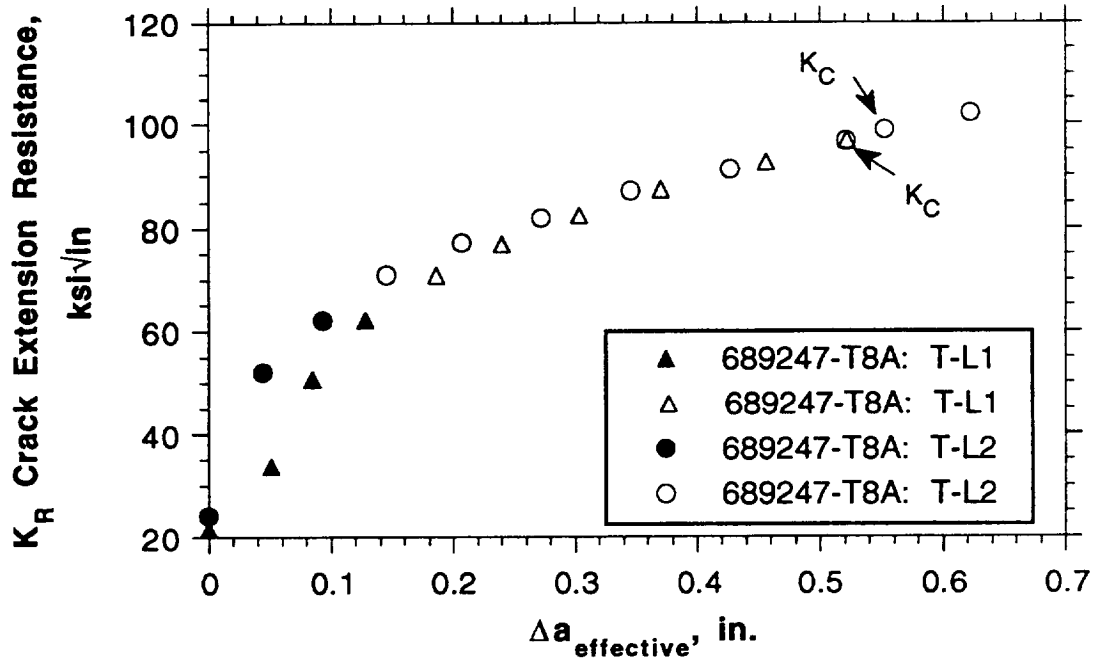


Figure 14. Crack extension resistance, K_R , as a function of $\Delta a_{\text{effective}}$ for duplicate T-L specimens from S. No. 689247-T8A. Specimens were solution heat treated, cold water quenched, stretched 8% and isothermally aged at 325°F. Closed symbols represent valid data, while open symbols represent data which failed the net section stress criterion.

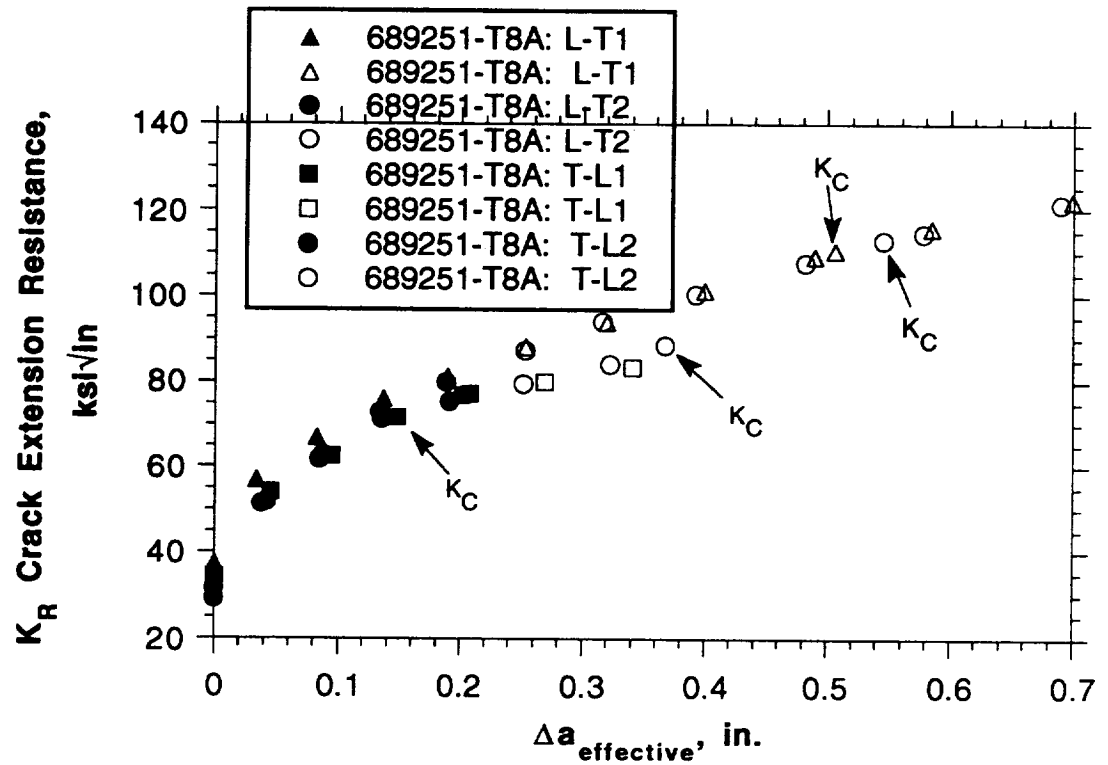


Figure 15. Crack extension resistance, K_R , as a function of $\Delta a_{\text{effective}}$ for duplicate L-T and T-L specimens from S. No. 689251-T8A. Specimens were solution heat treated, cold water quenched, stretched 8% and isothermally aged at 325°F. Closed symbols represent valid data, while open symbols represent data which failed the net section stress criterion.

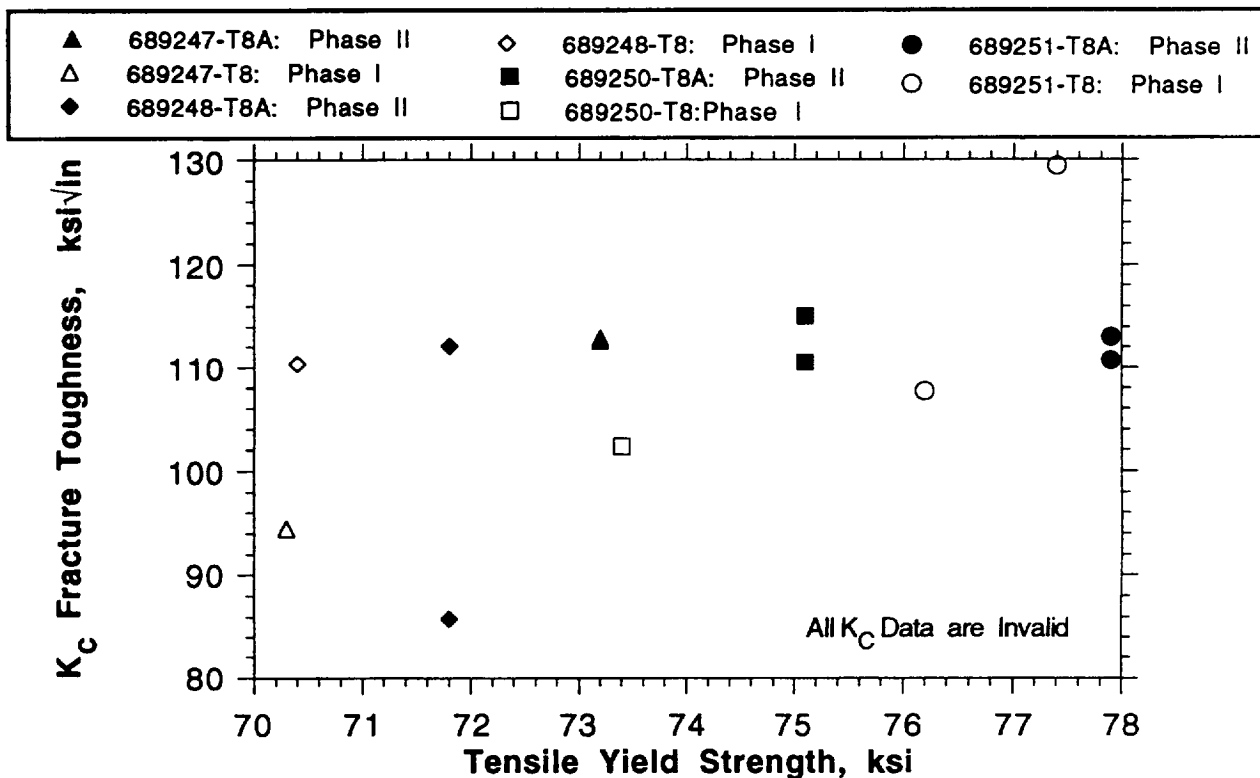


Figure 16. K_C fracture toughness (L-T) as a function of tensile yield strength (L) for peak aged condition of I/M 2XXX sheet produced in Phase II. Specimens were solution heat treated, cold water quenched, stretched either 8% or 2% (see text) and aged at 325°F. Data from Phase I, where different preheating, heat treating and aging practices were used, are also included.

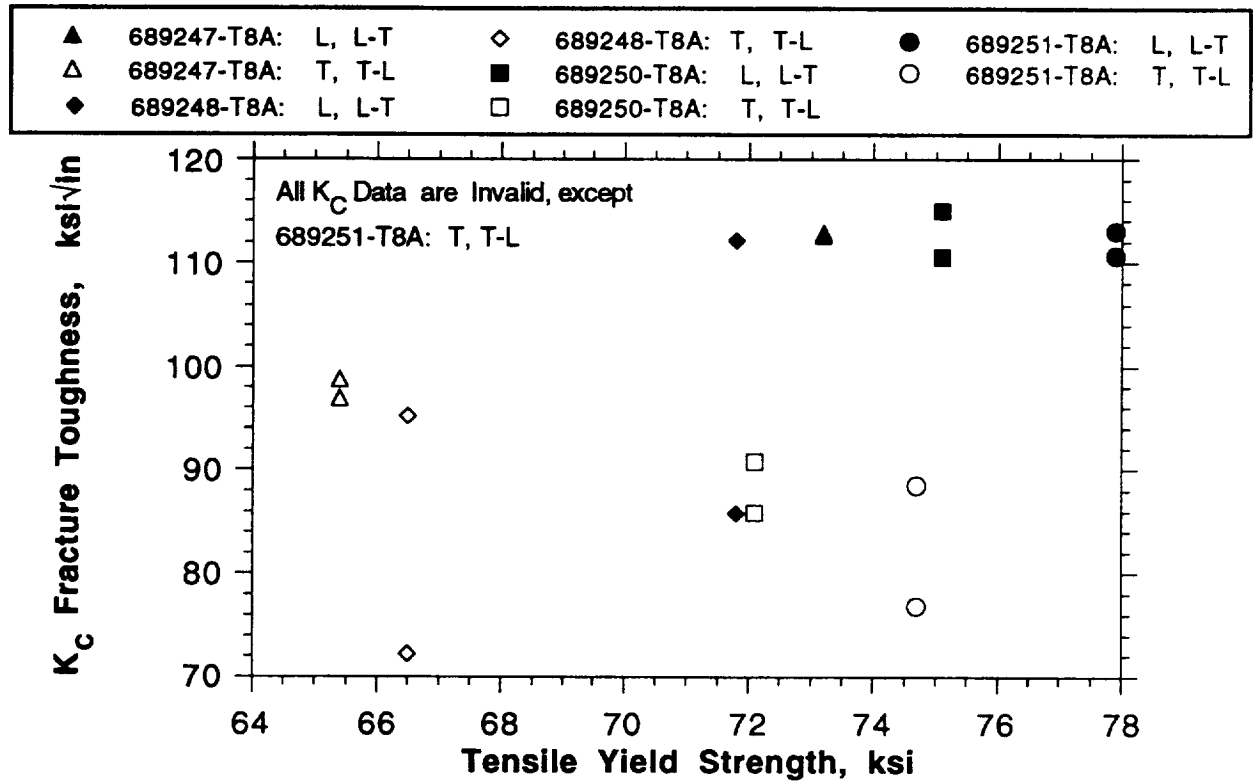


Figure 17. L-T and T-L K_C fracture toughness as a function of L and T tensile yield strength I/M 2XXX sheet peak aged at 325°F in Phase II.

SUBTASK 1(i). I/M 2XXX AND 6XXX ALLOY DEVELOPMENT (Boeing)

Principal Investigator: Dr. W.E. Quist

Objectives

The overall objective of the "Aluminum-Based Materials for High Speed Aircraft" program is to explore and develop the best candidate aluminum-base materials for possible major structural applications on a future HSCT. The two primary objectives of this study are as follows:

- A. To identify the most promising aluminum-base materials with respect to major structural use of the HSCT and to further develop those materials.
- B. To assess these materials through detailed trade and evaluation studies with respect to their structural efficiency of each candidate material on the HSCT.

Program Plan

The original program was comprised of eleven (11) tasks, with another being added in 1993. They are:

- (1)** I/M 2XXX and 6XXX Alloy Development
- (2)** I/M Al-Cu-Li-Mg-Ag Alloy Development
- (3)* P/M 2XXX Alloys
- (4) Al-Si-Ge Alloy Development
- (5)* Toughness Study of P/M Al-Fe-X System
- (6) Processing-Based Improvements in the Mechanical Isotropy and Intermediate Temperature Damage Tolerance of Al-Fe-V-Si Alloy 8009
- (7)** Toughness Study of DMMCs
- (8) Investigation of the Formation of the Ω in Modified 2009 and Characterization of the Modified Alloys' Thermomechanical Properties
- (9) Accelerated Exposure Study

- (10)**Materials Technology Trade-Off Studies For The Aircraft
 - (11)**(New in 1993) Fracture Toughness Test Development
 - (12) (Number 11 in 1992) Administration and Reporting
-
- * Boeing participation in 1992
 - ** Boeing participation in 1993

In 1992 Boeing participated in six of the program tasks; 1, 2, 3, 5, 7 and 10. This was revised (for Boeing) for the 1993 follow-on program by;

- Deleting Tasks 3 and 5 (specifically Tasks 3A and 5A which were, in fact, deleted from the entire program,
- Expanding the testing program in Task 2,
- Adding technical Task 11 dealing with the development of fracture toughness tests using alloys 2024 and RX 818.

Boeing's role in Tasks 1, 2, and 7, is to perform HSCT program critical evaluation tests to determine if the subject materials are approaching, or meeting, required program goals. In Task 10, Boeing is performing trade studies on candidate materials to determine their relative effectiveness with respect to actual structural requirements and needs. The duration for the overall program was originally scheduled for 12 months, and was to be completed by December 31, 1992. As noted, many tasks have now been modified and extended to 24 months, and are now scheduled for completion by December 31, 1993.

Progress for Report Period

Boeing activity in support of their several contract tasks was more limited than anticipated during the subject reporting period. The primary reasons for this situation were:

- A. No alloys were received for evaluation by Boeing, either from the materials suppliers or the University of Virginia, during the January through May 1993 time period. The evaluation of new and/or improved alloys developed during the contract period was anticipated to be a major Boeing contribution to this effort. Tests were to be performed on alloys from Subtasks 1A, 1B, 2C, and 7A. The goal of the Boeing tests is to provide a consistent reference for several important engineering properties, including strength, fracture toughness, fatigue, and thermal stability. The test matrix is basic, but referee tests of this type have been found to uncover many inconsistencies, discrepancies and property shortfalls. The 1992 Boeing test plan is shown in Table I. The original 1993 program is shown in Table II and the Revision 1 1993 program is shown in Table III.
- B. The actual signing of the modified and extended 1993 contract between the Boeing Co. and the University of Virginia did not taken place until June 1993. Consequently, the evaluation of fracture testing methods for determining K_{app} on 2024 and RX 818 (new Task 11) has been delayed (as a contractual issue), as this task is a part of the modified contract effort.

General Discussion of Tasks 1A, 1B, 2C, and 7A; Alloy Development

Based on engineering property data generated to date by the suppliers and UVA, two materials systems are emerging as front runners for HSCT use, two or three others require further evaluation, and two appear not suitable, considering their present state of development. At present, the Weldalite type alloys (RX 818 and modifications), and alloys based on the 2519 system appear the most promising based on their strength-toughness blend and thermal stability. The limited data developed to date for alloys

based on the 6013 system, P/M 2XXX alloys, and metal matrix composites (MMCs) with 2XXX matrices dictate that additional development and evaluation are required to establish the viability of these materials for HSCT use. The high temperature aluminum alloys, based on the Al-Fe-X compositions, demonstrate extreme strain rate and temperature sensitivity with respect to their fracture toughness. Furthermore, data generated during this program has shown that there is not an easy remedy for this problem. Therefore, at this time these types of materials do not appear suitable for primary structure on the HSCT, and will not be pursued further under the present contract. Likewise, studies on the germanium containing aluminum alloys that are strengthened by very fine incoherent precipitates, will also be discontinued. This system will require additional fundamental studies before it can be moved toward production as a commercial product.

Substantive interaction was anticipated between Boeing, NASA, UVA, and the materials suppliers concerning the specifics of the alloy systems to be developed and evaluated. This would include items relating to alloy design, heat treatment, relevant processing issues, and cost. Improvements in Boeing participation have been made in these areas during the past year, and this level of participation will be maintained, and perhaps enhanced.

Acknowledgments

The valuable contributions of Ludwig Suju (Design), Ken Barlow (Durability), Don Rudee (Fracture Test Laboratory) and Mike Hyatt and John Lee (Materials) are gratefully acknowledged.

Table I. Boeing Test Matrix For NASA/UVA/Boeing Program For Al Alloy Development-1992

Test Type	Subtask	Subtasks with Boeing Participation					
		Subtask 1A (page 20) 2XXX Ingot (Alcoa)	Subtask 1B (page 27) 6XXX Ingot (Alcoa)	Subtask 2C (page 36) Weldalite Type (Reynolds)	Subtask 3A (page 41) 2xxx P/M (Alcoa)	Subtask 5A (page 54) Al-Fe-X (Alcoa)	Subtask 7A (page 74) DMMC-2009 (Alcoa)
Tensile Strength R.T., L, LT -65 F, L. 215 F, L		4	4	4	4	4	4
		2	2	2	2	2	2
		2	2	2 at 275 F	2	2 at 350 F	2
Thermal Stability (tensile-L) Room Temp. 275 F/2500hrs		From TS above	From TS above	From TS above	From TS above	From TS above	From TS above
		2	2	2	2	2	2
Microstructure Room Temp. 275 F/100hr 275 F/1000 275 F/2500		1	1	1	1	1	1
		1	1	1	1	1	1
		1	1	1	1	1	1
		1	1	1	1	1	1
Kahn Toughness No Exposure L-T T-L 275 F/2500hr L-T		2	2	2	2	2	2
		2	2	2	2	2	2
		2	2	2	2	2	2
da/dn, CCP 2 Hz 60 Hz							

TABLE II. Boeing Test Matrix For NASA/UVA/Boeing Program For Al Alloy Development-1993, R1.

Subtask	Subtasks with Boeing Participation						
	Subtask 1A (page 20) 2XXX Ingot (Alcoa)	Subtask 1B (page 27) 6XXX Ingot (Alcoa)	Subtask 2C (page 36) Weldalite Type (Reynolds)	Subtask 3A (page 41) 2xxx P/M (Alcoa)	Subtask 5A CANCEL	Subtask 7A (page 74) DMMC-2009 (Alcoa)	
Test Type							
Tensile Strength R.T.-L, LT -65 F, L. 215 F, L	4	4	4	4		4	
	2	2	2	2		2	
	2	2	2+2 at 275 F	2		2	
Thermal Stability (tensile-L) Room Temp. 275 F/2500hrs	From TS above	From TS above	From TS above	From TS above		From TS above	
	2	2	2	2		2	
Microstructure Room Temp. 275 F/100hr 275 F/1000 275 F/2500	1	1	1	1		1	
	1	1	1	1		1	
	1	1	1	1		1	
	1	1	1	1		1	
Kahn Toughness No Exposure 275 F/2500hr L-T T-L L-T	2	2	2	2		2	
	2	2	2	2		2	
	2	2	2	2		2	
da/dn, CCP 2 Hz 60 Hz							

TABLE III. Boeing Test Matrix For NASA/UVA/Boei. Program For Al Alloy Development-1993, R2.
(current)

Test Type	Subtask				
	Subtask 1A I/M 2XXX (Alcoa)	Subtask 1B I/M/ 6XXX (Alcoa)	Subtask 2C RX 818 (Reynolds)	Subtask 7A DMMC-2009 (Alcoa)	Subtask 11 2024*/RX818 (Boeing)
Tensile Strength R.T., L,LT -65 F, L. 215 F, L	4	4	4	4	
	2	2	2	2	
	2	2	2+2 at 275 F	2	
Thermal Stability (tensile-L) Room Temp 275 F/ 2500 Hrs.					
	2	2	2	2	
Microstructure Room Temp. 275 F/100 Hrs 275 F / 1000 Hrs 275 F/ 2500 Hrs	1	1	1	1	
	1	1	1	1	
	1	1	1	1	
	1	1	1	1	
Fracture Toughness R-Curve Kapp No Exposure L-T Kahn Tear Test No Exposure L-T T-L 275 F/2500 Hrs L-T Charpy Test No Exposure L-T T-L					2 / 1
	2	2		2	4 / 2
	2	2		2	4 / 2
	2	2	2	2	
					4 / 2
					4 / 2
					4 / 2

* For Both 0.063" AND 0.125" Thick Panel

**SUBTASK 1(ii). I/M 2XXX and 6XXX ALLOY DEVELOPMENT
(McDonnell Douglas Aerospace)**

Principal Investigator: Mr. Ravi Kahandal

Abstract

NASA-LaRC has provided the University of Virginia (UVa) with a grant to investigate aluminum-based materials for use on future high-speed aircraft. UVa has directed material suppliers to develop aluminum alloys and metal-matrix composites (MMCs) with improved elevated temperature properties and stability. McDonnell Douglas Aerospace-Transport Aircraft Unit (MDA-TA) and Boeing have been selected to evaluate the material properties of the improved materials and conduct trade studies using these properties. For the first six months of 1993, delays in material delivery precluded testing activities.

Introduction

The economic viability of the next generation of supersonic transport depends upon the timely development of materials and structures which can perform efficiently for extended periods in an elevated temperature environment. The University of Virginia (UVa), as directed by NASA-LaRC, has assembled a team of material suppliers experienced in alloy development in a program to address this challenge. The overall objective of this program is to investigate and develop improved aluminum alloys and metal-matrix composites (MMCs) as candidates for application on a high speed civil transport (HSCT). These materials will be developed to meet target properties supplied by HSCT airframers McDonnell Douglas Aerospace-Transport Aircraft Unit (MDA-TA) and Boeing. The most promising candidates will be evaluated in baseline designs to obtain optimized material and structural vehicle concepts.

In addition to guiding the material development efforts by supplying target properties, MDA-TA will evaluate several developmental alloys to measure their ability to achieve these goals. MDA-TA will then use improved material properties to conduct HSCT structural sizing studies, vehicle optimization, and calculate aircraft configuration weight.

Approach

The approach for this program includes a six month material development effort followed by six months of evaluation and structural/vehicle studies. MDA-TA will perform material evaluation in Tasks 1A, 1B, 2D, 3B, and 7B according to the test matrix shown in Table 1. In addition, MDA-TA trade studies will be performed in Task 10B.

Results/Discussion

Material development efforts continued throughout the six-month period ending July 31, 1993. As a result, no material was delivered to MDA-TA for evaluation. MDA-TA placed a purchase order with Reynolds Metals for three sheets of RX818 material. Delivery of this material is scheduled for October 15, 1993. As a result, material evaluations of this material will continue into 1994.

The second semi-annual program review was held January 19-20, 1993, at Hampton, Virginia. Mr. Kahandal represented MDA-TA. He detailed our plans for involvement and our recently revised test matrix (Table 1).

Ravi Kahandal and Jim Hannah attended the third semi-annual program review August 9-10 at Hampton, Virginia. As we had no testing progress to report due to our lack of material, Mr. Kahandal presented an update of the HSR Design Integration Trade Study (DITS) currently under contract at MDA. This presentation is included at the end of this subtask.

TABLE 1. Test Matrix for Evaluating Candidate Materials

TEST	ORIENTATION	TESTS
FRACTURE TOUGHNESS (ASTM E399) [2]	L-T, T-L	4
SALT-FOG CORROSION (ASTM B117) [2]		
BLANK COUPONS	NA	4
INTERFERENCE-FIT FASTENERS [3]	NA	4
STRESS CORROSION CRACKING (ASTM G49) [2,4]	LT	18
MACHINING TRIALS		
CUTTING	NA	6
DRILLING/REAMING	NA	6
FORMING TRIALS		
BRAKE FORMING [5]	L, 30, 45, 60, LT	50
HYDROFORMING	NA	5
JOINING STUDY		
WELDING [6]	NA	6
ADHESIVE BONDING	NA	6
CHEMICAL PROCESSING		
CHEM	NA	2
MILLING		
ANODIZING	NA	2
TOTAL TESTS/ALLOY		113

[1] MATERIAL REQUIRED: 1000 SQUARE INCHES/LOT; MULTIPLE LOTS ACCEPTABLE; 12-INCH MINIMUM SHEET WIDTH

[2] TESTING BEFORE AND AFTER THERMAL EXPOSURE

[3] SIX EACH Ti FASTENERS INSTALLED WET AND DRY AT STANDARD INTERFERENCE PER SPECIMEN

[4] SPRING-LOADED FLAT TENSILE SPECIMENS TESTED BY ALTERNATE IMMERSION

[5] MINIMUM BEND RADIUS: 2 SPECIMENS/RADII FOR 5 RADII

[6] TIG, LASER, CAPACITOR DISCHARGE, AND FLASH WELDING TECHNIQUES USED SUCCESSIVELY UNTIL ACCEPTABLE WELDS PRODUCED

TASK 2. I/M Al-Cu-Li-Mg-Ag ALLOY DEVELOPMENT

Principal Investigator, Reynolds:	Dr. A. Cho
Principal Investigator, UVA:	Dr. J.M. Howe
Principal Investigator, Boeing:	Dr. W.E. Quist
Principal Investigator, Douglas:	Mr. R. Kahandal

Objectives

The objectives of the TASK 2 is to optimize a precipitate strengthened ingot metallurgy alloy based on the Al-Cu-Li-Mg-Ag system, and to meet the property and thermal stability requirements of the High Speed Civil Transport Research Program. A concurrent goal is to understand the effects of thermal exposure on the microstructural/property evolution of the alloy as a function of time and temperature in order to help composition optimization and to develop techniques for predicting the evolution of the alloy during long term service environments.

Property Goals

Boeing Aircraft Company proposed several ambitious property goals for ingot metallurgy aluminum alloys for damage tolerant HSCT applications. It is desired that the combination of tensile yield strength and Kapp. fracture toughness fall within the range between 70/140/ ksi/ksi-inch^{1/2} to 80/100 ksi/ksi-inch^{1/2} after exposure to an anticipated elevated temperature service environment of about 275°F(135°C).

Background

Successful development of the high speed civil transport system (HSCT) depends on the availability of high performance elevated temperature materials. Among the conventional aluminum alloy systems, 2XXX series alloys are commonly used for elevated temperature applications because Cu bearing particles exhibit greater thermal stability. For example, alloys 2618 and 2519 contain a large volume fraction of coarse intermetallic particles,

which not only enhance thermal stability, but also contribute to alloy strength. Unfortunately, coarse intermetallic particles are only marginally effective as strengthening agents while being deleterious on fracture toughness. Therefore, conventional 2XXX alloys offer limited strength and fracture toughness capability.

Among conventional aluminum alloy systems, only 7XXX series alloys could potentially meet the proposed property goals, but only prior to any thermal exposure. 7XXX series alloys are strengthened by a combination of metastable GP zones and $MgZn_2$ precipitates which provide a good combination of high strength and fracture toughness. However, these precipitate phases are not stable above 100°C, therefore, 7XXX series alloys are not suitable for elevated temperature applications.

Recent work at Reynolds Metals Company has demonstrated that a new proprietary Al-Cu-Li-Mg-Ag alloy (RX818) could potentially meet Boeing's requirements for high combinations of strength and fracture toughness. RX818 is mainly strengthened by thermodynamically stable phases which form an extremely fine distribution of precipitates (i.e. T_1 and S'-like phases). These are effective in providing high combination of strength and fracture toughness because the formation of large intermetallic particles is avoided. A high level of property stability in RX818 has been established in thermal exposure studies at Reynolds. Further improvement of thermal stability of the alloy could be achieved by adding optimum amounts of dispersoids in addition to the precipitate distribution. In the TASK 2 program, the optimum amounts of precipitates and dispersoids will be established to improve the mechanical properties and thermal stability of RX818 alloy.

Approach

To accomplish the above objectives, TASK 2 program consists of the following subtasks:

Subtask 2A: Evaluate RX818 Variation Alloys as Model Materials to Understand the Role of Various Strengthening Phases During Thermal Exposure.

(Reynolds Metals Company)

Subtask 2A1:

Evaluate the three variants of RX818 alloy with modified Mg and Ag content to examine the effect of T_1 and S'-like phases on thermal stability of RX818 alloy.

Subtask 2A2:

Examine the effect of dispersoids on thermal stability and mechanical properties of the RX818 alloy - This alloy has a moderate level of dispersoids for conventional casting.

Subtask 2A3:

Examine the effect of dispersoids on thermal stability and mechanical properties of the RX818 alloy - This provides a high level of dispersoids by Spray Deposition Technique.

Subtask 2B: Study the microstructural evolution of the Al-Li-Cu-Mg-Ag System with the RX818 alloy
(UVA Participation)

Subtask 2C: Al-Cu-Li-Mg-Ag Alloy Development
(Boeing Participation)

Subtask 2D: Al-Cu-Li-Mg-Ag Alloy Development
(Boeing Participation)

Subtask 2A: Evaluate RX818 Variation Alloys as Model Materials to Understand the Role of Various Strengthening Phases During Thermal Exposure.

Subtask 2A1: Evaluate the three variants of RX818 alloy with modified Mg and Ag content to examine the effect of T₁ and S'-like phases on thermal stability and mechanical properties during long term thermal exposure.

Summary Of Previous Work

Three levels of Mg and Ag contents are selected with fixed Cu and Li contents as three RX818 variant alloys. To meet the material requirement, four ingots were cast and rolled to .125" gauge unrecrystallized sheet for evaluation.

Compositions

	<u>Cu</u>	<u>Mg</u>	<u>Li</u>	<u>Zr</u>	<u>Ag</u>	<u>Si</u>	<u>Fe</u>
(target)	3.6	.8	1.0	.14	.4	<.08	<.08
64627(actual)	3.8	.8	.9	.13	.4	.06	.06
(target)	3.6	.8	1.0	.14	.8	<.08	<.08
64641(actual)	3.6	.76	.8	.14	.8	.06	.07
(target)	3.6	.4	1.0	.14	.4	<.08	<.08
64653(actual)	3.6	.4	.8	.14	.4	.05	.07
64667(actual)	3.4	.4	.8	.14	.5	.04	.07

Tensile tests and plane stress fracture toughness test results, by 16" wide center notched panel tests in longitudinal direction, were reported in the previous report. The data include both for T8 temper material and for T8 temper material after a thermal soak of 1,000 hours at 275°F.

All the alloys tested showed an excellent combination of strength and fracture toughness in T8 temper. After the thermal exposure, tensile strengths increased by 2-3 ksi and the ductility

(tensile elongation) by 3-4% at the same time. However, fracture toughness(K_c) decreased by 20-30 ksi-inch^{1/2}. The highest K_{app}. fracture toughness value after thermal exposure was achieved by S-64653 which contains lower Mg and lower Ag. The results showed that there are no benefits of Ag and Mg content higher than the baseline alloy for fracture toughness stability during the thermal exposure.

Stress Corrosion Cracking Test On T8 And T8 + Thermal Exposure

Stress corrosion cracking (SCC) resistance tests were conducted with long transverse sheet specimens of two variant alloys, S.No.64627 and 65653.

i. Material Description

<u>S.No.</u>	<u>Process History</u>
64627	Solution Heat treat for 1 hr. at 990°F Cold water quenched Stretch 5% Age 16 hrs. at 320°F Age 1,000 hrs. at 275°F
64653	Solution Heat treat for 1 hr. at 990°F Cold water quenched Stretch 5% Age 16 hrs. at 320°F

ii. Test Procedure

Flat, constant strain, long transverse tensile specimens were assembled into large stressing frames. Triplicate specimens of each material were stressed at 50 ksi prior to exposure in alternate immersion for 30 days, according to the guidelines of ASTM G49. After stressing, the frames were waxed, specimen gauge sections were degreased with acetone, and exposure to the alternate immersion environment was initiated.

Specimens were examined each working day to detect failures. The exposures continued until failure was detected or 30 days had elapsed.

iii. Test Results

No specimen was failed during the 30 day test duration.

Subtask 2A2. Examine the effect of dispersoids on thermal stability and mechanical properties of RX818 alloy - moderate level of dispersoids for conventional casting.

Previous Work

In this work, Zirconium, Vanadium and Manganese additions are being examined among the peritectic elements. For the initial five compositions of 30 lbs. permanent mold ingots were selected and cast. The target and actual compositions are as follows:

Compositions:

	<u>Cu</u>	<u>Li</u>	<u>Mg</u>	<u>Ag</u>	<u>Zr</u>	<u>V</u>	<u>Mn</u>
65836 (target)	3.5	1.0	.4	.4	.17	.1	.3
(actual)	3.4	.99	.52	.34	.15	.12	.3
65837 (target)	3.5	0.8	.4	.4	.17	.1	.3
(actual)	3.5	.86	.39	.22	.18	.12	.3
65838 (target)	3.0	1.2	.4	.4	.17	.1	.3
(actual)	3.1	1.21	.4	.36	.15	.12	.29
65839 (target)	3.5	1.0	.4	.4	.17	.1	--
(actual)	3.35	1.04	.4	.34	.17	.12	--
65840 (target)	3.5	1.0	.4	.4	.17	--	--
(actual)	3.5	1.0	.39	.36	.16	.01	--

The ingots were rolled to .090" gauge sheet for microstructure and mechanical property evaluation. Metallographic examination of the 0.090" gauge sheet samples in T8 temper showed various degrees of recrystallization depending on the alloy chemistry. The grain structures of the five alloys are shown in Figure 1. Four variant alloys containing Mn and V, S.Nos. 65836, 65837 65838 and 65839, are recrystallized at various degrees. S.No. 65840 containing only Zr, is not recrystallized. Tensile test results and fracture toughness values of T8 temper materials after thermal exposures are listed in TABLE 1. The tensile properties of all five variants in T8 temper material undergo

complex property changes during the initial stage of the thermal exposures at 275°F. No significant changes occurred in strength or fracture toughness between the samples exposed for 1,000 hours and the samples exposed for 2,500 hours.

Additional Experiment

Among the five alloy variants examined earlier, S.No. 65840 was the only variant which retained unrecrystallized grain structure after solution heat treatment. The cause of the various degrees of recrystallization for the four other variants were not clear at the time. To provide more information regarding the effect of dispersoid forming elements on the grain structure and fracture toughness after thermal exposure, additional experiments were conducted. Four compositions, 65836, 65837, 65838 and 65840, were repeated by 66932, 66933, 66934 and 66936, respectively. To evaluate the effect of V and Mn, a new composition, 66937, was cast to be compared against 65839.

i. Composition Selection and Casting

The five compositions of 30 lb, permanent mold ingots were cast, and the target and actual compositions are as follows:

Compositions:

	<u>Cu</u>	<u>Li</u>	<u>Mg</u>	<u>Ag</u>	<u>Zr</u>	<u>V</u>	<u>Mn</u>
66932(target)	3.5	1.0	.4	.4	.16	.1	.3
(actual)	3.49	1.11	.43	.43	.17	.11	.19
66933(target)	3.5	0.8	.4	.4	.16	.1	.3
(actual)	3.46	.82	.42	.46	.19	.11	.34
66934(target)	3.0	1.2	.4	.4	.16	.1	.3
(actual)	2.92	1.21	.4	.44	.18	.12	.33

(con't)

Compositions:

	<u>Cu</u>	<u>Li</u>	<u>Mg</u>	<u>Ag</u>	<u>Zr</u>	<u>V</u>	<u>Mn</u>
66936(target)	3.5	1.0	.4	.4	.16	--	--
(actual)	3.42	1.02	.39	.42	.17	--	--
66937(target)	3.5	1.0	.4	.4	.16	--	.3
(actual)	3.50	1.0	.41	.43	.18	--	.32

ii. Fabrication

The ingots were homogenized, scalped and hot rolled to 0.125" gauge sheet. The hot rolled sheet was then cold rolled to .090" gauge sheet. The final gauge sheet products were solution heat treated at 990°F for 1 hour followed by cold water quench. T8 temper sheet was stretched by 5% and aged at 320°F for 16 hours as a standard T8 temper practice.

iii. Microstructural Examination

Optical metallographic examination was conducted in the T8 temper sheet and the micrographs are shown in the Figure 2. S.No.66932 and S.No. 66936 are unrecrystallized. S.No.66933 and S.No.66937 are recrystallized and S.No.66934 is only partially recrystallized. It appears that alloys with higher Li or alloys containing only Zr without V or Mn, are more stable against onset of recrystallization.

S.No. 66932 contains relatively high Li and only 0.19 Mn. S.No. 66936 does not contain Mn nor V. Therefore, these two variants are unrecrystallized. S.Nos.66933 and 66937 contain high level of V and Mn. Therefore, these variants are recrystallized. S.No. 66934 contains both V and Mn but also a high level of Li, therefore, this variant is only partially recrystallized. Similar observations can be made from the earlier five alloy variants as

shown in Figure 1.

The various degree of recrystallization of these materials can be explained by Mn and V interaction with Zr to suppress forming the coherent Al_3Zr phase. It is not the present scope of this program for a quantitative examination of the particle density of Al_3Zr phase. At present, it is not clear why Li content plays a role in recrystallization behavior.

The degree of recrystallization was reflected in the strength and fracture toughness of the material.

iv. Mechanical Properties

Mechanical property test results of the 0.090" gauge sheet in T8 temper before and after a thermal exposure are listed in TABLE 2. Due to a mistake during the T8 temper test sample preparation, there were no tensile properties available for S.No.66936 in T8 temper. Fracture toughness tests by 10" wide, center notched, fatigue pre-cracked panel tests were conducted on the materials after the thermal exposure. Due to the limitation of the amount of material available (30 lb. ingots), only two fracture toughness test specimens per composition variant were available to evaluate the effect of thermal exposure. Therefore, a decision was made that the two specimens would be used to evaluate the fracture toughness values of T8 temper material and T8+2,500 hours of thermal exposures at 275°F.

v. Discussion

Effect of Recrystallization - The test results for the tensile and fracture toughness tests (K_c and K_{app} .) in T8 and T8+2,500 hour exposure at 275°F are listed in Table 2. Fracture toughness by K_c and K_{app} . for all ten variant alloys of T8 temper material after a thermal exposure, are plotted in Figure 3 and Figure 4, respectively. The data are presented in three groups by their degree of recrystallization, namely, unrecrystallized,

partially recrystallized and fully recrystallized. The effect of grain structure on strength and fracture toughness after thermal exposure are demonstrated by Figure 3 and Figure 4. The recrystallized variants with low Li content, S.Nos.65837 and 66933 show the highest Kc values in T8 temper and maintained Kc value of 126 and 114 ksi-inch^{1/2}, respectively, after the 2,500 hours exposure at 275°F. However, the tensile yield stresses of these recrystallized variants are lower than those of unrecrystallized variants. Conversely, unrecrystallized variants show higher strengths but lower fracture toughness than their counterparts. Scanning electron microscopic examination of the fracture surfaces reveals brittle inter-subgranular fracture behavior of the unrecrystallized variants, as shown in Figure 5 for S.Nos. 65840 and 66936. It is believed that the precipitation of T₁ particles along the subgrain boundaries during the thermal exposures at 275°F would lead to the such behavior. Figure 6 and Figure 7 show the ductile fracture behavior of the recrystallized variants, S.Nos.66933 and 66937, respectively.

These observations suggest that materials with recrystallized microstructures with low Li content would be favored for higher fracture toughness applications at a medium strength level, and materials with unrecrystallized microstructures would be favored for higher strength applications with a limited fracture toughness capability. More detailed TEM study of the microstructural evolution during the thermal exposure is planned for the future.

Effect of Mn and V addition - Metallographic examination of all ten variant alloys revealed that the addition of Mn and/or V promotes recrystallization. However, to evaluate the impact of Mn and V addition on the fracture toughness after thermal exposure, the comparisons should be made within alloy variants with similar grain structure and similar strengths.

Among the three unrecrystallized variants, S.Nos. 66932, 66936 and 65840, additional dispersoids in S.No. 66932 appear to be deleterious for fracture toughness as shown in Figure 3 and

Figure 4. Among the recrystallized variants, S.Nos. 66937, 65836, 65839 are selected to evaluate the effect of dispersoids on fracture toughness. These three alloys have similar alloy compositions (nominally 3.5%Cu-1.0%Li-.4%Mg-.4%Ag) and similar strengths except the dispersoid contents. S. No. 65839 which contains Zr and V shows the lowest fracture toughness. The highest fracture toughness value was achieved from S.No.66937 containing Zr and Mn without V (see Figure 3 and Figure 4). In conclusion, no beneficial effect of adding V has been found.

vi. Conclusions

- Alloys with Zr alone retained unrecrystallized structures after solution heat treatment.
- Alloys with additional dispersoids (Mn, V) recrystallized after solution heat treatment.
- The recrystallized alloy variants with low Li content exhibited ductile fracture behavior and retained high fracture toughness even after 2500 hours of thermal exposure at 275F.
- The recrystallized alloy variants showed lower strength compared to the unrecrystallized variants.
- Alloy variants containing Zr and Mn without Vanadium exhibited better toughness at similar strength levels than the alloy containing V.

Subtask 2A3: Examine the effect of dispersoids on thermal stability and mechanical properties of the RX818 alloy - Alloy produced with a high level of dispersoids by the Spray Deposition technique.

Composition selection and casting by Spray Deposition:

The total amount of fine coherent dispersoid particles in conventionally cast materials are very limited. One way to increase the amount of these coherent dispersoid particles is to employ a casting technique with a faster solidification rate.

In this work, the Spray Deposition technique was selected to produce material with high volume fraction of coherent dispersoids. The main reason for selecting the Spray Deposition technique among the other rapid solidification techniques was its economic feasibility for commercial scale production.

Five compositions of 30 lb permanent mold ingots were cast as starting stock material for Spray Deposition casting. The compositions are as follows:

<u>Compositions:</u>							
<u>S.No.</u>	<u>Cu</u>	<u>Li</u>	<u>Mg</u>	<u>Ag</u>	<u>Zr</u>	<u>V</u>	<u>Mn</u>
65831(target)	3.5	1.0	.4	.4	.3	.2	--
(actual)	3.45	1.0	.43	.29	.29	.18	.01
65832(target)	3.5	1.0	.4	.4	.3	.2	.5
(actual)	3.6	1.04	.43	.38	.28	.18	.44
65833(target)	3.5	1.0	.4	.4	.25	.2	.3
(actual)	3.6	1.1	.43	.44	.26	.17	.32
65834(target)	3.5	1.0	.4	.4	.25	.1	.3
(actual)	3.39	1.02	.41	.43	.22	.09	.3
65835(target)	3.0	1.2	.4	.4	.3	.2	--
(actual)	3.58	1.21	.42	.46	.27	.17	--

Fabrication

Prof. E. Lavernia's group, from the University of California at Irvine, completed the casting of five spray deposited billets. The billets were machined to 3" diameter billets and extruded to .25" x 1.5" cross section bars. Since these alloys were new to Prof. Lavernia's group, the amount of charge material provided by Reynolds Metals Company was not sufficient to establish the most optimum processing conditions. As a result, some of the billets were very small and of questionable quality. These extrusions were hot rolled to 0.125" gauge and then cold rolled to 0.090" gauge sheet. The final gauge sheet products were solution heat treated at 990°F for 1 hour followed by cold water quench. T8 temper sheet were stretched by 5% and aged at 320F for 16 hours as a standard T8 temper practice.

Microstructure

Optical micrographs of the five alloys in the final temper condition were shown in the previous progress report. The alloys containing Zr and no Mn, S.No. 65831 and S.No.65835, were completely unrecrystallized and the alloys containing both Zr and Mn, S.No.65832, S.No. 65833 and S.No. 65834 were fully recrystallized with coarse recrystallized grains. This observation proves that the presence of Mn interferes strongly with Zr and prevents formation of coherent Al_3Zr dispersoid particles which is known for its effectiveness of preventing recrystallization. It appears that V content does not show a strong effect on the recrystallization behavior.

Mechanical properties

The tensile test results of T8 temper sheet from the Spray Deposition technique were discussed in the report from the previous reporting period. Based on the comparison of tensile

properties, there were no significant differences in properties between the materials from the conventional processing and the Spray deposition technique. It should be noted that the strengths of these alloys are strongly influenced by the degree of recrystallization. The higher strengths achieved among the Spray Deposition alloys are from the two unrecrystallized alloys, S.Nos.65831 and 65835, both of which do not contain Mn. S.No. 65835 shows a higher strength than S.No.65831 due to a higher Cu and Li content.

Due to the narrow sheet material from the Spray Deposited billets, it was decided to utilize Kahn tear tests as a fracture toughness indicator test. Tensile and Kahn Tear test results from the material, after thermal exposure at 275°F for various lengths of time, are listed in TABLE 3. Tensile yield stresses and propagation energy(P.E.) from Kahn Tear tests from the five variants alloys after thermal exposures at 275°F are plotted in Figure 8. As stated earlier, the material quality of these billets are very questionable, therefore, we do not have confidence in the quality of the test results. We would like to defer technical interpretation of the test result until additional experiments can be conducted.

TABLE 1

Tensile Test and Plane Stress Fracture Toughness Test Results by 10" wide Center Notched Panel from cold rolled 0.090" gauge sheet of five RX818-T8 type alloys after thermal exposures at 275°F for 1,000 hours (-2's) and 2,500 hours (-3's)

<u>S.No.</u>	<u>UTS(ksi)</u>	<u>TYS(ksi)</u>	<u>El(%)</u>	<u>Kc</u>	<u>Kapp.</u>
65836-2	77.3	74.0	9.0	105.7	81.1
-3	76.6	74.0	8.5	93.3	77.4
65837-2	72.3	67.6	9.0	139.7	93.3
-3	72.3	68.5	8.5	126.0	88.1
65838-2	73.7	70.6	8.0	92.5	75.8
-3	73.6	70.7	5.5	91.2	72.9
65839-2	78.0	75.0	7.0	87.2	73.3
-3	78.2	75.1	7.0	82.4	67.7
65840-2	83.6	79.8	6.5	80.4	71.6
-3	82.8	78.4	8.5	88.7	73.2

Note:

All the tensile properties are averaged from duplicate test results.

Kc and Kapp. values are in Ksi-(inch)^{1/2} and tested with single 10" wide center notched and fatigue precracked specimens.

TABLE 2

Tensile tests and plane stress fracture toughness test results of
0.090" gauge RX818 type alloys in T8 temper(-1's) and after
thermal exposure at 275°F for 2500 hours(-2's)

<u>S.No.</u>	<u>UTS(ksi)</u>	<u>TYS(ksi)</u>	<u>El.(%)</u>	<u>Kc</u>	<u>Kapp.</u>
66932-1	79.6	76.5	8.0	N.A.	N.A.
-2	81.5	78.5	8.5	76.9	67.6
66933-1	74.0	69.9	9.0	140.5	97.5
-2	76.5	73.2	10.2	114.8	83.9
66934-1	69.5	65.1	10.0	136.9	93.6
-2	73.2	70.8	10.5	91.0	74.4
66936-1	N.A.	N.A.	N.A.	N.A.	N.A.
-2	79.5	76.7	8.8	97.1	79.1
66937-1	75.4	70.9	9.0	150.0	100.3
-2	78.6	74.5	9.3	99.7	88.1

Note:

All the tensile properties are averaged from duplicate test results.

Kc and Kapp. values are in Ksi-(inch)^{1/2} and tested with single 10" wide center notched and fatigue precracked specimens.

TABLE 3

Tensile and Kahn Tear test results for Spray Deposition RX818-T8 type variant alloys after thermal exposures at 275F for various length of time

<u>S.No.</u>	<u>hrs./275F</u>	<u>UTS(ksi)</u>	<u>TYS(ksi)</u>	<u>El.(%)</u>	<u>Tear Strg.(ksi)</u>	<u>P.E.(in*lb/in²)</u>
65831	as T8	78.8	74.8	9.5		
	500				18.1	297
	1000				16.7	342
	2500	78.6	73.1	7.0	18.7	419
65832	as T8	72.6	69.7	10.5		
	500				17.9	417
	1000				16.9	360
	2500	73.3	69.1	9.0	16.7	290
65833	as T8	69.8	67.2	12.5		
	500				16.0	187
	1000				8.2	36
	2500	66.8	63.0	7.5	9.1	21
65834	as T8	68.9	67.1	10.5		
	500				19.0	270
	1000				18.8	266
	2500	69.5	67.2	10.5	18.3	270
65835	as T8	83.9	80.6	9.5		
	500				13.7	186
	1000				13.0	135
	2500	79.6	73.3	6.5	13.4	135



65838

65837

65836



65840

65839

Photomicrographs of longitudinal cross sections of 0.090" gauge RX818-T8 type sheet, S.Nos.65836, 65837, 65838, 65839 and 65840. Electro etched. Magnification; 100x

Figure 1



66934

66933

66932



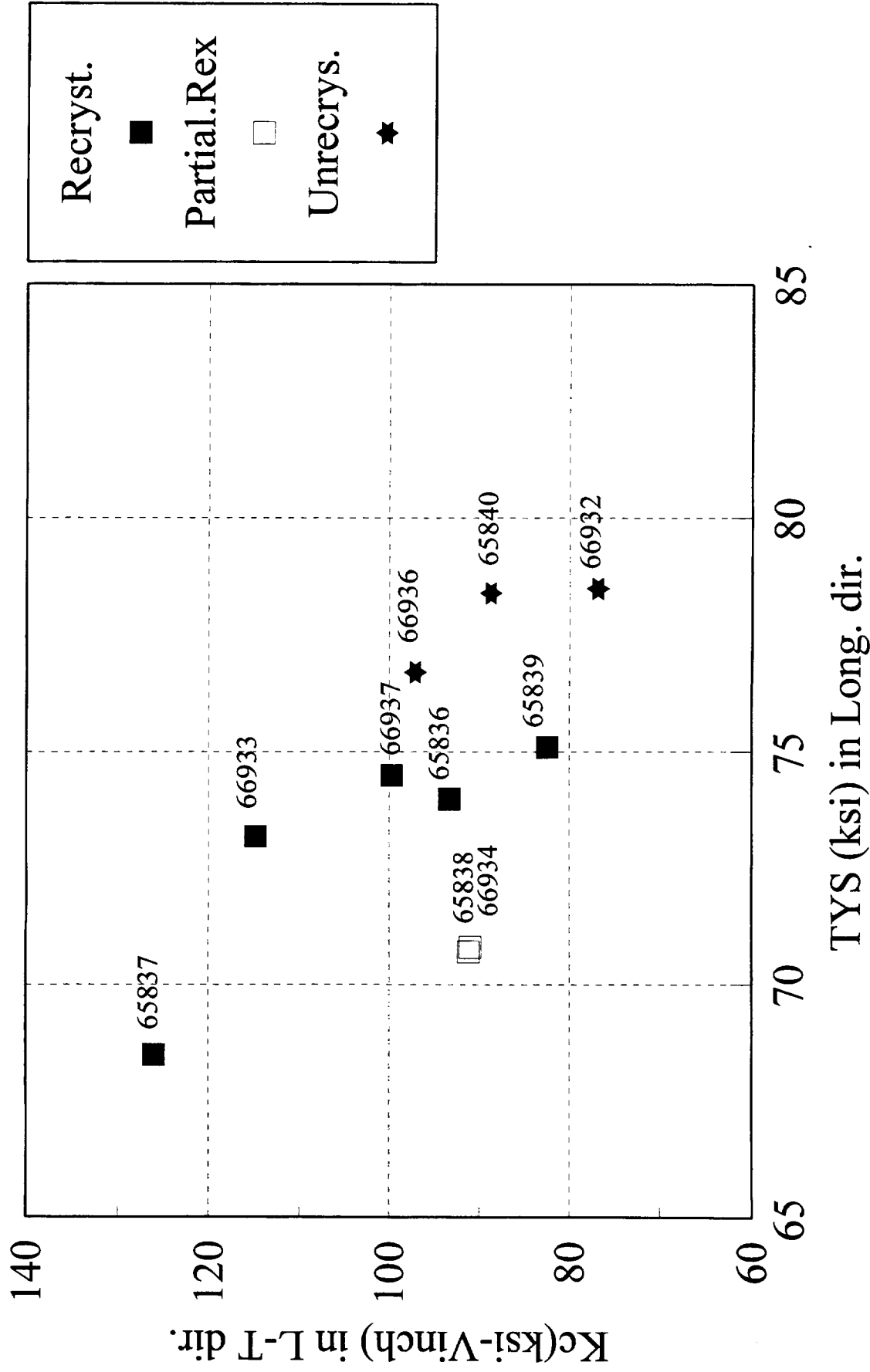
66937

66936

Photomicrographs of longitudinal cross sections of 0.090" gauge RX818-T8 type sheet, S.Nos.66932, 66933, 66934, 66936 and 66937. Electro etched. Magnification; 100x

Fracture Toughness of RX818-T8 type Variants

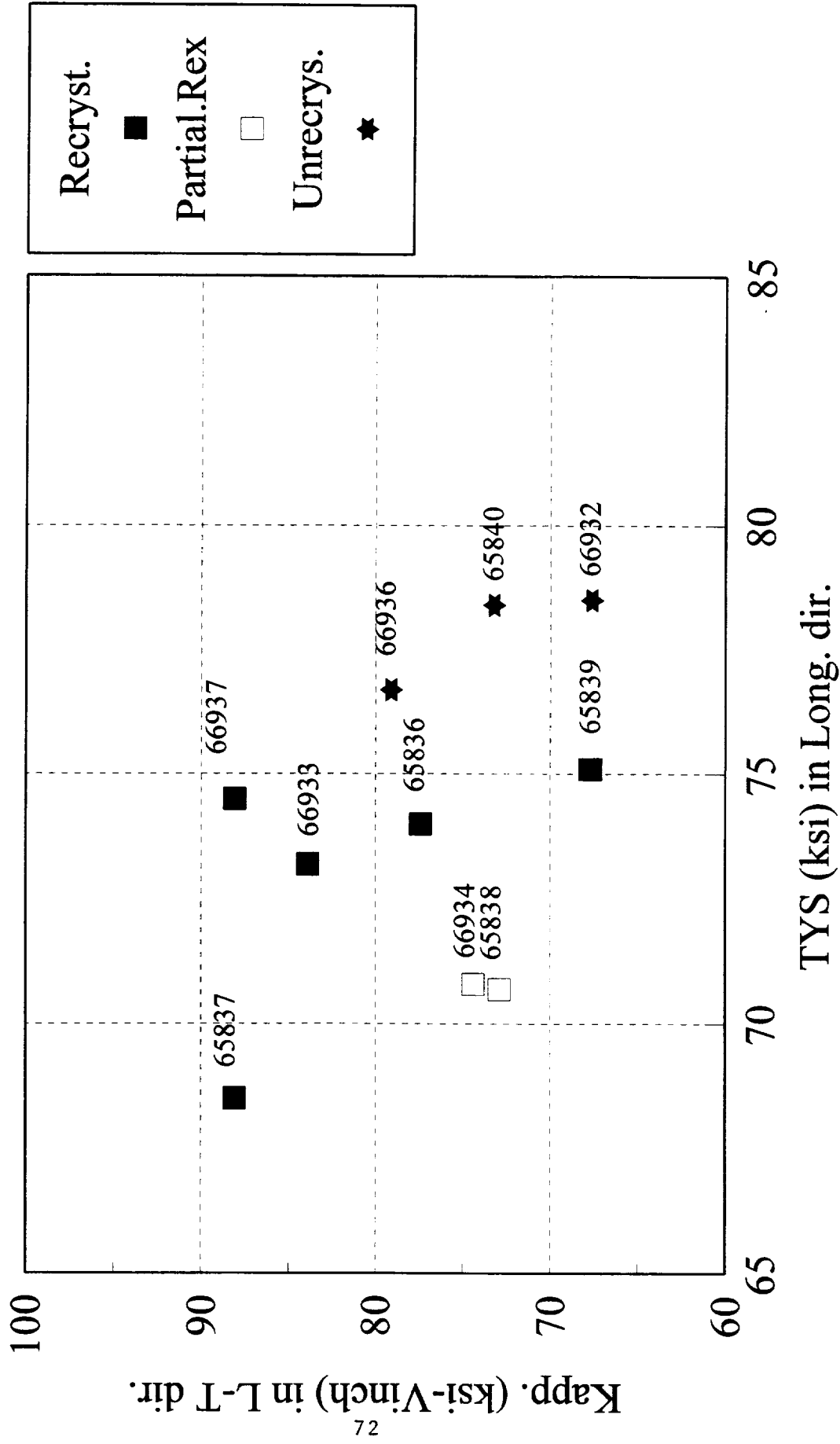
Kc vs. TYS after 2500 hrs. Exposure at 275F



UVA93A1.pre

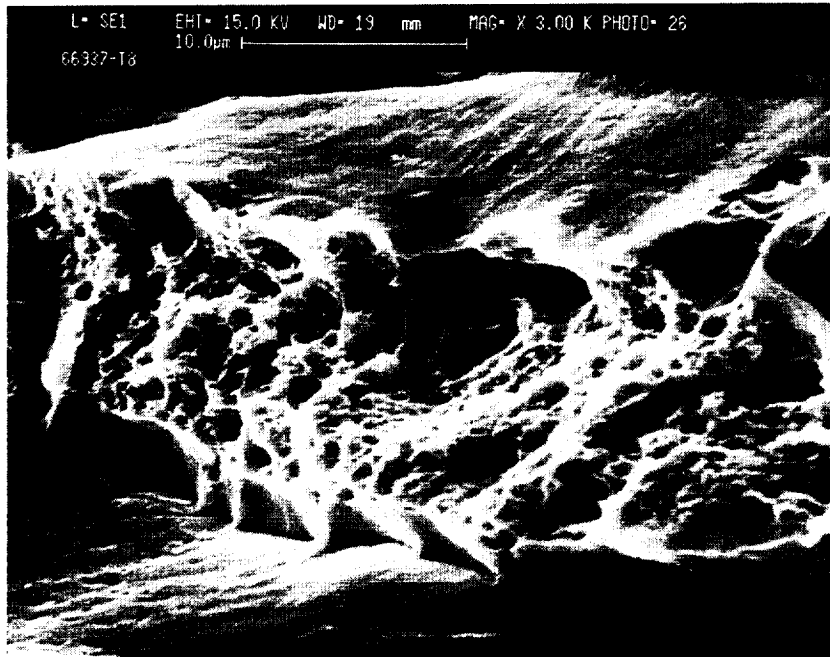
Figure 3

Fracture Toughness of RX818-T8 type Variants Kapp.vs. TYS after 2500 hrs. Exposure at 275F

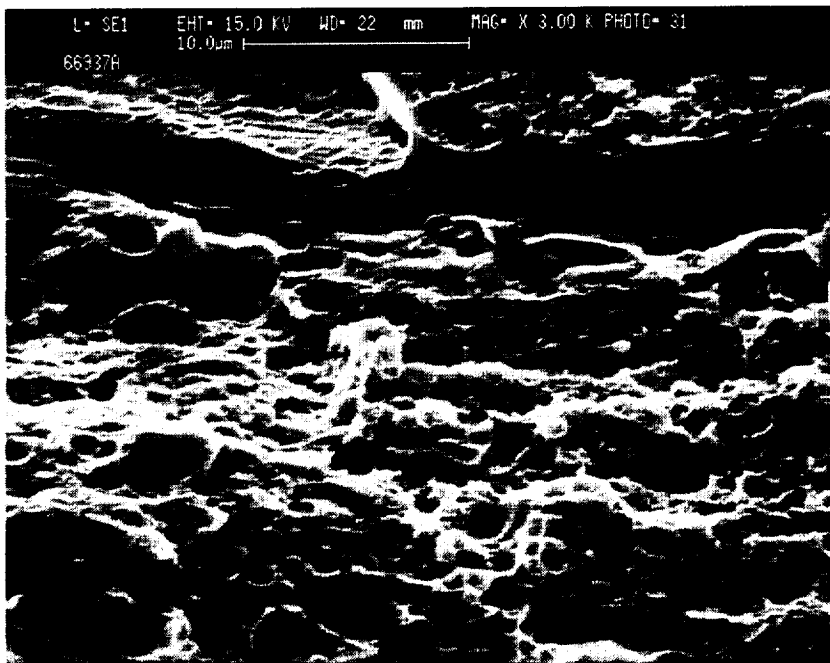


UVA93A1.pre

Figure 4

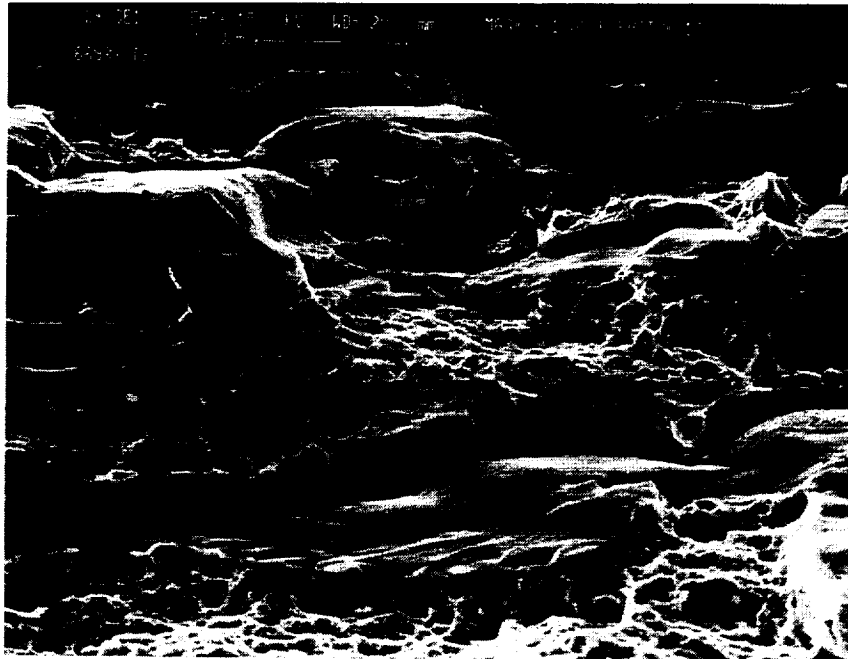


(a)



(b)

Scanning electron micrograph of fractured surface of Recrystallized RX818 type alloys. a) S.No. 66937-T8
(b) S.No. 66937A; T8+2500h at 275°F

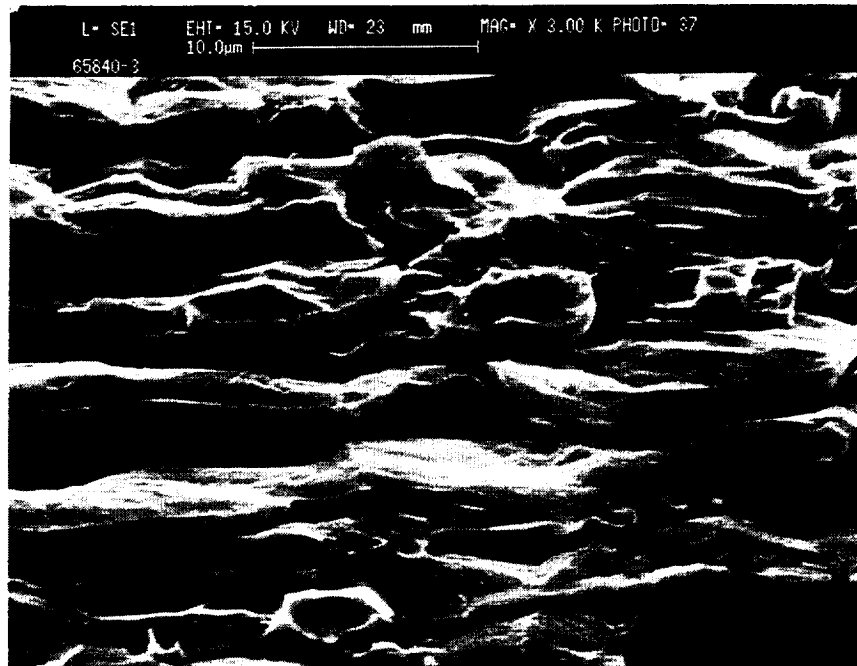


(a)

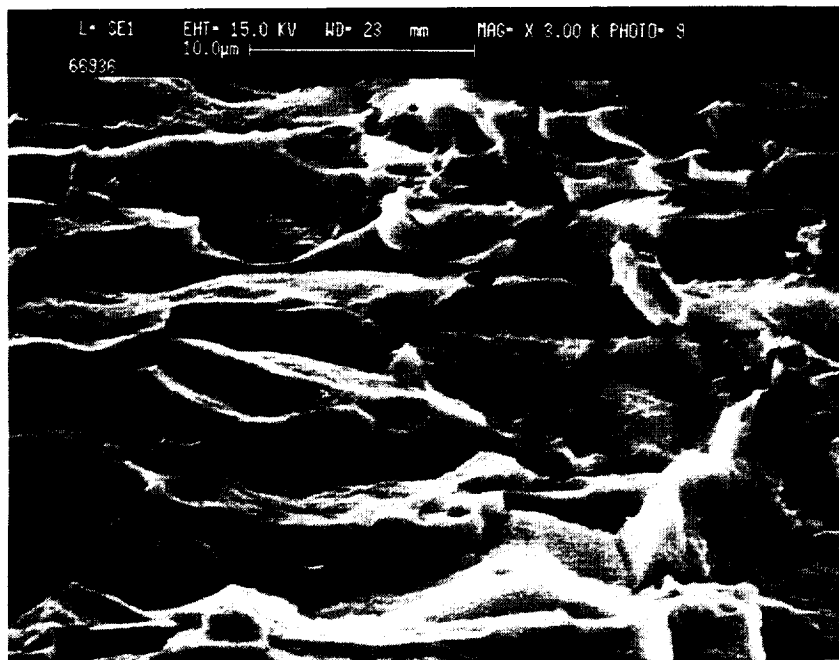


(b)

Scanning electron micrograph of fractured surface of Recrystallized RX818 type alloys. a) S.No.66933-T8
(b) S.No.66933A; T8+2500h at 275°F



(a)

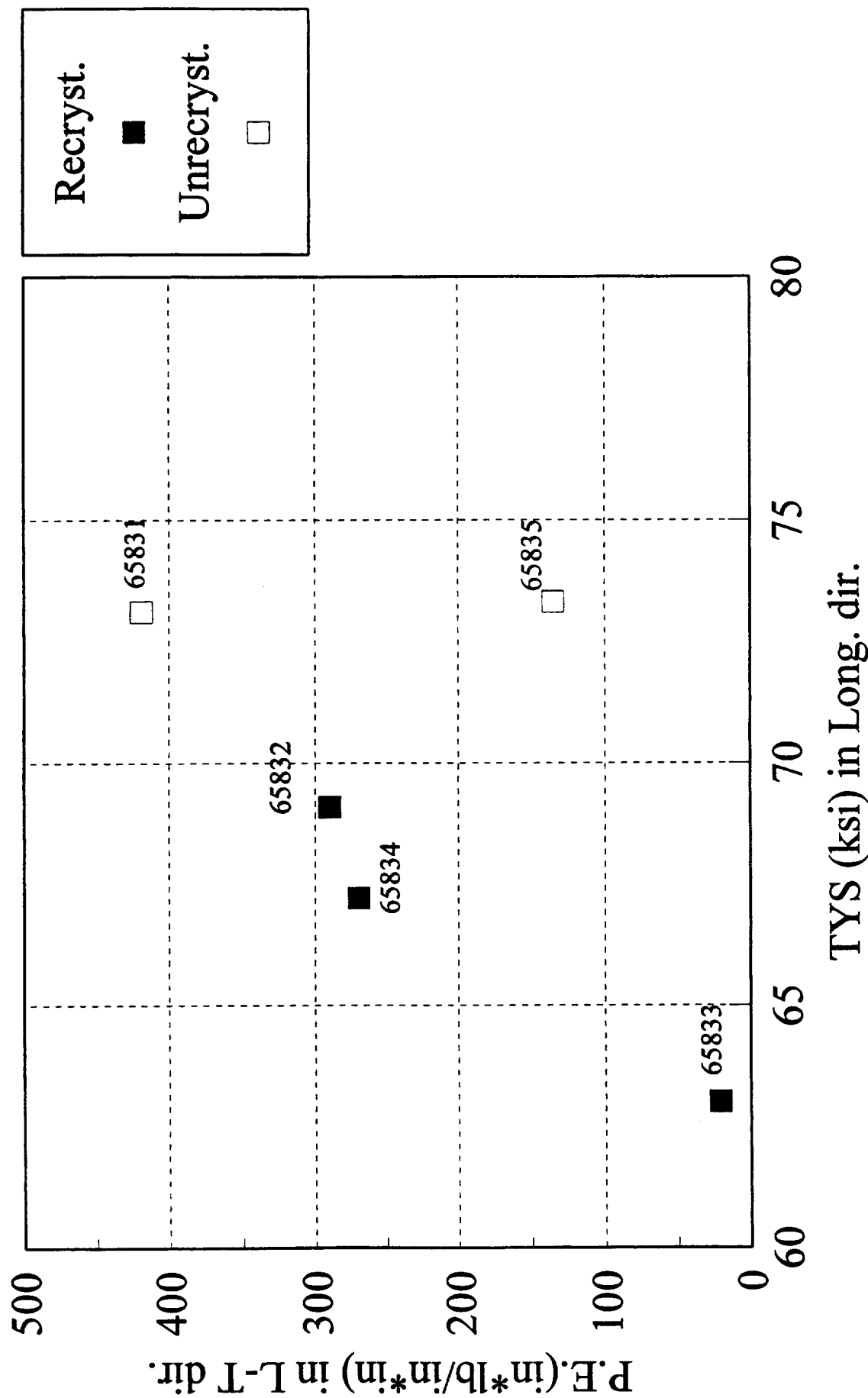


(b)

Scanning electron micrograph of fractured surface of Unrecrystallized RX818 type alloys (a) S.No. 65840; T8+2500h at 275°F. (b) S.No. 66936; T8+2500h at 275°F

Fracture Toughness of Spray Deposition Alloy Variants

Propagation Energy vs. TYS after 2500 hrs. Exposure at 275F



**SUBTASK 2B. A STUDY OF THE MICROSTRUCTURE/PROPERTY
EVOLUTION CHARACTERISTICS OF THE Al-Li-Cu-Mg-
Ag SYSTEM WITH RX818 (University of Virginia)**

Principal Investigator: Prof. J.M. Howe
Research Associate: Dr. Y. Mou

Objectives

The main objectives for the first six months of the second year for this subtask were: i) to quantify the coarsening behavior of matrix T_1 plates in RX818 alloy as a function of time and temperature, ii) to examine the microstructure of the alloy as a function of time and temperature in order to reveal any microstructural changes that might be important in terms of the alloy properties, and iii) to determine the microstructures of differential scanning calorimetry (DSC) samples of RX818 alloy produced at NASA-Langley in order to better understand the DSC data. Results from each of these areas are summarized below.

Results

i) Coarsening Behavior of Matrix T_1 Plates Versus Time and Temperature

Quantitative precipitate size distributions and volume fractions for matrix T_1 plates in RX818 alloy (Lot. No. 64667) in the initial -T8 condition (20 hrs at 163°C (325°F)) and after additional aging for total times of 1006 and 2518 hrs at 163°C (325°F) were provided in the previous six month report for this grant. Additional precipitate data generated for the same initial microstructure (RX818 alloy aged 20 hrs at 163°C (325°F)) after aging for 1006 and 2518 hrs at temperatures of 107°C (225°F) and 135°C (275°F) are shown in Figs. 1 through 4. The diameter and thickness distributions were obtained using the same procedure described in the previous report where at least 1000 precipitates

were measured in each sample. Note that the particle diameters and thicknesses are normalized by the average diameter and thickness in each of the graphs.

The average diameter, thickness, number density, volume fraction and aspect ratio of the matrix T_1 plates versus aging time at 107°C (225°F), 135°C (275°F) and 163°C (325°F) are shown in Figs. 5(a) through (e), respectively. From the data in Figs. 5(a) and (b), it is apparent that the average diameter and thickness of the T_1 plates increases systematically with both aging time and temperature. As might be expected, the largest change occurred at the highest temperature of 163°C (325°F), with the average diameter increasing from about 45 nm after 20 hrs of aging to 91 nm after 2518 hrs (by a factor of two), and the average thickness increasing from about 1.5 nm (about two unit cells of the T_1 phase) to about 5.8 nm thickness (by a factor of about 4). These increases were accompanied by a decrease in the average aspect ratio (diameter/thickness) of the T_1 plates in the 163°C (325°F) sample from about 30:1 to 16:1, as shown in Fig. 5(e).

At the other extreme in temperature, the average diameter and thickness of the T_1 plates in the 107°C (225°F) sample increased only slightly, with the average diameter increasing from 45 nm to 60.1 nm and the thickness increasing from 1.5 nm to 3.2 nm. Interestingly though, the average aspect ratio of this sample decreased from the initial -T8 value of 30:1 to about 19:1 after 2518 hrs at 107°C (225°F). A similar trend occurred for the 135°C (275°F) sample, where the average aspect ratio of the T_1 plates was 18:1 after an additional 2518 hrs aging (Fig. 5(e)). Thus, it appears that the T_1 plates in all of the samples approach a similar aspect ratio (about 17:1) after prolonged aging even though their average diameters and thicknesses, i.e., their sizes, were still much different.

Similar to the particle size behavior of the T_1 plates, the number density of the precipitates displayed systematic behavior with respect to aging time and temperature, changing the most for the highest aging temperature, as shown in Fig. 5(c). For example, there was a slight tendency for the number density of the T_1 plates to increase with an additional aging of 1006 hrs, with the increase being proportional to the aging temperature. Similarly, the number density then decreased in all of the samples with further aging to 2518 hrs, with the largest decrease occurring for the highest temperature of 163°C (325°F). These changes were fairly insignificant for the 107°C (225°F) sample but substantial for the 163°C (325°F) sample, where for example, the number density changed from $3.2 \times 10^{12}/\text{mm}^3$ at 1006 hrs to $7.2 \times 10^{11}/\text{mm}^3$ after 2518 hrs aging.

The volume fraction of the T_1 precipitates displayed perhaps the most unusual behavior with additional aging at the various temperatures after the -T8 condition. As seen in Fig. 5(d), the volume fraction of the 163°C (325°F) sample increased to about 0.03 (3%) after aging for 1006 hrs and then decreased slightly with further aging to 2518 hrs, indicating that the maximum amount of T_1 phase had precipitated by 1006 hrs and that coarsening of the precipitates was occurring beyond this time. In contrast, the volume fraction of T_1 plates in the 135°C (275°F) sample increased to only about 0.02 after 1006 hrs and then to 0.03 after 2518 hrs. Hence, although the T_1 particle distribution was undergoing a coarsening process as indicated by the size and aspect ratio data in Figs. 5(a) and (b), concomitant precipitation of a substantial amount of additional T_1 phase also occurred between 1006 and 2518 hrs at 135°C (275°F), i.e., growth of new precipitates occurred in addition to coarsening of existing particles. In the 107°C (225°F) sample, the volume fraction of T_1 phase increased with increasing aging time but was only 0.02 after 2518 hrs at this temperature,

indicating that a substantial amount of additional T_1 phase could precipitate with further aging at this temperature. Other significant microstructural features were also noticed in the 107°C (225°F) sample and these are discussed in the following section.

ii) Microstructural Changes During Long-Term Aging of RX818 Alloy

T_1 was the primary phase for all of the aging times examined at 163°C (325°F), from the -T8 temper to 2518 hrs of aging. In contrast, a substantial amount of S' phase and some δ' precipitates were found in the -T8 sample that was aged for an additional 2518 hrs at 107°C (225°F). Figure 6 shows a dark-field TEM image of the microstructure of this sample. The sample is in a $\langle 110 \rangle$ matrix orientation and one variant of T_1 plates is edge on and bright in the figure. In addition, a fairly large number of S' rods are evident in the microstructure and these appear as gray lines which are nearly horizontal and vertical in the figure. In addition, a few δ' precipitates, which appear as bright circles in the micrograph, are also evident. The amount of S' phase in the 107°C (225°F) microstructure has not been quantified but it is substantially coarser than in the -T8 sample and may have a significant effect on the mechanical properties of the alloy. Only a small amount of δ' phase was evident in the microstructure, but in contrast, none was seen in the initial -T8 sample.

The appearance of S' and δ' precipitates in the microstructure together with an increase in the volume fraction of T_1 phase with aging up to 2518 hrs at 107°C (225°F) indicate that substantial changes occur in RX818 alloy at this temperature, even though coarsening of the major T_1 strengthening precipitate is much less at this temperature than at 163°C (325°F). In addition, the T_1

volume fraction data indicate that there is still appreciable supersaturation of solute after the initial -T8 aging treatment (20 hrs at 163°C (325°F)). This supersaturation increases as the additional aging temperature decreases so that a substantial amount of the metastable S' and δ' phases may precipitate at lower temperatures. The volume fraction data indicate that there could still be considerably more precipitation of these phases with further aging beyond 2518 hrs at 107°C (225°F), and this issue needs to be examined as longer aging times become available for study.

iii) Analysis of DSC Samples from NASA-Langley

Figure 7 shows a 5°C/min DSC scan from the RX818 alloy sample aged for 2518 hrs at 107°C (225°F) after the initial -T8 treatment. Three separate DSC samples were heated in the calorimeter at 5°C/min to either 212°C, 280°C or 312°C and quenched at a rate of about 140°C/min from these temperatures using the liquid nitrogen attachment to the DSC cell. These experiments were performed at NASA-Langley Research Center [R. Shenoy, NASA-Langley Research Center, unpublished research].

Each DSC sample was then cut into two thin slices using a diamond saw and electropolished to produce a thin foil suitable for TEM examination. Figures 8(a-c) show bright-field TEM images of the microstructures of the 212°C, 280°C and 312°C samples near $\langle 110 \rangle$ and $\langle 112 \rangle$ zone axis orientations. Qualitatively, the 212°C sample in Fig. 8(a) was not much different from the original 2518 hr sample except that the T_1 precipitates looked perhaps a little coarser and more widely distributed. At 280°C, the microstructure was quite different, as evident from Fig. 8(b), where many of the T_1 plates had dissolved and the remaining plates were considerably thicker. In addition, a number of other plates (arrows) which appear to be those of the Θ precipitate were observed in the microstructure and a few relatively coarse S laths were also

visible. Figure 8(c) shows the 312°C microstructure, which was qualitatively similar to the 280°C microstructure except that the Θ precipitates (arrows) were more numerous and coarser than at 280°C. There was also fairly substantial variability in the microstructure from area to area in this sample.

TEM investigation of the DSC samples indicates that the first major endotherm in the DSC traces at around 212°C is due to dissolution of T_1 plates and possibly other small precipitates such as S' laths. The major exotherm at 280°C appears to be associated with the dissolution of coarse T_1 plates, accompanied by precipitation of Θ . This process continues until 312°C.

One concern in interpreting the DSC samples is that they were not quenched from the maximum DSC temperature instantaneously, as is usually done to capture high-temperature microstructures in Al alloys. The samples were cooled at a rate of about 140°C/min using the liquid nitrogen attachment to the DSC cell. This factor is probably not very significant at lower temperatures such as 212°C but may allow significant precipitation to occur during cooling of DSC samples from higher temperatures such as 312°C. The actual effect of the cooling rate from the DSC scans on the microstructure is not known at present and needs to be determined. An attempt was made to duplicate the DSC scan using a laboratory furnace, but we were not able to duplicate the 5°C/min heating rate of the DSC apparatus. It is also worth noting that cold-stage ion milling was used to remove surface oxide produced during electropolishing of some DSC samples. However, this process was discontinued because it was found to produce a noticeable change in the precipitate distribution. This change was significant and would definitely alter quantitative particle size data from this alloy. Hence, it was necessary to produce two sets of samples from the DSC cell in order to have sufficient material (about four slices) to obtain good TEM samples for all of the temperatures.

Summary

Quantitative precipitate size and volume fraction data were obtained for the matrix T_1 plates in RX818-T8 alloy after additional aging times of 1006 and 2518 hrs at 107°C (225°F), 135°C (275°F) and 163°C (325°F). The average size of the matrix T_1 plates increases above the -T8 material for all of the additional aging times and temperatures with the magnitude of the increase being proportional to the aging temperature. The average aspect ratio of the T_1 plates approaches 17:1 for all of the additional aging treatments. The maximum volume fraction of T_1 plates in this alloy is about 0.03 (3%) and this is reached after about 1006 hrs of aging at 163°C (325°F) and 2518 hrs of additional aging at 135°C (275°F). The maximum volume fraction of T_1 phase is only 0.02 after 2518 hrs of additional aging at 107°C (225°F) and a substantial amount of S' and some δ' phase also precipitate at this temperature. Initial results from TEM analysis of DSC samples indicate that the major endothermic peak in the DSC scan of the 2518 hrs sample at 107°C (225°F) involves dissolution and precipitation of T_1 phase while the exothermic peak involves precipitation of Θ and dissolution of coarse T_1 . More work is needed to determine the effect of cooling in the DSC cell on the microstructures of the DSC samples.

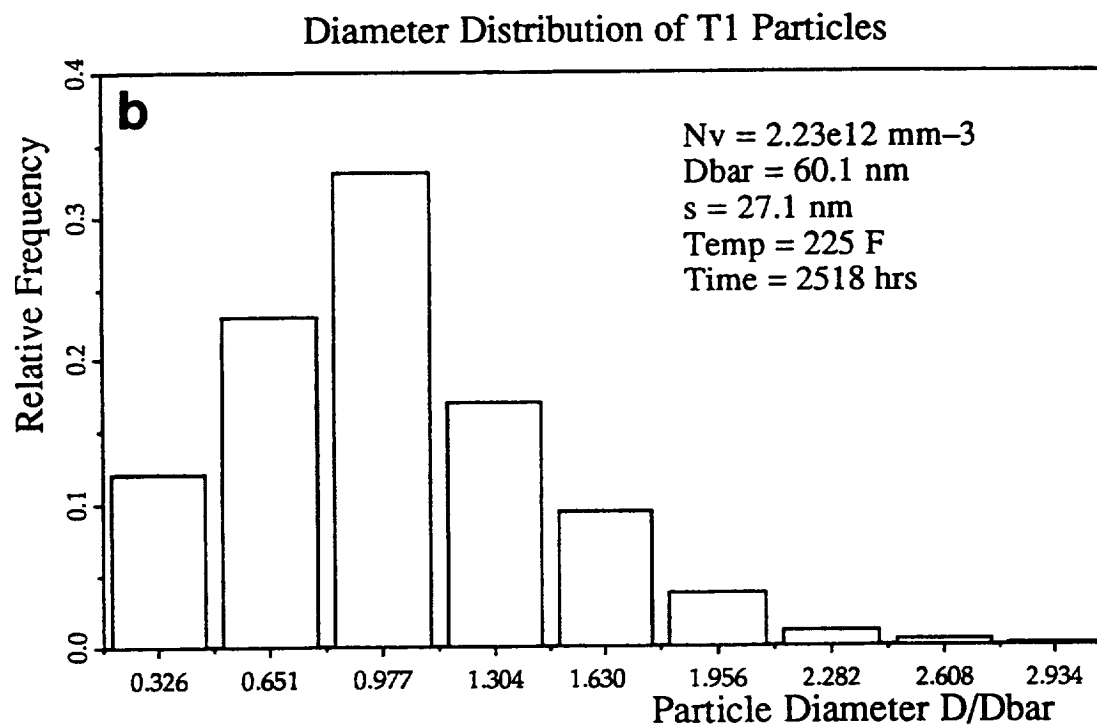
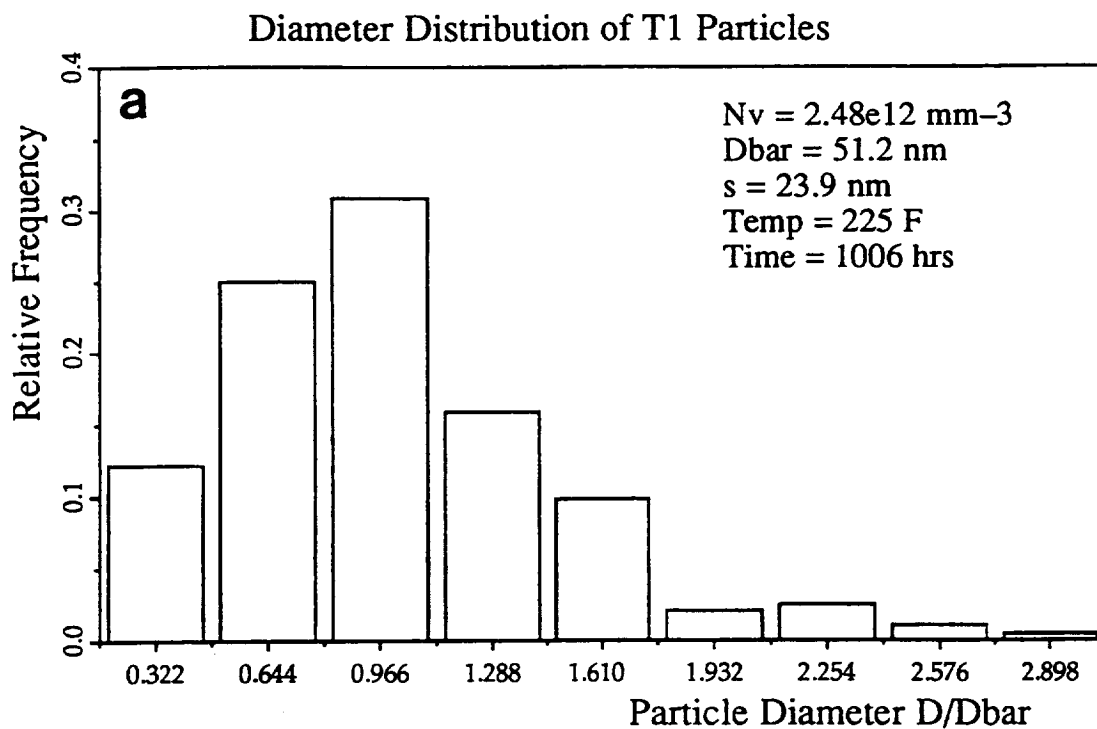


Figure 1. Diameter distributions of matrix T₁ plates in RX818 alloy aged for: (a) 1006 and (b) 2518 hrs at 107°C (225°F).

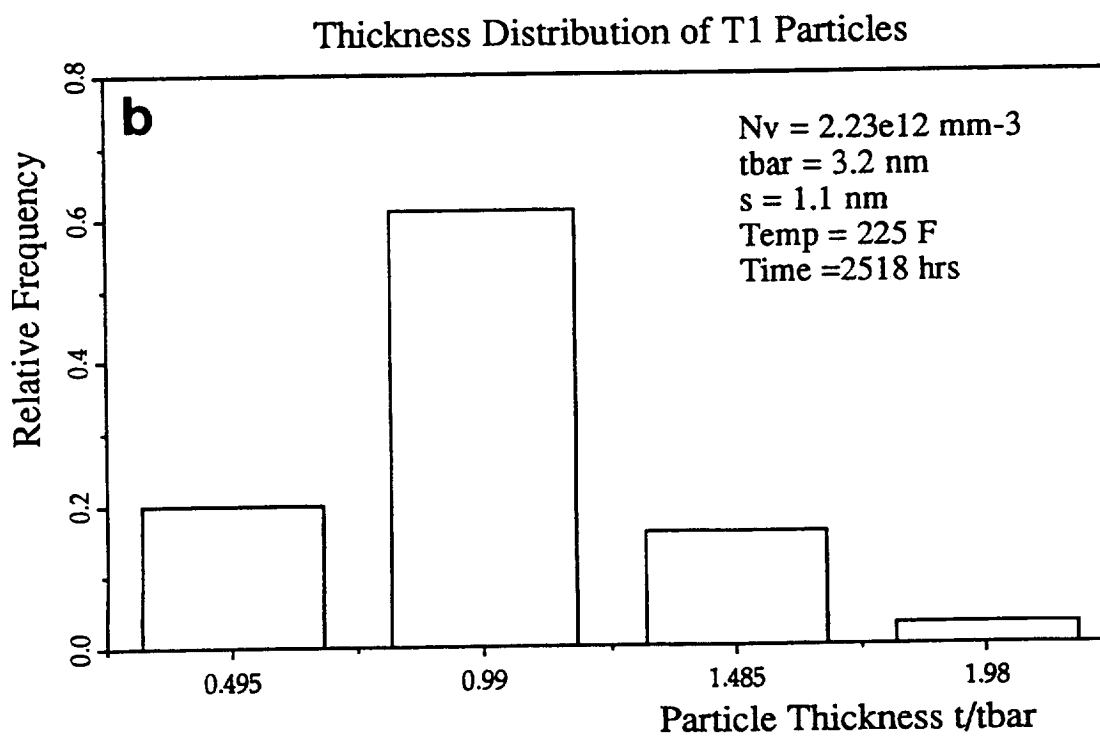
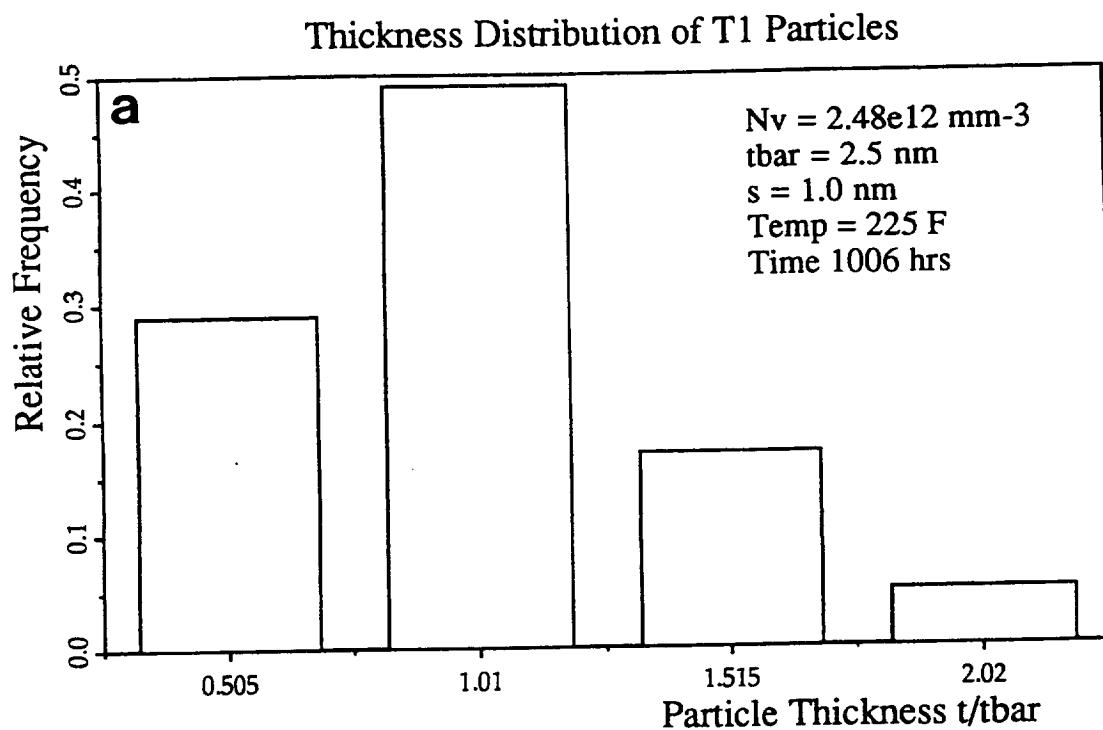


Figure 2. Thickness distributions of matrix T1 plates in RX818 alloy aged for: (a) 1006 and (b) 2518 hrs at 107°C (225°F).

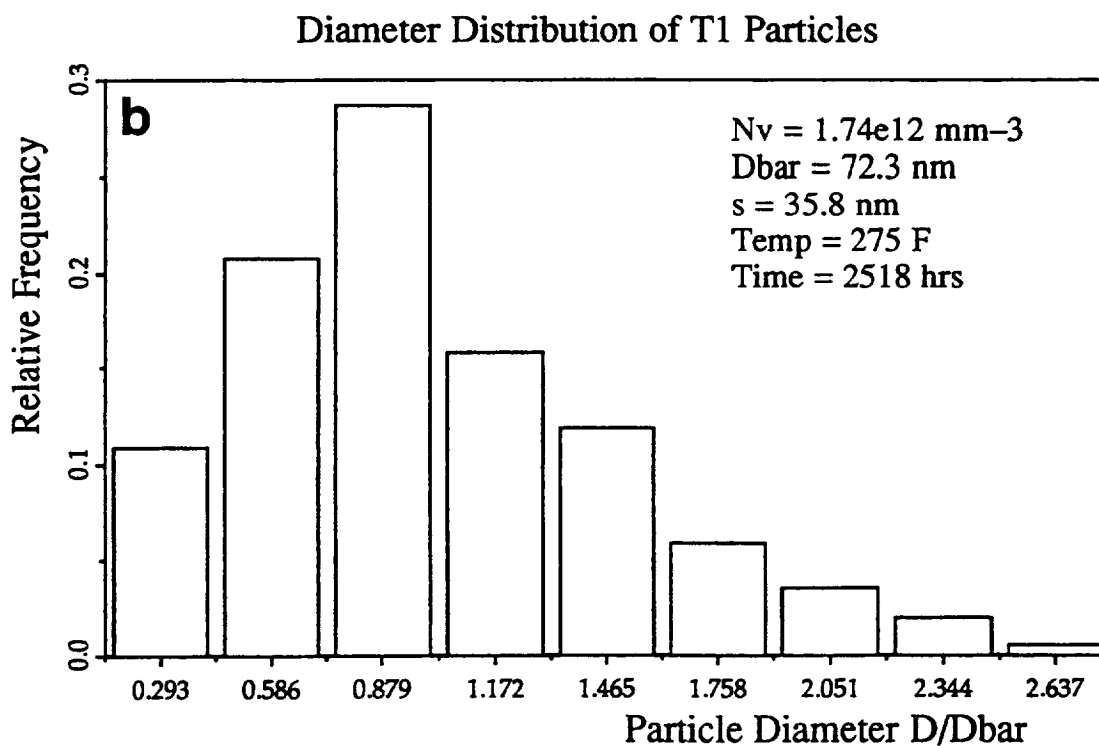
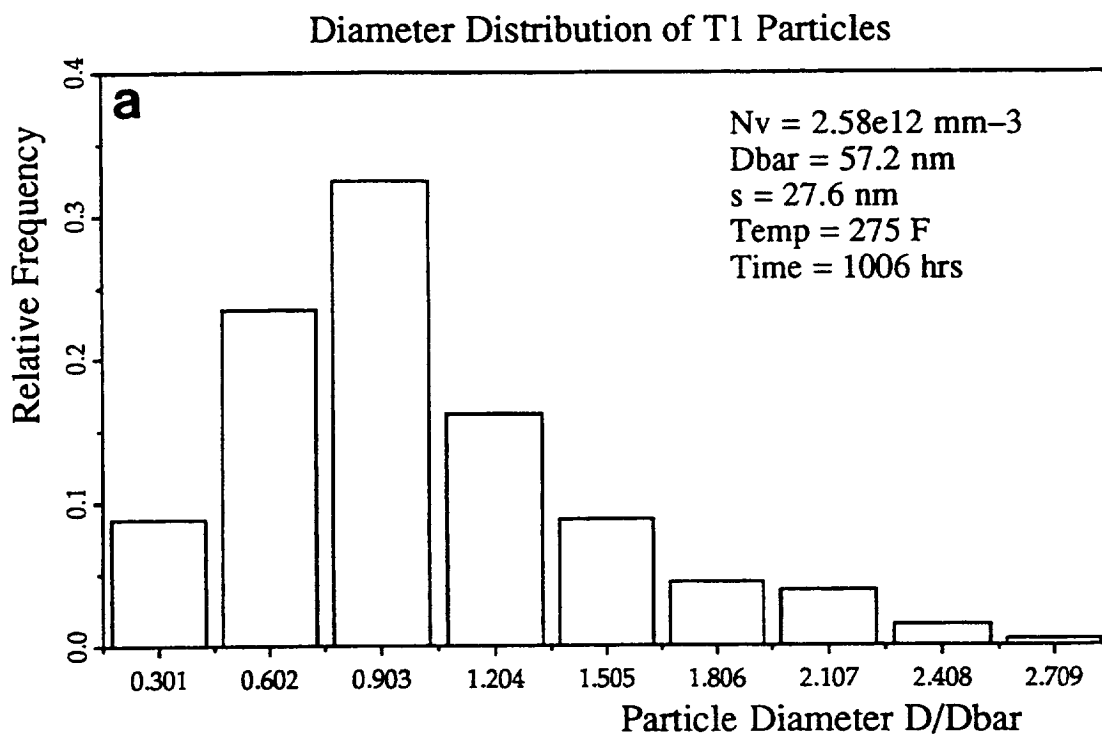


Figure 3. Diameter distributions of matrix T₁ plates in RX818 alloy aged for: (a) 1006 and (b) 2518 hrs at 135°C (275°F).

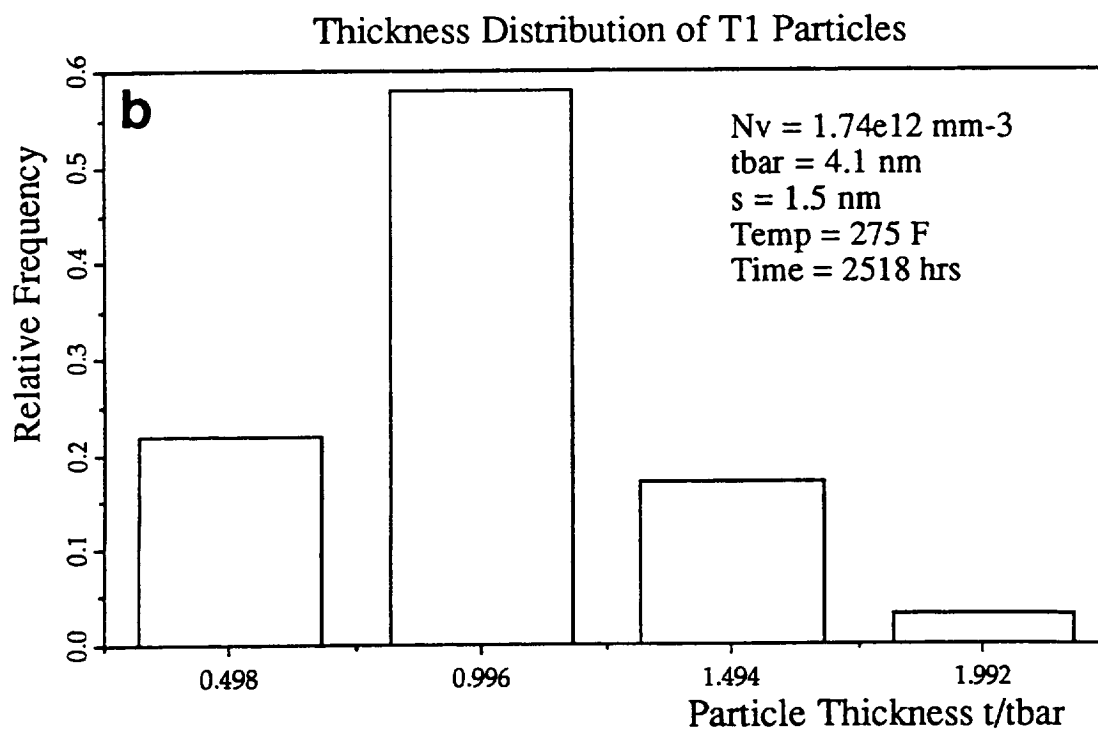
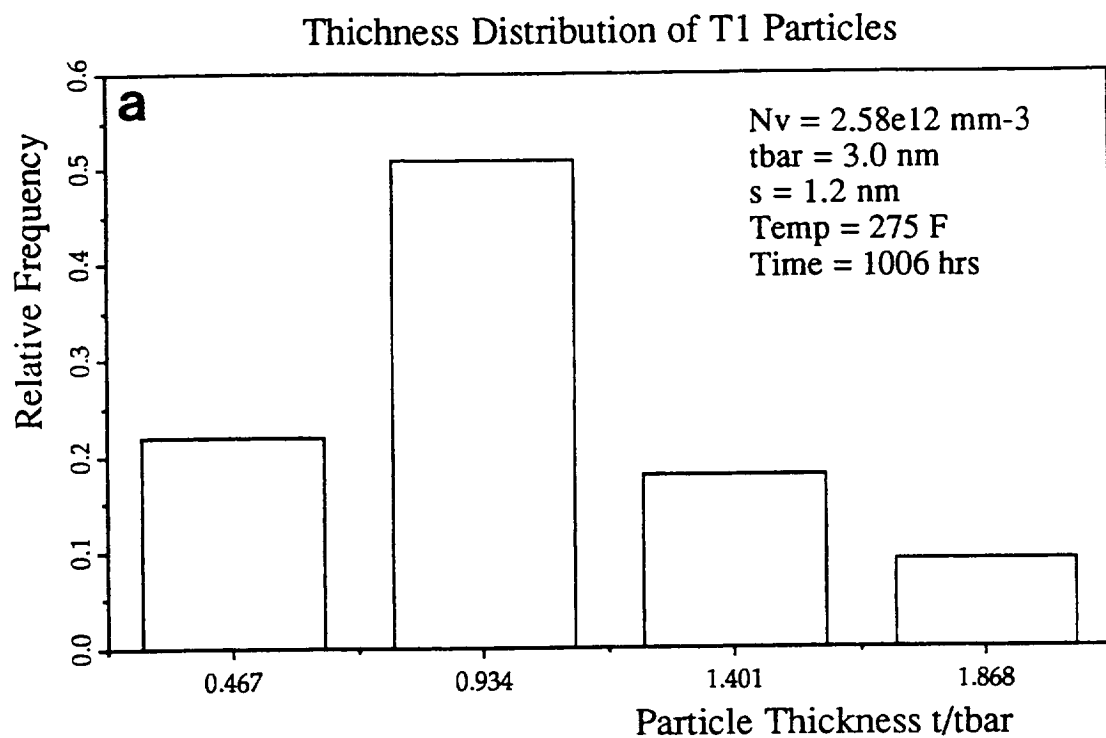


Figure 4. Thickness distributions of matrix T₁ plates in RX818 alloy aged for: (a) 1006 and (b) 2518 hrs at 135°C (275°F).

Figure 5. Coarsening behavior of matrix T₁ plates as a function of time and behavior.

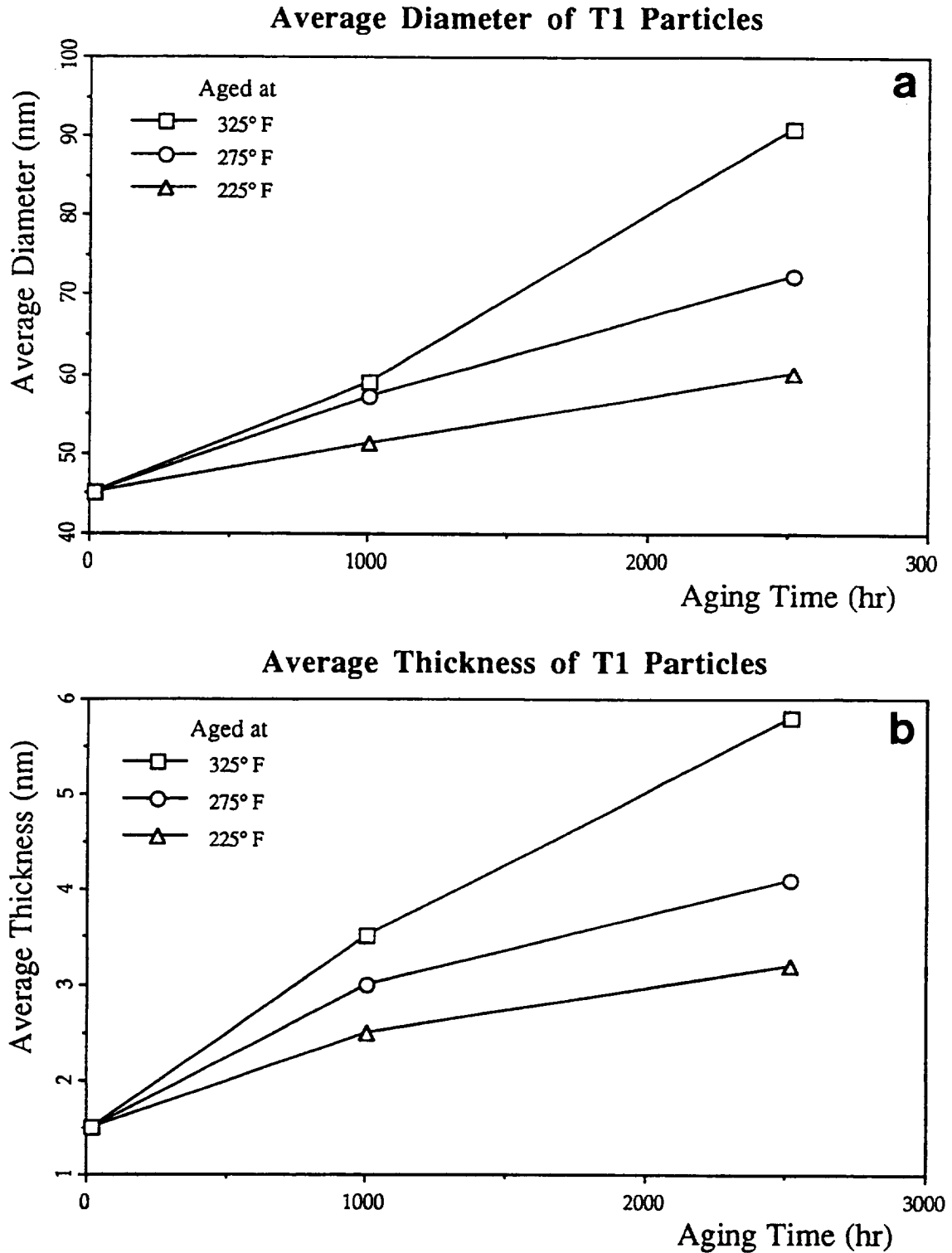


Figure 5. (a) Average diameter, (b) thickness, (c) number density, (d) volume fraction, and (e) aspect ratio of matrix T₁ plates as a function of aging time in RX818 alloy aged for 1006 and 2518 hrs at 107°C (225°F), 135°C (275°F) and 163°C (325°F) after initial -T8 aging treatment.

Figure 5. Continued.

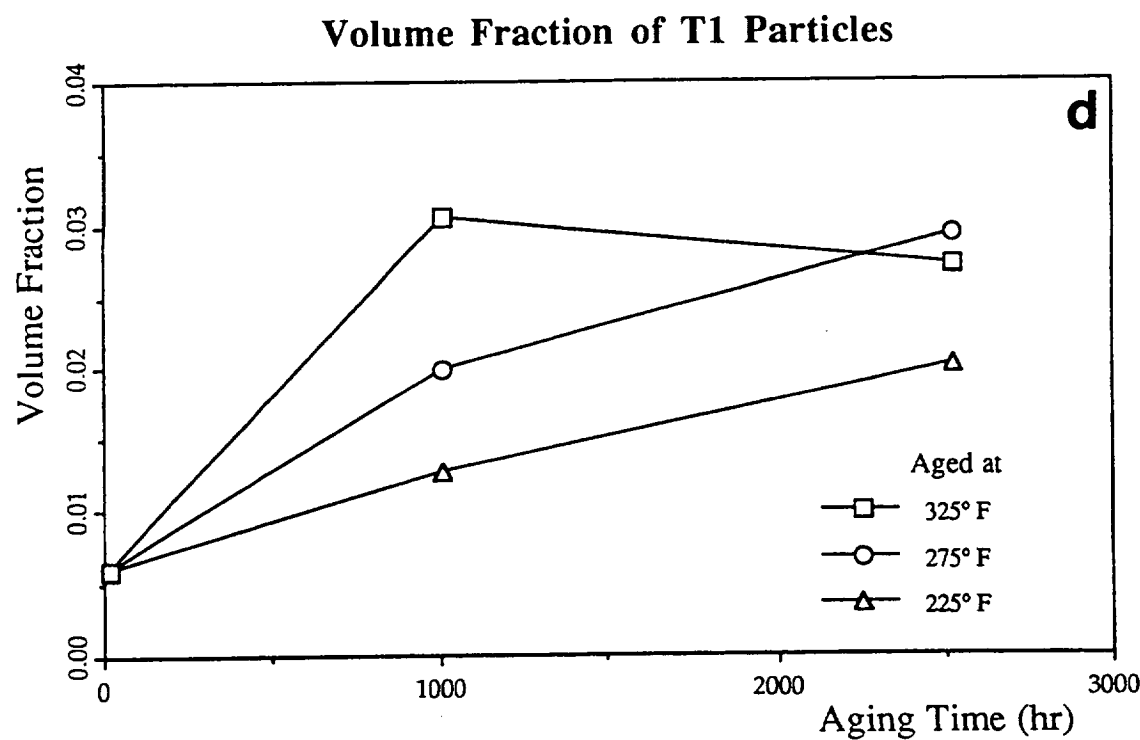
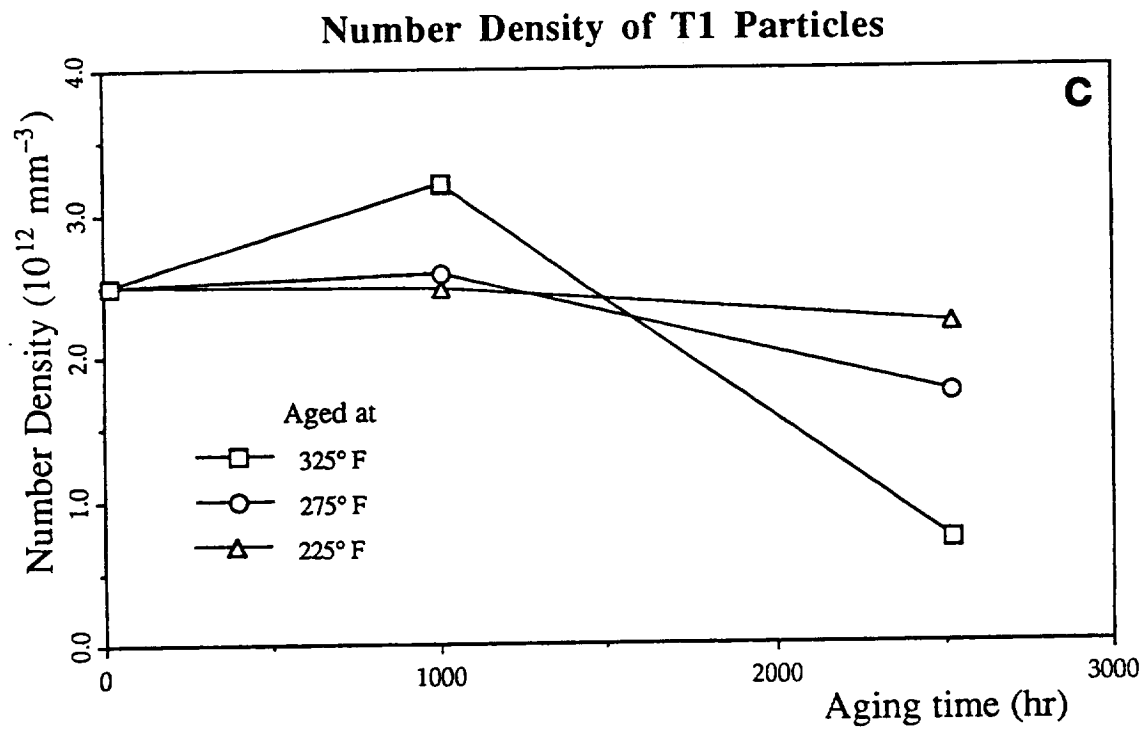


Figure 5. Concluded.

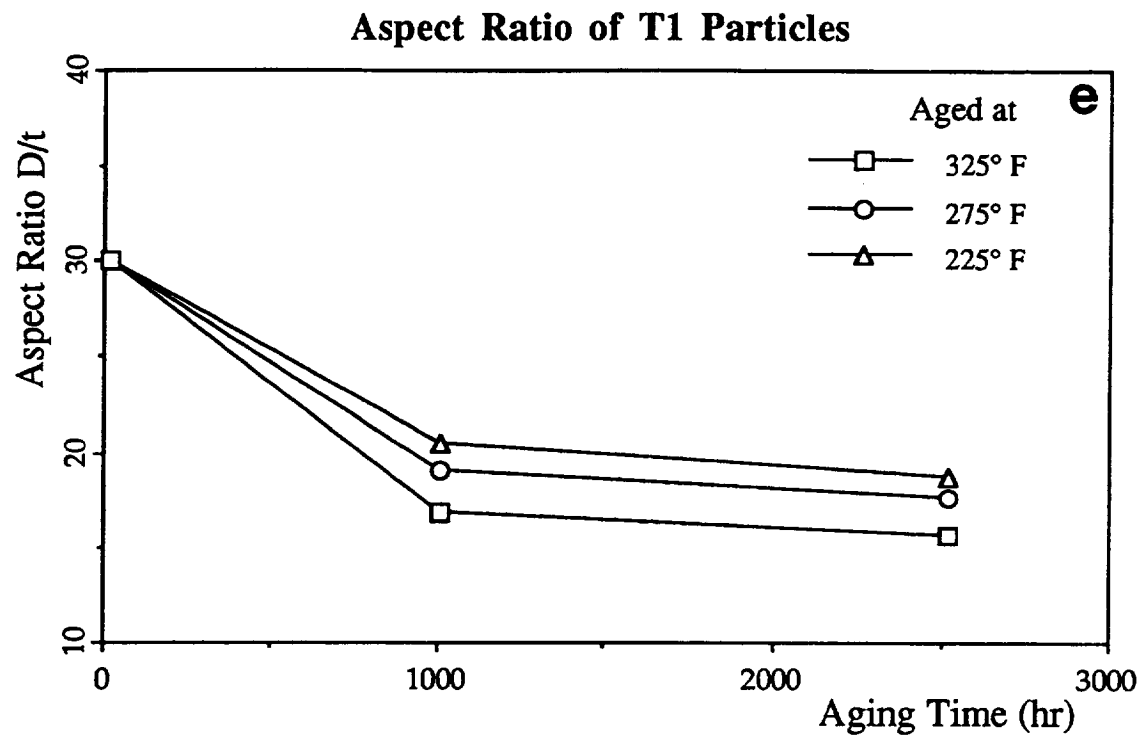




Figure 6. Dark-field TEM image showing S' laths (arrows) and δ' spheres in the sample aged for 2518 hrs at 107°C (225°F) after the initial -T8 treatment.

Sample: WELDALITE, T8, 225F, 2518HRS
 Size: 53.1100 mg
 Method: C: 3E15.01
 Comment: 5C/MT; 01/12/93; MS=53.11MG; MR=31.42MG+14.63=46.05 MG (AL)

DSC

File: 3E15.01
 Operator: SHENOY
 Run Date: 12-Jan-93 16: 19

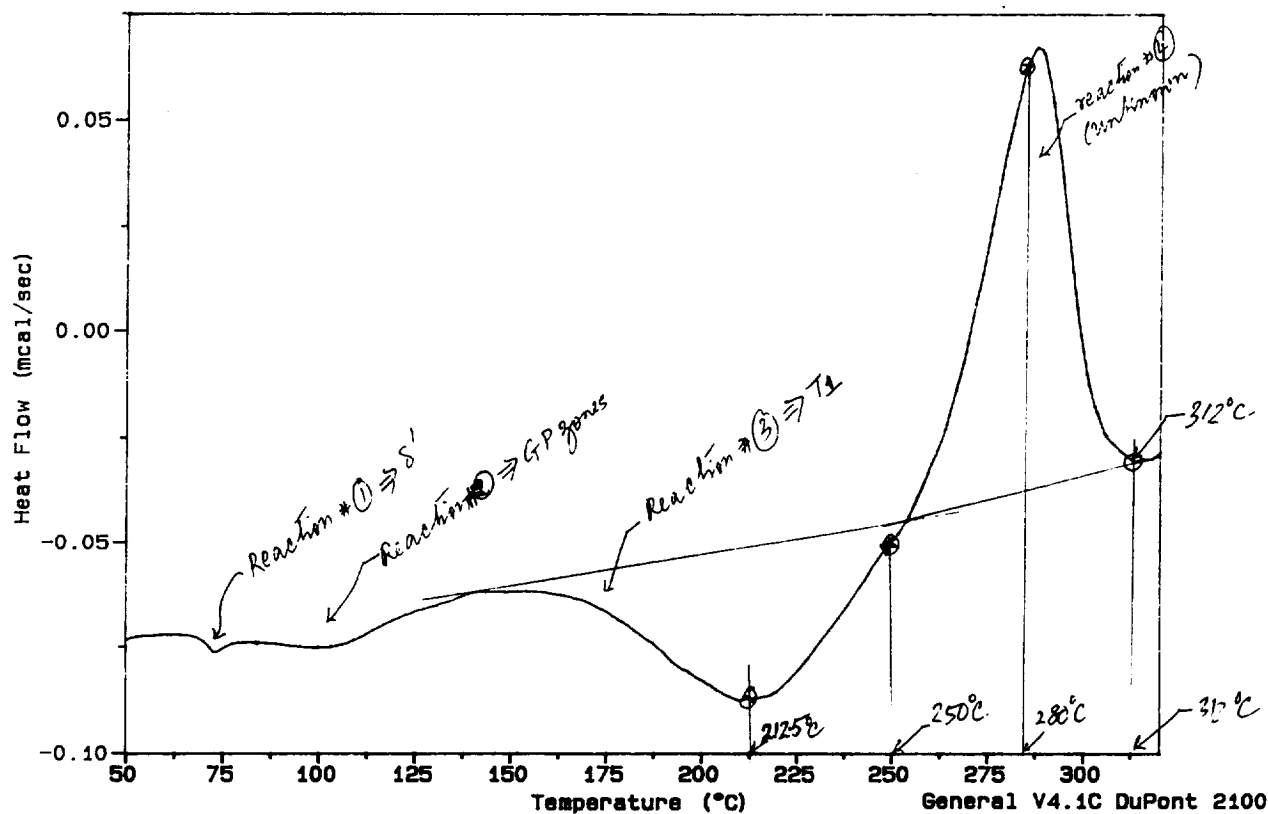


Figure 7. DSC scan (from Dr. R. Shenoy) from RX818 sample aged for 2518 hrs at 107°C (225°F) after the -T8 temper. The DSC scan rate was 5°C/min.



Figure 8. Bright-field TEM images of DSC samples at: (a) 212°C, (b) 280°C and (c) 312°C. The zone axis is near $\langle 110 \rangle$ in (a) and $\langle 112 \rangle$ in (b) and (c).

**SUBTASK 2C. Al-Cu-Li-Mg-Ag ALLOY DEVELOPMENT
(Boeing)**

Principal Investigator: Dr. W.E. Quist

See Subtask 1(i).

**SUBTASK 2D. Al-Cu-Li-Mg-Ag ALLOY DEVELOPMENT
(Douglas)**

Principal Investigator: Mr. R. Kahandal

See Subtask 1(ii).

TASK 3. CHARACTERIZATION OF ALLOY 1143 (Alcoa)

Principal Investigator: Dr. Lynne M. Angers

Objective

The objective of this task is to evaluate the Russian alloy 1143 as a damage tolerant aluminum based material for the lower wing and fuselage of a Mach 2.0 aircraft. The material must meet preliminary strength and toughness targets at room temperature and then several criteria associated with elevated temperature service (e.g., retention of room temperature properties after exposure, performance at the operating temperature and resistance to creep deformation).

Procedure

A purchase order requesting sheet and plate of 1143 to the Aviation Industry in Moscow was initiated. Ten pieces of alloy 1143 sheet (3 mm x 400 mm x 1300 mm) and two pieces of alloy 1143 plate (50 mm x 400 mm x 900 mm) were ordered. Five of the ten pieces of sheet and one of the two pieces of plate are to be provided in the T651 temper. The remaining material is to be provided in the F-temper.

Results and Discussion

Material has not yet arrived. No progress on this task.

TASK 4A. Al-Si-Ge-X ALLOY DEVELOPMENT (UVa)

Principal Investigator: Dr. E.A. Starke, Jr.
Graduate Student: Mr. Holger Koenigsmann

Task Objective

The objectives of this research are to determine the microstructural evolution and the concomitant property variations in a new class of experimental aluminum-based alloys that contain Si, Ge and Cu as the major alloying elements. The stability of the microstructures at moderate temperatures, and the critical dependence of hardness and strength on alloy composition and types of phases present are being investigated. This program uses theoretical concepts for selecting solute additions for an I/M age hardenable aluminum alloy that has the potential for high strength at moderate temperatures.

Introduction

We have recently developed an age-hardenable Al-Si-Ge alloy that utilizes a fine and uniform distribution of incoherent SiGe particles. These diamond cubic particles have a very small critical size for the transition from shearing to looping by dislocations at the yield stress. These features result in a high degree of hardening for a small volume fraction of particles [1,2].

As compared to precipitates in other age-hardenable aluminum alloys, the SiGe particles should be more thermally stable because of the low solubility of Si and Ge in Al and the incoherent precipitate interface. However, the Al-Si-Ge alloys are not strength competitive. The addition of Cu has the effect of increasing the number of precursory clusters during quenching which act as nucleation centers for the diamond SiGe precipitates during aging, thus increasing the hardness level [3,4].

Summary of Previous Results

Diamond structure SiGe particles in ternary Al-Si-Ge alloys are found to nucleate at a much finer scale and with a lower tendency to overage than binary Al-Si or Al-Ge alloys. The precipitate density in the ternary alloys is an order of magnitude higher than in the binary alloys. The aging characteristics of the ternary alloy are not affected by prior low temperature aging or preaging cold work [3,4].

Sn, In and Mn strongly interact with vacancies leading to slower precipitate nuclei formation and coarsening of the precipitates than observed for the ternary alloys. Mg additions to the ternary alloys lead to the formation of fine Mg_2Si precipitates and coarse SiGe precipitates. Zr additions to the ternary alloys lead to the formation of coarse $(AlSi)_3Zr$ precipitates and reduce the driving force for the nucleation of SiGe precipitates. Zn and Ag have a negligible affinity to bind with vacancies and their addition does not affect the nucleation of SiGe precipitates [3].

The addition of less than 2.5 wt.% Cu also does not affect the distribution of the SiGe particles but does increase the hardness level by about 60%. However, Cu contents of more than about 2.5 wt.% result in the nucleation of Θ' (Al_2Cu) precipitates in addition to the diamond SiGe precipitates; the rapid coarsening of the Θ' precipitates leads to a rapid overaging of the quaternary alloy [3].

Experimental Procedure

The chemical compositions of the alloys studied during this report period are given in Table 1. Alloys 3 and 4 differ from alloys 1 and 2 by a reduction of the Ge content in order to reduce the cost of the alloy without significantly affecting the properties. Furthermore, alloys 3 and 4 have nearly identical compositions except for Cu so that the influence of Cu independent

of other factors can be investigated. The alloys were homogenized at 500°C (without Cu), 490°C (with Cu), or 480°C (with Cu, Mg, and Ag) for 30 hrs. The grain size was determined according to Underwood [5] and the values are given in Table 2. The homogenized alloys were hot rolled and solution heat treated at 490°C (without Cu), 480°C (with Cu), or 470°C (with Cu, Mg, and Ag) for 1 hr. Alloys 1 and 2 were then aged at 160°C for up to 16 days. An additional set was aged at 120°C for up to 32 days. Alloys 3 and 4 were aged at 160°C for up to 16 days and alloy 5 was aged at 160°C for 36 hours. Microhardness values were taken at room temperature. Samples for TEM were prepared using standard techniques and examined in a Philips EM 400T. The average radii of the diamond precipitates were determined by quantitative stereological methods [6] and corrected for truncation and overlap [7]. Foil thicknesses were determined under two-beam conditions from the oscillations in intensity of convergent beam diffraction patterns [8].

Samples of all alloys were peak-aged at 160°C. Tensile tests were performed with peak-aged alloys 3 through 5 in the longitudinal direction [9], and Kahn tear tests were performed with peak-aged alloys 3 and 4 in both longitudinal and transverse directions [10]. In addition, tensile and Kahn tear tests were performed on alloy 2014-T4 for comparison. The fracture surfaces were investigated using a SEM JSM-35. Other peak-aged samples of alloys 1, 2, and 4 were kept in oil baths at 200°F (93°C), 250°F (121°C) and 300°F (149°C), and the microhardness values determined over a period of 10 days at the temperature of the corresponding oil bath using a Nikon High-Temperature Microhardness Tester QM.

Results and Discussion

The hardness curves for alloys 1 and 2 aged at 160°C and at 120°C are shown in Figs. 1 and 3, respectively, and the relationship between the cube of the average radii of the diamond precipitates and the aging time at 160°C and 120°C is shown in

Figs. 2 and 4, respectively (the full time scale is 400 hrs for 160°C, but 800 hrs for 120°C). Note that the smaller radii shown in the previous report are due to an error in the overlap correction. Figure 5 shows the hardness curves for alloys 3 and 4 aged at 160°C, and Figure 6 shows the relationship between the cube of the average radii of the diamond precipitates and the aging time. Figure 7 compares the microstructure of alloys 1 (Figs. 7a and 7b) and 2 (Figs. 7c and 7d) after aging at 160°C for 24 hours (Figs. 7a and 7c) and 384 hours (Figs. 7b and 7d) at a magnification of 400,000X (<011> beam direction).

The relationship between the cube of the average radii and the aging time is in all cases linear within the errors of measurement. This is consistent with the coarsening theory prediction of Lifshitz [11] and Wagner [12]. The coarsening rate for alloys 1 and 2 is significantly higher at 160°C than at 120°C as can be expected from the exponential temperature dependence of the diffusion coefficient. The average radii of the diamond precipitates are higher for alloy 2 than for alloy 1. This can be explained by the fact that the composition of alloy 2, when considering the size difference between Si and Ge, results in a higher strain energy compared to alloy 1. This, in turn, results in a higher critical energy for the formation of stable nuclei and, therefore, in a larger critical size of the nuclei.

The coarsening theory by Lifshitz and Wagner predicts that the variation of the mean radius, r , with time, t , is given by [13]:

$$r^3 - r_o^3 = 8\gamma D C_o V_m^2 (t - t_o) / 9RT \quad (1),$$

where r_o is the mean particle radius when coarsening commences at the time t_o , γ is the specific precipitate-matrix interfacial free energy, D and C_o are the diffusivity and the equilibrium molar

concentration at the given temperature, T , respectively, V_m is the molar volume of the precipitate, and R has its usual meaning. The interfacial energy was estimated from the slope of the graphs in Figs. 2, 4, and 6 using equation (1). Diffusivity data of Si in Al and Ge in Al were taken from the literature [14]. The ratio between Si and Ge was taken into account for each alloy, but the influence of Cu was neglected. The equilibrium concentration was roughly estimated [15] as 0.2 wt.% and the molar volume was calculated based on the values given in the literature [2] for the diamond cubic structures of Si and Ge. The values for the interfacial energy shown in Figs. 2, 4, and 6 should be considered as first approximations.

Table 3 shows the results of the tensile tests performed with peak-aged alloys 3 through 5 in the longitudinal direction and compares them with alloy 2014-T4. The magnitude of the results for alloys 3 and 4 is in accordance with earlier results from alloys of similar composition. The yield strength is in good agreement with the theoretical upper limit (also shown in Table 3) described by the modified Orowan equation [1]:

$$\Delta\sigma_p \approx Gb\sqrt{f}/d \quad (2),$$

where $\Delta\sigma_p$ is the contribution of the SiGe particles to the yield strength, G is the shear modulus of the matrix (26 GPa), b is the Burgers vector (0.284 nm), f is the volume fraction, and d is the diameter of the particles (both determined by TEM). Note that this calculation does not consider the contribution of Θ' . The tensile properties for alloy 5 are significantly higher than those for alloy 4 although the peak-hardness values differ only slightly. TEM analysis of peak-aged alloy 5 revealed the presence of diamond SiGe precipitates, Θ' , Θ'' , and some S' . The tensile properties of alloys 3 through 5 are significantly lower than those of alloy

2014-T4. The fracture surfaces of alloys 3 through 5 indicated dimpled rupture in a transgranular mode. The fracture surfaces of alloys 3 through 5 show in Figure 8 (at a magnification of 500X) which shows that all fracture was by transgranular dimple rupture.

Table 4 shows the results of the Kahn tear tests performed with peak-aged alloys 3 and 4 in both longitudinal and transverse directions. The unit propagation energy which can be used as a relative index of fracture toughness is significantly higher for alloys 3 and 4 than for alloy 2014-T4. Furthermore, this value is higher for alloy 4 than for alloy 3 if samples tested either in the longitudinal or in the transverse direction are compared, although the tensile tests revealed a larger strain after fracture for alloy 3.

Figure 9 shows the results of the microhardness measurements for alloys 1 and 2 carried out at the temperature of the corresponding oil bath. The slopes of the curves for the quaternary alloys are significantly higher than those for the ternary alloys at the same temperature. In all cases, the slopes decrease with increasing time. These results correspond qualitatively to the coarsening behavior of the strengthening precipitates investigated by TEM. The results of similar measurements carried out for alloy 4 are shown in Fig. 10. The slopes of the curves are significantly lower than those for alloy 2 possibly due to the lower Cu content which might result in a lower coarsening rate of Θ' .

Conclusions

Although the Al-Si-Ge-X alloys are considerably better than the Al-Si and Al-Ge binary alloys and show better strength/conductive relationship than any aluminum conductor wire, they do not (at least at this time) possess better structural properties than the less expensive 2014. Consequently, they do not appear to be attractive candidate alloys for the high speed

research program in the time frame required. This program will be moved to the NASA LA²ST basic research program.

References

1. E. Hornbogen and E.A. Starke, Jr., "Theory Assisted Design of High Strength Low Alloy Aluminum", Acta Met. 41, 1993, pp. 1-16.
2. E. Hornbogen, A.K. Mukhopadhyay, and E.A. Starke, Jr., "Nucleation of the Diamond Phase in Aluminium-Solid Solutions", Z. Metallkde 83, 1992, pp. 577-584.
3. E. Hornbogen, A.K. Mukhopadhyay, and E.A. Starke, Jr., "Precipitation Hardening and Microstructural Stability in Al-Si-Ge-Cu Alloys", Proc. 3rd Int. Conf. "Aluminum Alloys - Their Physical and Mechanical Properties," Trondheim, Norway, June 22-26, 1992, pp. 199-207.
4. E. Hornbogen, A.K. Mukhopadhyay, and E.A. Starke, Jr., "Precipitation Hardening of Al-(Si,Ge) Alloys", Scripta Met. 27, 1992, pp. 733-738.
5. E.E. Underwood, Metals Handbook, Vol. 8, ASM, 1973, pp. 42-43.
6. E.E. Underwood and E.A. Starke, Jr., Quantitative Stereological Methods for Analyzing Important Microstructural Features in Fatigue of Metals and Alloys", Proc. ASTM-NBS-NSF Symp. "Fatigue Mechanisms," Kansas City, Mo., May 1978, ASM, 1979, pp. 633-682.
7. E.E. Underwood, Quantitative Stereology, Addison-Wesley, 1970, pp. 187-188.
8. W.A. Cassada, III, "The Effect of Germanium on the Precipitation Behavior and Mechanical Properties of an Al-2Li Alloy," M.S. Thesis, UVA, 1985, pp. 72-75.
9. Standard E8-91, Standard Test Methods of Tension Testing of Metallic Materials, ASTM, 1991.
10. J.G. Kaufman and M. Holt, Fracture Characteristics of Aluminum Alloys, Alcoa Research Laboratories Technical Paper No. 18, 1965.
11. I.M. Lifshitz and V.V. Slyozov, "The Kinetics of Precipitation from Supersaturated Solid Solutions," J. Phys. Chem. Solids 19, 1961, pp. 35-80.

12. C. Wagner, "Theorie der Alterung von Niederschlaegen durch Umloesen (Ostwald-Reifung)," Z. Elektrochemie 65, 1961, pp. 581-591.
13. J.D. Boyd and R.B. Nicholson, "The Coarsening Behavior of Theta" an Theta' Precipitates in Two Al-Cu Alloys," Acta Met. 19, 1971, pp. 1379-1391.
14. M. Bishop and K.E. Fletcher, "Diffusion in Aluminum," Int. Met. Rev. 17, 1972, pp. 203-225.
15. I.J. Polmear, Light Alloys, Hodder & Stoughton, 1989, p. 18.
16. S.H. Goods and L.M. Brown, "Overview: The Nucleation of Cavities by Plastic Deformation," Acta Met. 27, 1979, pp. 1-15.

Table 1. Chemical Composition of Alloys.

Composition						
No.	Alloy (wt.%)	At.%				
		Si	Ge	Cu	Mg	Ag
1	Al-0.71Si-2.60Ge	0.69	0.98	--	--	--
2	Al-1.10Si-1.55Ge- 2.70Cu	1.08	0.59	1.18	--	--
3	Al-1.02Si-0.95Ge	0.99	0.36	--	--	--
4	Al-1.00Si-0.99Ge- 2.57Cu	0.98	0.38	1.12	--	--
5	Al-1.00Si-0.97Ge- 4.47Cu-0.35Mg-0.50Ag	1.00	0.37	1.97	0.40	0.13

Table 2. Comparison of Grain Size.

Grain Size Determination		
Material	Mean Intercept Length (μm)	Equivalent Grain Size Number
Al-1.02Si-0.95Ge	208 \pm 21	1.2 \pm 0.3
Al-1.00Si-0.99Ge- 2.57Cu	244 \pm 25	0.7 \pm 0.3
Al-1.0Si-0.97Ge- 4.47Cu-0.35Mg-0.5Ag	161 \pm 17	1.9 \pm 0.3

Table 3. Comparison of Tensile Properties.

Tensile Tests				
Material	$\Delta\sigma_p$ (MPa)	σ_{YS} (MPa)	σ_{TS} (MPa)	ϵ_f (%)
Al-1.02Si-0.95Ge	77	73	137	24
Al-1.00Si-0.99Ge-2.57Cu	76	168	280	10
Al-1.0Si-0.97Ge-4.47Cu-0.35Mg-0.5Ag	--	281	410	3
2014-T4	--	344	486	21

$\Delta\sigma_p$: Theoretical contribution of SiGe particles to the yield strength

σ_{YS} : Yield strength

σ_{TS} : Tensile strength

ϵ_f : Strain after fracture

Strain rate: 10^{-3} s^{-1}

Orientation of first three alloys: 0° to rolling direction

The first three alloys were peak-aged at 160°C .

Table 4. Comparison of Fracture Properties.

Kahn Tear Tests			
Material	Tear Strength (MPa)	TYR	Unit Propagation Energy (J/mm ²)
Al-1.02Si-0.95Ge (L)	179	2.45	0.248
Al-1.02Si-0.95Ge (T)	170	--	0.190
Al-1.00Si-0.99Ge-2.57Cu (L)	299	1.78	0.304
Al-1.00Si-0.99Ge-2.57Cu (T)	274	--	0.216
2014-T4	545	1.58	0.113

TYR: Tear strength to tensile yield strength ratio

Orientation: L - longitudinal

T - transverse

The first four alloys were peak-aged at 160°C.

Al-0.71w/oSi-2.60w/oGe
Al-1.10w/oSi-1.55w/oGe-2.70w/oCu

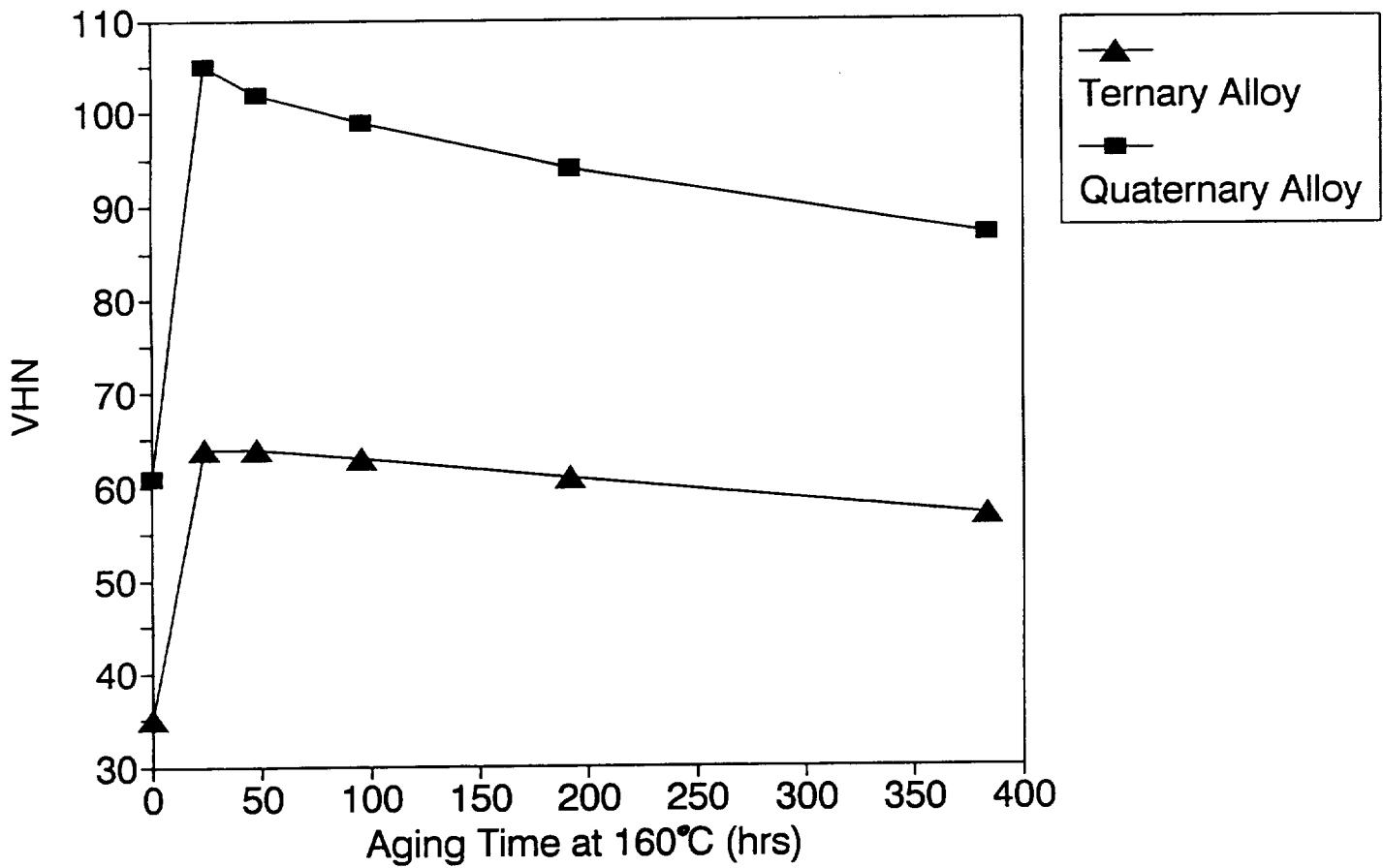


Figure 1. Hardness curves for alloys 1 and 2 aged at 160°C.

Coarsening of Diamond Precipitates in Al-Si-Ge/Al-Si-Ge-Cu at 160°C

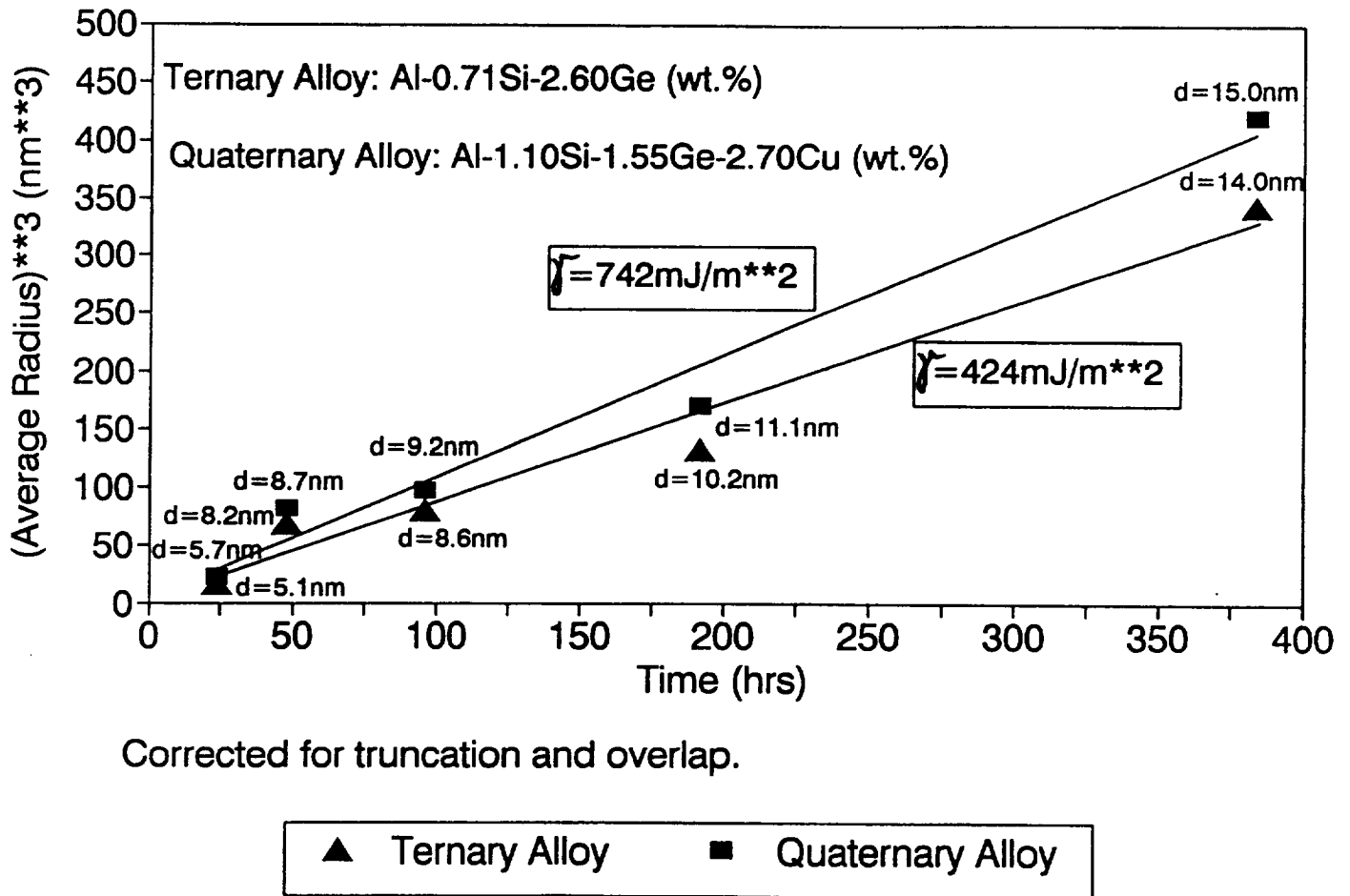


Figure 2. Coarsening behavior of diamond precipitates in alloys 1 and 2 at 160°C.

Al-0.71w/oSi-2.60w/oGe
Al-1.10w/oSi-1.55w/oGe-2.70w/oCu

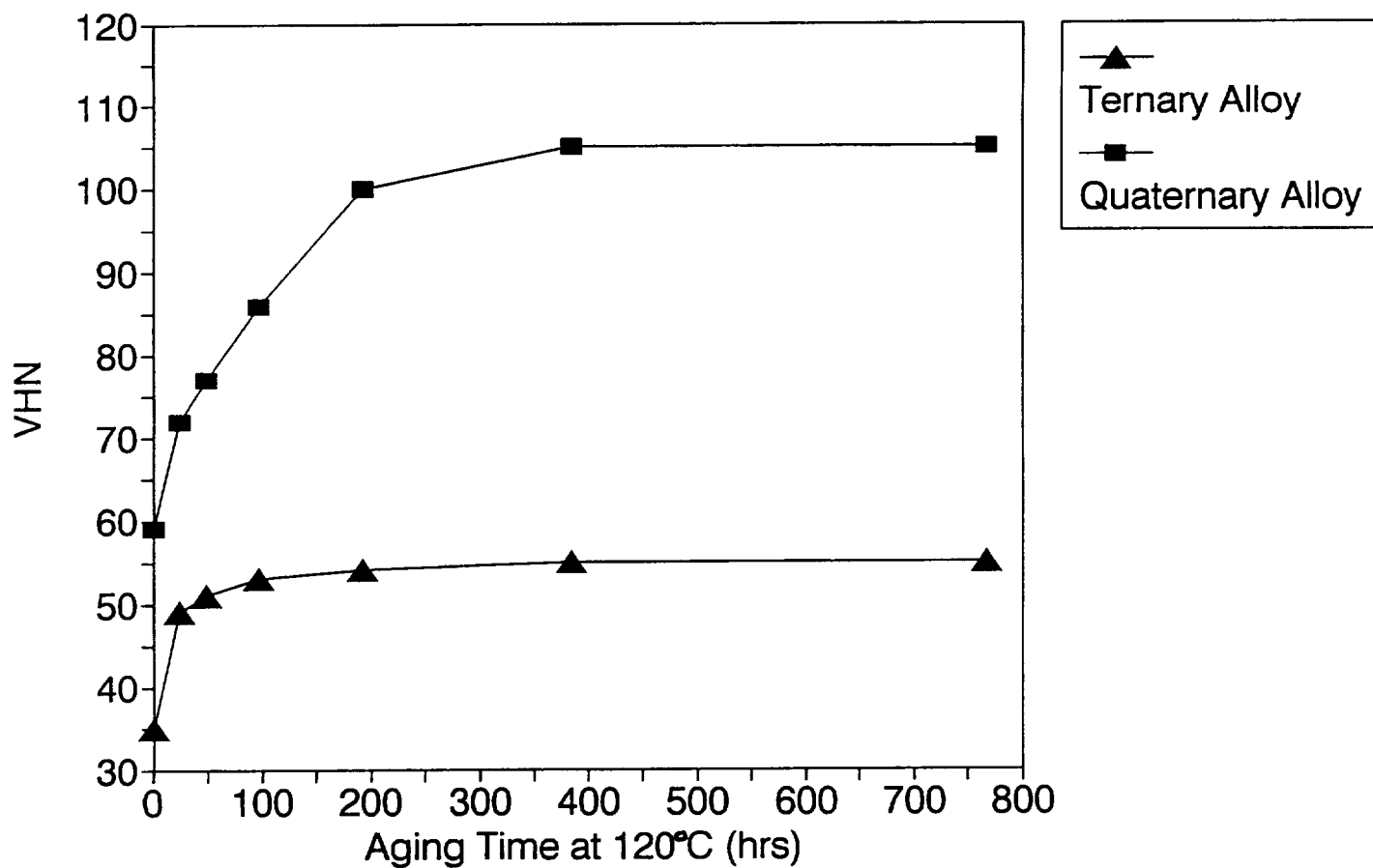


Figure 3. Hardness curves for alloys 1 and 2 aged at 120°C.

Coarsening of Diamond Precipitates in Al-Si-Ge/Al-Si-Ge-Cu at 120°C

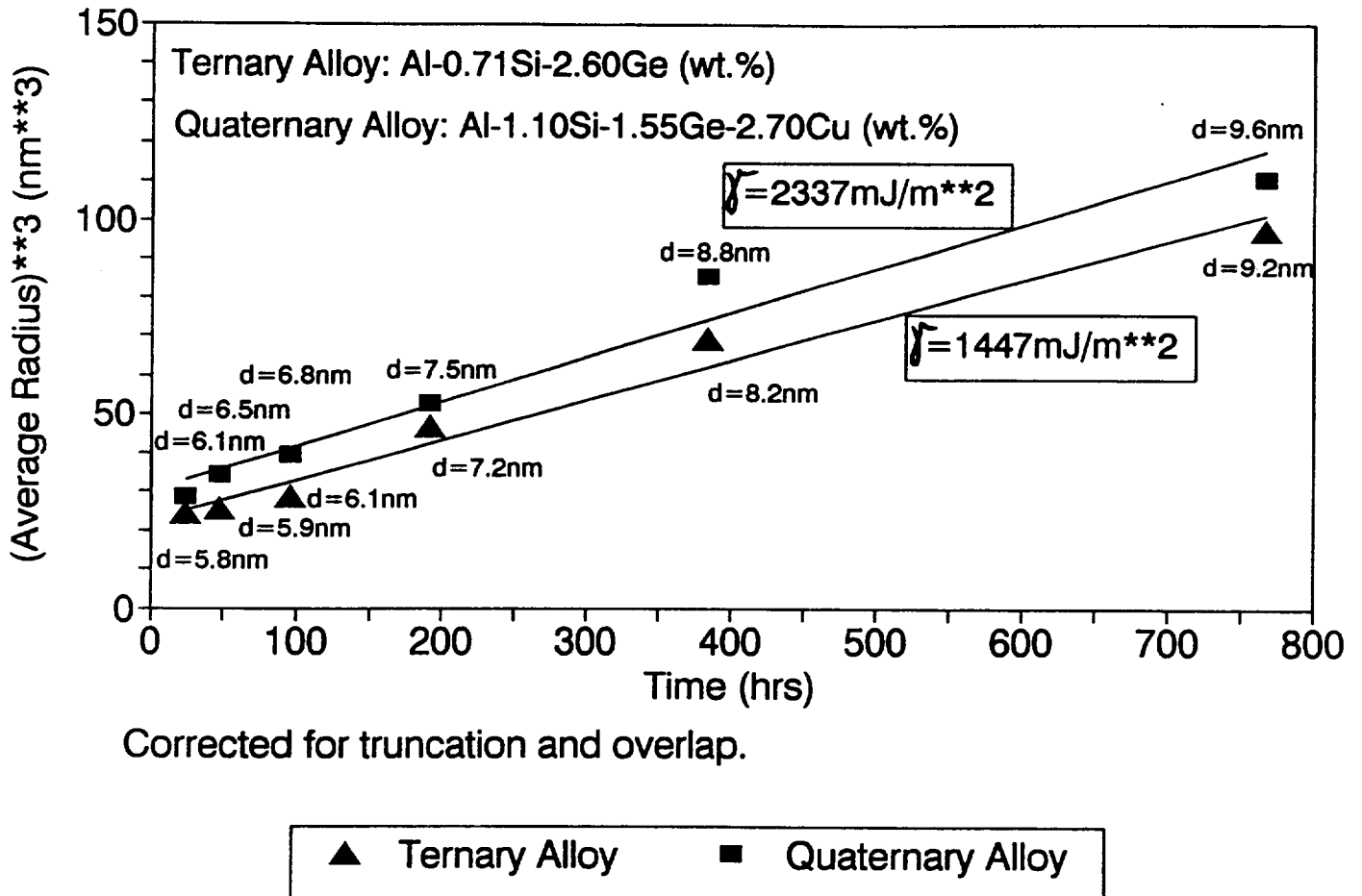


Figure 4. Coarsening behavior of diamond precipitates in alloys 1 and 2 at 120°C.

Al-1.02Si-0.95Ge (wt.%)
Al-1.00Si-0.99Ge-2.57Cu (wt.%)

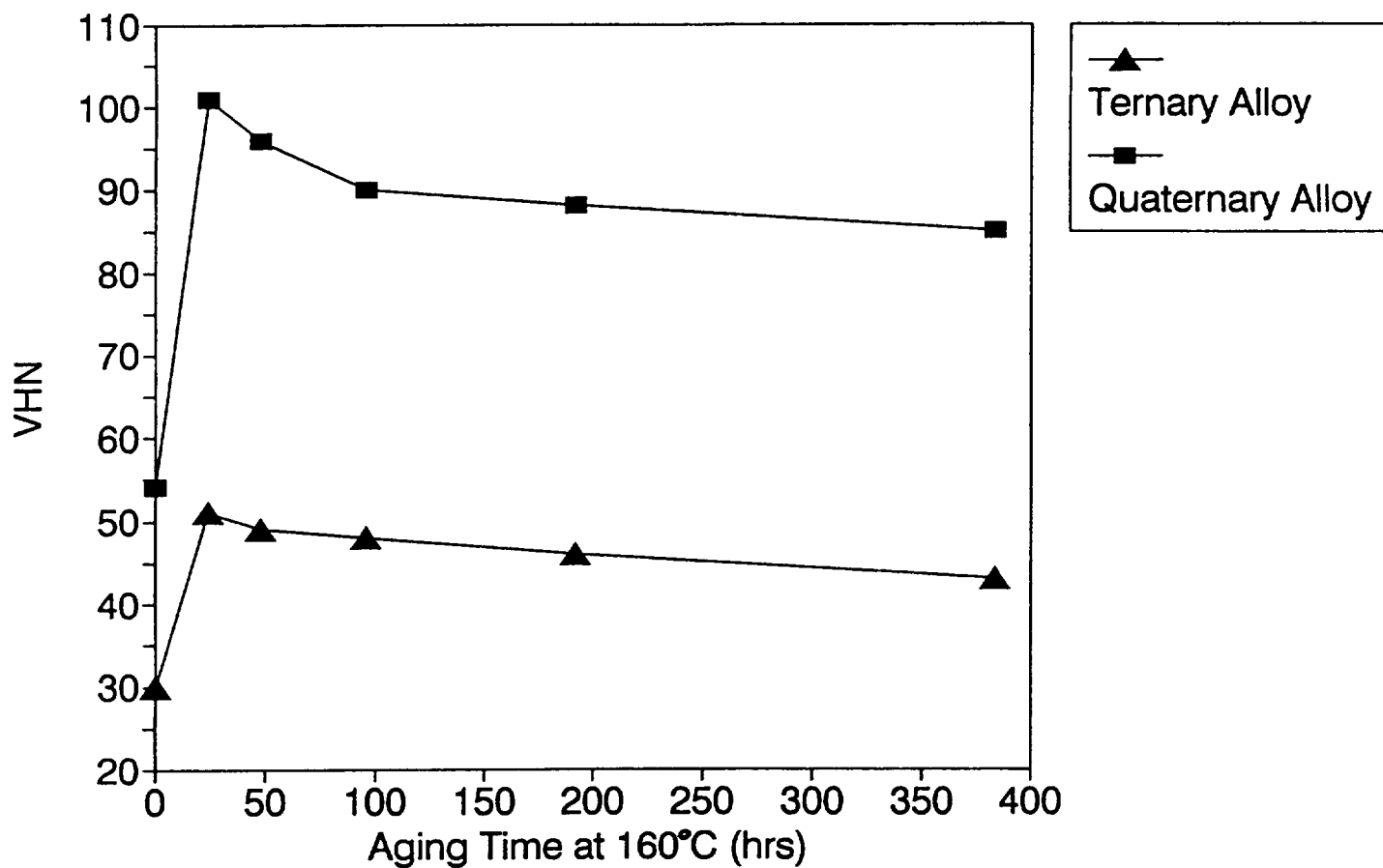
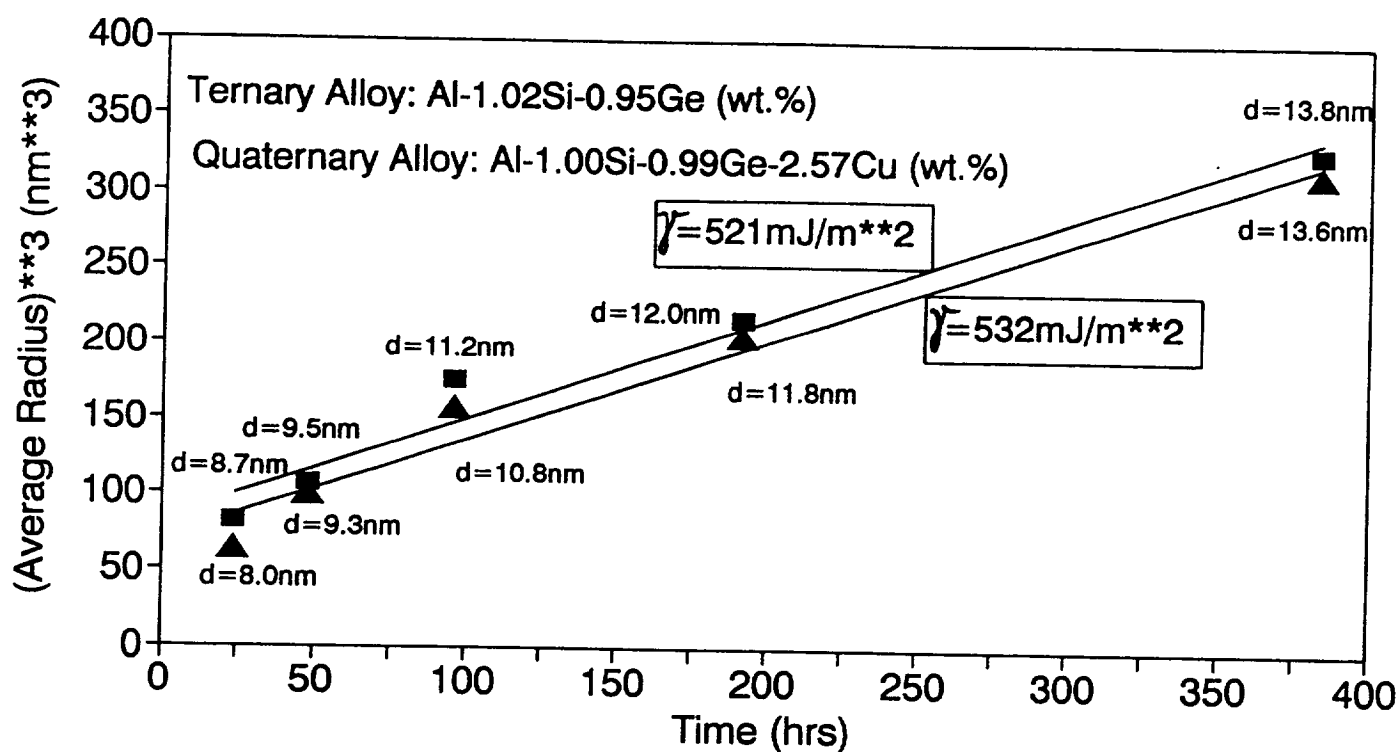


Figure 5. Hardness curves for alloys 3 and 4 aged at 160°C.

Coarsening of Diamond Precipitates in Al-Si-Ge/Al-Si-Ge-Cu at 160°C



Corrected for truncation and overlap.



Figure 6. Coarsening behavior of diamond precipitates in alloys 3 and 4 at 160°C.

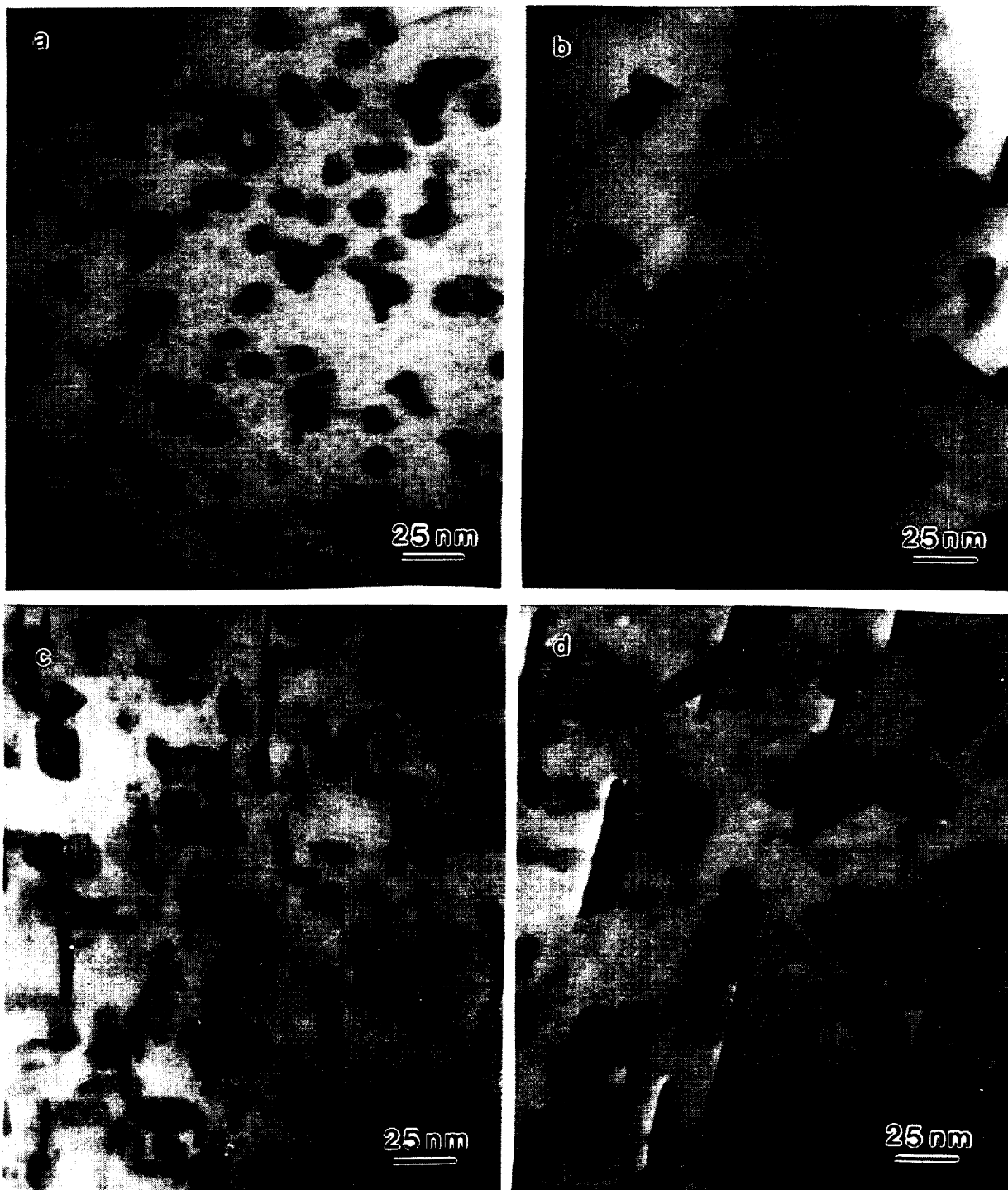


Figure 7. Microstructure of alloys 1 (a, b) and 2 (c, d) at a magnification of 400,000 times after aging for 24 hrs (a, c) and 384 hrs (b, d). $\langle 011 \rangle$ Al orientation.

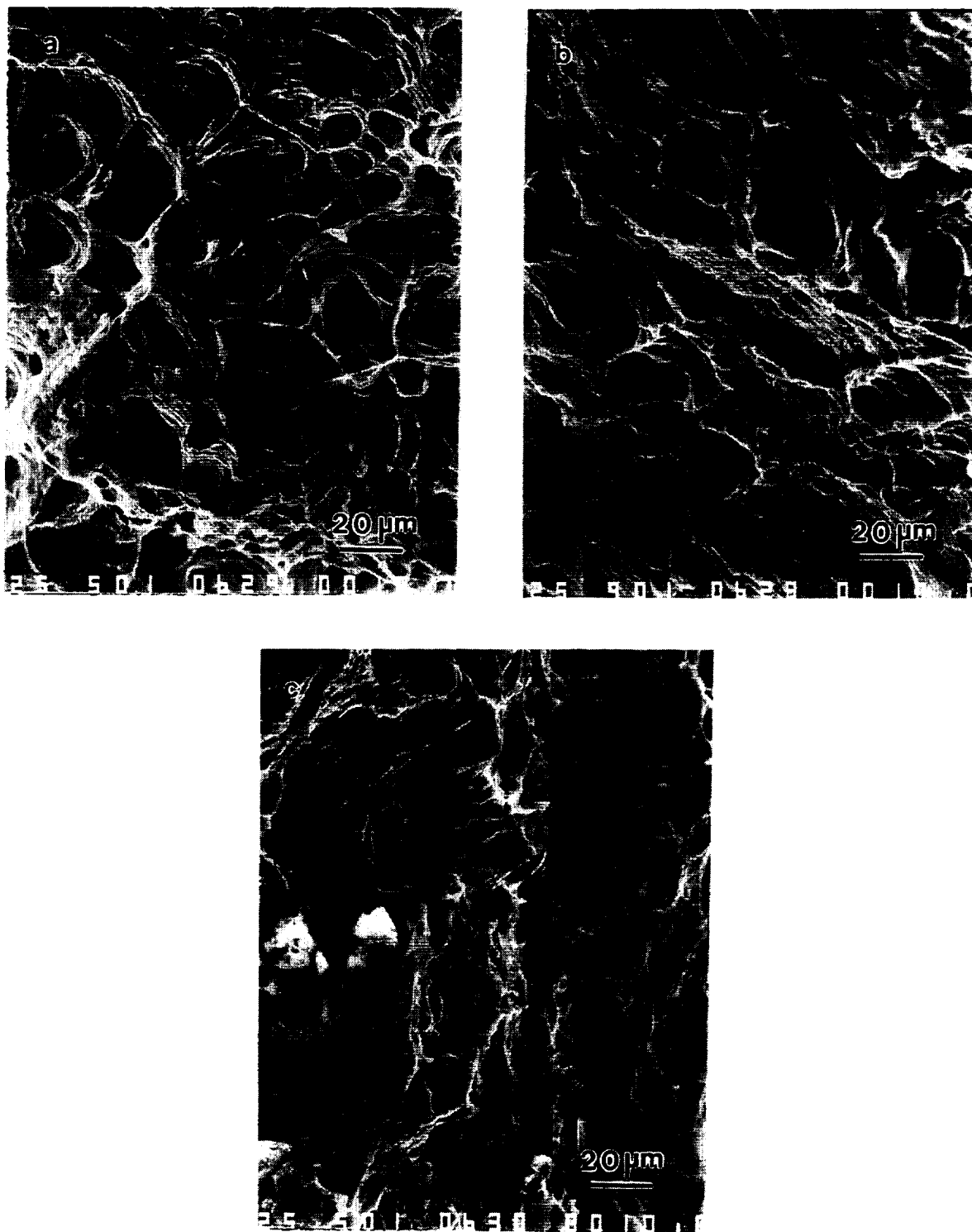
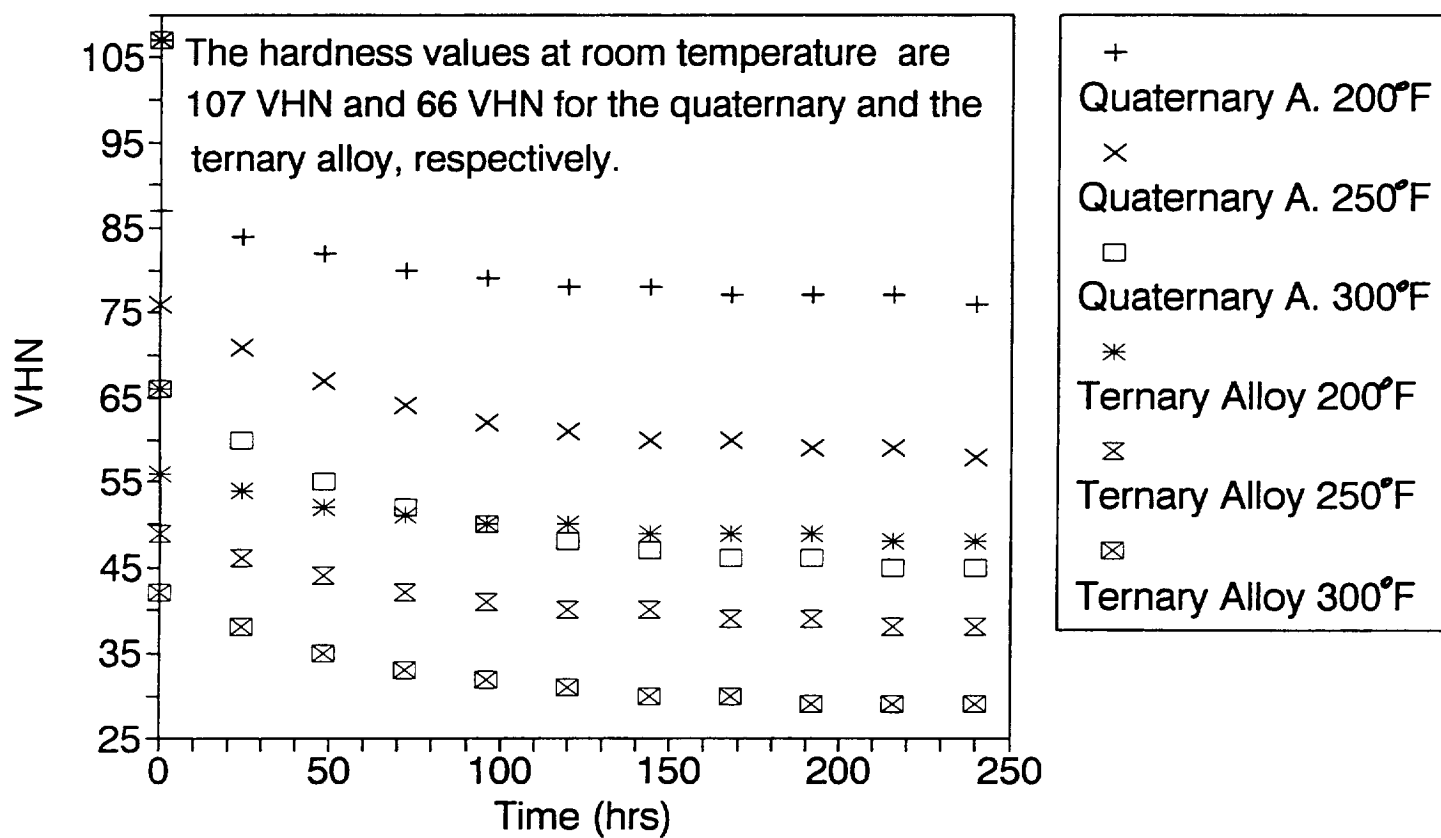


Figure 8. Fracture surfaces of alloys 3 (a), 4 (b), and 5 (c) at a magnification of 500 times.

Hot Hardness Measurements

Al-0.71Si-2.6Ge & Al-1.1Si-1.55Ge-2.7Cu

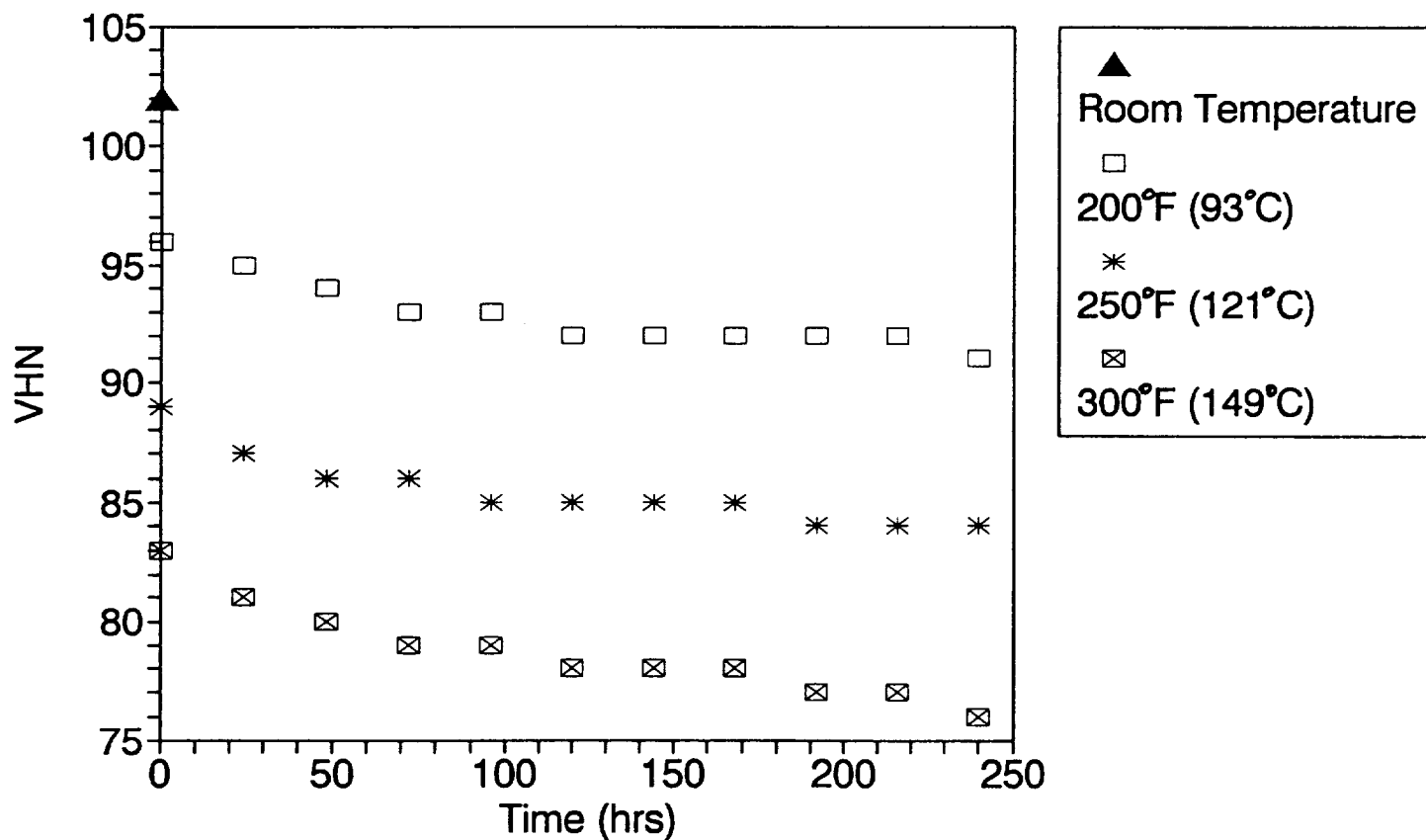


Peak-aged at 160°C.

Figure 9. Microhardness measurements at elevated temperatures for alloys 1 and 2.

Hot Hardness Measurements

Al-1.00Si-0.99Ge-2.57Cu (wt.%)



Peak-aged at 160°C.

Figure 10. Microhardness measurements at elevated temperatures for alloy 4.

**TASK 4B. TEXTURE AND PRECIPITATE EFFECTS ON MECHANICAL
PROPERTIES AND ANISOTROPY OF Al-Cu-Mg-X ALLOYS
(UVa)**

Co-Principal Investigators: Dr. E.A. Starke, Jr.
Dr. G.J. Shiflet
Post Doctoral Fellow: Dr. Birgit Skrotski

Task Objective

The objectives of this research are to determine the effect of texture in unrecrystallized and recrystallized modified 2519 on the precipitation of the Ω and Θ' phases in the T6 and T8 conditions and the associated relationship with anisotropy of mechanical properties. In addition, the effect of an applied stress (both elastic and plastic) on nucleation and growth of the strengthening precipitates will be examined.

Introduction

Texture Effects: Plastic yielding in a polycrystalline material requires that the critical resolved shear stress be reached on a number of slip systems (usually five) in order to maintain compatibility across the grain boundaries. This requirement is necessary if all grains are to undergo the same deformation as the overall deformation. The externally applied stress necessary for this condition depends on the direction of the applied stress and the crystallographic texture of the material. Most treatments of this problem are based on the theories of Taylor [1] and Bishop and Hill [2] and relate to single phase materials. These theories have been clearly presented by Backofen [3]. Applying the principle of minimum internal plastic work in the crystal, Taylor derived a factor M which relates the stress necessary for plastic flow to the critical resolved shear stress of the crystal. The value of M is a function not only of the crystal orientation but also of the enforced shape change and the geometrical arrangement of the slip

systems, i.e., the texture of the material. The Taylor factor:

$$M = \delta\gamma_T / \delta\epsilon \quad (1)$$

is the smallest total shear strain to give the total macroscopic strain. For face centered cubic metals there are 384 combinations of the five independent slip systems. For a random texture M is equal to 3.06 using the Taylor method.

The extent of texture strengthening, i.e., the effect of texture on yield stress, may be illustrated by considering the variation of M with orientation for axisymmetric flow in fcc metals with a fiber texture. The dependence of the Taylor factor, M , on orientation for cubic metals has been determined by Chin and Mammel [4] and is plotted in the crystallographic triangle of Fig. 1. The contour lines in Fig. 1 are lines of equal M -value (or equal strength). Introduction of strong [111] or [100] textures would change the strength compared to a randomly textured material by +20% and -25%, respectively. Although sheet textures are usually not as sharp as the fiber texture examples discussed here, they can still result in significant anisotropy of strength and strain to failure in sheet and plate products.

Precipitate Effects: Plastic anisotropy of a single phase material is usually changed when it is strengthened by second phase particles. The effect depends on both shape and habit planes of the precipitates and may reduce anisotropy or increase anisotropy [5-10]. Hosford and Zeisloft [6] proposed a model, for explaining their observation of the effect on anisotropy of Θ' on {100} planes in an Al-Cu alloy. Their model is based on maintaining compatibility by plastic deformation and partly by rotation of the Θ' platelets. The Hosford model, which we will call the plastic strain model, can be described by:

$$\sigma = M\tau_m(1-f) + f\sigma_p N_a \quad (2)$$

where τ_m is the matrix critical resolved shear strength, f and σ_p are the volume fraction and effective flow strength of the precipitate and N_a is the average value of N for the three platelet orientations, i.e., N is determined from the effective strain in the precipitate due to the applied strain and averaged for the different precipitate orientations.

Bate et al. [9,10] used the model of Brown and Stobbs [11,12], which describes strain hardening in dispersion hardened alloys containing non-deforming particles, to account for anisotropic effects. This model, called the elastic inclusion model, can be represented by:

$$\sigma_{ij} = 2\mu f \gamma_{ijkl} \varepsilon_{kl}^p \quad (3)$$

where μ is the shear moduli of the inclusion and matrix (the assumption is that they are the same), f is the volume fraction of inclusions, ε^p is the plastic strain discontinuity and γ_{ijkl} is the accommodation tensor, determined by the shape and orientation of the inclusion. Although both models qualitatively describe the effect of precipitates on anisotropy, the elastic inclusion model is probably more realistic if the precipitates are not sheared by moving dislocations.

Nucleation and Growth of Precipitates: In general, nucleation of precipitates in an age hardenable aluminum alloy can be described by:

$$\Delta G = V\Delta G_v + A\gamma + V\Delta G_s \quad (4)$$

where ΔG_v is the change in free energy when a precipitate forms, V is the volume of the new phase, A is the area of the interface

between the matrix and the precipitate, γ is the energy of the new surface formed, and ΔG_S is the increase in elastic strain energy per unit volume of precipitate. The first term is always negative and the second and third terms are always positive. Precipitates that have large coherency strains or result in strains being produced in the matrix due to volume differences between the precipitate and the matrix, may nucleate preferentially on dislocations, subgrain or grain boundaries.

Coherency strains are usually considered to stabilize a single-phase field; i.e., they shift the solvus into the equilibrium two phase field. Externally imposed strains may change the stability of a phase and may move the solvus line either into the single-phase or two-phase regions. Consequently, externally applied stresses and internal stresses associated with second phase particles can affect both nucleation of precipitates and coarsening behavior [13-16].

In summary, deformation and recrystallization textures can have a significant effect on anisotropy of mechanical properties in sheet and plate material. The precipitates in age hardenable aluminum alloys may superimpose an additional anisotropy which may either add to or subtract from that imposed by the crystallographic texture. In addition, deformation prior to aging affects nucleation of precipitates that have large coherency strains or interfacial energies. Since the dislocation structure which results from the deformation will not be uniform, nucleation of precipitates will not occur with the same frequency on all possible habit planes, an additional complication. Also, for applications where both stress and moderate temperature increases occur, shifts in phase fields and coarsening behavior of precipitates may be affected.

Experimental Procedure

The modified 2519+Ag alloy studied thus far was provided by Alcoa and designated by heat number 689248. The as-received

material was recrystallized sheet with a chemical composition of 6.13wt.%Cu, 0.43wt.%Mg, 0.31wt.%Mn, 0.53 wt.%Ag, 0.14wt.%Zr, 0.08wt.%V, 0.06wt.%Fe, 0.03wt.%Si, balance Al. The as-received material was solution heat treated for one hour at 520°C and quenched in cold water. The {111}, {200}, and {220} pole figures were determined on the heat treated material using the Schultz reflection method and filtered Cu K α radiation. The aging response of the alloy was determined as a function of time at 163°C by Vickers hardness measurements. The yield strength, ultimate tensile strength, reduction in area, strain hardening coefficient, and r values (width strain/thickness strain) were determined from tensile tests on samples in the T6 and T8 conditions in the rolling direction, transverse direction and at 45° to the rolling direction.

Results and Discussion

The {111}, {200} and {220} pole figures are presented in Fig. 2. All pole figures indicate that the texture is completely random and confirm that the sheet product is completely recrystallized, as suggested earlier by Alcoa. The texture is not the normal recrystallized texture usually observed in aluminum alloys. The random texture may be associated with the high volume fraction of constituent phases which could have resulted in deformation zones during rolling. The deformation zones would then serve as sites for recrystallization during subsequent heat treatment. A uniform distribution of hard second phase particles larger than one micron are very efficient in producing deformation zones during warm working. It has been shown that such a structure results in a random texture in aluminum alloys after recrystallization heat treatments [17].

The aging response at 163°C is shown in Fig. 3. The results of the mechanical property measurements are given in Table 1. The data indicate that the sheet product is very isotropic, i.e., no differences in properties were observed as a function of

orientation. Although this was expected for the as-solution heat treated condition, it was somewhat of a surprise for the T6 and T8 conditions since plate precipitates on a particular habit plane normally have an effect on anisotropy. However, since precipitates on [111] planes normally increase anisotropy and precipitates on [100] planes normally decrease anisotropy, and since both types are present in this alloy, their effects canceled. The yield and ultimate strengths are graphically presented in Fig. 4.

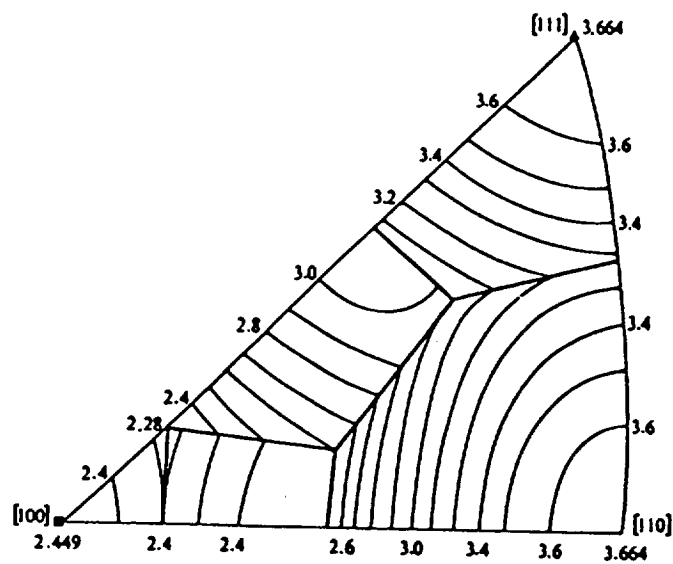
References

1. G.I. Taylor, "Plastic Strain in Metals," J. Inst. Metals **62**, 1938, p. 307.
2. J.F.W. Bishop and R. Hill, "Theory of Plastic Distortion of a Polycrystalline Aggregate under Combined Stresses," Phil. Mag. **42**, 1951, p. 414.
3. W.A. Backofen, Deformation Processing, Addison-Wesley, 1972.
4. G.Y. Chin and W.L. Mammel, "Generalization and Equivalence of the Minimum Work (Taylor) and Maximum Work (Bishop-Hill) Principles for Crystal Plasticity," Trans. Metall. Soc. AIME **245**, 1969, p. 1211.
5. J. Althoff, K. Drefahl and P. Wincierz, "Charakterisierung der Mechanischen Anisotropie Stranggepresster Aushaertbarer Aluminiumlegierungen (Presseffekt) durch Kurven des Fließens und r-Werte," Z. Metallk. **62**, 1971, p. 765.
6. W.F. Hosford and R.H. Zeisloft, "The Anisotropy of Age-Hardened Al-4% Cu Single Crystals During Plane-Strain Compression," Metall. Trans. **3**, 1972, p.113.
7. P. Jabson and W.T. Roberts, "Directionality in a Precipitation-Hardened Alloy," Metall. Trans. A **8**, 1977, p. 2013.
8. S.P. Agrawal and W.F. Hosford, "The Anisotropy of Al-4 Wt Pct Cu Single Crystals Tested in Plane-Strain Compression," Metall. Trans. **7**, 1976, p. 1867.
9. P. Bate, W.T. Roberts and D.V. Wilson, "The Plastic Anisotropy of Two-Phase Aluminum Alloys - I. Anisotropy in Unidirectional Deformation," Acta Met. **29**, 1981, p. 1797.

10. P. Bate, W.T. Roberts and D.V. Wilson, "The Plastic Anisotropy of Two-Phase Aluminum Alloys - II. Anisotropic Behavior in Load-Reversal Tests," Acta Met. 30, 1982, p. 725.
11. L.M. Brown and W.M. Stobbs, "The Work-hardening of Copper-Silica: I. A Model Based on Internal Stresses, with no Plastic Relaxation," Phil. Mag. 23, 1971, p. 1185.
12. L.M. Brown and W.M. Stobbs, "The Work-hardening of Copper-Silica: II. The Role of Plastic Relaxation," Phil. Mag. 23, 1971, p. 1201.
13. W.C. Johnson and C.S. Chiang, "Phase Equilibrium and Stability of Elastically Stressed Heteroepitaxial Thin Films," J. Appl. Phys. 64, 1988, p. 1155.
14. C.S. Chiang and W.C. Johnson, "Coherent Phase Equilibria in Systems Possessing a Consolute Critical Point," J. Mat. Res. 4, 1989, p. 678.
15. W.C. Johnson, T.A. Abinandanan and P.W. Voorhees, "The Coarsening Kinetics of Two Misfitting Particles in an Anisotropic Crystal," Acta Met. Mat. 38, 1990, p. 1349.
16. T.A. Abinandanan and W.C. Johnson, "Coarsening of Elastically Interacting Coherent Particles, I. & II," Acta Met. Mat. 41, 1993, p. 17 & p. 27.
17. J.C. Williams and E.A. Starke, Jr., "The Role of Thermomechanical Processing in Tailoring the Properties of Aluminum and Titanium Alloys," in Deformation, Processing and Structure, ed. George Krauss, ASM, Metals Park, Ohio, 1984, p. 279.

Table 1. Tensile Properties of Modified 2519+Ag #689248.

Sample	$R_{p0.2}$ [MPa]	R_m [MPa]	A [%]	n	r	r_m	Δr
RD, SHT	167.0	(408.9)	24.3	0.316	-		
TD, SHT	172.8	(403.1)	24.2	0.302	0.49		
TD, SHT	166.2	(402.5)	24.1	0.309	0.64		
45, SHT	175.1	(401.3)	24.3	0.299	0.38		
45, SHT	187.3	(409.0)	24.1	0.276	0.71		
RD, 20h/ 163°C	483.3	534.7	12.3	0.070	0.74		
RD, 20h/ 163°C	476.7	536.5	11.9	0.069	0.61		
TD, 20h/ 163°C	478.3	523.3	11.5	0.070	0.71	0.72	-0.18
TD, 20h/ 163°	484.5	530.0	12.4	0.070	0.45		
45°, 20h/ 163°C	469.3	519.5	14.1	0.070	0.71		
45°, 20h/ 163°C	472.9	521.4	12.5	0.081	0.90		
RD, 2%+ 16h/163°C	477.0	527.3	13.6	0.084	0.67		
RD, 2%+ 16h/163°C	471.0	525.1	13.7	0.083	0.66		
TD, 2%+ 16h/163°C	470.8	519.1	13.3	0.081	0.52	0.71	-0.17
TD, 2%+ 16h/163°C	467.4	517.3	10.9	0.081	0.66		
45°, 2%+ 16h/163°C	466.8	516.2	11.2	0.082	0.69		
45°, 2%+ 16h/163°C	469.7	517.3	10.6	0.082	0.89		



Avg. $\bar{M} = 3.06$

Figure 1. The dependence of the Taylor Factor, M , on orientation for cubic crystals.

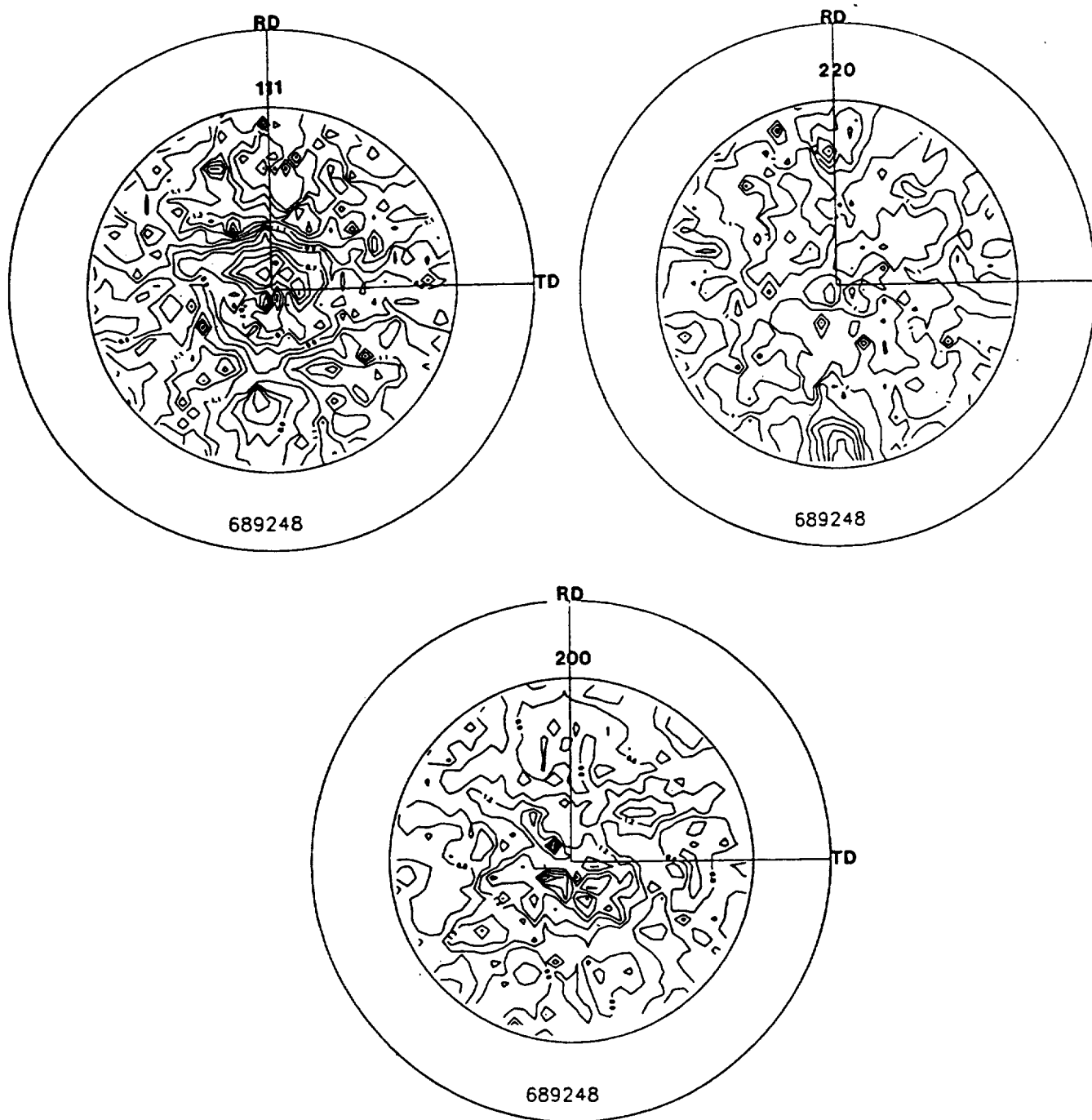


Figure 2. Pole figures for modified 2519+Ag sheet.

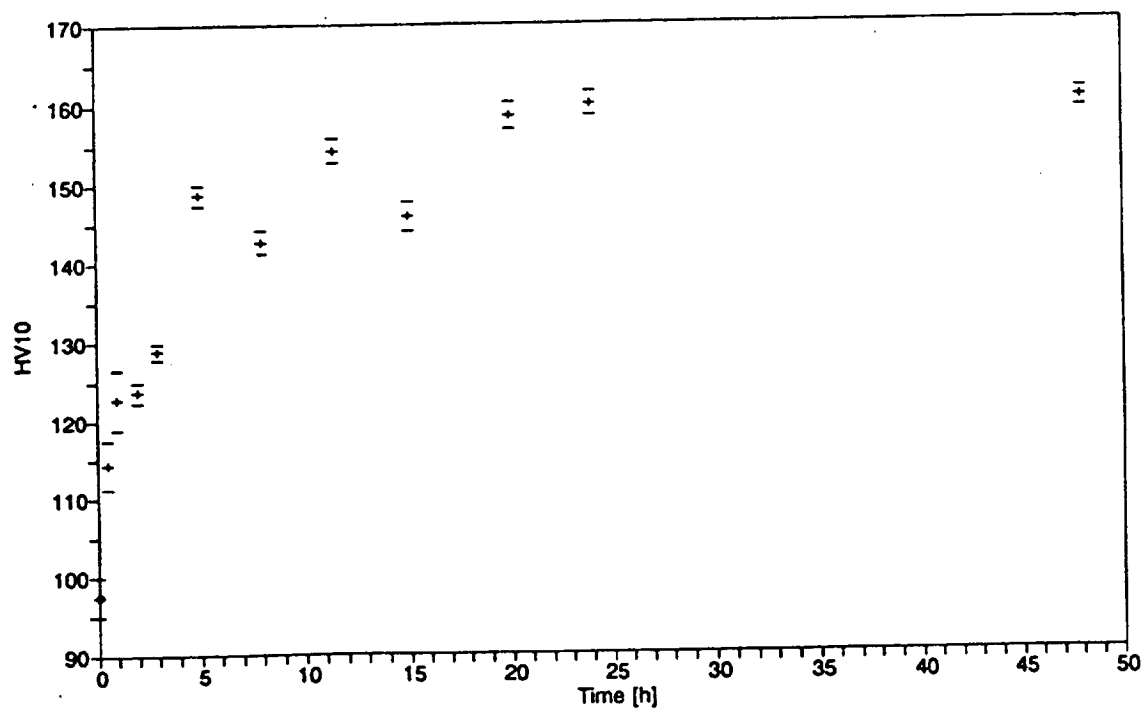


Figure 3. Aging Response at 163°C for Modified 2519+Ag Sheet After Solution Heat Treatment for One Hour at 520°C.

Figure 3. Aging response at 163°C for modified 2519+Ag sheet after solution heat treatment for one hour at 520°C.

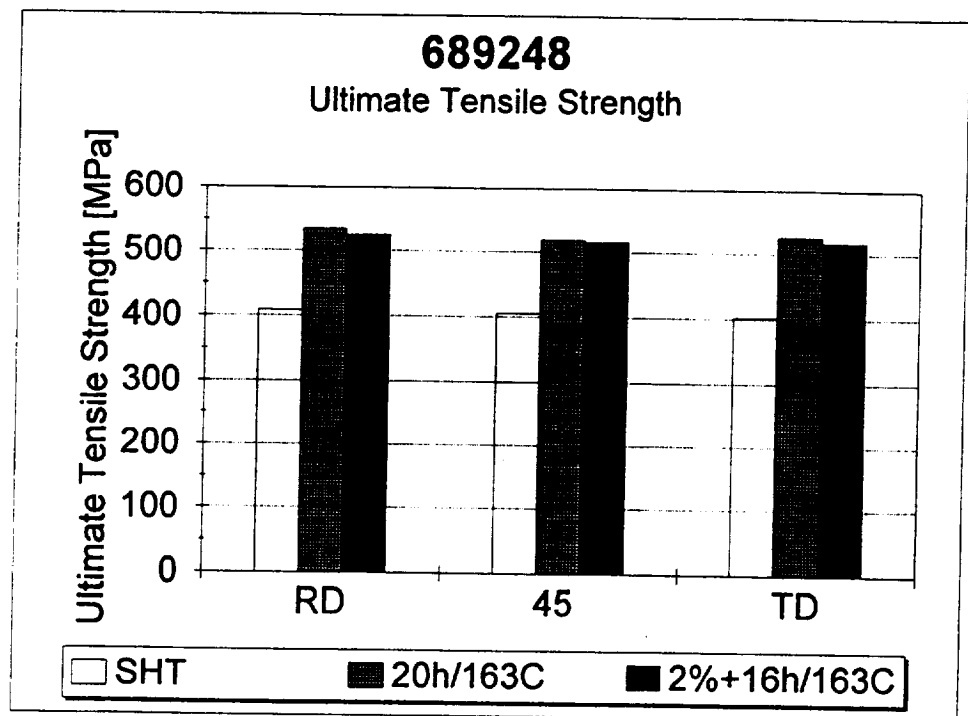
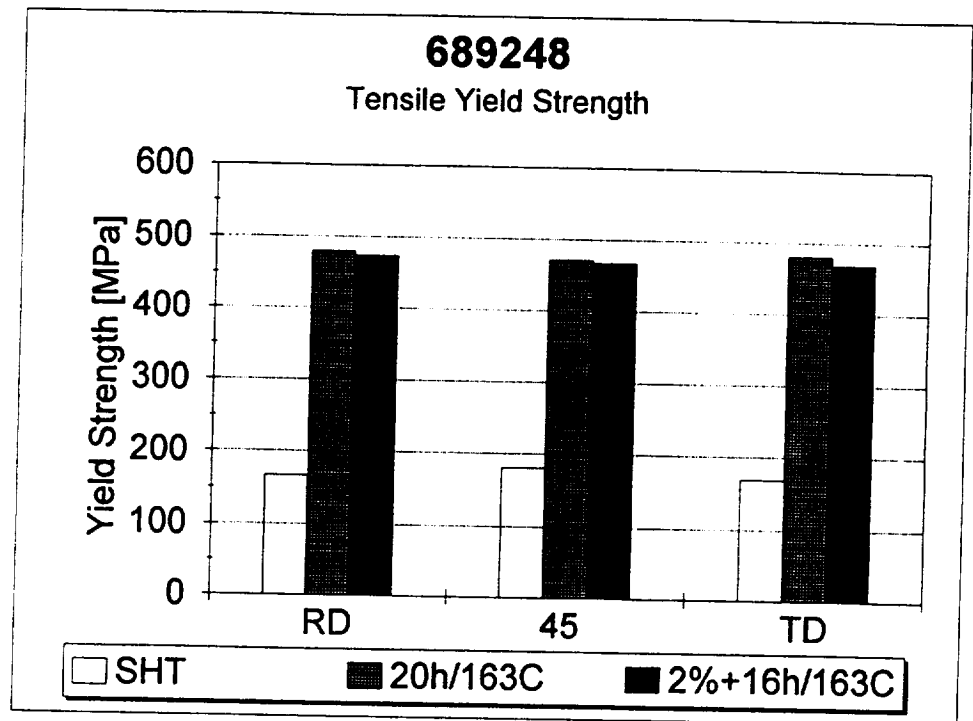


Figure 4. Tensile properties for modified 2519+Ag sheet.

Task 6. PROCESSING-BASED IMPROVEMENTS IN THE MECHANICAL ISOTROPY AND INTERMEDIATE TEMPERATURE DAMAGE TOLERANCE OF Al-Fe-V-Si ALLOY 8009 (UVa)

Principal Investigator: Professor Richard P. Gangloff
Research Associate: Dr. Sang-Shik Kim

Objective

The overall objectives of this task are to: (a) reduce mechanical anisotropy, and (b) improve the intermediate temperature/prolonged time fracture resistance of the 8009 alloy composition for high speed airframe applications. These objectives are being accomplished by optimizing the processing of rapidly solidified powder metallurgy 8009. The third objective is to establish micromechanical mechanisms for the time-temperature dependent deformation and fracture of 8009-type alloys with ultrafine grain size, metastable solute, and a significant volume fraction of small dispersoid phase.

The first two objectives were emphasized in Year 1 of this research in collaboration with Dr. Michael S. Zedalis at the Allied-Signal Corporate Research Laboratories. As described in the first annual progress report [1], Allied-Signal Inc. successfully produced a matrix of 8009 sheet and plate products based on melt spinning with and without an inert cover gas, and including a wide range of rolling/thermal parameters. Experiments at Allied Signal characterized the temperature-dependent tensile strength, elongation and ductility of these materials, while work at the University of Virginia (UVa) and Fracture Technology Associates (FTA) measured time- and temperature-dependent fracture toughness from a J-integral vs crack extension "R-curve" method. Experiments were also conducted at UVa and FTA to examine the interpretation and reproducibility of the fracture toughness measurement procedure.

Year 2 work at UVa is emphasizing the third objective: that of gaining mechanistic understanding of the deleterious effects of

increased temperature and decreased strain rate on the fracture resistance of 8009-type alloys.

Progress During Report Period

During this reporting period, mechanisms for the unique time-temperature plastic deformation and fracture behavior of HTA 8009 were examined. The proposed mechanisms, including delamination toughening, external and internal hydrogen embrittlement, dynamic strain aging, slip localization with nil work hardening due to dislocation climb and dynamic recovery, have been reviewed and critically assessed.

For each heat of 8009, the effects of thermomechanical processing on the deformation and fracture behavior of HTA 8009 were examined at ambient and elevated temperatures. The possible mechanism for the change in deformation and fracture behavior with thermomechanical processing in 8009 was discussed.

Mechanisms for Time-Temperature Dependent Fracture of 8009

As shown in Figure 1, regardless of processing route and product form, the fracture toughness of 8009 decreases with increasing temperature. Toughness further decreases with decreasing strain rate at constant temperature, at least 25°C and above. It has been demonstrated that 8009 fails by microvoid coalescence, regardless of testing condition [1]. This notion is based on stereoisaging fractographic analysis of matching fracture surfaces previously conducted by Porr [2]. The morphology and distribution of voids, however, differ significantly depending on the testing temperature and strain rate. At 25°C, microvoids nucleated and grew at oxide-matrix interfaces, and coalesced by the joining of a second distribution of smaller spherical voids that initiated at dispersoids and dispersoid clusters between the oxide nucleated voids. Consequently, the crack surface of 8009 fractured at 25°C reflects a bimodal distribution of dimples. At elevated temperatures, on the other hand, coalescence of oxide-

nucleated voids occurred by shear instability between growing voids on planes parallel to the loading axis. Decreasing loading rate has a similar effect on the fracture morphology of 8009 as increasing temperature.

Several mechanisms were proposed for this unique time-temperature dependent behavior, including: (1) delamination toughening [3], (2) hydrogen or oxygen environment embrittlement [4,5], (3) internal hydrogen embrittlement from processing [6], (4) micromechanics [2], (5) dynamic strain aging (DSA) [7,8], and (5) slip localization with nil work hardening due to dislocation climb [2].

The idea of reduced delamination toughening in 8009 at intermediate elevated temperature was based on the macroscopic SEM observation of extruded 8009 showing significant prior particle boundary delamination at 25 and 300°C, but not at 175°C [3]. Boundary failure results in a loss of through-thickness specimen constraint if the height of the out-of-plane cracks are on the order of the crack tip plastic zone, and if the height exceeds spacing so that shear operates under plane stress on planes at 45° to the Mode I crack. Delamination therefore increases the initiation and growth fracture toughness. Previous studies by Porr [2] and the present fracture toughness experiments with plate and sheet forms of 8009 indicate that the delamination mechanism is not a central factor for the time-temperature dependence of K_{IC} , and does not contribute to the excellent ambient temperature fracture toughness. Unlike extruded 8009, plate and sheet 8009 do not exhibit considerable delamination, regardless of the testing condition.

The effect of internal and external hydrogen on the fracture toughness of 8009 was thoroughly examined by Porr and Gangloff [2,9]. They observed that prolonged heat treatments in vacuum, or reduced total dissolved hydrogen content by autoclaving, have no effect on fracture toughness. It was concluded that hydrogen in 8009 may be similarly and strongly bonded (or trapped) in each

product form and at both 25°C and 175°C. Very high temperature, perhaps over 350°C, is required to chemically produce atomic hydrogen in the 8009 microstructure. Recently, a thermal desorption spectroscopy study of 8009 plate conducted at UVA confirms that hydrogen in 8009 is strongly bonded up to 400°C [10]. It is likely that hydrogen in 8009 is beneficially chemically trapped by strongly bonded hydrated oxides and is not released in atomic form for embrittlement at temperatures on the order of 25 to 250°C.

In the ensuing section, fracture mechanisms, based on dynamic strain aging and enhanced plastic instability are discussed.

Dynamic Strain Aging

Dynamic strain aging is a widely accepted mechanism for the time-temperature dependence of tensile elongation to fracture for 8009-type alloys [7,8,11]. It was often observed that Al-Fe-X alloys, including 8009 and Al-Fe-Ce alloys, show minima in tensile elongation and a corresponding reduced or negative strain rate sensitivity within the temperature range between 150 and 200°C. Based on this observation and STEM measurement of high solid solution Fe concentration (0.5 atom%), Skinner et al. [8] suggested that dynamic strain aging occurs in 8009 at intermediate temperatures due to the sluggish diffusion of substitutional Fe and V present in the matrix and causes the loss of tensile ductility.

The DSA argument focuses on work hardening and strain rate sensitivity effects on flow localization and necking. While elongation to fracture in a uniaxial tensile specimen may decline due to DSA induced plastic instability, it is unclear how this result relates to the more relevant crack tip or notch root process zone that is under complex triaxial deformation and elastic constraint. As shown in Figure 2, the dislocation structure of deformed 8009 is unique in that classical forest dislocation structures are not formed. Therefore, interaction

between solute atom and forest dislocation networks, the proposed mechanism of classic dynamic strain aging, is questionable.

As discussed in the previous progress report, the fracture toughness of high purity, ultrafine grain size, dispersoid strengthened Exxon DS Aluminum also decreases with increasing temperature and decreasing strain rate, despite the low solute content in the matrix. If dynamic strain aging is a main cause for the reduced toughness at elevated temperature, then the toughness of Exxon DS Aluminum should not decrease with increasing temperature. The present study disproves DSA as a likely mechanism for time-temperature dependent fracture of 8009.

Plastic Instability and Flow Localization

8009 fails by microvoid processes, regardless of processing route and testing condition. Microvoiding can be divided into three steps, including nucleation, growth and coalescence. As previously reported by Porr [2], voids nucleate at oxide-matrix interfaces for 8009 and in sheets parallel to the applied stress. When particle radius is smaller than 1 μm , the critical strain required to nucleate microvoids by particle decohesion is given by [12]:

$$\epsilon_1^n = Kr(\sigma_c - \sigma_m)^2$$

where K is a material constant related to the volume fraction of particles, r is the particle radius, σ_c is the critical cohesive strength of the interface and σ_m is a macroscopic mean-normal stress. Models of microvoid nucleation suggest that, in general, increased test temperature and reduced strain rate, which are likely to promote local recovery effects at particle sites, will reduce the maximum interface stress; thus making it more difficult to achieve the condition for decohesion of the particle/matrix interface. With the same token, nucleation strain for microvoid can be decreased due to the reduction in interface strength and

local hydrostatic tension. In fact, Porr showed that oxide voids nucleate at lower strains in 8009 as temperature increases.

Once a microvoid has nucleated in a plastically deforming matrix, the resulting stress-free surface of the void causes a localized stress and strain concentration in the adjacent plastic field [12]. With continuing plastic flow of the matrix, the microvoid will undergo a volumetric growth and shape change which amplifies the distortion imposed by the remote uniform strain field. The overall growth rate of microvoids increases as yield strength and strain hardening rate fall. Therefore, increased temperatures and reduced strain rates will tend to promote the growth of microvoids. The aforementioned changes in nucleation and growth rate with increasing temperature and/or decreasing strain rate, however, are equally true for conventional aluminum alloys which generally have enhanced ductility at elevated temperatures.

The final step in the process of ductile fracture is coalescence of growing voids. In this stage, the growing voids link together, and fracture occurs. 8009 has a different void coalescence mechanism depending on testing temperature and loading rate, with stable void growth with possible void sheeting at 25°C or fast loading rate, compared to localized shear instability at elevated temperatures or slow loading rates. Such a change in coalescence mechanism is very likely due to the change in the magnitude of plastic instability and flow localization in 8009 with different testing conditions.

For conventional aluminum alloys, ductility increases with increasing temperature because of both local recovery at void nucleating particles and an increasing strain rate sensitivity of the flow stress. Increasing strain rate hardening tends to homogenize plastic flow and to reduce the tendency for shear localization between growing microvoids. Plastic instability and flow localization in 8009 can be enhanced at elevated temperature and/or slow strain rate by several reasons.

a. Negative Strain Rate Sensitivity

Thomason proposed that flow localization is enhanced with decreasing strain rate sensitivity [13]. He argues that the degree of instability, as expressed by the ratio of the microscopic yield-shear stress (K_n), in the intervoid matrix at incipient void coalescence, to the macroscopic yield-shear stress (K), $(K_n/K)_{SR}$, is exponentially proportional to the strain rate sensitivity (m). He further argues that flow localization is likely when m is lower than 0.15. For conventional Al alloys, m increases with increasing temperature. For 8009, however, m is low and maybe negative at temperatures between 175 and 200°C [8,11]. Therefore, flow localization is likely in this temperature range.

The negative strain rate sensitivity in 8009 at intermediate temperatures is generally attributed to dynamic strain aging, as reported by Skinner et al. [8]. Besides dynamic strain aging, the unique dislocation behavior in dispersion-strengthened ultrafine grain size materials can induce a negative or diminutive strain rate sensitivity. As proposed by Edwards et al. [14] for zinc containing a large volume fraction of small Al_2O_3 or W particles with a typical grain size of 1 to 3 μm , generation of mobile dislocations at particles and adjacent limited matrix recovery can cause strain rate insensitivity (low m) at certain combinations of strain and temperature. It is assumed that above a threshold stress, each dispersed particle is a dislocation source, rather than an obstacle, in an otherwise source-deficient material. A slight increase in strain rate would raise the interface stress and cause a small additional fraction of particles to generate mobile dislocations. As a consequence, flow stress could be reduced.

b. Dynamic Recovery and Formation of Lüders Band

Lloyd and Westengen proposed that rapid dynamic recovery at elevated temperatures in ultrafine grain sized materials causes enhanced plastic instability and flow localization [15-18]. Westengen conducted detailed tensile studies of fine grain sized aluminum alloys (Al-0.8Mn-0.2Fe in wt.% and produced by strip casting) as a function of grain size, temperature and strain rate [15]. The average grain size of these alloys ranges from 1.5 μm to 0.8 μm with 9% volume fraction of $\text{Al}_{16}(\text{Mn,Fe})$ and $\alpha\text{-Al}(\text{Mn,Fe})\text{Si}$ particles. He found that below a critical grain size, intragranular dislocation substructure does not develop during tensile deformation. The strain rate sensitivity is approximately 0.02 and remains constant up to 127°C. Lloyd made a similar observation for ultrafine grain sized Al-6 wt.% Ni alloys [17]. Both attributed the lack of intragranular dislocation substructure during deformation to the annihilation and redistribution of dislocations due to enhanced dynamic recovery process in ultrafine grain sized materials. When the grain size is similar to or less than the mean free path for dislocations (1 - 2 μm), the formation of dislocation cell structures is no longer favored within the grain interior. The lack of dislocation substructures in the interior of grains, and avalanches of dislocations from grain boundaries, can lead to low work hardening and localized deformation. Specifically, Westengen suggested that plastic instability is initiated by an abrupt increase in mobile dislocation density from grain boundary sources, causing a drop in the flow stress and the formation of Lüders bands [15]. However, such dislocation sources within the small grains were neither specified nor evidenced.

c. Dislocation Climb over Particles

Porr suggested that enhanced plastic instability and flow localization is specifically due to dislocation climb over dispersoids at elevated temperatures or low strain rates in 8009

[2]. He argues that once dislocations are free of the dispersoids by climb, dislocations locally concentrate in the aluminum matrix and cause high strain concentrations at prior powder particle boundaries, dispersoid clusters and high angle grain boundaries. Ductility losses may occur by shear localization, as well as a reduction in work hardening and flow stress.

The dislocation climb mechanism in 8009 is based on the Humphrey and Kalu model which considers that the rate of dislocation accumulation at non-shearable spherical particles is balanced by the rate of dislocation climb and/or diffusional relaxation around the particles at sufficiently high temperature and slow strain rate [19]. A schematic illustration of the change in dislocation-particle interaction for different strain rates is shown in Figure 3. This model predicts that the critical strain rate, above which dislocations accumulate at particles, is approximately $4 \times 10^{-6} \text{ sec}^{-1}$ at 25°C and $2 \times 10^{-1} \text{ sec}^{-1}$ at 175°C for 8009 with an average silicide particle size of 80 nm. Essentially, a four to five order of magnitude increase in the critical strain rate is predicted for increasing temperature from 25°C to 175°C . As shown in Figure 4, K_{IC} for 6.3 mm thick 8009 plate at 25°C is significantly reduced at a loading rate of about 10^{-5} mm/sec . Data from Porr for a similar 8009 extrusion show that such a toughness decrease occurs at a critical loading rate of about 10^{-2} mm/sec for fracture at 175°C . Accordingly, the toughness experiments indicate that the critical strain rate is increased by three orders of magnitude for increasing temperature from 25°C to 175°C . It is necessary to compare actuator displacement rates in this analysis because of uncertainties associated with calculating crack tip strain rate. It is also necessary to arbitrarily define the transition point in K_{IC} vs temperature data.

The HK model prediction of "critical" strain rate versus temperature, along with data representing 8009, are plotted in

Figure 5. For conditions where strain rate, temperature and particle diameter cause the value of $\ln(\dot{\epsilon}'Td^3)$ to lie left of the deformation transition lines, dislocations climb (or diffusional relaxation occurs) around particles faster than they accumulate; when right of the line, particle-dislocation interactions result in hardening, and presumably, more homogeneous slip. Crack tip strain rate at $K = K_{IC}$ was approximated for each loading rate and based on continuum mechanics crack tip strain distribution. Even though there is a substantial discrepancy between the predictions of the climb-based model for dislocation bypassing of silicides and localization in the surrounding aluminum, and the time dependence of K_{IC} measured at 25°C compared to 175°C, overall agreement is encouraging.

The climb motion of dislocations surmounting particles was not decisively evidenced by the previous TEM examinations of tensile deformed 8009 at elevated temperatures. However, as shown in Fig. 2, the present study strongly suggests weakened dislocation-particle interactions at elevated temperature. At 25°C, a high density of dislocations is equally evidenced around oxide and silicide particles. Stress concentration around oxides and dispersoids would be equally high enough to nucleate voids at their interfaces with the matrix. Voids will first nucleate at large particle-matrix interfaces (e.g., oxide-matrix interfaces) and coalesce by joining the smaller voids formed around dispersoids. At 175°C, dispersoids are free of dislocations due to the weakened dislocation-particle interactions. Voids, nucleated at oxide-matrix interfaces, may then grow by localized shear plastic flow between oxides.

Dislocation climb has been relatively well studied for crept oxide dispersion strengthened (ODS) nickel-based superalloys [20,21]. Schröder and Arzt [20], for example, unequivocally documented dislocation climb in γ' -forming ODS superalloy Inconel MA 6000 with an average grain size of 0.5 μm by utilizing a weak

beam, dark field TEM technique. For superalloys where the dislocation climb mechanism is dominant, a slope change in the \log (creep rate) - \log (stress) curve is often observed [22]. For 8009 [23] and other ultrafine grain sized materials [24], such a break was reported. For example, tensile creep strain rate data for extruded 8009, obtained by Leng et al. [25], indicated that a single linear relationship does not exist between $\log (d\epsilon/dt)$ and $\log \sigma$ for 8009.

Lagneborg [22] and Arzt et al. [24] suggest that the $\log (d\epsilon/dt)$ - $\log \sigma$ slope change is due to dislocation climb. During climb, the strongly deflected region of an arrested dislocation which is closest to a particle may swing out of the slip plane and surmount the particle. As a result, particles experience back stress caused by the creation of extra dislocation line length during the bypassing. The resulting minimum threshold stress for climb gradually increases with increasing applied stress until it reaches the Orowan stress. The dependence of the threshold stress on applied stress gives rise to a pronounced break in the $\log(d\epsilon/dt)$ - $\log \sigma$ curve.

Concluding Remarks on Fracture Mechanisms

The present study strongly indicates that the reduced tensile ductility and fracture toughness of 8009 at intermediate temperatures and slow strain rates is due to enhanced plastic instability and flow localization. Figure 6 suggests the enhanced flow localization in macroscopic scale at intermediate temperature in tensile deformed 2.3 mm thick Preprogram 8009 sheet at a strain rate of 5×10^{-4} /sec. At 175°C, fracture surface is slant to the tensile axis with an approximate angle of 40°, while that at 25°C is roughly perpendicular to the tensile axis.

As reviewed in the previous section, flow localization in 8009 at intermediate temperature can be caused by several reasons,

including strain rate insensitivity (low m) either by dynamic strain aging or unique dislocation-recovery combination, dynamic recovery and dislocation evasion of silicide dispersoids. Deformation and fracture studies on Exxon DS Aluminum disproves dynamic strain aging mechanism as a central factor for the reduced damage tolerance in 8009. The present TEM examination demonstrates that tensile deformed 8009 plate has a unique dislocation structure compared to that of conventional ingot metallurgy aluminum alloys. Intragranular dislocation cell structures, commonly observed in deformed medium to coarse grain sized aluminum alloys, are not observed in 8009 plate. The overall dislocation density is extremely low, especially after high temperature deformation. Tensile deformed 8009 at elevated temperatures reflects a high rate of dynamic recovery, dislocations arranging themselves into subboundaries with neater, less ragged arrays.

Enhanced dynamic recovery, perhaps due to dislocation climb over particles, at elevated temperature would lead to low work hardening and enhanced plastic instability developing locally intense shear bands between oxide particles. The strain to produce void coalescence at elevated temperature is therefore significantly reduced, leading to lower tensile ductility and fracture toughness. Reportedly, some ultrafine grain size alloys exhibit work softening phenomena during tensile deformation. This is reviewed in recent papers by Kuhlmann-Wilsdorf et al. [27,28]. They proposed that reduced Hall-Patch strengthening during deformation, as a result of a declining critical stress for the propagation of glide dislocations through the grain boundaries, is responsible for work softening. Porro conducted a notched tensile bar experiment for extruded 8009 and reported work hardening, albeit at a near-zero rate, rather than work softening [2]. Rowley recently conducted extensive compression experiments with 8009 plate and observed mild hardening, at least for plastic

strains up to 4% and specific temperature-strain rate conditions [29].

Effect of Thermomechanical Processing

Thermomechanical processing was performed on extruded 8009 at Allied-Signal Inc. to: (1) improve fracture toughness isotropy by obtaining a uniform microstructure, and (2) improve elevated temperature fracture resistance by refining oxide layers on prior ribbon particle boundaries and by introducing beneficial dislocation structures by cold deformation. This second reason is particularly compelling given the hypothesized importance of flow localization associated with nil work hardened dislocation substructures in normally worm-processed 8009.

Thermomechanical processing has been proven to effectively reduce the fracture toughness anisotropy in 8009. LT oriented 8009 extrusion has approximately 50% higher initiation toughness than that for the TL orientation at 25°C [1]. The TL orientation is intrinsically less tough because of a prior ribbon boundary crack path. Delamination does not occur because K_{IC} is low for TL orientation. Delamination for the LT extrusion magnifies the difference in toughness. The degree of toughness anisotropy for a extruded 8009 decreases with increasing test temperature. Figure 7 shows the blunting line offset fracture toughness values for 2.6 mm thick Modification A 8009 sheet at 25 and 175°C for the LT and TL orientations. The data were obtained by Fracture Technology Associates (FTA) employing the ASTM-standard unloading compliance method to define $J-\Delta a$. It appears that the TL orientation has higher toughness than LT. The final rolling direction for cross rolling is always perpendicular to the initial extrusion direction. Accordingly, if an orientation is expected to be lower toughness, it would be the LT case in cross-rolled plate, as controlled by fracture along the original extrusion-aligned prior ribbon boundaries. Compared to the 8009 extrusion, however, toughness anisotropy is significantly reduced. Also, blunting

line offset fracture toughness magnifies the effect of orientation.

The second task of improving elevated temperature fracture toughness by refining oxide layers and introducing beneficial dislocation structures was not accomplished by thermomechanical processing. As shown in Figure 8, thermomechanical processing has more or less deleterious effects on both room and elevated temperature fracture toughnesses. The effects of thermomechanical processing are two-fold; increased rolling reductions, both hot and cold, affect the oxide population and perhaps the dislocation substructure. These factors are likely to each influence the intrinsic deformation and fracture resistance of 8009-type alloys. Additionally, rolling affects yield strength, work hardening and flow localization; these factors, coupled with intrinsic fracture resistance, affect temperature-dependent K_{IC} .

Refined oxide layers and reduced interspacing between those layers in 8009 with rolling reduction were demonstrated in the previous progress report. SEM micrographs of as-received conventional 8009 plate and sheet showed that the average interplanar spacing between the oxide stringers on prior ribbon particle boundaries is reduced from 7 μm for 6.3 mm thick plate to 2 to 5 μm for 1.0 mm thick sheet. To examine the effect of the oxide population on ductile fracture process, assume that variable rolling practices do not affect the dislocation structure of 8009. Considering 25°C fracture, rolling could increase the applied strain required for void nucleation because of a reduced size of single oxides or dispersed oxide clusters. However, when particle radius is larger than 1 μm , void nucleation is not affected by particle radius [12] (since the oxide radius in 1.0 mm thick 8009 sheet is close to 1 μm , nucleation may not be strongly affected by the change in the size of oxides as a result of thermomechanical processing). Alternately, void growth could be facilitated by rolling reduction, because of decreased intraribbon particle spacing between the void nucleating oxides. That is, less

secondary void nucleation and growth are required as the ligament between primary oxide-nucleated voids decreases. It is not possible to predict the trend in tensile ductility from these opposing trends. The data in Figure 8 suggest that either void nucleation is actually enhanced by rolling, perhaps because of increasingly close oxides on adjacent ribbon surfaces and interacting strain fields, or because void growth is enhanced as discussed above and dominates fracture.

Considering fracture at 175°C, and assuming that rolling has not altered the tendency for shear localization, rolling could increase the applied strain for void nucleation, as argued for the 25°C case, and also due to the reduced size of localized deformation bands that intersect ribbon boundaries to enhance nucleation at oxides. To a first approximation, rolling reductions in prior ribbon particle thickness may not affect void growth if governed by local shear. The data in Figure 8 suggest some deleterious effect of rolling on elevated temperature tensile ductility and fracture toughness, perhaps due to enhanced microvoid nucleation as argued for the room temperature case.

Previously, TEM micrographs demonstrated that cold rolling to 1.0 mm thicknesses of sheet forms subgrain boundaries within the existing solidification-produced subgrains, resulting in further refined subgrain structure [1]. Since such boundaries are sinks for dislocation annihilation during deformation, dynamic recovery would be generally favored for the finer subgrain structure. The enhanced dynamic recovery would lead to lower work hardening and intensify the localized deformation. Reduced work hardening and flow localization would, in turn, induce strong shear bands between voids formed at oxide layers. SEM fractographs in thinner gauges of Conventional 8009 sheet, as shown in Figure 9, strongly suggest the enhanced plastic instability and flow localization with thermomechanical processing. The void impingement-type coalescence mechanism is notable on the fracture surface of thinner gauges of 8009 even at 25°C.

If the aforementioned notion is correct, the same gauge thickness of cold rolled 8009 should have higher ductility and toughness at each temperature than the hot rolled counterpart. The magnitude of dynamic recovery during hot rolling, favoring a shear localization prone microstructure, would be greater. Intriguingly, however, any difference in fracture toughness between cold rolled and hot rolled Modification A 8009 sheet falls within the error range, as shown in Figure 10. Moreover, intermediate annealing after cold rolling has no deleterious effect on both tensile ductility and fracture toughness. One plausible explanation is that, with such a severe rolling of almost 1000% reduction, the microstructure of each sheet may have fully recovered. This notion needs further confirmation.

Conclusively, cold rolling does not enhance the fracture toughness of 8009. In contrast Westengen observed that a 4% cold prestrain by rolling produced a 50% increase in the tensile elongation to fracture for an ultra-fine grain size aluminum alloy. He suggests that this is due to suppressed plastic instability, achieved by activating dislocation sources throughout the grains which otherwise do not have a mobile dislocation density to enable work hardening. Such dislocation sources within the small grains were neither specified nor evidenced. Additionally, uniaxial tensile elongation data, governed by necking instability, may not be relevant to ductility and fracture toughness. In the present study, the magnitude of the rolling reduction was between 100% and 1000% of the original thickness. Dislocations which are activated at a relatively early stage of rolling deformation may be annihilated during the final stage of rolling.

It is presently not possible to establish the relative contribution of oxide-based factors and slip localization/work hardening-based factors to fracture toughness.

Current and Potential Problem Areas

None.

Conclusions

- Rapid solidification and rolling process variations do not improve "intermediate temperature/slow strain rate embrittlement" of 8009.
- Time-temperature-dependent degradation in 8009 fracture toughness is not due to delamination toughening, hydrogen embrittlement, DSA, or extrinsic crack tip micromechanics.
- 8009 fracture is generally by microvoid processes initiated at boundary oxides; a single size of shallow dimples characterizes low toughness cracking.
- The likely mechanism for time-temperature-reduced toughness is localized plastic deformation between growing microvoids nucleated at prior particle boundary oxides; flow instability accelerates stable void growth-to-coalescence.
- Flow localization appears to be promoted by several factors, including low work hardening without dislocation substructure, dynamic recovery, dislocation evasion of silicides, and discontinuous dislocation emission.
- Thermomechanical processing degrades fracture toughness due to the reduced oxide sheet spacing and/or dynamic recovery and reduced work hardening.

References

1. NASA-UVa Light Aerospace Alloy and Structures Technology Program Supplement: Aluminum-Based Materials for High Speed Aircraft, A Semi-Annual Progress Report, July to January (1993).
2. W.C. Porr, Jr., "Elevated Temperature Fracture of Advanced Powder Metallurgy Aluminum Alloy 8009", PhD dissertation, University of Virginia, Charlottesville, VA (1992).
3. K.S. Chan, "Evidence of a Thin Sheet Toughening Mechanism in Al-Fe-X Alloy", Metall. Trans. A 20A, 1989, pp. 155-164.

4. W.C. Porr, Jr., Y. Leng and R.P. Gangloff, "Elevated Temperature Fracture Toughness of P/M Al-Fe-U-S", in Low Density High Temperature P/M Alloys, W.E. Frazier, M.J. Koczak and P.W. Lee, Eds., TMS-AIME, Warrendale, PA, 1991, pp. 129-155.
5. C.D.S. Tuck, "The Embrittlement of Al-Zn-Mg and Al-Mg Alloys by Water Vapor", Metall. Trans. A 16A, 1985, pp. 1503-1514.
6. Y.-W. Kim, "Effect of Non-Uniform Microstructure and Hydrogen in High Temperature PM Aluminum Alloy Al-8.4Fe-7.2Ce", Progress in Powder Metallurgy 43, 1987, pp. 13-31.
7. E. Bouchard, L. Kubin, and H. Octor, "Ductility and Dynamic Strain Aging in Rapidly Solidified Aluminum Alloys", Metall. Trans. A 22A, 1991, pp. 1021-1028.
8. D.J. Skinner, M.S. Zedalis, and P. Gilman, "Effect of Strain Rate on Tensile Ductility for a Series of Dispersion-Strengthened Aluminum-Based Alloys", Mat. Sci. And Eng. A119, 1989, pp. 81-86.
9. W.C. Porr, Jr., A.P. Reynolds, Y. Leng, and R.P. Gangloff, "Elevated Temperature Cracking of RSP Aluminum-Alloy 8009-Characterization of the Environmental Influence", Scripta Metall. Mater. 25, 1991, pp. 2627-2632.
10. S.W. Smith and J.R. Scully, "Hydrogen Trapping and Its Correlation to the Hydrogen Embrittlement Susceptibility of Al-Li-Cu-Zr Alloys", in Hydrogen Effects on Material Behavior, N.R. Moody and A.W. Thompson, eds., TMS-AIME, Warrendale, PA, in press (1995).
11. S. Mitra, "Elevated Temperature Mechanical Properties of a Rapidly Solidified Al-Fe-V-Si Alloy", Scripta Metall. Mater. 27, 1992, pp. 521-526.
12. P.F. Thomason, "The Mechanics of Microvoid Nucleation and Growth in Ductile Metals", in Ductile Fracture of Metals, Pergamon Press, Oxford, England, 1990, pp. 30-55.
13. P.F. Thomason, "The General Effects of Fluid Hydrostatic Pressure, Temperature and Strain-Rate on the Mechanics of Ductile Fracture and the Conditions for Spontaneous Nucleation and Coalescence of Microvoids", in Ductile Fracture of Metals, Pergamon Press, Oxford, England, 1990, pp. 94-114.

14. G.R. Edwards, T.R. McNelley, and O.D. Sherby, "Diffusion-Controlled Deformation of Particulate Composites", Phil. Mag. 32 (6), 1975, pp. 1245-1264.
15. H. Westengen, "Plastic Instability During Tensile Deformation of a Fine Grained Al--2 wt% Fe--0.8 wt% Mn Alloy", in Microstructural Control in Aluminum Alloys: Deformation, Recovery and Recrystallization, eds. E.A. Chia and H.J. McQueen, TMS-AIME, Warrendale, PA, 1986, pp. 109-122.
16. H. Westengen, "Tensile Deformation of a Fine-Grained Al-alloy", in Strength of Metals and Alloys, ed. R.C. Gifkins, ICMA 6, Melbourne, Australia, 1982, pp. 461-466.
17. D.J. Lloyd, "Deformation of Fine-Grained Aluminum Alloys", Metal Science, May, 1980, pp. 193- 198.
18. D.J. Lloyd and L.R. Morris, "Luders Band Deformation in a Fine Grained Aluminum Alloy", Acta Metall. 25, 1977, pp. 857-861.
19. F.J. Humphreys and P.N. Kalu, "Dislocation-Particulate Interactions During High Temperature Deformation of Two-Phase Aluminum Alloys", Acta Metall. 35, 1987, pp. 2815-2829.
20. J.H. Schröder and E. Arzt, "Weak Beam Studies of Dislocation/Dispersoid Interaction in an ODS Superalloy", Scripta Metall. 19, 1985, pp. 1129-1134.
21. V.C. Nardone and J.K. Tien, "Pinning of Dislocations on the Departure Side of Strengthening Dispersoids", Scripta Metall. 17, 1983, pp. 467-470.
22. R. Lagneborg, "Bypassing of Dislocations Past Particles by a Climb Mechanism", Scripta Metall. 7, 1973, pp. 605-613.
23. Y. Leng, W.C. Porr, Jr., and R.P. Gangloff, "Time Dependent Crack Growth in P/M Al-Fe-V-Si at Elevated Temperatures", Scripta Metall. Mater. 25, 1991, pp. 895-900.
24. E. Arzt and J. Rösler, "High Temperature Deformation of Dispersion Strengthened Aluminum Alloys", in Dispersion Strengthened Aluminum Alloys, eds. Y-W. Kim and W.M. Griffith, TMS-AIME, Warrendale, PA, 1988, pp. 31-55.
25. M.E. Fine and E.A. Starke, Jr., eds., Rapidly Solidified Powder Aluminum Alloys, ASTM STP 890, ASTM, Philadelphia, PA, 1986.

26. Y. Leng, W.C. Porr, Jr., and R.P. Gangloff, "Tensile Deformation of 2618 and Al-Fe-Si-V Aluminum Alloys at Elevated Temperatures", Scripta Metall. Mater. 24, 1990, pp. 2163-2168.
27. H.G.F. Wilsdorf and D. Kuhlmann-Wilsdorf, "Worksoftening and Hall-Petch Hardening in Extruded MA Alloys", in Risø International Symposium on Materials Science: Modelling of Plastic Deformation and Its Engineering Applications, S.I. Anersen, J.B. Bilde-Sørensen, N. Hansen, D. Juul Jensen, T. Leffers, H. Lilholt, T. Lorentzen, O.B. Pedersen, and B. Ralph Eds., Risø National Laboratory, Roskilde, Denmark, 1992, pp. 511-517.
28. D. Kuhlmann-Wilsdorf and H.G.F. Wilsdorf, "The Theory of Worksoftening in High-Performance Alloys", in Phys. Stat. Sol. 172(b), 1992, pp. 235-248.
29. M.A. Rowley, "Characterization of the Viscoplastic Response of High Temperature Alloys", MS Thesis, University of Virginia, Charlottesville, VA, 1993.

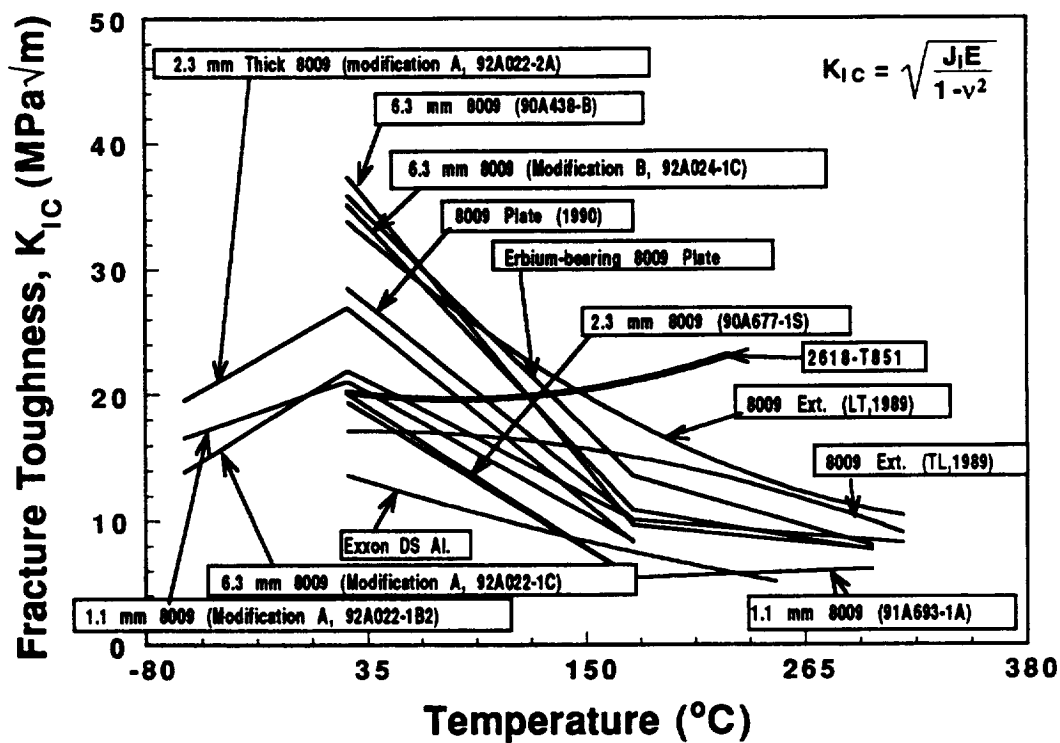
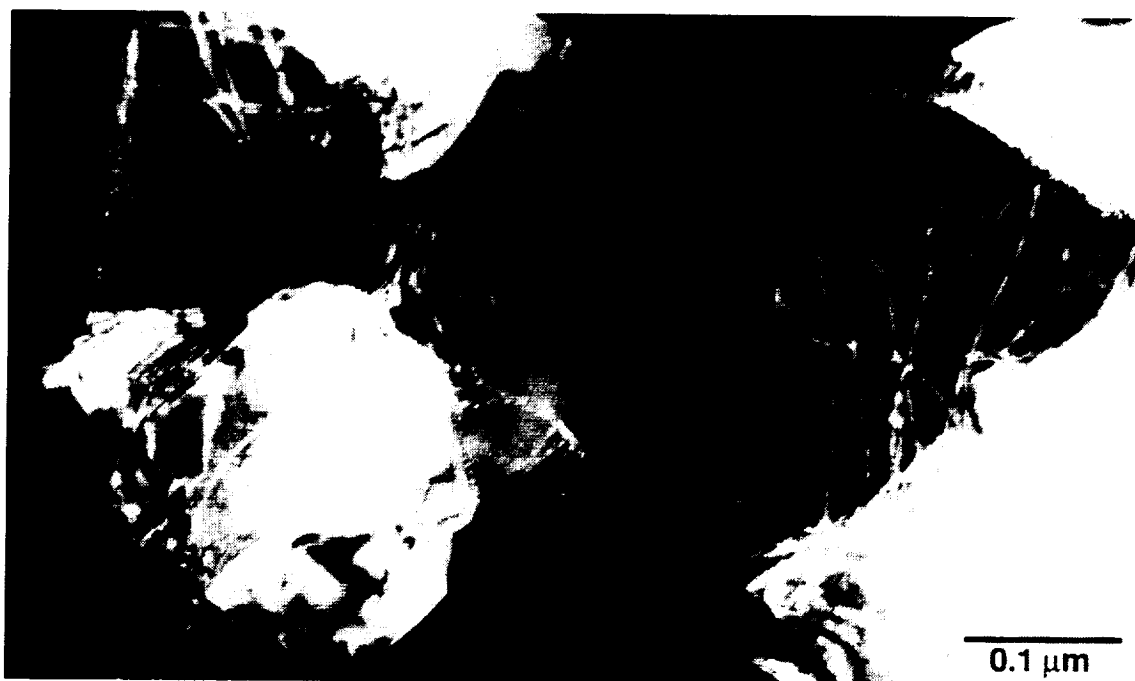


Figure 1. Initiation fracture toughness of various product forms of 8009 as a function of temperature at a constant displacement rate of 2.5×10^{-3} mm/sec. Fracture toughness experiments were restricted to -60, 25, 175 and 300°C. The trend lines are simply fit to these discrete results.



(a)



(b)

Figure 2. TEM micrographs of tensile deformed 6.3 mm thick 8009 plate at (a) 25°C and (b) 200°C.

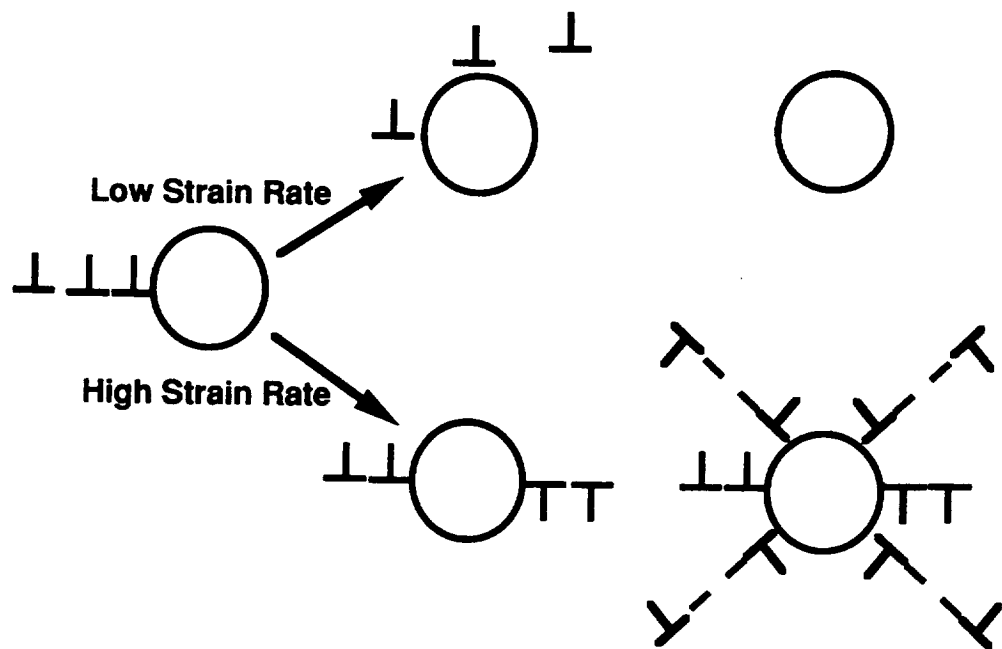


Figure 3. Schematic illustration of the change in dislocation-particle interaction for different strain rates; after Humphrey and Kalu [19].

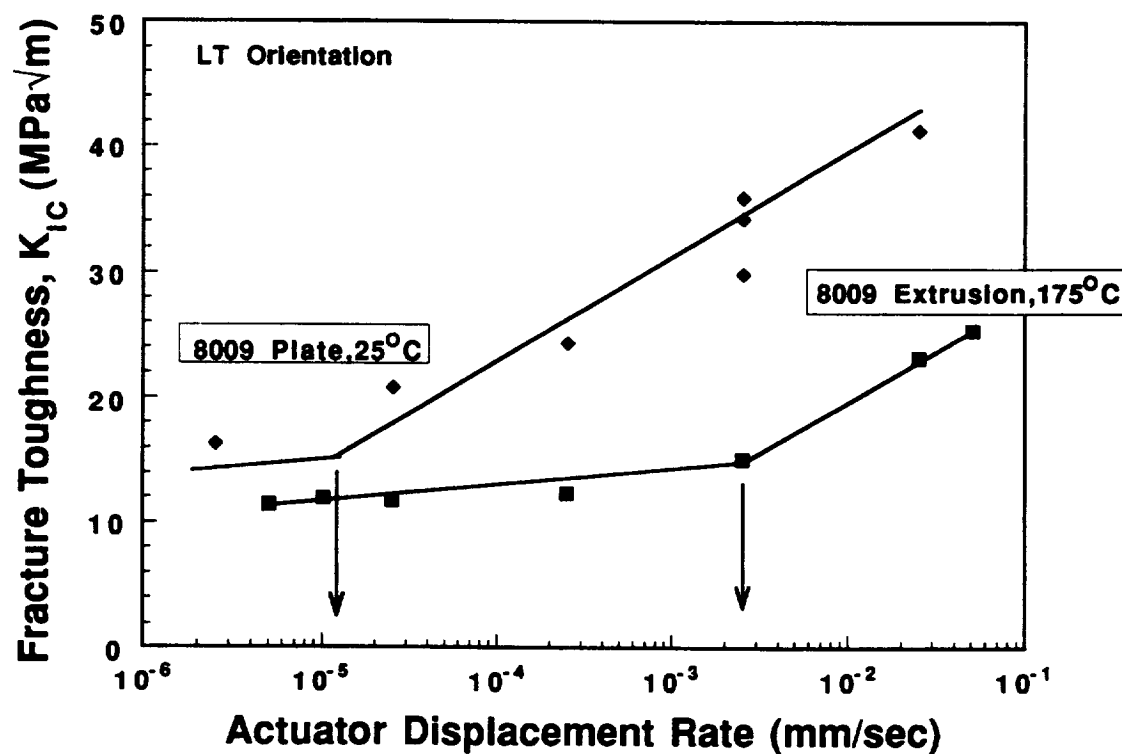


Figure 4. Effect of actuator displacement rate on the initiation fracture toughness of 8009 plate at 25°C and extrusion at 175°C.

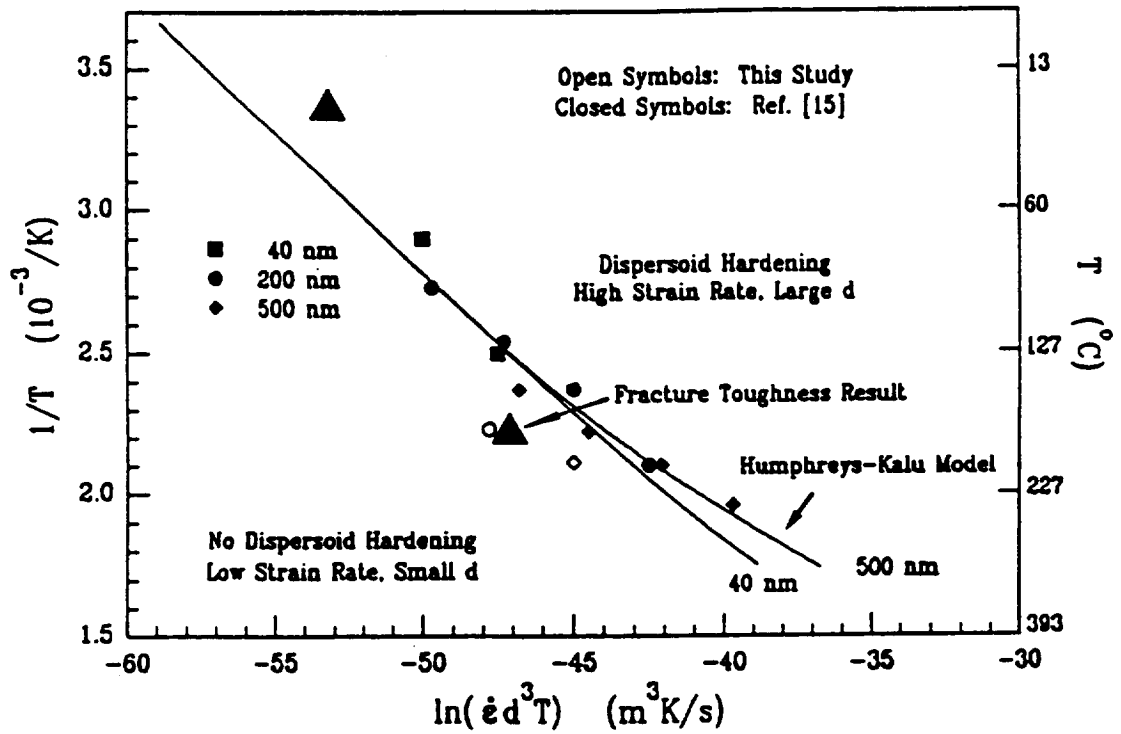


Figure 5. Theoretical transition for climb assisted dispersoid bypassing of dislocation as a function of particle size, temperature, and strain rate, as predicted by the HK model.



(a)



(b)

Figure 6. Macroscopic side profiles of 2.3 mm thick Preprogram 8009 sheet fractured: (a) 25°C and (b) 175°C, at a nominal strain rate of 5×10^{-4} /sec.

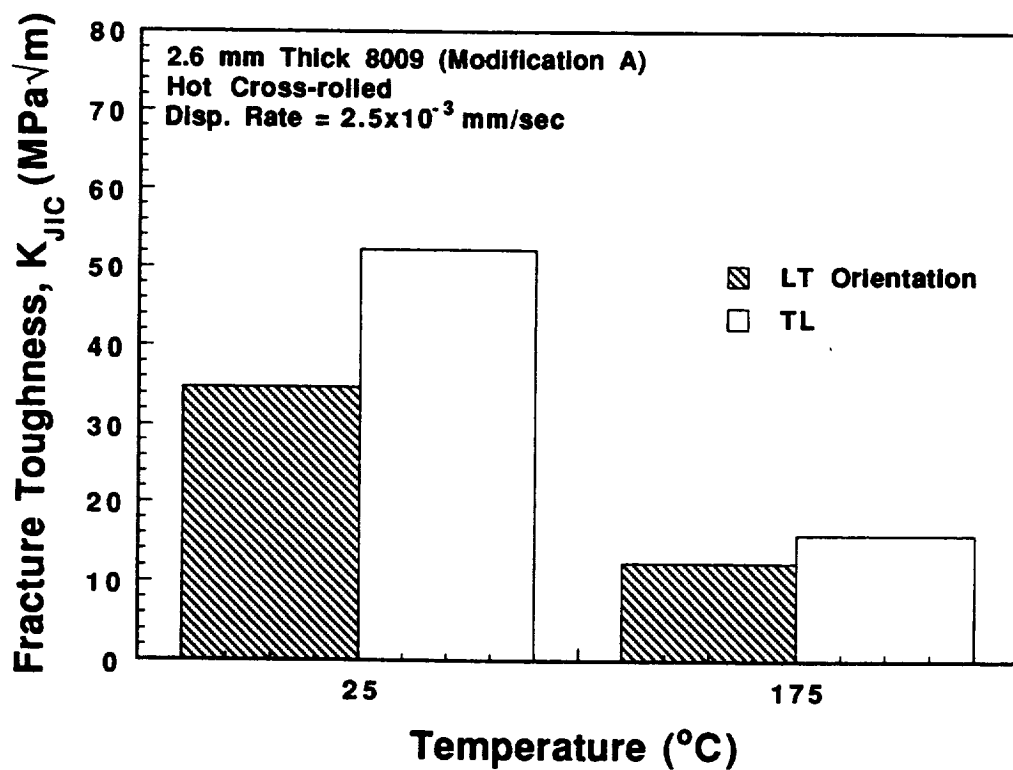


Figure 7. Effect of orientation on the fracture toughness of 2.6 mm thick Modification A 8009 sheet (Data obtained by FTA).

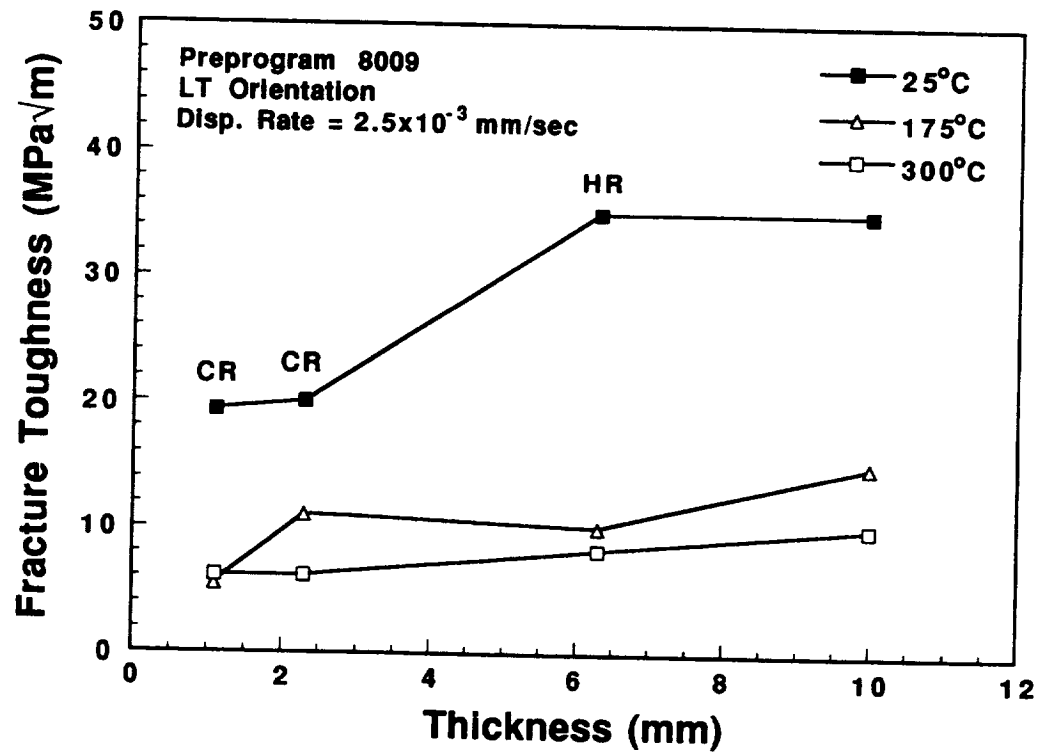
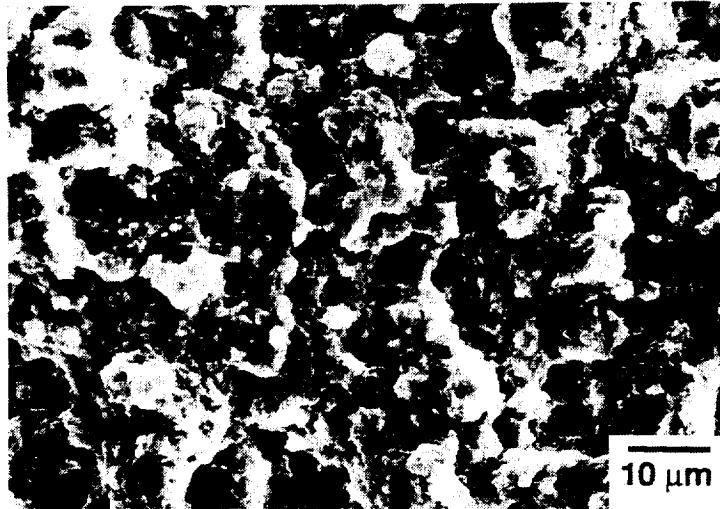


Figure 8. Effect of thermomechanical processing on the fracture toughness of Preprogram Vintage 8009. HR is hot rolled plate and CR is cold rolled sheet 8009.



(a)



(b)

Figure 9. SEM fractographs of Preprogram 8009 with gauge thickness of: (a) 6.3 mm and (b) 2.3 mm, tested at 25° C and 2.5×10^{-3} mm/sec.

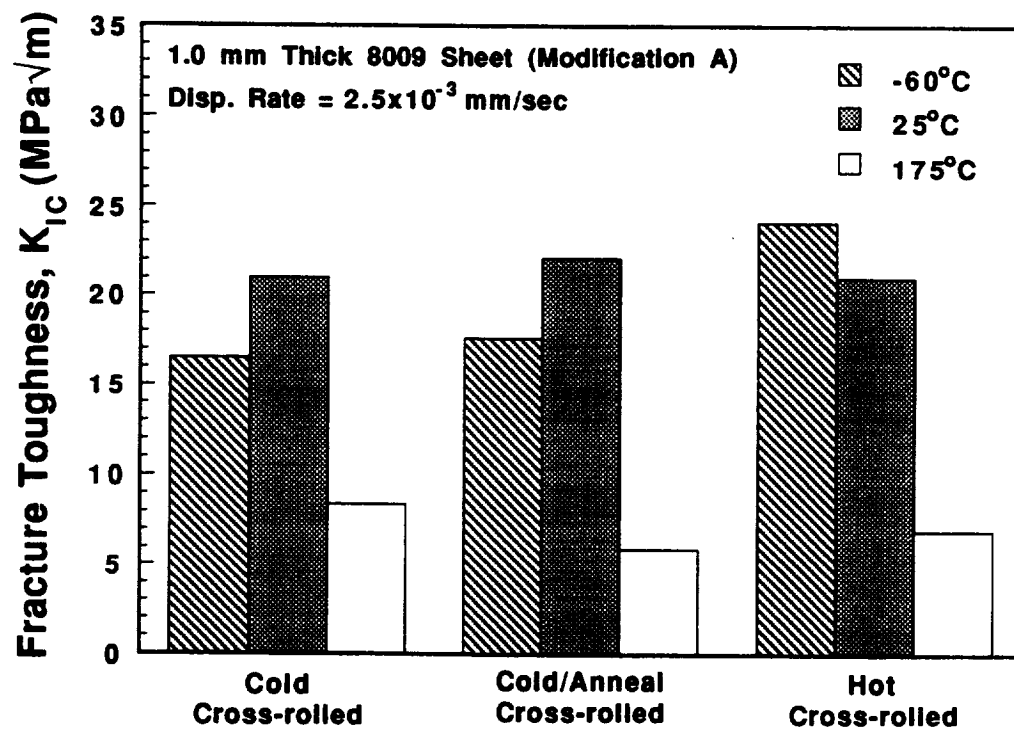


Figure 10. Effect of rolling temperature and annealing on fracture toughness of 1.0 mm thick Modification A 8009.

**TASK 8. INVESTIGATION OF THE FORMATION OF THE Ω PHASE IN
MODIFIED 2009 AND CHARACTERIZATION OF THE
MODIFIED ALLOYS' THERMOMECHANICAL PROPERTIES
(UVA)**

Principal Investigator: Prof. Frank Wawner
Graduate Student: Qiong Li

Introduction

Work reported in the second semi-annual report (UVA report under Grant No. NAG-1-745, for the period 7/1/92-12/31/92) demonstrated that the Ω phase and σ phase coarsening behavior was slower than Θ' phase. Characterization was continued on the alloys' microstructure, heat treatment response, thermal stability, and mechanical properties. The present report presents results obtained during the period 1/1/93-6/30/93.

Objective and Technical Approach

The objective of this investigation is to modify 2009 (a product of Advanced Composite Materials Corporation) with Ag to enhance the formation of the Ω phase in the SiC particulate reinforced Al-Cu-Mg matrix composite in order to increase the composite's elevated temperature stability.

The technical approach initially being taken is to fabricate potential matrix alloys at UVA to determine optimum Cu/Mg ratio and optimum amount of Ag in order to generate a maximum volume fraction of the semi-coherent Ω phase. Initial composite samples will be produced by compocasting at UVA, incorporating SiC into the alloy composition determined to be best. Microstructural studies of these composites will be made to ascertain if the Ω phase is retained after introduction of the ceramic particles. If it is not, other iterations of matrix composition will be made to

achieve maximum Ω in the composite. After establishing the optimum composition, APMC will produce a P/M sample for evaluation at UVA of the material's thermomechanical properties and stability.

Experimental Procedure

Since the objective of this study is to modify 2009 (an Al-Cu-Mg/SiC particulate material), it is necessary to evaluate composite samples to determine if the introduction of ceramic particles alters the type of phases that precipitate in the matrix. To expedite determination of the Ω phase in matrix of the composite, composite samples are being produced at UVA by powder metallurgy technique. An aluminum powder (a 2519 variant) was provided by Dr. Lynne Angers of Alcoa. The Al powder (composition Al-5.72Cu-0.54Mg-0.51Ag-0.31Mn-0.1V-0.57Zr) was mixed with SiC particles and mounted in a cylindrical mold, then hot pressed at 540°C, 70 MPa. Examining this hot pressed sample showed that there is uniform particle distribution in the composite. The composite sample was solutionized, water quenched and aged at 200°C. The aged composite sample was examined in the TEM to identify phases in the matrix of the composite.

A bulk intermetallic compound, σ phase ($\text{Al}_5\text{Cu}_6\text{Mg}_2$), was produced for determination of its elastic properties. The crucible containing the metallic charge was placed in a glove box for producing the intermetallic compound in an Ar atmosphere. The resulting intermetallic compound ($\text{Al}_5\text{Cu}_6\text{Mg}_2$) was annealed for homogenization in an Ar atmosphere at 620°C for 211 hours, followed by furnace cooling. An A11M alloy sample was deformed in a tensile test and then prepared for TEM to study dislocation interaction with Ω precipitates.

Results and Discussion

I. Composite

A composite was successfully made by P/M technique. The Al powder was supplied by Alcoa with composition Al-5.72Cu-0.54Mg-0.51Ag-0.31Mn-0.1V-0.57Zr; the SiC particles were from HSC. The particle size mean value was 17 μm . TEM investigations showed encouraging results. The Ω phase was observed in the matrix of the Al/SiC composite. The TEM micrograph in Fig. 1 shows the Ω phase in the matrix along $\langle 011 \rangle_{\text{Al}}$ zone axis. The diffraction pattern shows the streaks along $\langle 111 \rangle_{\text{Al}}$ and the Ω phase reflections. Other phases also appear in the micrograph (s' phase). Near the $\langle 001 \rangle$ zone axis, some Θ' and s' can be seen in Fig. 2. Figure 3 depicts the Ω phase and s' phase in the matrix and a SiC particle with interfacial precipitates. Since there are elements like Mn, Zr, V in the matrix, constituent particles also formed. Figure 4 shows a Al-Cu-Zr particle in the matrix. Some interfacial precipitation and PFZ can be seen around interface. The intermetallic inclusion could coarsen after hot rolling and eventually will act as a crack initiation site [1]. Because these constituent particles are not stable during the processing, the matrix proposed for APMC composite fabrication will not include the constituent forming elements. The SiC particles will act as a grain finer and strengthening agent. Absence of the constituent particles should improve fracture toughness. Some other features observed are shown in Fig. 5. Here some fine grains formed in a band and no precipitates were observed in these grains/subgrains. This may result from a lack of extrusion. Based on these results, the matrix composition submitted to APMC for composite fabrication will be the Al1M (Al-3.2Cu-0.45Mg-0.4Ag) alloy. The composites to be fabricated will contain 15 volume percent SiC particles with size of 4 micron. It is anticipated that some of the material will be available for evaluation within 60 days.

II. Coarsening

a) Coarsening behavior of Ω and σ phase.

The relationship of the maximum size of the σ phase versus exposure time at 200°C is plotted in Fig. 6, which demonstrates a slow coarsening rate. The coarsening behavior follows a power law, $r \propto t^{1/5.6}$, compared with $t^{1/3}$ for Lifshitz-Slyozov-Wagner (LSW) theory prediction. For the Ω phase, Fig. 7, the maximum precipitate size versus exposure time at 200°C shows a different trend from the σ phase. The coarsening behavior of Ω phase indicates that it grows at a rapid rate up to 100 hours then the length of the Ω plates begins to shrink. This is because the matrix is no longer in a supersaturation condition which keeps the Ω phase with a very high aspect ratio. After 100 hours self coarsening occurs which causes the Ω phase to thicken in width and shorten in length. Compared to the σ phase, the Ω phase coarsening behavior is more likely following a log law rather than a power law. The log law gives a slower growth rate than the power law, but at 200°C the self coarsening eventually will occur and the length of Ω plates will shrink. At lower temperature the self coarsening is delayed, for example, at 140°C, the length of the Ω phase continues to rise slowly after more than 100 hours [2].

b) Comparison of Ω and σ precipitate size distribution with LSW theory.

A statistical analysis of size distribution, Fig. 8, shows the size distribution of the σ phase and comparison with LSW coarsening theory prediction. The solid line in each figure represents the "quasi-steady-state" distribution predicted by the LSW theory of Ostwald ripening and given by the function $f(r,t)=g(t)p^2h(p)$ [3], where $g(t)$ is a function of time only, $p =$

r/r , and $h(\rho)$ is given by:

$$h(\rho) = [3/(\rho+3)]^{7/3} [(-3/2)/(\rho-3/2)]^{11/3} \exp[\rho/(\rho-3/2)] \quad \text{when } \rho < 3/2;$$

$$h(\rho) = 0 \quad \text{when } \rho > 3/2$$

Of the distributions shown, none of them obeys the LSW distribution which predicts a rapid drop-off in number of particles at sizes greater than the most probable size. The distribution shows that the sizes of the σ phase are uniform and the most probable size is smaller than the LSW theory prediction. The distribution after 26.2 hours at 200°C shows a skew to smaller sizes. The distribution after 100 hours at 200°C shows a skew to larger sizes. The distribution after 405 hours at 200°C shows even greater skewing to larger sizes. The graph shows that the LSW theory prediction envelopes the distribution of the σ phase which means a narrow distribution. It should be noted that LSW theory is for spherical particle coarsening. The small size, narrow size distribution and very low coarsening rate of the σ phase could promote the thermal stability and the mechanical properties of the alloy at elevated temperatures. Figure 9 shows the size distributions of the Ω phase. Of the distribution shown, none of them obeys the LSW distribution which predicts a rapid drop-off in number of particles at sizes greater than the most probable size. The distributions are asymmetrical with longer tails at larger diameters and a maximum particle size equal to twice the average value. The distribution 26.2 hours at 200°C shows a skew to the right which is quite different from the distribution of the σ phase. This implies that the Ω phase has a faster growth rate than the σ phase. The other two distributions show the same skew. The Ω size distributions are well spread through the p axis. The LSW

prediction does not envelope the distributions as it did with the σ phase. Considering truncation in the foil, the overall error is about 10% and the histogram of the smaller sizes will shift to the left side. If we consider 10% error, the size distribution of the Ω phase would be even wider.

III. Fabrication of the σ Phase and Determination of Some of its Mechanical Properties.

The property data on the σ phase is essential for estimating interfacial energy and strengthening effect. Therefore, an experiment was designed to measure G , E , ν and σ_y of the σ phase.

In order to obtain property data on the σ phase a sample was prepared as described in the experimental section and characterized. Results from x-ray diffraction experiments, shown in Fig. 10, confirmed that the intermetallic compound formed is $\text{Al}_5\text{Cu}_6\text{Mg}_2$ and with a small amount of Al_4Cu_9 .

The ultrasonic technique was used to determine shear modulus (G) and Poissons' ratio (ν). These values were then used to calculate Young's modulus (E). The values for these material constants are given below.

$$V_L = 6.216 \text{ mm}/\mu\text{sec.} \quad V_T = 3.270 \text{ mm}/\mu\text{sec} \quad \rho = 4.90 \text{ g/cm}^3$$

$$V_T = \sqrt{G/\rho} \quad G/\rho = V_T^2 = 10.693 \text{ mm}^2/\mu\text{s}^2$$

$$G = 52.41 \text{ GPa}$$

$$E = 2G(1 + \nu) \quad [2(1 - \nu) / (1 - 2\nu)]^{1/2} = V_L / V_T = 1.901$$

$$\nu = 0.308$$

$$E = 2G(1 + \nu) = 137.1 \text{ GPa} \quad E = E_0 / e^{-pb}, \quad \rho = 0.05 \text{ (porosity fraction)}$$

$$b = 3 \text{ (empirical constant)}$$

$$E_0 = 159.3 \text{ GPa}$$

$$G_0 = 60.89 \text{ GPa}$$

Table 1 gives the data for Young's modulus and shear modulus of the σ phase with porosity and without porosity.

Table 1

5% porosity	Fully dense	5% porosity	Fully dense
<u>E (GPa)</u>	<u>E_o (GPa)</u>	<u>G (GPa)</u>	<u>G_o (GPa)</u>
137.1	159.3	52.41	60.89

Hardness tests were made on the σ ingot at ambient and elevated temperature. The data, plotted in Fig. 11, shows a high value for the room temperature (Vickers hardness=546 Kg/mm²) and that 70% of this value was retained at 350°C. Because this intermetallic compound is extremely brittle, there is no work hardening, hence the yield strength can be calculated as one third of the Vickers hardness ($\sigma_y = H_v/3$). This gives a high yield strength for the σ phase, $\sigma_y = 1784$ MPa. This implies that the precipitates should be very resistant to being cut by dislocations, hence possible strengthening by the Orowan mechanism.

IV. Interfacial Energy Calculation for Ω and σ

Using literature data and data determined in the present study, it is possible to estimate interfacial energy for the Ω and precipitates for comparison with other phases. Rationale and calculations for the two phase are presented below.

a) Ω phase

Alloy Cu-3.2%, Mg-0.4%, Ag-0.4% (wt%). Consider the Ω phase as a Θ phase, both have the same composition (Al₂Cu).

Use Zener-Hillert equation [4]: (where Al= α , Cu= β)

$$r = \frac{2\gamma V^\alpha (1 - x_\beta^{\alpha\beta})}{RT (x_\alpha^{\alpha\beta} - x_\beta^{\beta\alpha}) \ln \left(\frac{x_\beta}{x_\beta^{\beta\alpha}} \right)}$$

$$\gamma = \frac{rRT (x_\alpha^{\beta\alpha} - x_\beta^{\beta\alpha}) \ln \left(\frac{x_\beta}{x_\beta^{\alpha\beta}} \right)}{2V^\alpha (1 - x_\beta^{\alpha\beta})}$$

From Al-Cu phase diagram one can find the data

$$x_\beta = 1.39 \text{ (atm.\%)} \quad x_\beta^{\beta\alpha} = 0.07 \text{ (atm.\%)} \quad x_\alpha^{\alpha\beta} = 32.6 \text{ (atm.\%)}$$

$$r = 1.5 \times 10^{-9} \text{ m} \quad V^\alpha = 10^{-5} \text{ m}^3/\text{mol} \quad T = 200^\circ\text{C}$$

r measured from HRTEM micrograph which is taken from Al1M aged at 200°C for 3 hours, the aspect ratio (l/r) is 60; T is aging temperature.

$\gamma_1 = 0.287 \text{ J/m}^2 = 287 \text{ erg/cm}^2$ (plate end interfacial energy): the coarsening direction

$\gamma_2 = 0.287/60 = 4.8 \times 10^{-3} \text{ J/m}^2 = 4.8 \text{ erg/cm}^2$ (plate side interfacial energy)

It is worth noting that the interfacial energy values γ_1 and γ_2 are calculated in the supersaturated condition. This condition will extend for a longer period at 150°C which corresponds to the temperature at Mach 2 speed. At equilibrium condition, for samples aged at 200°C for 405 hours, the aspect ratio l/r becomes smaller and the interfacial energy value would be higher for γ_1 and γ_2 .

b) σ phase

In general the interfacial energy γ between two solid phases can be split into two parts:

$$\gamma = \gamma_{\text{geom}} + \gamma_{\text{chem.}}$$

Since the chemical term in interfacial energy is fairly small and negative in Cu-Al [6], the chemical term can be neglected here. The model used to estimate the interfacial energy of σ phase is based on the approximation of $\gamma = \gamma_{\text{geom}}$. The interfacial energy, γ , is calculated considering only the contribution of misfit dislocations. Chemical interaction is neglected. If the chemical term is considered, the value of interfacial energy estimated below would be lower.

A simple array dislocation model which is used for estimating low angle grain boundaries is applied here.

$\gamma = E_0 \delta (A' - \ln \delta)$, where

$$\delta = 2(a_1 - a_2) / (a_1 + a_2) = 0.0257 \quad E_0 = Gb / 4\pi(1 - \nu), \quad A' = \ln(\alpha b / r_0)$$

$$G = 2G_\sigma G_{\text{Al}} / (G_\sigma + G_{\text{Al}}) = 35 \text{ GPa}, \quad G_\sigma = 60.89 \text{ GPa}, \quad G_{\text{Al}} = 25 \text{ GPa},$$

$$b = 2 \times 10^{-10} \text{ m}, \quad \alpha = 1, \quad r_0 = 4 \times 10^{-10} \text{ m}$$

$$\gamma = \underline{0.064 \text{ J/m}^2}$$

Using the misfit dislocation model (Van de Merwe model) [5], one can also calculate interfacial energy. Since there is a small misfit between the σ phase and the matrix of 2.57% or in literature 2.8% [7], the misfit dislocations can build up a periodic strain near the interface region. Figure 12 shows that the periodic lobes caused by misfit dislocations create strain in the matrix near interface. The misfit dislocations spacing, p , is

about 7.0 nm; here the period of the strain lobes is considered as misfit dislocation spacing.

$$\gamma = \frac{GC}{4\pi^2} (1 + \beta - (1 + \beta^2)^{1/2} - \beta \ln [2\beta (1 + \beta^2)^{1/2} - 2\beta^2])$$

where: $v_{\sigma} = 0.308$, $v_{Al} = 0.33$,

$$C = \frac{(a_1 + a_2)}{2}, \quad p = \frac{2(a_1 + a_2)}{a_1 - a_2},$$

$$\beta = \frac{2\pi G_{\sigma} b}{p [(1-v_{\sigma}) + (1-v_{Al}) \frac{G_{\sigma}}{G_{Al}}] G.}$$

Table 2

<u>$\gamma(\text{J/m}^2)$</u>	<u>β</u>	<u>$p(\text{\AA})$</u>
0.0586	0.133	70 measured in Al1M
0.0539	0.116	80 computed by simple equation
0.0462	0.091	102 computed by misfit dislocation model [7]
0.0415	0.078	120 measured in composite [7]

Considering the error of measurement, $p=80\text{\AA}$ was picked to calculate the interfacial energy γ . Finally, γ_{σ} is determined as 0.054J/m².

c) Comparison of Interfacial Energy of Some Precipitates

Table 3

	<u>σ/Al</u>	<u>Ω/Al</u>	<u>δ'/Al</u>	<u>$\Theta'(\text{Cd})$</u>	<u>Θ'/Al</u>	<u>Θ''/Al</u>	<u>γ'/Ni</u>
$\gamma(\text{J/m}^2)$	0.054	0.287	0.014 [8]	0.25 [9]	1.53[9]	0.53 [9]	0.014 [10]
shape	cubic	plate	sphere	plate	plate	plate	cubic

In Al alloy precipitates with a low value of interfacial energy have a spherical shape, such as δ' ; those with high value interfacial energy have a plate shape, such as Θ' , with intermediate value of interfacial energy. The precipitates have a cubic shape, such as σ . The Ω phase has a interfacial energy value very close to Θ' phase in Al-4%Cu alloy with Cd addition which reduces the interfacial energy of Θ' and hence it's coarsening rate [9]. The σ phase has an interfacial energy and misfit value between Θ' and δ' phases, and it has a cubic shape as Starke [11] predicted. Both δ' and Θ' phases are non-equilibrium and less thermally stable than an equilibrium phase. At elevated temperature the δ' and Θ' phases will eventually transform to the equilibrium phase. The Ω and σ phases are equilibrium phases and can be found in the phase diagram and can be made by simply adding each element and melting together. Comparing the σ phase in aluminum to the $\gamma'(\text{Ni}_3\text{Al})$ phase in the Ni-base superalloys, they both are cubic phases and have a coherent-coplanar relationship with their matrix. They have close values of interfacial energy 0.054 J/m² for the σ phase and 0.014 J/m² for the γ' phase. Hence, they both possess low coarsening rates, and they both are stable at elevated temperatures. The $\gamma'(\text{Ni}_3\text{Al})$ phase gives effective

strengthening in the Ni-base superalloys. Therefore the σ phase could be an effective precipitate in aluminum alloys at elevated temperature. The σ phase is a unique phase in aluminum alloys; it is an equilibrium phase, coherent and coplanar with matrix, cubic shaped phase, with low interfacial energy, and very low coarsening rate. The comparison of the interfacial energies in Table 3 indicates that the estimate of the value of the interfacial energies for Ω/Al and σ/Al is very reasonable.

d) Comparison of Properties of the Ω and σ Phases

Table 4

	G (GPa)	E (GPa)	H _v (Kg/mm ²)	ν	σ_y (MPa)	P (g/cc)	δ (%)	γ (J/m ²)	T _m (°C)	shape
Ω	35*	105[12]	400[13]	0.33*	1306†	4.34	8.3[14]	0.287	591[15]	plate
σ	61	160	546	0.308	1784†	4.90	2.57	0.054	710[15]	cubic

* estimated data. † estimated from hardness data.

V. Effect of Deformation on Ω Phase Formation

A spray formed Al alloy sample N202 (Al-6.23Cu-0.36Mg-0.4Ag-1.84Mn-0.31Zr-0.27V-0.19Ti) stretched (2%) from Lockheed Corp. was aged and analyzed in the TEM. The deformed alloy can be considered as a simulation of the matrix of a composite in which dislocations are created due to the CTE difference during the fabrication process. Because the Θ' and s' phases have a larger misfit than the Ω phase, the Θ' and s' phases energetically favor formation on dislocations for reducing system energy. Therefore, a pre-ageing stretch will promote more Θ' and s' phases and reduce Ω phase formation. Figure 13 shows the high density of dislocations

in the alloy which was stretched 2% before aging. The stretched sample then was aged at 177°C for 12 hours (T82). The TEM micrograph, Fig. 14a, displays the S' and Ω phases in the alloy along the $\langle 011 \rangle_{Al}$. Along $\langle 001 \rangle_{Al}$ direction, the Θ' and S' phases can be seen in Fig. 14b. The SAD pattern in upper left corner shows reflections of all three phases. The strong Θ' and S' reflections imply a high density of these phases exist in the alloy. After solutionizing the stretched sample at 525°C, 12 hours, then aging at 200°C for 4 hours, the amount of Θ' , S' phases in the alloy was reduced and the amount of Ω phase increased. Figure 15 shows the relatively high density of the Ω phase in the alloy aged after dislocations were annealed out. Figure 16 demonstrates the changes of the density of the Θ' and s' phases in $\langle 011 \rangle_{Al}$ SAD pattern as the solutionization time increases. Figure 16a represents the SAD pattern of the alloy aged at 177°C for 12 hours after stretching the alloy. Figure 16b shows the SAD pattern of the alloy aged at 177°C for 12 hours after the alloy was solutionized at 525°C for 2.5 hours which annealed some dislocations out of the alloy. Figure 16c shows the SAD pattern of the alloy aged at 200°C for 4 hours after the alloy was solutionized at 525°C for 12 hours which annealed out most dislocations caused by deformation. The SAD patterns demonstrate the decrease in the amount of the Θ' and S' phases as solutionization time increases or the density of dislocations caused by deformation decreases. A conclusion can be drawn from these observations: in order to obtain the maximum amount of Ω phase, deformation such as a pre-aging stretch should be avoided.

VI. Deformation and Strengthening

Plate-like precipitates are usually observed when the misfit strain in the habit plane is relatively high, while spherical

precipitates are generally observed when it is low. High-strength Al alloys are frequently hardened by plate-like precipitates. The increase in strength is partially due to the misfit strain and its localization at the perimeter of the plate, but it can also be shown that increased strengthening should be observed on a geometric basis. Since strengthening in a thermal glide is determined entirely by the maximum in the force-distance relation for the precipitate-dislocation interaction, plates strengthen much more efficiently. They provide more obstacles and intersect more glide planes, since the width of the plate face is larger than the diameter of a sphere of equivalent volume. The misfit strain around the plate could be included in the strengthening model by considering the increase in effective size. A TEM investigation was designed to demonstrate the interaction of dislocation and plate-like precipitates (Ω phase), hence the strengthening mechanism.

A TEM sample was taken from a tensile sample near the fracture surface. TEM observations demonstrate a shearing mechanism which involved dislocation-precipitate interaction. Figure 17 shows WBDF image of the dislocations in the deformed alloy (Al1M T6 after tensile testing). Some bent dislocations can be seen near the Ω phase and very strong strain contrast. Figure 18 shows that some straight lines run through the Ω phase, some wavy lines in the Ω phase and some evidence of cutting. For a closer look at the lines in the Ω phase, the sample was tilted to near $\langle 001 \rangle$ direction and using an Ω reflection to display the image. Figure 19a depicts the antiphase boundaries in the Ω phase which implies dislocations cut through the Ω phase and created a large number of antiphase boundaries. The distance between the APB is in range 2 ~ 4 nm which is much denser than for coherent phases in literature. Figure 19b depicts low density APBs form in the Ω phase due to coarsening in Al1MM alloy. The high density of APB and new surfaces created by shearing may give a significant contribution to strengthening of the alloy. An edge on view in

Fig. 20 shows the wavy shape in the Ω phase and steps created by dislocation shearing. Figure 21 schematically illustrates this. Finally, a high resolution TEM study confirmed the dislocation shearing mechanism. Figure 22 is a high resolution TEM micrograph, which shows a lattice image of the shearing. Figure 23 is a higher magnification of the dislocation shearing the Ω phase. From Figs. 22 and 23 the anti-phase boundary caused by shearing can be seen. It is worth noting that since Ω/Al interphase is not fully coherent, the APB in the Ω phase is not the same as in a completely coherent particle. Dislocation shearing creates a fault which combines antiphase boundary and dislocations. It is expected that chemical strengthening due to the increase in Al/Ω interfacial area during cutting, order effects which give rise to antiphase boundaries upon cutting, and coherency strains induced by the lattice parameter differences between Ω and matrix could contribute to the strengthening effects of Ω plates.

Conclusions

- A composite with the Ω phase in the matrix was fabricated successfully. A nonuniform Ω phase distribution was found in the matrix.
- In order to promote more Ω phase in the alloy, deformation must be minimized.
- A very slow coarsening rate of the σ phase was found at 200°C, which implies Al alloys strengthened by the σ precipitate phase could have superior thermal stability at elevated temperature.
- The σ phase has narrow size distribution, the Ω phase has a size distribution wider than the σ phase and skews to large size.
- The intermetallic σ phase possesses a high hardness value at room temperature ($H_v=546 \text{ Kg/mm}^2$) and may lead to a high yield

strength (1784 MPa). At 350°C, the hardness of the intermetallic σ phase retained 70% of its room temperature value.

- The Young's and shear modulus and Poisson's ratio of the intermetallic σ phase were measured as $E=159.3$ GPa, $G=60.89$ GPa, respectively, and Poisson's ratio $\nu_\sigma=0.308$.
- According to Van de Merwe model and Zener-Hillert equation the interfacial energy of the σ and Ω phase is estimated to be $\gamma_\sigma=0.054$ (J/m²) and $\gamma_\Omega=0.287$ (J/m²).
- In deformed Al1M alloy, the Ω phase was found to be sheared by dislocations and formed high density APB. This implies that chemical strengthening could have some effect, in addition to coherency strengthening, modulus hardening and order hardening, on the mechanical properties and fracture in an Al alloy with Ω precipitates.

References

1. T.G. Nieh, R.A. Rainen and D.J. Chellman, "Microstructure and Fracture in SiC Whisker Reinforced 2124 Aluminum Composites", The Fifth International Conference on Composite Materials (ICCM-V), eds. W.C. Harrigan, Jr., J. Strife and A.K. Dhingra, 1985, pp. 825-843.
2. V.D. Scott, S. Kerry, R.L. Trumper, "Nucleation and Growth of Precipitates in al-cu-Mg-Ag Alloys", Materials Science and Technology **3**, October 1987, pp. 827-835.
3. M.S. Zedalis and M.E. Fine, "Precipitation and Ostwald Ripening in Dilute Al Base-Zr-V Alloys", Met. Trans. **17A**, 1986, p. 2187.
4. H.I. Aaronson and J.K. Lee, Precipitation Processes in Solids, eds. K.C. Russell and H.I. Aaronson, TMS-AIME conf. Pub., Warrendale, PA, 1978.
5. G.J. Shiflet, "Low Energy Dislocation Structures Caused by Phase Transformations", Mat. Sci. Eng. **81**, 1986, p. 61.

6. A.R. Miedema and F.A. Broeder, "On the interfacial Energy in solid-Liquid and solid-Solid Metal combinations", Z. Metallk. 70, 1979, p. 14.
7. R. Schueller, A.K. Sachdev, and F.E. Wawner, "Interfacial Structures of the Cubic σ Phase", Scripta Metall. 27-10, 1992, p. 1289.
8. S.F. Baumann and D.B. Williams, "Experimental Observations on the Nucleation and Growth of δ' (Al_3Li) in Dilute Al-Li Alloys", Met. Trans. 16A, 1985, p. 1203.
9. J.D. Boyd and R.B. Nicholson, "The Coarsening Behavior of θ " and θ' Precipitates in Two Al-Cu Alloys", Acta Metall. 19, 1971, p. 1379.
10. A.J. Ardell, "An application of the Theory of Particle Coarsening: The r' Precipitate in Ni-Al Alloys", Acta Metall. 16, 1968, p. 511.
11. E.A. Starke, Jr., Treatise on Materials Science and Technology, Vol. 31, eds. A. Vasudevan and R. Doherty, Academic Press (1989), pp.35-63.
12. L.F. Mondolfo, Aluminum Alloys: Structure and Properties, Butterworths, London, 1982, p. 257.
13. E.R. Petty, Journal of the Institute of Metals, vol. 89, 1960-1961, p. 342.
14. A. Garg and J. Howe, "Nucleation and Growth of Ω Phase in Al-4.0Cu-0.5Mg-0.5Ag Alloy - An In-situ Hot-State TEM Study", Acta Met. 39, 1991, p. 1939.
15. Aluminum Properties and Physical Metallurgy, ed. J.E. Hatch, ASM, 1984.

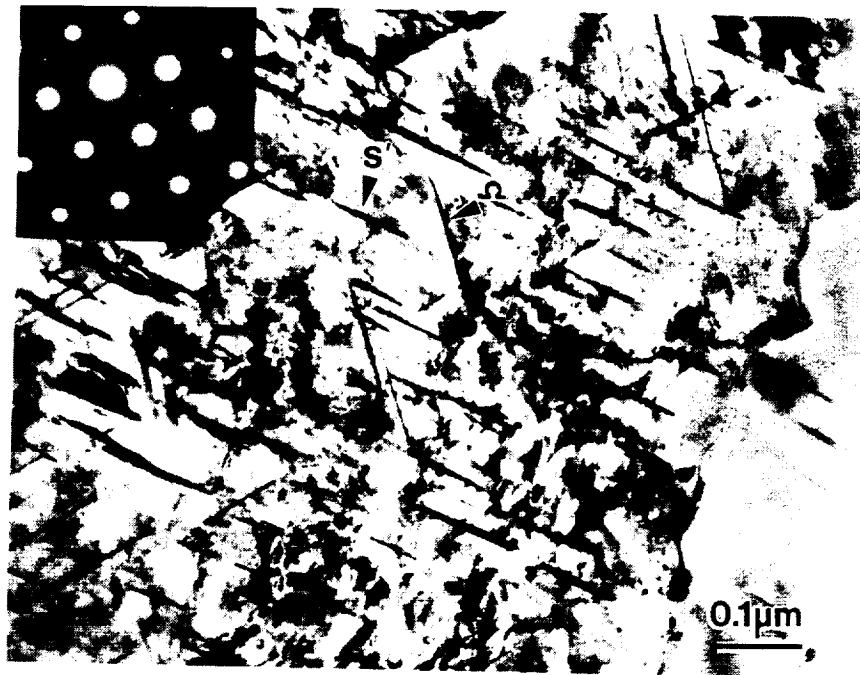


FIGURE 1. The Ω phase along $\langle 011 \rangle$ Al zone axis in the matrix of Al/SiC composite.



FIGURE 2. some θ' and s' phases appear near $\langle 001 \rangle$ zone axis in the matrix of Al/SiC composite.

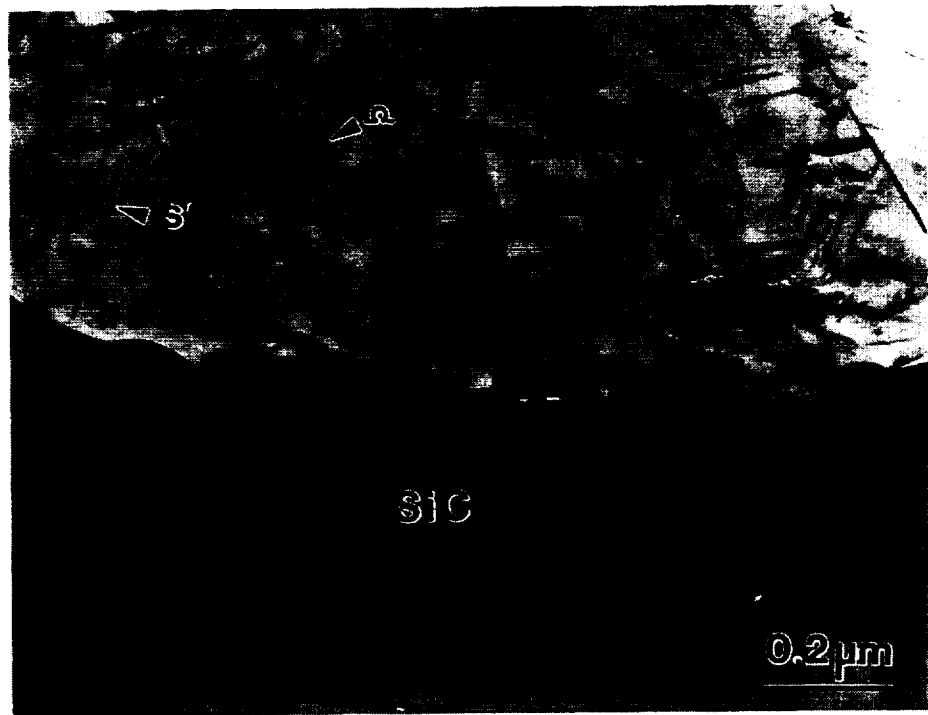


FIGURE 3. The Ω phase, s' phase in the matrix and SiC particle and interfacial precipitation.

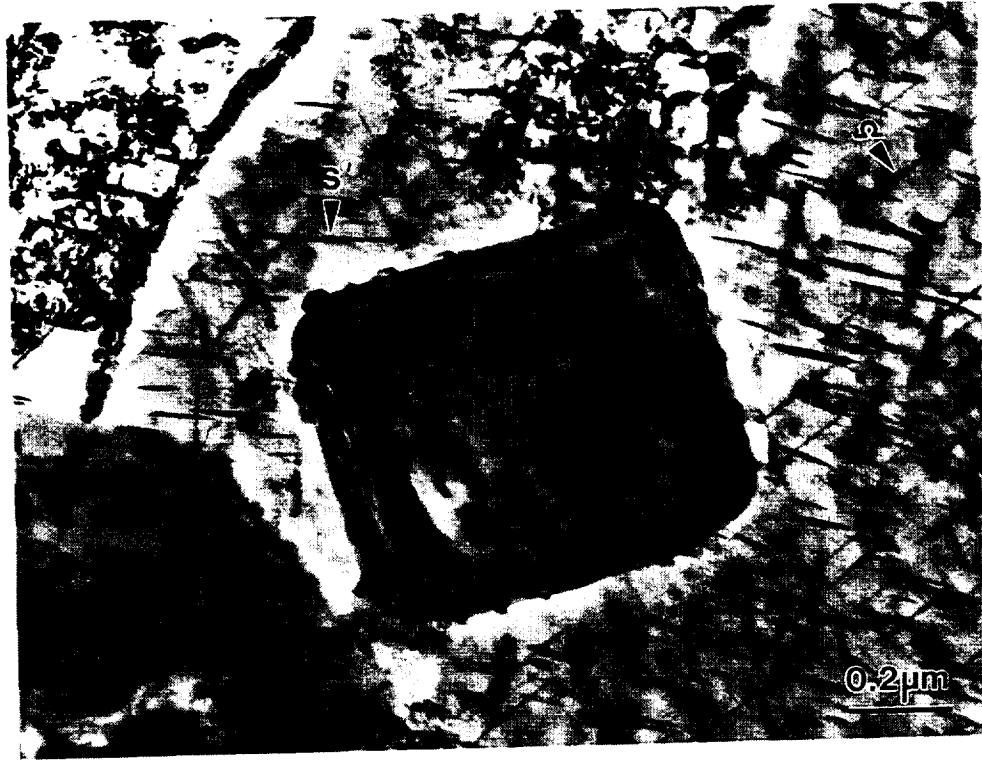


FIGURE 4. An Al-Cu-Zr constituent particle in the matrix. Boundary precipitation can be seen.



FIGURE 5. Some fine grains formed in a band and no precipitates was observed in these grains/subgrains.

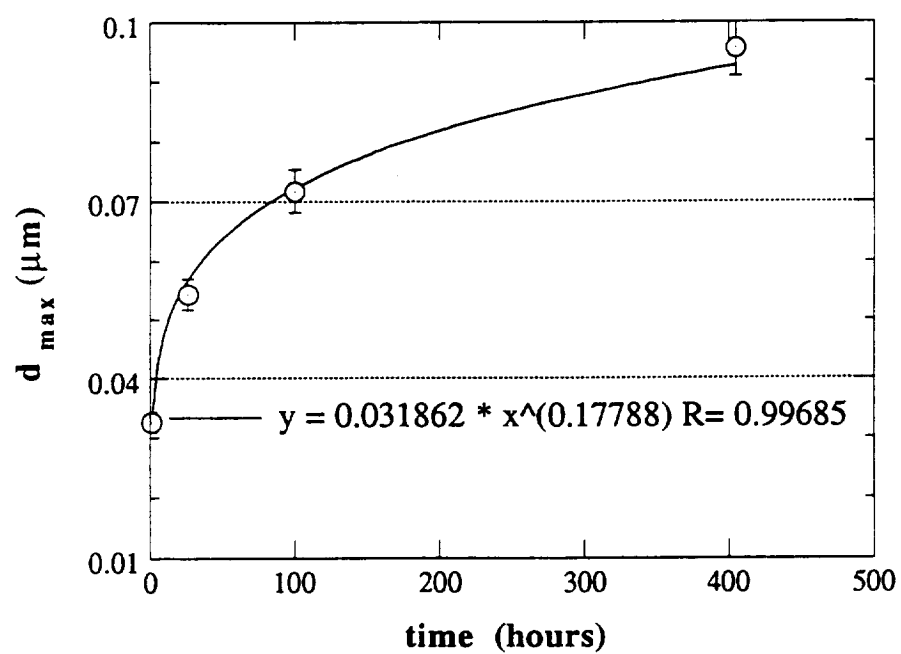


FIGURE 6. The relationship of the maximum size of the σ phase versus exposure time at 200°C .

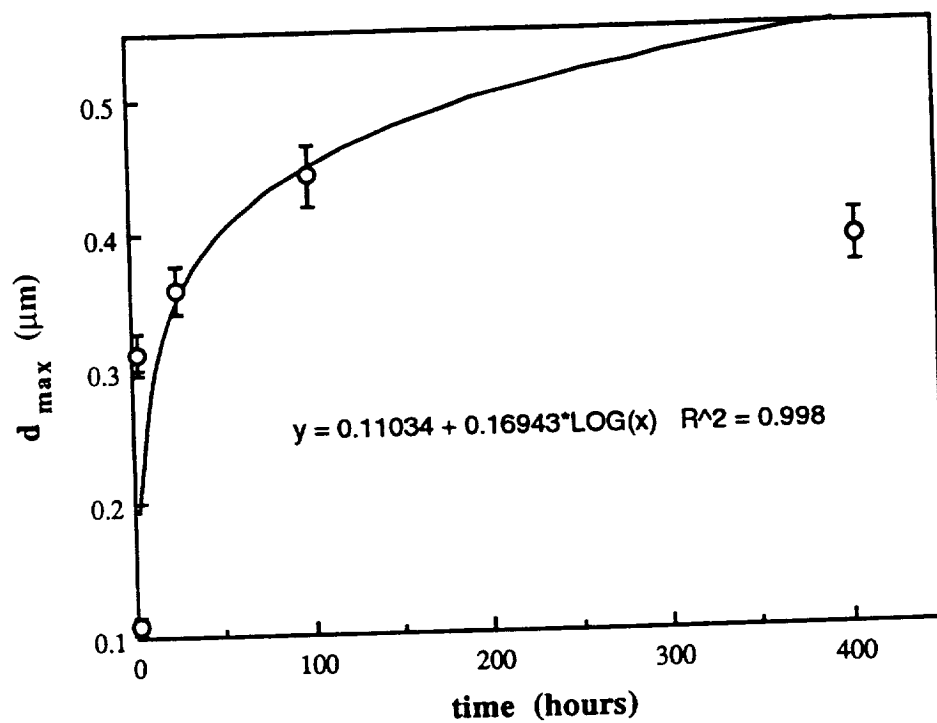


FIGURE 7. The relationship of the maximum size of the Ω phase versus exposure time at 200C.

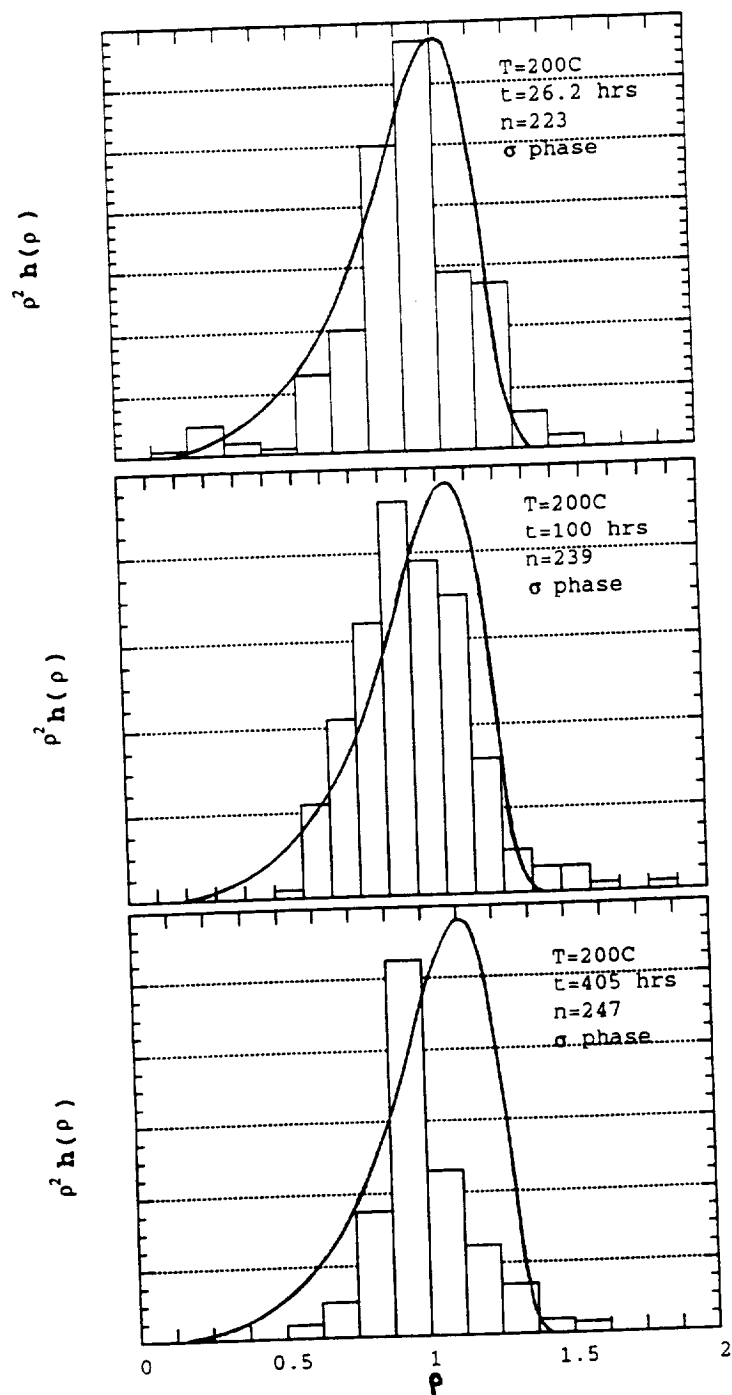


FIGURE 8. The size distribution of the σ phase at 200°C with different time and comparison with LSW coarsening theory prediction.

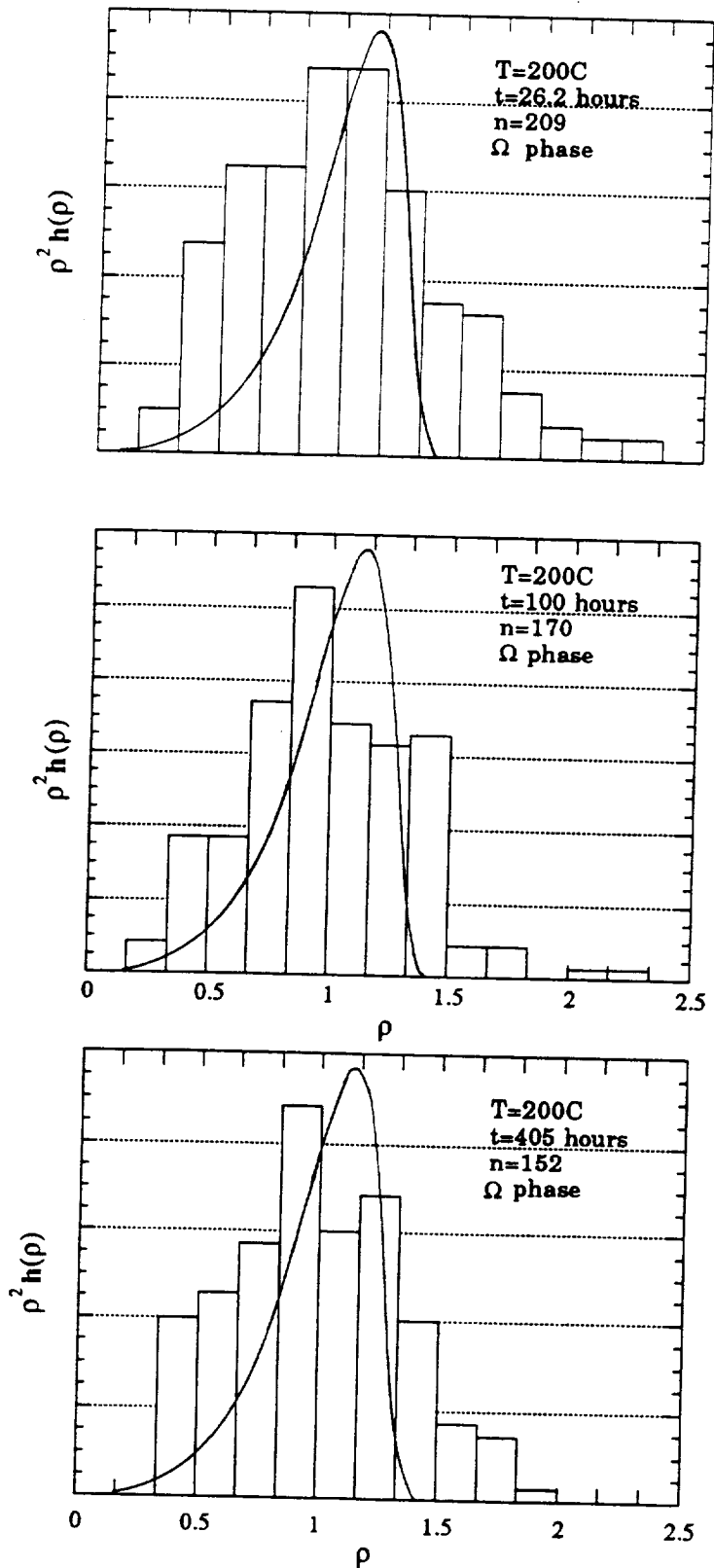


FIGURE 9. The size distribution of the Ω phase at 200°C with different time and comparison with LSW coarsening theory prediction.

FN: LISTUFF.NI ID: LI'S POWDER ONCE AGAIN SCINTAG/USA
 DATE: 04/09/93 TIME: 14: 44 PT: 0.45000 STEP: 0.03000 WL: 1.54060

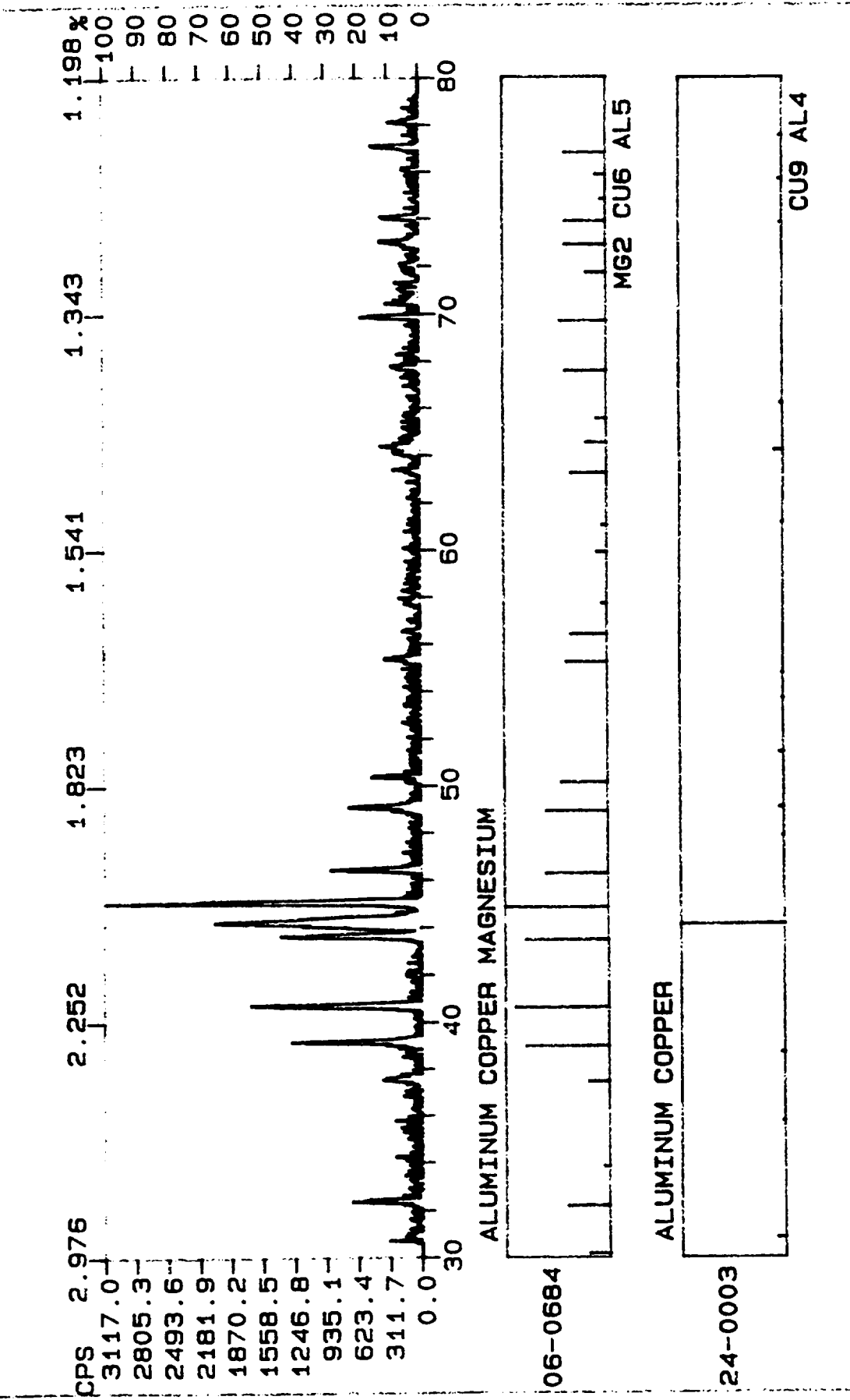


FIGURE 10 x-ray diffraction pattern showing the bulk
 intermetallic compound is the σ phase

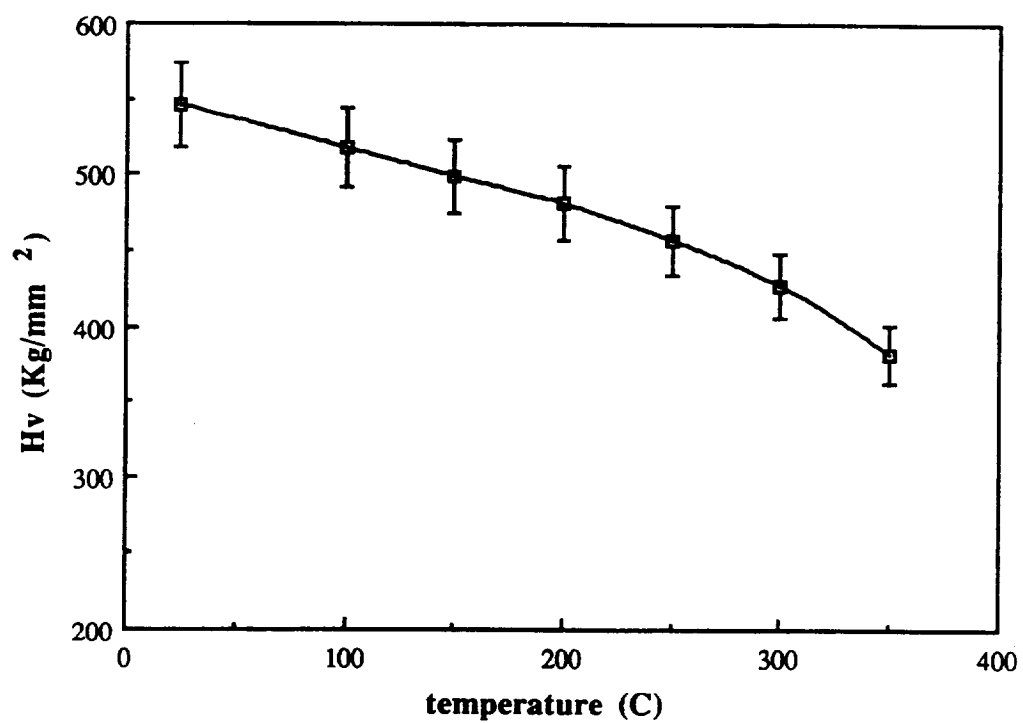


Figure 11. Hot stage hardness results showing the σ phase is quite stable as temperature increases.

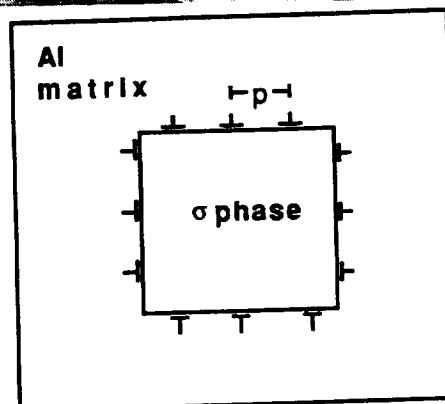
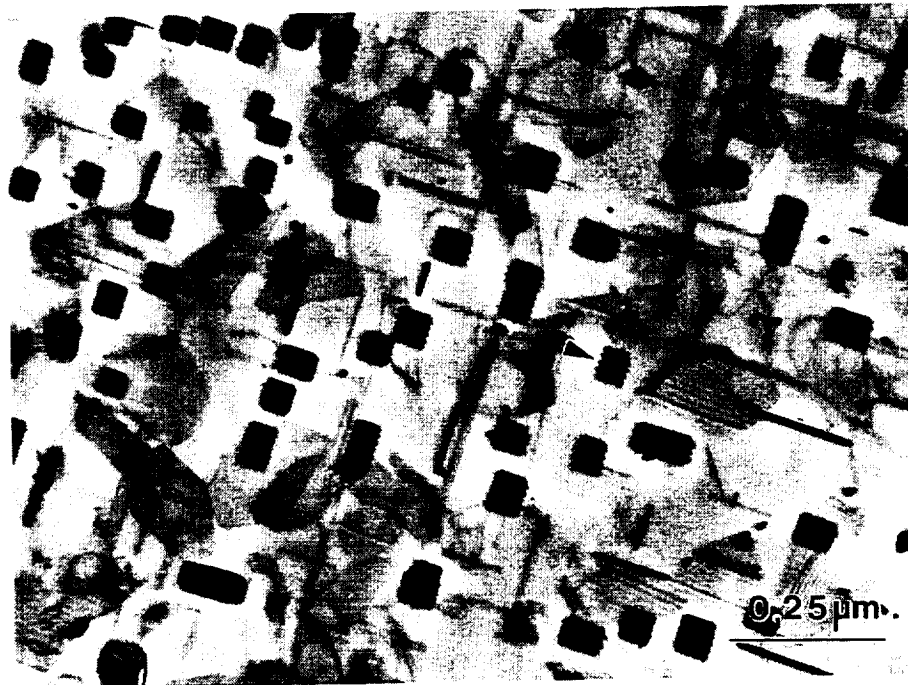


FIGURE 12. Periodic strain lobes in the matrix near the interface caused by misfit dislocation and the schematic illustration.



FIGURE 13. High density dislocations in a sprayed alloy (Al-6.23Cu-0.36Mg-0.4Ag-1.84Mn-0.31Zr-0.27V-0.19Ti) which was stretched 2% before aging.

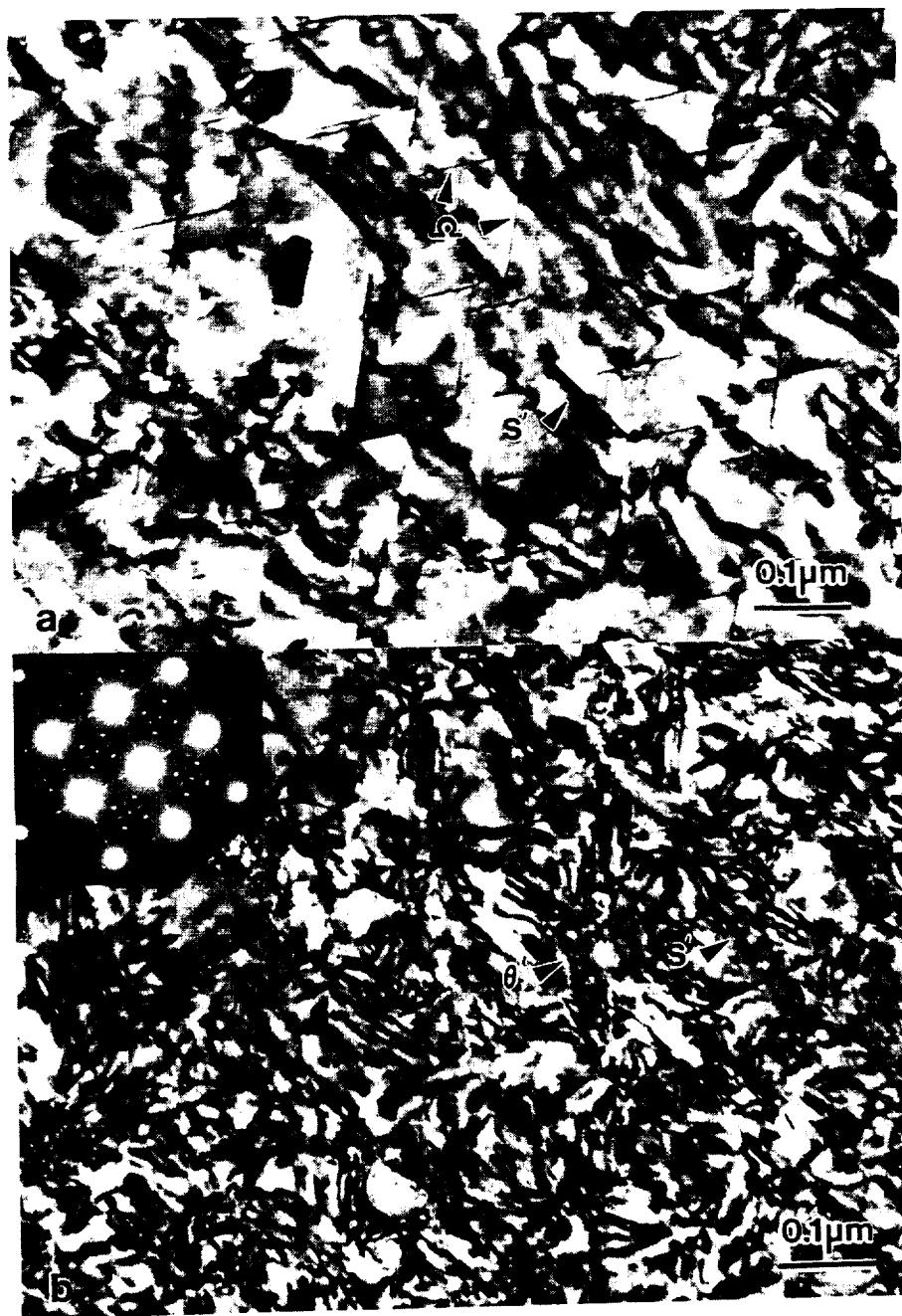


FIGURE 14. a) The s' and Ω phases in the alloy $B=\langle 011 \rangle_{Al}$. b) the θ' and s' phases formed in the alloy $B= \langle 001 \rangle_{Al}$. The alloy was aged at 177C for 12 hours after deformation.

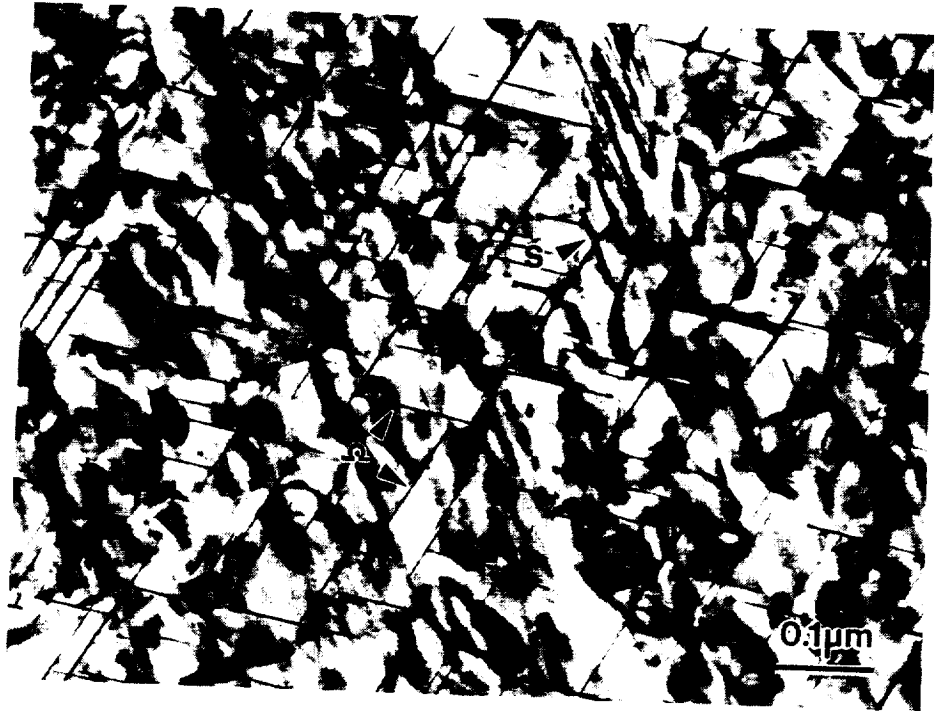


FIGURE 15. A relatively high density of the Ω phase in the alloy aged after dislocations were annealed out (solutionized at 525°C, 12 hours then aged at 200°C for 4 hours).

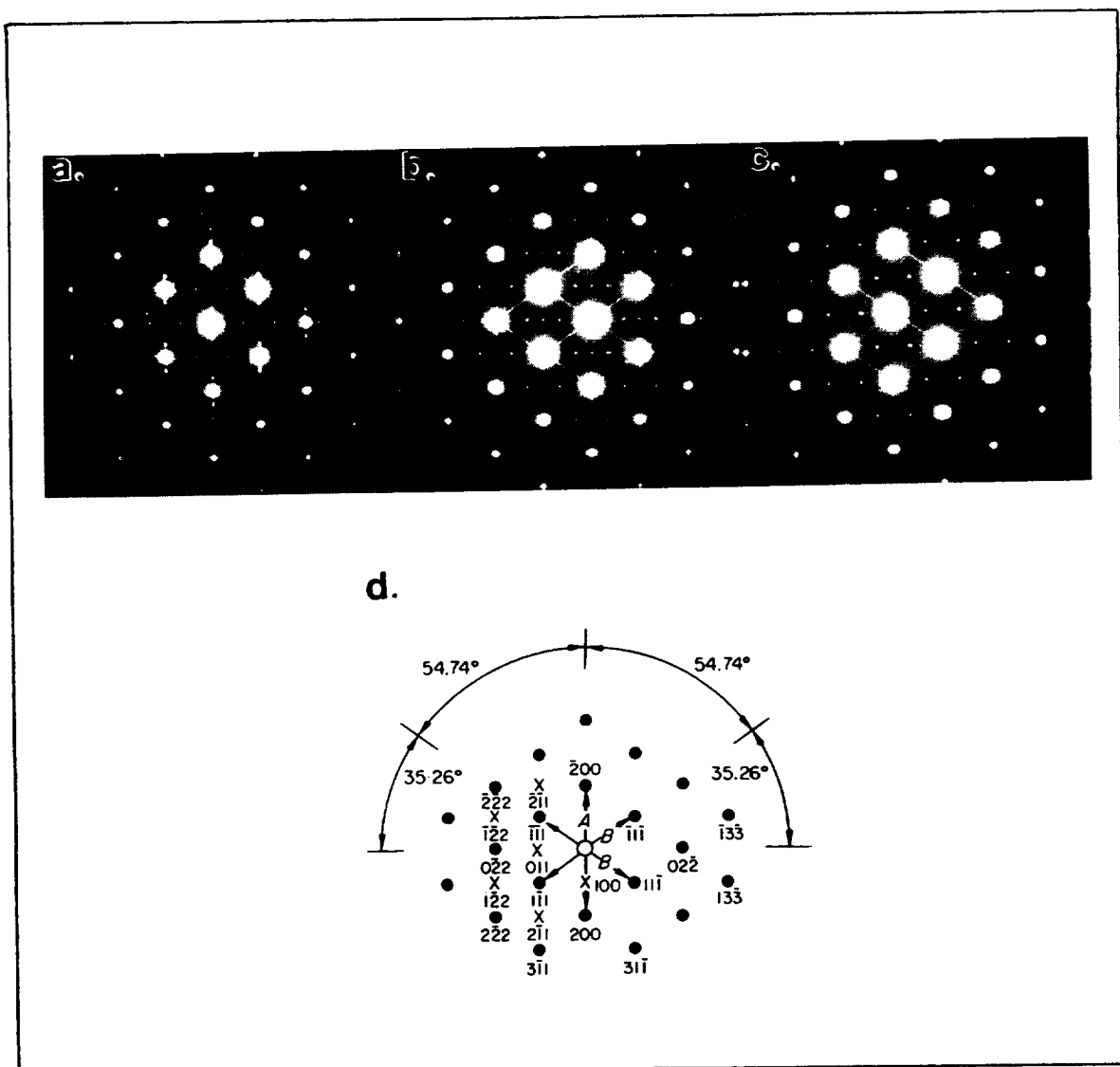


FIGURE 16. The density change of the θ' and s' phases as the solutionization time increases in $\langle 011 \rangle_{Al}$ SAD pattern. a) SAD pattern of the alloy aged at 177°C for 12 hours after stretching the alloy. b). SAD pattern of the alloy aged at 177°C for 12 hours after the alloy solutionized at 525°C for 2.5 hours which annealed some dislocations out in the alloy. c) SAD pattern of the alloy aged at 200°C for 4 hours after the alloy solutionized at 525°C for 12 hours which annealed out most dislocations caused by stretching.



FIGURE 17. WBDF image of the dislocations in a deformed alloy (A11M T6 after tensile test).

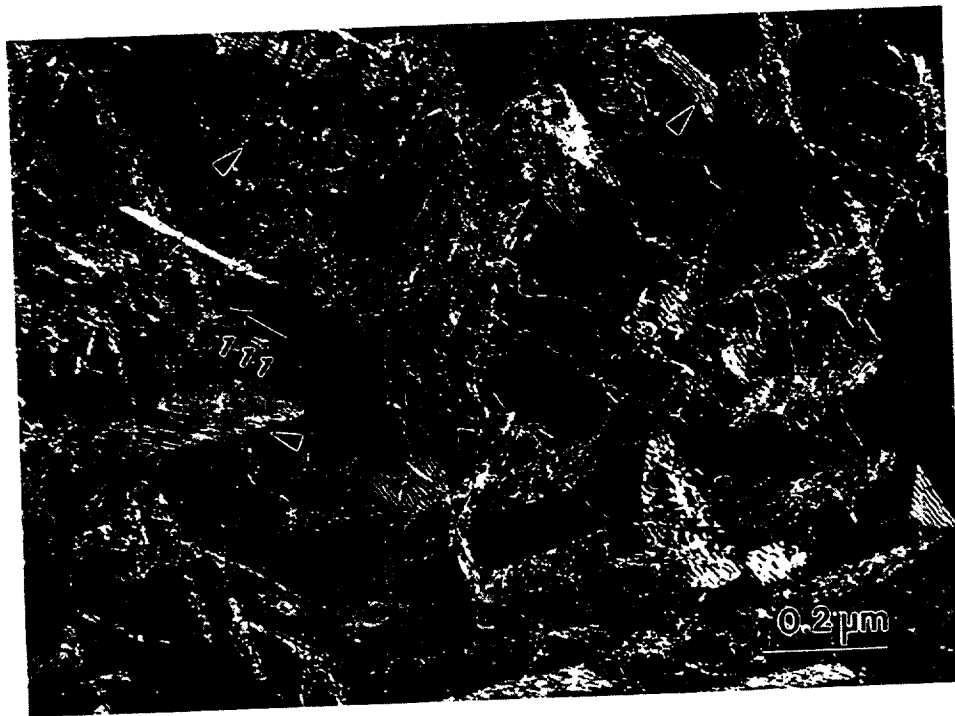


FIGURE 18. Evidence of dislocation shearing: some straight lines run through the Ω phase, some wavy lines in the Ω phase and some evidence of cutting.



FIGURE 19. a.) High density APB formed in the Ω phase which due to many dislocations cut through b.) Low density APB formed due to coarsening.



FIGURE 20. The wavy shape Ω phase and the step created by dislocation shearing, an edge on view.

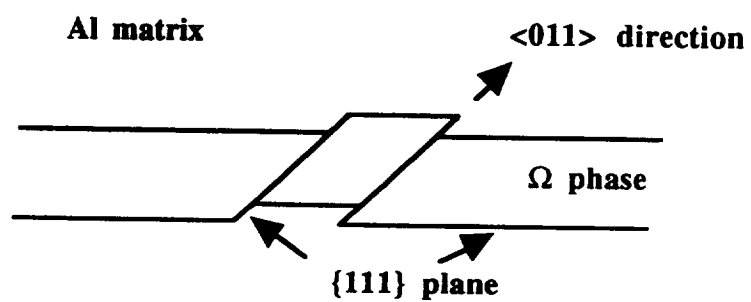


FIGURE 21. Schamatic illustration of the edge on view of the Ω phase cut by a dislocation.

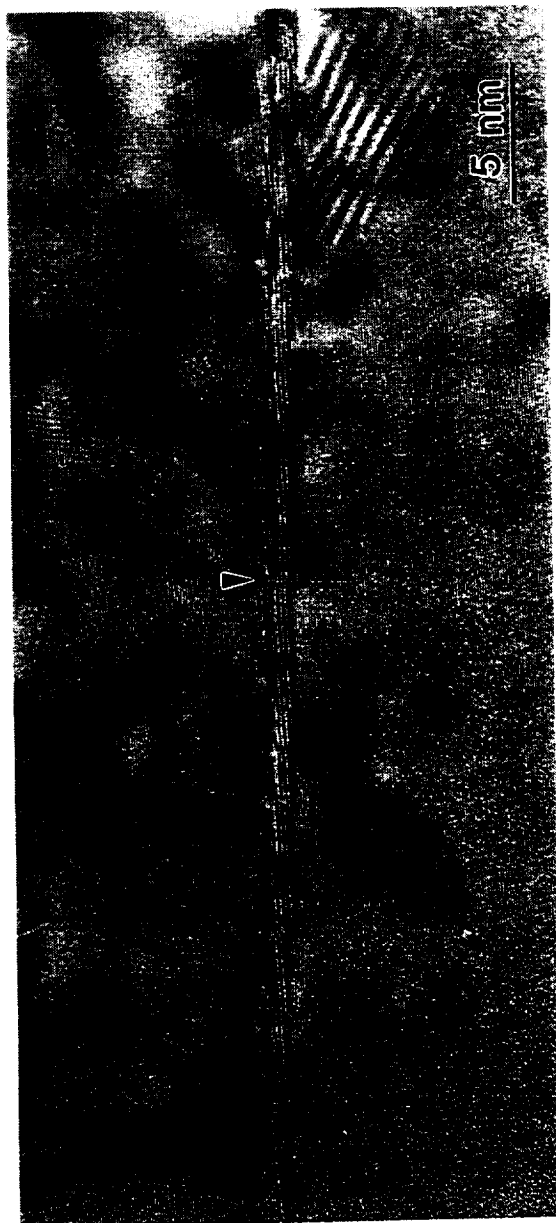


FIGURE 22. High resolution TEM micrograph showing a lattice image of the Ω phase cut by dislocation shearing .

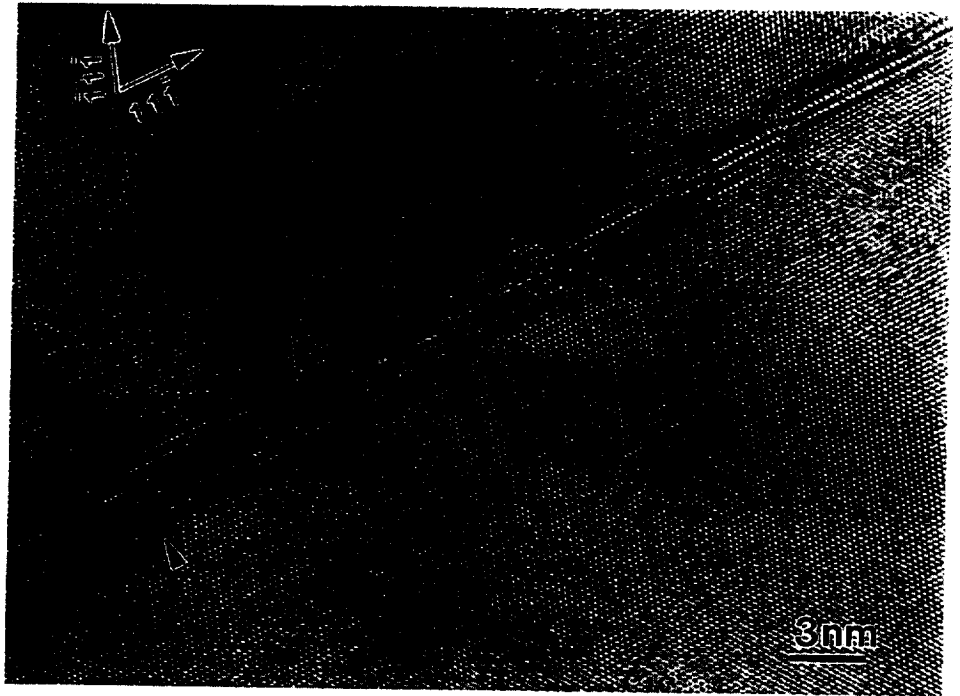


FIGURE 23. High magnification of the Ω phase cut by dislocation shearing.

TASK 10A. Trade Studies in Support of an Aluminum HSCT (Boeing)

Principal Investigator: Mr. Peter G. Rimbos

This task was subdivided into four Phases as shown in Fig. 1. As no materials properties were generated during the subject program that could be reduced to property allowables for use in the design studies, it was not possible to initiate Phases I, III, and IV of the trade studies. However, substantial progress has been made in Phase II, particularly with respect to the development of structural and manufacturing concepts that would be particularly applicable to an "Aluminum" HSCT.

The aluminum structural design and manufacturing concepts for the wingbox, wing strake, and fuselage remain unchanged for 1993 except for minor modifications in the design details. These modifications are the result of design refinements and structural stress optimization. Once conversion of all design variables is accomplished, final modifications will be done to the structural concepts matrices. See Figs. 2 and 3. These design concepts are grouped into four major design families: (A) integrally stiffened, (B) sandwich, (C) hybrid concepts, and (D) conventional skin/stringer construction. The details are described below:

- A. ***Integrally Stiffened.*** Three arrangements are included: extruded stringers, orthogrid, and isogrid according to airplane location and type and magnitude of loading.
- B. ***Sandwich.*** Arrangements include two variations on sandwich edge treatments according to location and loading.
- C. ***Hybrids*** (*conventionally stiffened thin-sandwich skins*). Included to study effects of hybrids on structural performance and cost. In addition, hybrids could

provide redundant load paths, fail safety, and better damage tolerance, among other benefits.

- D. **Conventional skin/stringer** (these concepts are not shown in Figs. 2, and 3). Included to provide a baseline from which to measure concept improvements in terms of both performance and cost. A detailed study of a conventional skin/stringer aluminum baseline wing box and strake was developed under NASA contract NAS1-19349 Task 8. Internal structural arrangements and local sizing for different areas of the overall wing were completed. This information is available for this study and could be used as a foundation for the baseline aircraft. Given the maturity of the conventional skin/stringer concepts, this will serve as a reliable baseline from which to compare, measure and calibrate the potential of other concepts, and improvements, in terms of both performance and cost.

To make the best use of materials, a tailored structural approach was used. Materials possessing, desired properties, along with novel structural arrangements that matched design and manufacturing process requirements at different locations, were selected. In developing each of the concepts, care was taken to address low-cost producible structure, as well as low weight and high performance.

Structural sizing of each of the design concepts is in progress. The analytical methods and tools are being developed under Boeing internal studies (Low-Cost Airplane Trade Studies - LCATS and Design Integrated Trade Study - DITS), and are close to the completion and verification process. The basic types of internal structural arrangements that can be accommodated for analysis are:

- Multi-spar: Sandwich and integrally stiffened panels such as isogrids and orthogrids.

- Multi-ribs: Stiffened skins such as conventional skin/stringer construction, corrugated stiffened skins among others.

Sizing will focus on those most promising concepts and processes to provide design data for weight and later cost estimation. To understand the sensitivity to material and structural concept changes, performance first will be evaluated and compared at the concept level. For 1993, the plan and schedule for these activities have been revised as shown in Figs. 4 and 5. This allows us to directly use and complement parallel NASA-funded programs where concept-level data will be assembled into a full airplane structural configuration. From this information, the most promising structural materials and desired property levels, together with structural design concepts, required product forms, and manufacturing processes can be identified.

Objectives:

- (1) To evaluate aluminum-based materials and processes in terms HST airplane performance.

Approach:

Phase I - Material Property Projections

- (1) Review/update LCATS property projections
- (2) Develop property projections for non-LCATS alloys
- (3) Develop prel. "allowables" for non-LCATS alloys

Phase II - Concept Weight Evaluation

- (1) Select concepts
- (2) Conduct structural analysis on selected concepts
- (3) Develop weights data

Phase III - Airplane Performance Evaluation

- (1) Develop three (3) airplane concepts/materials
- (2) Develop point-design weights
- (3) "Fly" airplanes for equivalent mission sizing

Phase IV - Technology Recommendations

- (1) Prepare list critical technical needs
- (2) Prepare technology recommendations

Deliverables:

Phase I - Material Property Projections

- (1) Material property projections.

Phase II - Concept Weight Evaluation

- (1) Concept relative weights.

Phase III - Airplane Performance Evaluation

- (1) Airplane concepts/materials
- (2) Mission-sized relative MTOWs

Phase IV - Technology Recommendations

- (1) List of technical needs
- (2) Technology recommendations

Figure 1. Task 10A-1992, Materials and Processes Technology Trade Studies For The Airframe.

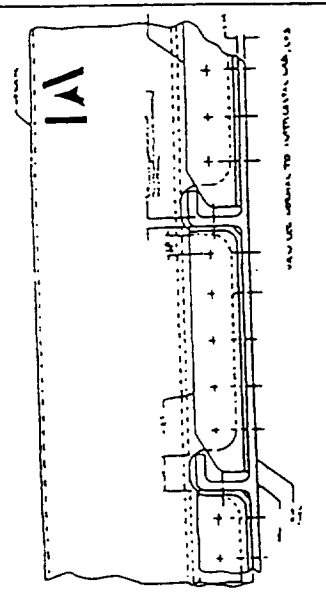
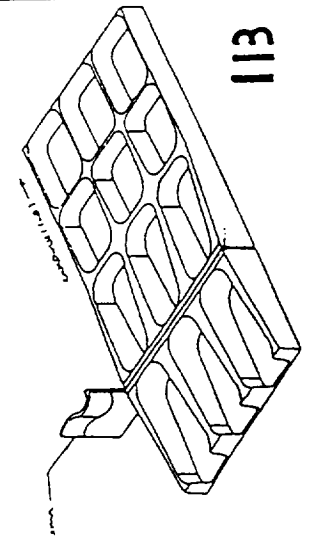
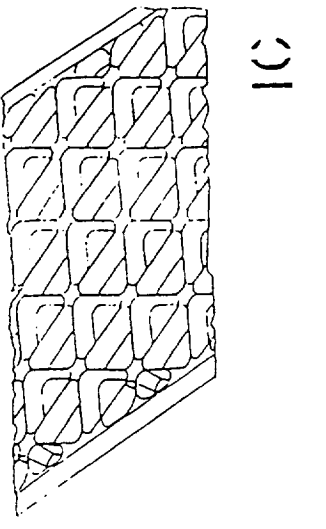
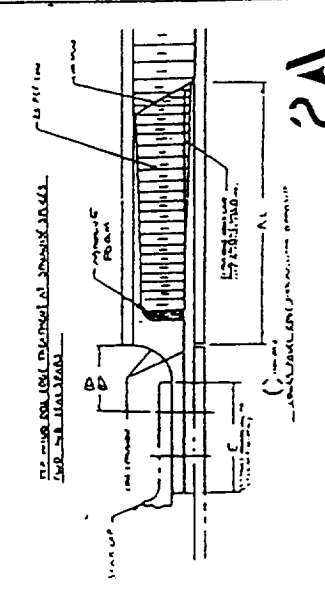
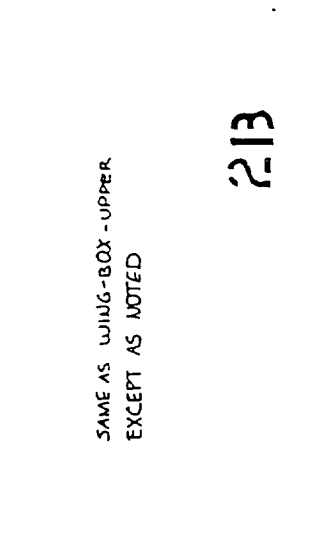
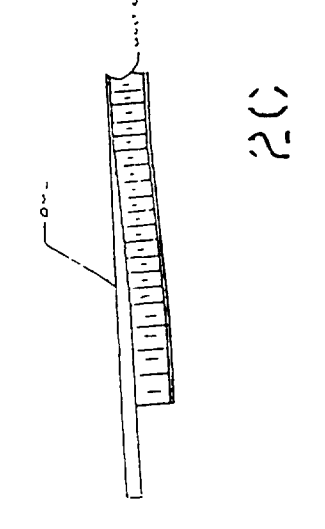
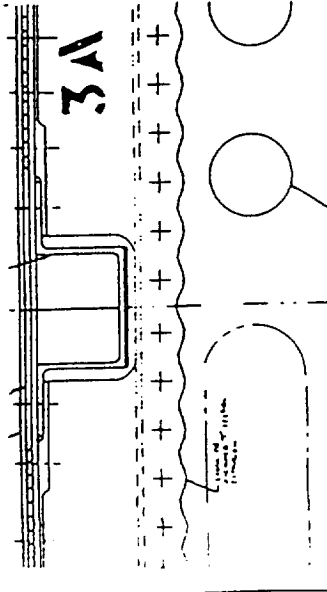
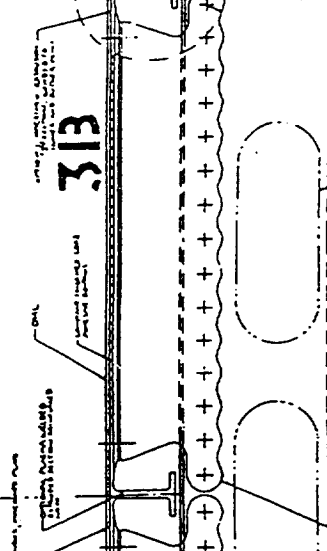
WING - ALUMINUM SKIN PANELS			STAKE - 1/2" x 1/4" x 1/2"	50331
TYPE	WING BOX - UPPER	WING BOX - LOWER		
INTERIORLY STIFFENED	 <p>1A</p>	 <p>1B</p>	 <p>1C</p>	
	 <p>2A</p>	 <p>2B</p>	 <p>2C</p>	
THIN SANDWICH STIFFENED PANELS	 <p>3A</p>	 <p>3B</p>	SAME AS UPPER AND LOWER WING BOX	

Figure 2. HSCT Wing - Aluminum Skin Panel Concepts

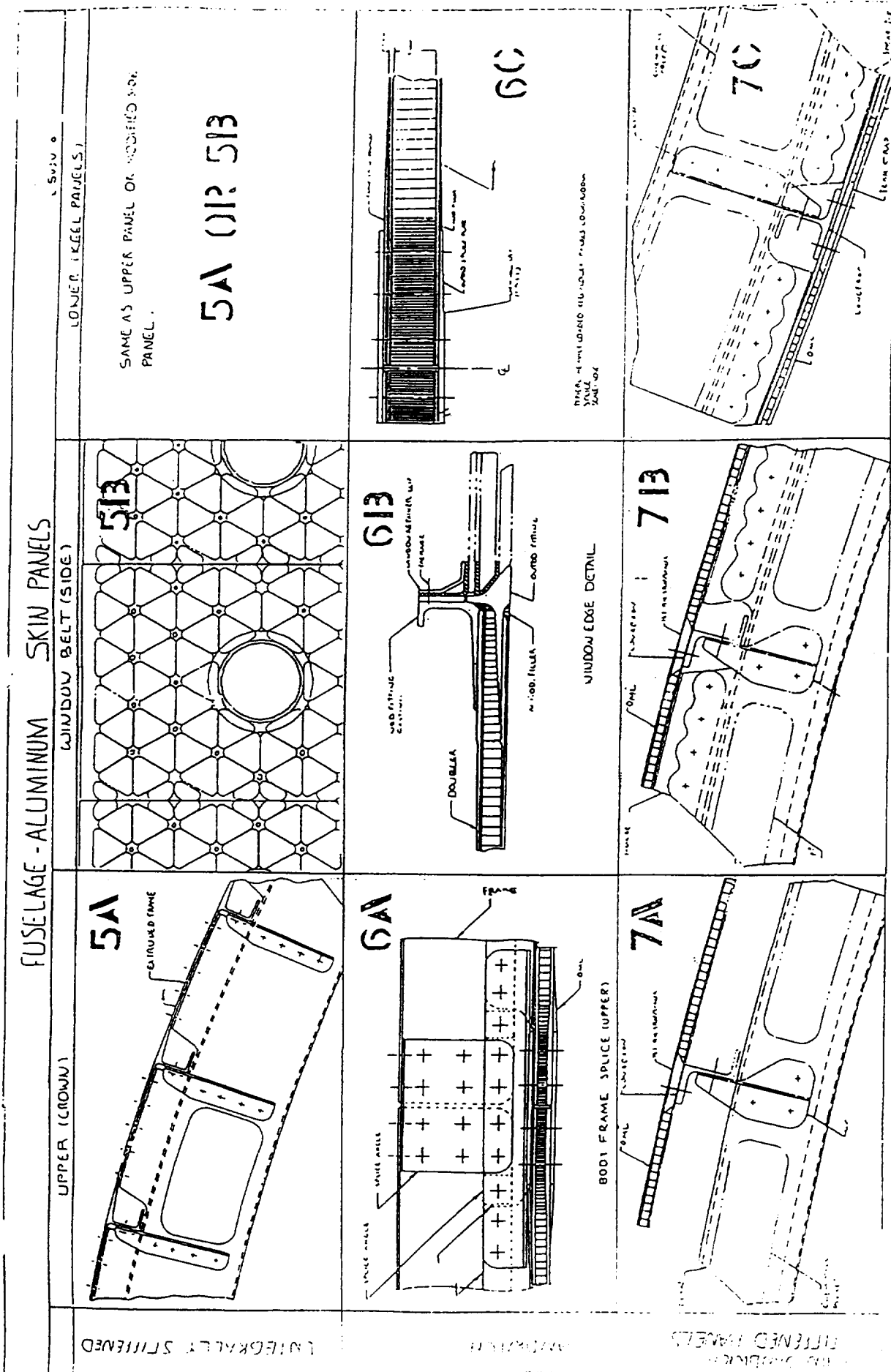


Figure 3. HSCT Fuselage - Aluminum Skin Panel Concepts

Objectives:

- (1) To evaluate aluminum-based materials and processes in terms HSCT airplane performance.

Approach:

Phase I - Material Property Projections

- (1) Review/update LCATS property projections
- (2) Review supplier updates

Phase II - Concept Weight Evaluation

- (1) Develop/update/select design concepts
- (2) Conduct structural analysis on selected concepts
- (3) Develop concept-level weights data

Phase III - Technology Recommendations

- (1) Prepare list critical technical needs
- (2) Prepare technology recommendations

Deliverables:

Phase I - Material Property Projections

- (1) Material property projections

Phase II - Concept Weight Evaluation

- (1) Concept-level relative weights

Phase III - Technology Recommendations

- (1) List of technical needs
- (2) Technology recommendations

Figure 4. Task 10A-1993, Materials and Processes Technology Trade Studies For The Airframe.

Phase	Title	1 9 9 3											
		JAN	FEB	MAR	APR	MAY	JUN	JUL	AUG	SEP	OCT	NOV	DEC
I	<i>Material Property Projections</i>	Preliminary "Allowables" ▼							Supplier Updates ▽				
II	<i>Concept Weight Evaluation</i>	Concept Selection ▼											
III	<i>Technology Development Recommendations</i>	Concept Downselection ▼											
		Concept Refinement ▽											
		Preliminary Panel Weights ▲											
		Preliminary Technology Recommendations ▽											

Figure 5. TASK 10A - 1993 MATERIAL TECHNOLOGY TRADE SCHEDULE FOR THE AIRFRAME

Kahn Tear Specimen

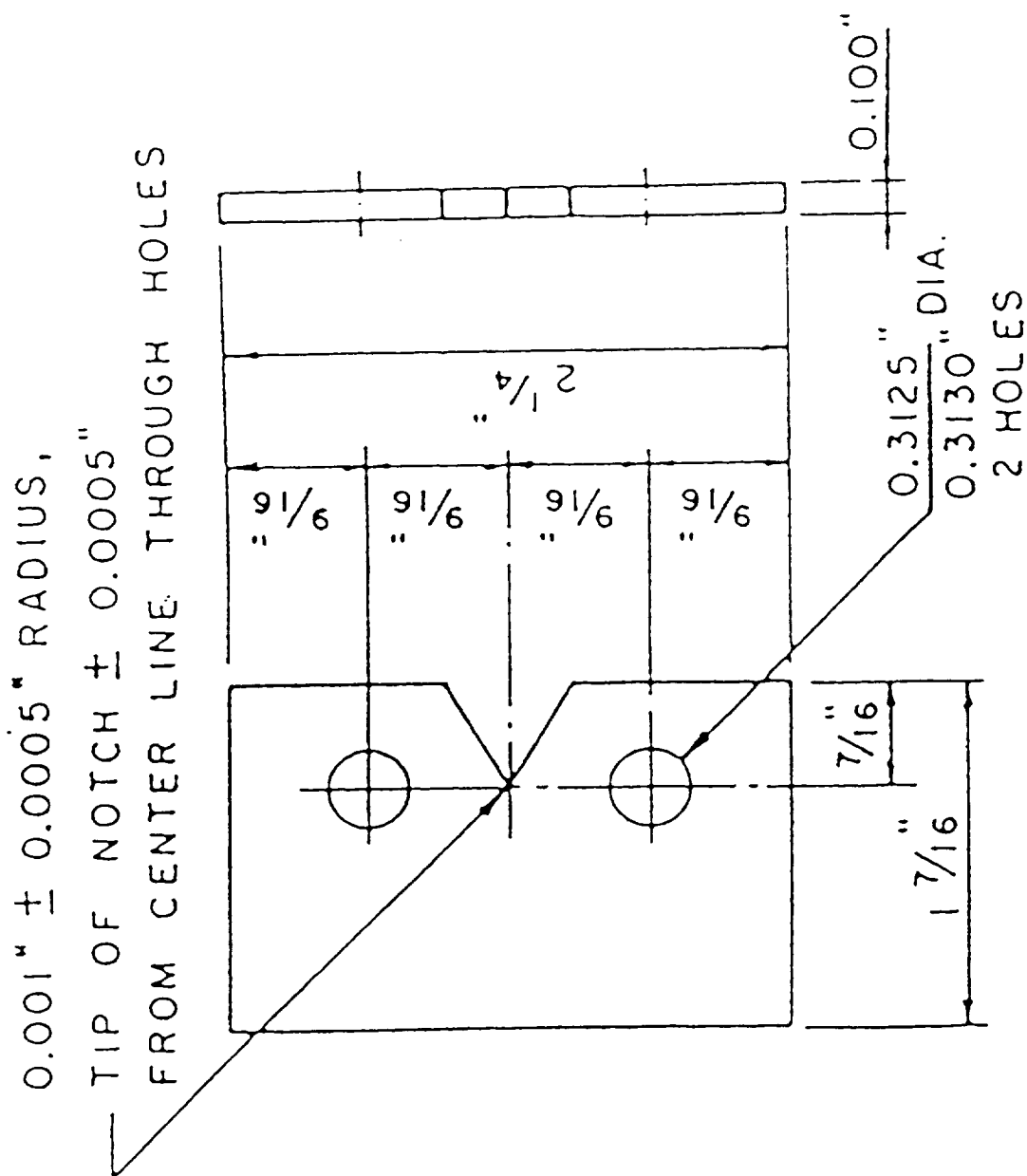


Figure 6. Kahn Tear Specimen. Specimen thickness can be varied somewhat from that shown to accommodate test material availability and experimental requirements.

Charpy V-Notch Specimens

Notch, Natural
Crack or < 0.001
Root Radius

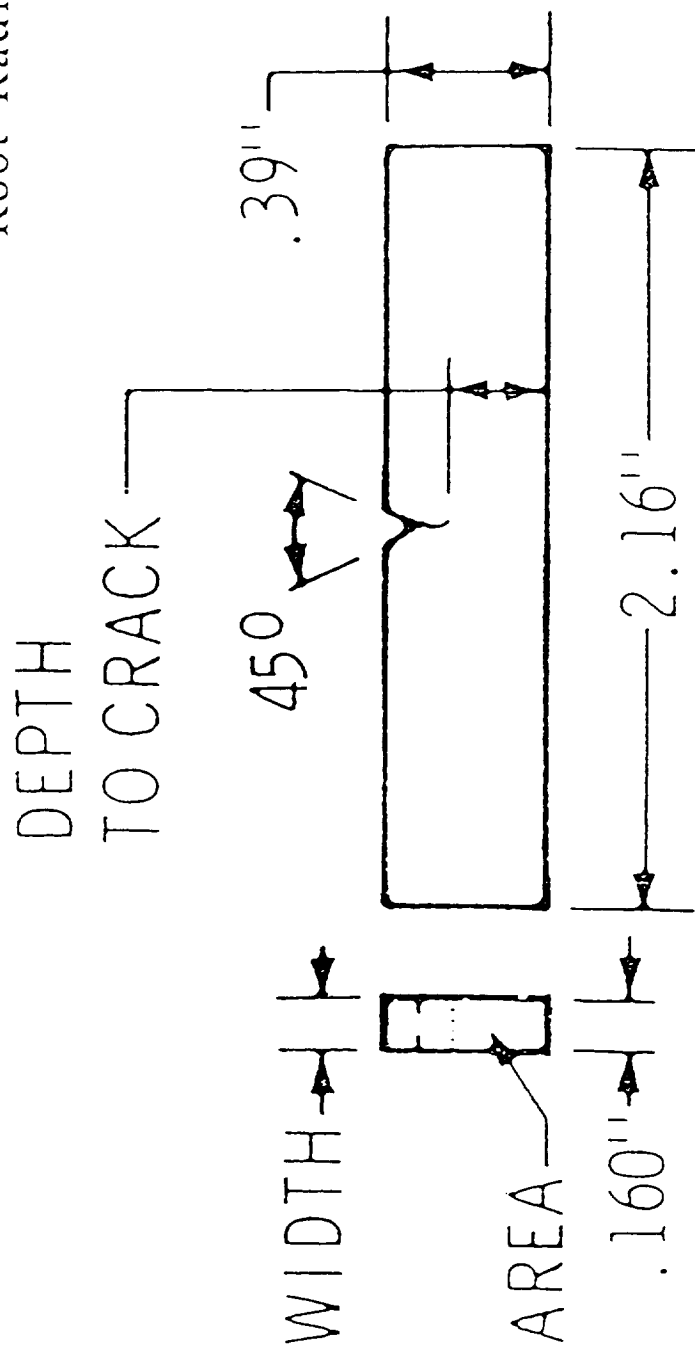


Figure 7. Charpy V-Notch Specimen. Specimen thickness is commonly varied between about 0.100 inch and 0.396 inch to accommodate test material availability and experimental requirements.

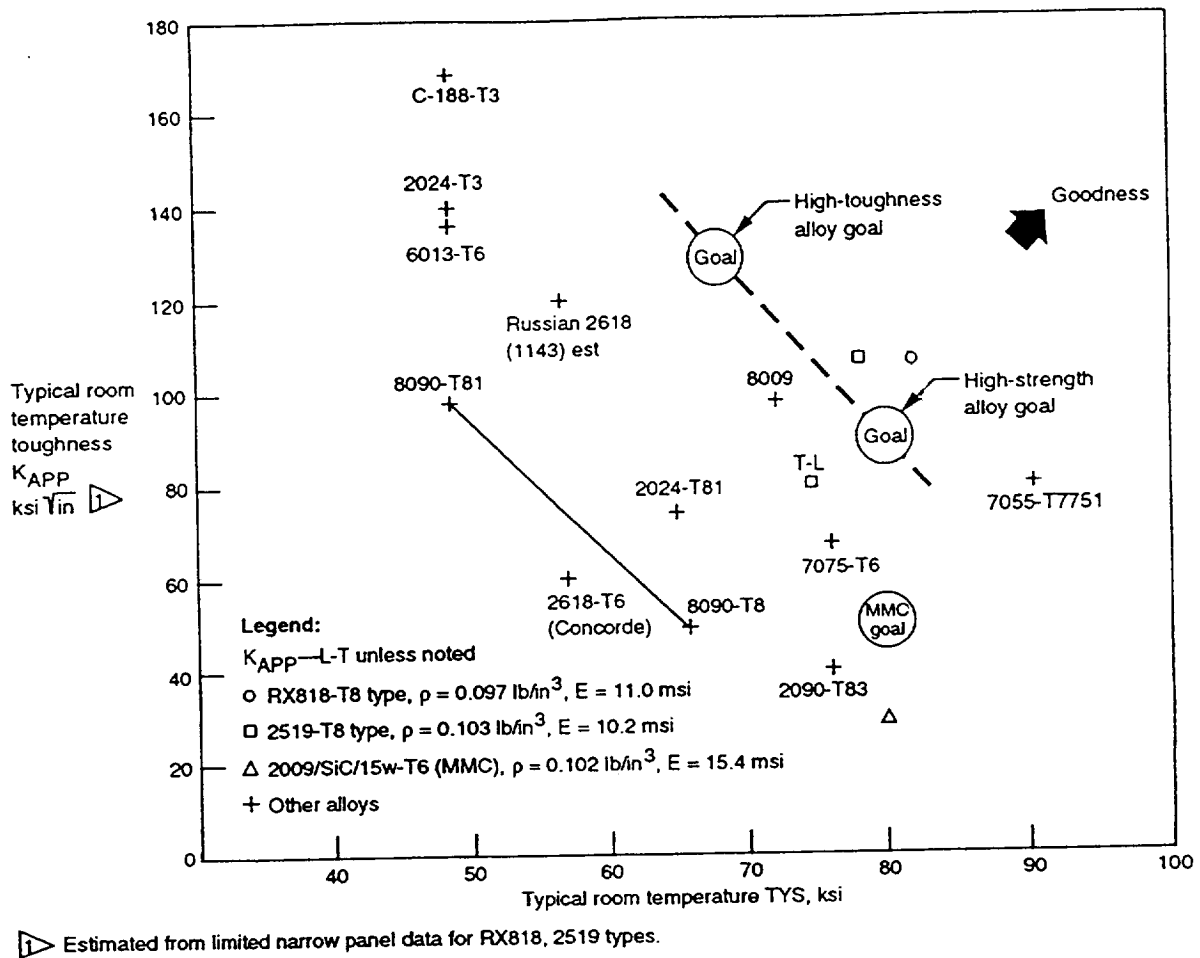


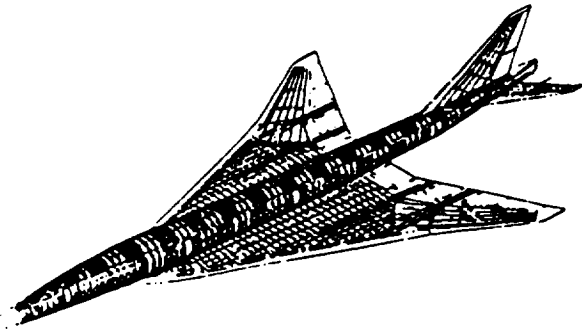
Figure 8. The Strength vs Fracture Toughness Characteristics of Several Aluminum Alloys that are Candidates for HSCT Use. These Properties are Contrasted Against Tentative Program Goals that were Established by Boeing early in the Program.

**TASK 10B. MATERIALS TECHNOLOGY TRADE-OFF STUDIES
 FOR THE AIRFRAME (Douglas)**

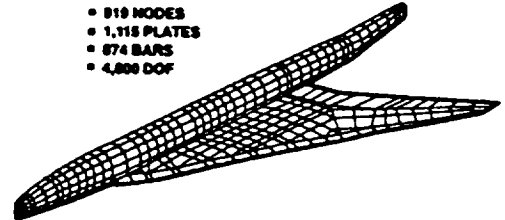
Principal Investigators: Mr. P. Kahandal
 Mr. A. Velicki

See Subtask 1(ii).

HSCT STRUCTURAL DESIGN AND INTEGRATION

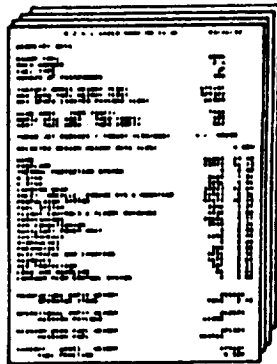


STRUCTURAL DEFINITION

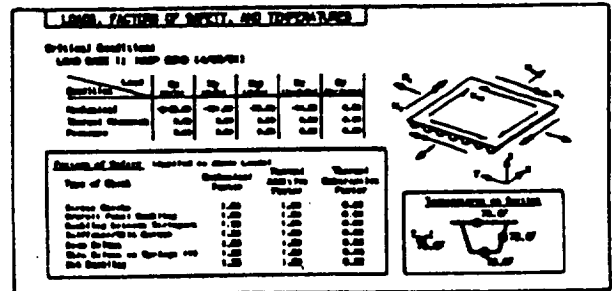


- 919 NODES
- 1,115 PLATES
- 874 BARS
- 4,886 DOF

FINITE ELEMENT MODEL DEVELOPMENT

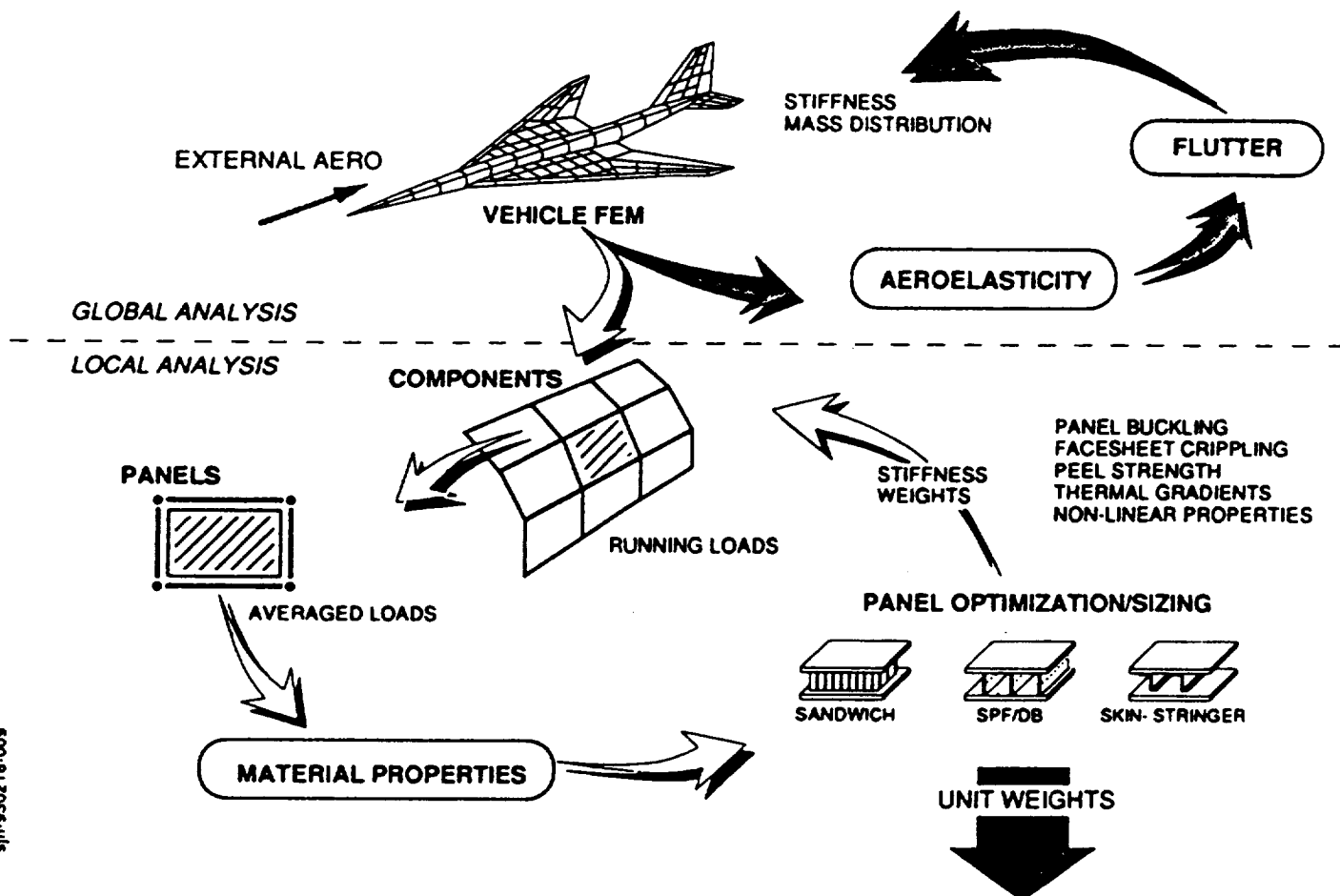


AIRFRAME WEIGHT DISTRIBUTION







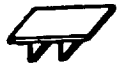








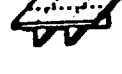
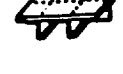
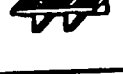

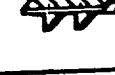


DETAIL PANEL ANALYSIS / OPTIMIZATION

STRUCTURAL ANALYSIS METHODOLOGY



STRUCTURAL CONCEPTS MENU

		MATERIAL FAMILIES				
		METALS		PMCs		OTHER
		ALUMINUM	TITANIUM	HI - MOD	HI - STR	
STRUCTURAL FAMILIES	SANDWICH STIFFENED	 HONEYCOMB	 SPF/DB			
	OPEN STIFFENER					
	CLOSED STIFFENER					
	BI-DIRECT STIFFENER					
	RECMD	8 WING PTS 9 FUSE PTS	8 WING PTS 9 FUSE PTS	8 WING PTS 9 FUSE PTS		

ANALYSIS PROCEDURE

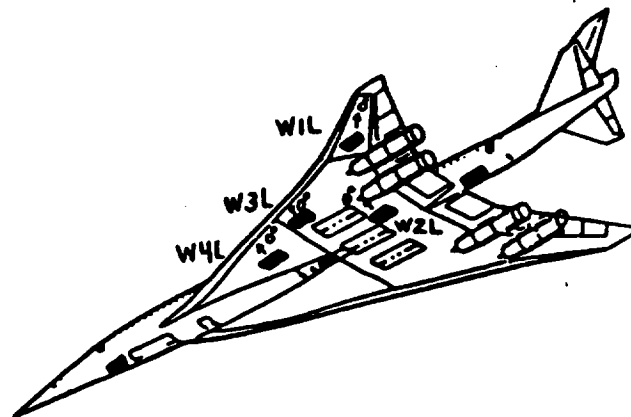
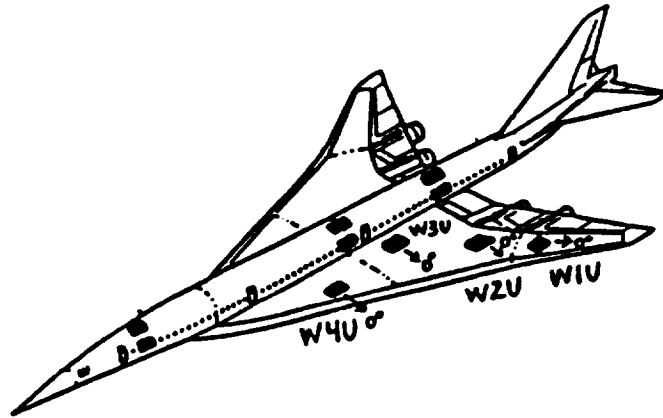
Use 40" x 40" Simply Supported Panels
Apply Initial Load Packages
Size for Strength, Stability, & Fatigue
Design Panel Joints
Determine Non-Optimum Factors
Determine Sensitivities to Panel Size
Determine Sensitivities to Mail Props
Determine Sensitivities to Thermal Grad

PANELS
BEING
STUDIED

Representative concepts are chosen for each Material/Structural family combination. More than one concept may be explored.

TWENTY (20) COMBINATIONS OF MATERIALS AND STRUCTURES ARE SIZED AT VARIOUS DESIGN LOCATIONS AT CRITICAL M2.0 AND M2.4 FLIGHT CONDITIONS. THESE ARE DOWNSSELECTED TO ONE METALLIC AND ONE COMPOSITE CONCEPT FOR EACH DESIGN LOCATION (8 WING PTS, 9 FUSELAGE PTS) BASED PRIMARILY ON WEIGHT.

WING PANEL POSITION DEFINITION



Note: 0° direction corresponds to N_x in applied loads

PANEL DESIGN/ANALYSIS

▷ ANALYZE/OPTIMIZE STIFFENED PANELS

▷ Z/J, HAT, BLADE, FOUR SHEET, HONEYCOMB

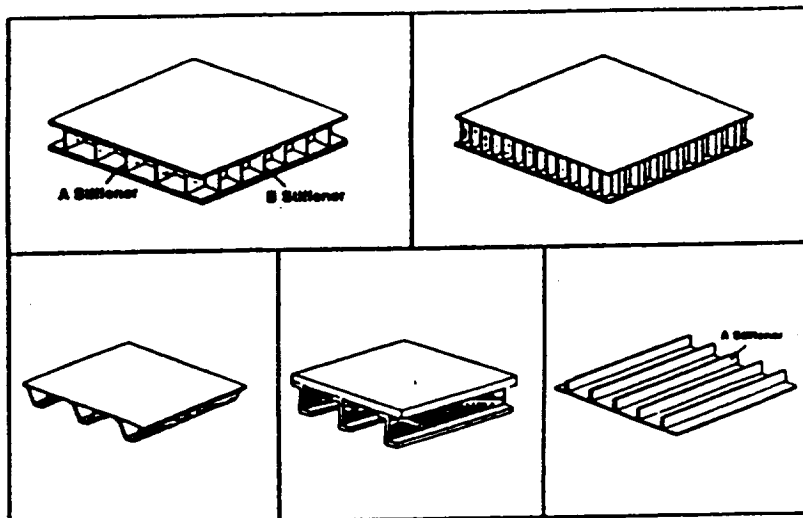
▷ BASIC STRESS CHECKS

◦ BASIC STABILITY CHECKS

- OVERALL PANEL STABILITY
- LOCAL BUCKLING

▷ PANEL FLUTTER CHECK

- Z/J, HAT, BLADE, FOUR SHEET





DESIGN / INTEGRATION TRADE STUDY MATERIAL PROPERTY DATABASE

6 CLASSES OF MATERIALS:

- **MONOLITHIC ALUMINUMS,**
- **DRA**
- **MONOLITHIC TITANIUMS,**
- **HIGH-MODULUS POLYMER COMPOSITES,**
- **HIGH STRAIN POLYMER COMPOSITES**
- **FIBER/METAL LAMINATES**

3 LEVELS OF RISK:

- **LOW**
- **MEDIUM**
- **HIGH**

TOTAL OF A MAXIMUM OF 18 MATERIALS

**DESIGN / INTEGRATION TRADE STUDY
MATERIAL PROPERTY DATABASE**



• RISK DEFINITION (BASED ON EXISTING AND DEVELOPMENTAL MATERIALS)

- LOW RISK -** MUST BE IN EXISTANCE TODAY. CHARACTERIZED, WITH KNOWN DEFICIENCIES. ACCUMULATED EXPOSURE HOURS IN EXPECTED USE ENVIRONMENT. SIGNIFICANT DURABILITY PROGRAMS PLANNED OR UNDERWAY.
- MEDIUM RISK -** A PROJECTION / EXTRAPOLATION. OFFERS ONE MAJOR IMPROVEMENT IN PROPERTIES. MATERIAL PROPERTY IMPROVEMENTS MUST BE ACHIEVABLE BY 1996.
- HIGH RISK -** A PROJECTION / EXTRAPOLATION. EXPERIMENTAL MATERIALS. PROJECTED OR EXTRAPOLATED PROPERTIES. THEORETICAL COMBINATIONS. MATERIAL PROPERTY IMPROVEMENTS MUST BE ACHIEVABLE BY 1998. TO ILLUSTRATE HIGH PAY-OFF BENEFITS.

DESIGN / INTEGRATION TRADE STUDY MATERIAL PROPERTY DATABASE

BASIC PROPERTIES COMMON TO ALL CLASSES

- **PHYSICAL PROPERTIES (DENSITY, CTE, K, C)**
- **MANUFACTURING CONSTRAINTS (MINIMUM GAGE)**
- **STIFFNESS (MONOLITHIC MATERIALS)**
- **PROPERTIES AT -65 F, RT, 250 F, 300 F, 350 F**

MATERIALS AND STRUCTURES DESIGN INTEGRATION TRADE STUDY SCHEDULE

NAS1-19345 Task 21			1993												1994		
NASA SOW	MDC WBS	TASK	FY 93												FY 94		
			-1	0	1	2	3	4	5	6	7	8	9	10	11	12	13
		Months from Go-Ahead	Jan	Feb	Mar	Apr	May	Jun	Jul	Aug	Sep	Oct	Nov	Dec	Jan	Feb	Mar
1.0	1000	INITIAL CONCEPT SCREENING	.	Δ	—	—	—	—	—	—	—	—	—	—	—	—	—
4.0	2000	PANEL LEVEL ANALYSIS			Δ	—	—	—	—	—	—	—	—	—	—	—	—
4.3	3000	SUB-COMPONENT LEVEL ANALYSIS							Δ	—	—	—	—	—	—	—	—
4.0	4000	VEHICLE LEVEL ANALYSIS				Δ	—	—	—	—	—	—	—	—	—	—	—
5.0	5000	VEHICLE ASSESSMENT										Δ	—	—	—	—	—
7.0	6000	RECOMMENDATIONS									Δ	—	—	—	—	—	—
	7000	PROGRAM MANAGEMENT															
	8000	REPORTS/REVIEWS															

- DELIVERABLES WOULD BE DOCUMENTED AND DELIVERED AS A SINGLE PACKAGE FOR EACH 1,000 SERIES

TASK 11. FRACTURE TOUGHNESS TEST DEVELOPMENT (Boeing)

Principal Investigator: Dr. W.E. Quist

General Discussion

A concern had arisen during the early part of the contract period concerning the proper method to evaluate the fracture toughness of the new or improved alloys developed during the present program. Therefore a round-robin testing program was developed that would utilize various test methods requiring only small amounts of material, with the purpose of determining which of these methods would give the closest correlation to valid wide center-cracked fracture toughness specimens.

Obtaining valid plane stress fracture toughness information was a necessary first step to the process. Fortunately, the needed data was available to the subject NASA program from an ongoing internal Boeing fracture toughness evaluation task on 2024-T3. Both technical and timing requirements were able to be met.

The valid plane stress fracture toughness tests of interest to the subject program are completed. The test procedures and results of two 60 inch wide by 96 inch long 2024-T3 L-T center cracked fracture toughness test panels have been forwarded to NASA. These panels were 0.063 and 0.125 inches thick, respectively, and come from stock that was slated for aircraft fuselage applications. The remnants of the two fracture toughness panels were cut into eight 14" by about 34" long L-T panels. An additional four L-T panels of similar size were cut from untested stock from which the 60" by 96" fracture panels were taken. Finally, four 14" by about 34" T-L panels were also taken from the subject untested stock. Boeing retained one L-T panel from both the tested and untested material (both thicknesses) and sent the remaining 10 L-T and 4 T-L panels (of each thickness) to NASA for

distribution to the participating laboratories. The layout diagrams for these panels were completed in late 1992 and are shown in the Boeing 1992 annual report for this program.

As a part of the contract effort, Boeing will test Kahn tear-test and Charpy V-notched specimens in conjunction with 9" wide center cracked specimens. The data will be evaluated and correlated with the fracture data from the valid fracture toughness tests on the 2024 and RX 818 alloys. Two tests will be made with each of these subsize specimens in the L-T and T-L test directions. See Figs. 6 and 7.

Data presented at the semiannual review meeting has been analyzed with respect to strength and fracture toughness and is shown in Fig. 8. Alloy XR-818 continues to look promising, but the recent exposure data for 7000 hrs. at 225°F indicates that there may be a serious stability issue at the use temperature for a Mach 2.0 HSCT. Grain boundary embrittlement of some type is suspected and will be explored at NASA, UVA and at Reynolds.

REPORT DOCUMENTATION PAGE			Form Approved OMB No. 0704-0188	
<small>Public reporting burden for this collection of information is estimated to average 1 hour per response, including the time for reviewing instructions, searching existing data sources, gathering and maintaining the data needed, and completing and reviewing the collection of information. Send comments regarding this burden estimate or any other aspect of this collection of information, including suggestions for reducing this burden, to Washington Headquarters Services, Directorate for Information Operations and Reports, 1215 Jefferson Davis Highway, Suite 1204, Arlington, VA 22202-4302, and to the Office of Management and Budget, Paperwork Reduction Project (0704-0188), Washington, DC 20503.</small>				
1. AGENCY USE ONLY (Leave blank)		2. REPORT DATE September 1996		3. REPORT TYPE AND DATES COVERED Contractor Report
4. TITLE AND SUBTITLE NASA-UVa Light Aerospace Alloy and Structures Technology Program: Aluminum-Based Materials for High Speed Aircraft Semi-Annual Report January 1, 1993 - June 30, 1993			5. FUNDING NUMBERS G NAG1-745 WU 537-06-20-06	
6. AUTHOR(S) E. A. Starke, Jr., Editor				
7. PERFORMING ORGANIZATION NAME(S) AND ADDRESS(ES) School of Engineering and Applied Science University of Virginia Thornton Hall Charlottesville, VA 22903			8. PERFORMING ORGANIZATION REPORT NUMBER	
9. SPONSORING / MONITORING AGENCY NAME(S) AND ADDRESS(ES) National Aeronautics and Space Administration Langley Research Center Hampton, VA 23681-0001			10. SPONSORING / MONITORING AGENCY REPORT NUMBER NASA CR-4754	
11. SUPPLEMENTARY NOTES Langley Technical Monitor: Dennis Dicus Final Report				
12a. DISTRIBUTION / AVAILABILITY STATEMENT Unclassified - Unlimited Subject Category 26 Availability: NASA CASI, (301) 621-0390			12b. DISTRIBUTION CODE	
13. ABSTRACT (Maximum 200 words) This report is concerned with "Aluminum-Based Materials for High Speed Aircraft" which was initiated to identify the technology needs associated with advanced, low-cost aluminum base materials for use as primary structural materials. Using a reference baseline aircraft, these materials concept will be further developed and evaluated both technically and economically to determine the most attractive combinations of designs, materials, and manufacturing techniques for major structural sections of an HSCT. Once this has been accomplished, the baseline aircraft will be resized, if applicable, and performance objectives and economic evaluations made to determine aircraft operating costs. The two primary objectives of this study are: (1) to identify the most promising aluminum-based materials with respect to major structural use on the HSCT and to further develop those materials, and (2) to assess these materials through detailed trade and evaluation studies with respect to their structural efficiency on the HSCT. This Semi-Annual Report covers the progress made from January 1, 1993, to June 30, 1993.				
14. SUBJECT TERMS Aluminum alloys, High speed aircraft, Composites			15. NUMBER OF PAGES 226	
			16. PRICE CODE A11	
17. SECURITY CLASSIFICATION OF REPORT Unclassified	18. SECURITY CLASSIFICATION OF THIS PAGE Unclassified	19. SECURITY CLASSIFICATION OF ABSTRACT	20. LIMITATION OF ABSTRACT	